BUCKLING OF AXIALLY COMPRESSED CYLINDRICAL SHELLS WITH LOCAL IMPERFECTIONS

Shankar by

S.Krishnakumar

B.Tech.,M.S.,M.I.E.Aust.,

submitted in fulfillment of the requirements

for the degree of

Doctor of Philosophy

in the

Department of Civil and Mechanical Engineering

UNIVERSITY OF TASMANIA

Australia

November 1988

I hereby declare that this thesis does not contain any material which has been accepted for the award of any other degree or diploma in any University, and that, to the best of my knowledge and belief, this thesis does not contain any copy or paraphrase of material previously written or published by any other person, except when due reference is made in the text of the thesis.

(S.Krishnakumar)

Krishnakumar Shankar

To

Father

CONTENTS

ABSTRACT

Thin cylindrical shells in axial compression are known to be highly sensitive to geometric imperfections. Previous theoretical and experimental investigations have mostly concentrated on imperfections of small amplitude extending over the whole surface or at least over the whole circumference of the cylinder. Local imperfections occurring naturally are often found to be similar in form to the diamond-shaped facets of the buckle pattern of the collapsed cylinder. The current study is aimed at investigating experimentally the effect of such facet-shaped dimples on the load bearing capacity of the axially loaded circular cylindrical shell and evaluating the applicability of the space frame theory in predicting the same.

The space frame theory predicts the secondary collapses observed in cylindrical shells under axial compression in terms of the buckling strengths of the diagonal members of an equivalent space frame having the geometry of the Yoshimura pattern. The proposed application of the space frame model to estimate the load carrying capacity of shells with diamond-shaped defects is based on the hypothesis that the effect of such a defect is similar to that of a facet of the same size in a buckled cylinder. Central to this model is the effective width of the flanges of the diagonal members of the space frame. In the present work modifications are introduced in the space frame theory to accommodate an analytical determination of the effective width of the flanges. Geometric constraints on the buckled configuration of the axially loaded cylinder are also investigated.

For the experimental investigations, a rigid compression testing machine was designed and fitted with a sensitive optical system, based on the grid reflection technique, to monitor the growth of initial imperfections and the imposed defects during loading. Over thirty high quality spun-cast epoxy shells were tested before and after imposing the defects. The preliminary tests conducted assess the validity of the space frame theory in predicting the secondary collapse loads and that of the geometric criteria developed for the post-buckling mode. The experiments with imposed defects investigate the effect of changes in the defect size on the collapse load, and the influence of additional defects imposed on the shell. In addition to evaluating the applicability of the space frame theory, the test results are used to develop empirical formulae for estimating the effect of facet-shaped local defects on the collapse of axially loaded circular cylindrical shells.

ACKNOWLEDGEMENTS

The author is greatly indebted to Dr.C.G.Foster for introducing him to the fascinating field of Shell Stability and for the constant encouragement, guidance and support he provided during every stage of this study. The fruits that are gathered herein are blossoms of the seeds sown and nurtured by Foster.

The author is also grateful to the many others without whose assistance this work could not have been completed. In particular he wishes to thank

: Mr.Basil Stiberc and the other staff members of the Engineering workshop for the manufacture of the testing apparatus and for their patient and prompt assistance in preparing the end-rings for the testing of each shell,

: Mr.Peter Jordan for preparing the drawings for the loading frame,

: all the other academic as well as non-academic staff members of the Engineering faculty for their encouragement and support,

: Mr.Pichit Rerkshanandana, discussions with whom led to the germination of many of the ideas presented herein,

: and the University of Tasmania for the financial assistance provided.

Finally the author would like to acknowledge the forbearance and the sacrifices of his wife and children, without which this study and the preparation of the thesis would not have been possible.

CHAPTER 1

INTRODUCTION

The present study was undertaken with the objective of investigating the effect of local defects on the buckling of axially compressed circular cylindrical shells, with the aid of the Space Frame Theory.

The effect of initial imperfections on the axial load carrying capacity of cylindrical shells has been the subject of a large number of investigations in the last four decades. Beginning with the earliest studies, in which imperfections of the same shape as the buckling modes of the cylinder were considered, a variety of imperfection shapes have been investigated, both theoretically and experimentally. These studies have conclusively shown that the stability of the cylindrical shell is extremely sensitive to very small imperfections extending over the whole surface or at least over the whole circumference of the cylindrical shell. While the emphasis has been on imperfections of small amplitude spanning over a large area, imperfections of large amplitude spanning over a small area have mostly been neglected. Thus, in spite of the large body of literature that has been produced on the effect of imperfections, if one were to ask "what is the effect of a single large dimple on the shell wall ?", the answer is not readily available. To be fair, it must be admitted that quite a substantial amount of information is available on the effect of circular and non-circular cut-outs. However other than

cut-outs, local defects, particularly of the nature of dimples or indentations on the shell wall, have received very little attention.

Imperfections in the form of local geometric deviations of the shell wall may easily be caused during the manufacturing stage, or in the course of handling and erection, or even under service conditions of the shell structure. Such imperfections are generally large, in the sense that the maximum deviation of the shell wall from the true cylindrical shape can be many times the thickness of the shell (even though they might cover only a small area of the surface of the cylinder), and thus do not come under the category of the small general imperfections which have formed the subject of most of the theoretical investigations conducted so far. Further, local defects when present on a shell, are usually present in addition to the general imperfections, which are more or less unavoidable. It is obviously of practical interest to investigate the detrimental effect of such local defects on the load bearing capacity of cylindrical shell structures.

Although local geometric deviations in the shell wall can be of many different shapes, one of the most commonly occurring forms, is that of the diamond shaped dimple, that is, the shape of a single buckle in the well-known Yoshimura pattern of the buckled cylinder. This, perhaps, is the most natural shape that a local deformation, say that caused by an accidental bump on the shell wall, can assume. Beer cans that have been kicked around, for example, usually have defects of this shape. The photograph on page 3, is another example of the

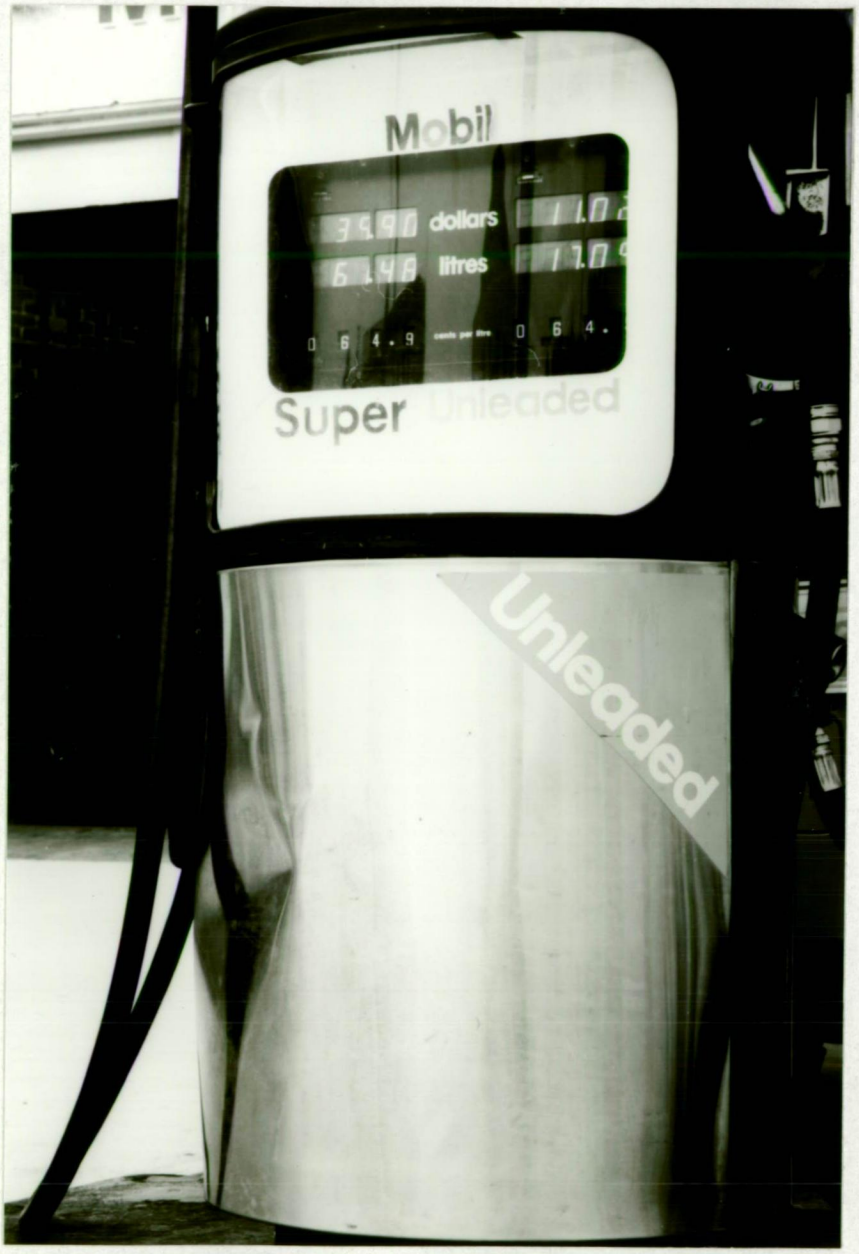

Figure 1
Local Defect in a Cylindrical Shell Structure

"naturally" occurring defect shape, that the author happened to notice in passing. It is interesting that the shell usually prefers to develop two nodes, at either end of the central (tangential) fold, rather than one, when it is subjected to a lateral impact. The reason for this preference is probably the same as that which motivates the axially compressed shell to assume the Yoshimura pattern, that is, the deformed surface in either case becomes a near developable surface. It may be observed that in both cases the diagonal members are not actually straight, hence the deformed pattern is not exactly diamond-shaped; but for practical purposes, it may be approximated by the diamond-shaped facet of the Yoshimura pattern.

On the basis of the similarity in the shape of such defects and the facets of the buckled configuration, it is conceivable that these defects behave like the facets in a buckled cylinder and that the collapse of a shell with diamond-shaped defects is similar to the secondary collapse of a shell with initial buckles of the same size. The secondary collapse of the axially compressed cylindrical shell is investigated using the space frame model, which approximates the post-buckled strength of the cylinder to that of an equivalent space frame having the geometry of the Yoshimura pattern. The basis for the model is the observation that the axial load carried by the buckled shell is mostly supported by internal stresses along the folds of the buckle pattern and hence the facets can be approximated by triangular frames. Making this approximation, the secondary collapse loads for the axially loaded cylindrical shell is predicted in terms of the buckling strengths of the diagonal members of the space frame.

Since there is not much empirical data available on the effect of local defects, the main objective of the proposed study has been to obtain experimental data by conducting a series of tests on shells of different dimensions with imposed defects of different sizes. This experimental data is used to assess the validity of the space frame theory in predicting the axial load bearing capacity of cylindrical shells with local defects. Buckling and post-buckling tests were also conducted on the shells before imposing the defects. The former was done to assess the extend of load reduction caused by factors other than the imposed defect, with a view to isolating, if possible, the detrimental effect of the imposed local defects. The post-buckling tests were conducted to obtain experimental data on secondary collapses, which was used to assess the basic theory of the space frame model.

The theoretical investigations presented in this work concern firstly the space frame theory and secondly the post-buckling modes of the axially compressed cylindrical shell. Regarding the space frame theory, the investigations were mainly carried out with a view to establishing the effective width of the diagonal members of the space frame, resulting in significant modifications to the originally proposed model. With regard to the second aspect, geometrical considerations of the observed buckle patterns are presented, which yield simple analytical expressions to predict the number of circumferential lobes in the post-buckling mode.

The first three chapters in the thesis, including this one, are introductory. In chapter two a survey of the developments in research on the buckling behaviour of axially loaded cylindrical shells is presented, providing the necessary background for the current work. Chapter three gives a brief description of the space frame theory as it was originally proposed by Foster.

The next three chapters deal with the theoretical investigations. In chapter four a large deflection analysis of simply supported isosceles triangular plates is conducted in an attempt to establish the effective width of the sides of the triangular facets of the space frame. While this attempt was unsuccessful, another approach was used to establish the effective width, which is presented in chapter five, along with the resulting modifications to the space frame theory. The geometrical aspects of the buckled configuration of the axially loaded cylindrical shell are investigated in chapter six.

The experimental work is presented in chapters seven, eight and nine. In chapter seven, the experimental set-up, loading frame and the optical system used to monitor the growth of initial imperfections as well as the imposed defects are described. Chapter eight presents the experiments conducted on shells without any imposed local defect. The results of the tests with imposed defects are presented in chapter nine. Based on these results, empirical relations are developed for predicting the effect of local defects.

Chapter ten provides the conclusion to the thesis.

CHAPTER 2

BUCKLING OF CYLINDRICAL SHELLS IN AXIAL COMPRESSION - HISTORICAL BACKGROUND

The Classical buckling load for an isotropic circular cylindrical shell in axial compression is given by

$$P_{cl} = \frac{2 \pi E t^2}{\sqrt{3 (1-\nu^2)}} \qquad (2.1)$$

where E is the Young's Modulus, ν the Poisson's ratio, and t the thickness of the shell. This solution was obtained before the First World War by Lorenz, Timoshenko and Southwell[1]. The classical load, however, is seldom realized in actual test conditions. In experiments conducted during the first half of the century, test results ranged between 15 and 60% of this theoretical value. The first attempt to explain the discrepancy between theory and experiment was made in 1934 by Donnell[2] who introduced a set of simplified non-linear equations for the large deflection analysis of cylindrical shells.

Donnell's non-linear theory is based on the assumptions of Kirchhoff-Love hypotheses and shallow shell approximations. The latter assumption restricts the validity of the theory to situations in which the normal deflection predominates over the in plane displacements. Despite this, owing to its relative simplicity and practical accuracy for short and moderately long cylinders, Donnell's theory has become

the basis of most of the theoretical investigations on the buckling and post-buckling of cylindrical shells. A more complete set of non-linear equations were developed around the same time by Flügge[3], without resorting to the shallow shell approximations. Flügge's theory is often employed to check the accuracy of Donnell's equations, or in situations where the latter is not applicable.

Donnell's classic paper[2] was followed by a series of theoretical and experimental investigations, which, spread over the next four decades, have led to a more complete understanding of the phenomenon of shell buckling and the special role played by initial imperfections in it. The major developments in bridging the gap between theory and experiment are summarized in the following sections.

2.1 Effect of Edge Restraints and Prebuckling Deformations

The classical theory ignores boundary conditions and approximates the prebuckling state with a membrane solution. Several researchers[4-11] investigated the effect of boundary conditions and the prebuckling bending deformations caused by edge restraints, by numerical as well as analytical methods. The final outcome of these investigations (when both effects are included) are summarized in Table 2.1. The first four cases (C1 to C4) correspond to clamped edge conditions, while the last four (S1 to S4) refer to simply supported end conditions. (The data presented in this table is from ref.11, and is in agreement with the numerical results of ref.10).

Table 2.1

Case	Boundary Conditions*	P/P_{cl}	N/N_{cl}
C1	$w = w_{,x} = u = v = 0$	0.92	0.95
C2	$w = w_{,x} = u = N_{xy} = 0$	0.92	0.95
C3	$w = w_{,x} = N_x = v = 0$	0.90	0.90
C4	$w = w_{,x} = N_x = N_{xy} = 0$	0.90	0.90
S1	$w = w_{,xx} = u = v = 0$	0.85	0.95
S2	$w = w_{,xx} = u = N_{xy} = 0$	0.50	N = 1
S3	$w = w_{,xx} = N_x = v = 0$	0.83	0.90
S4	$w = w_{,xx} = N_x = N_{xy} = 0$	0.50	N = 1

The constant values given in Table 2.1, of course, pertain only to thin shells of medium length. Thick short shells, which buckle in the axisymmetric mode, have higher buckling loads, and very long shells fail by Euler buckling at lower loads. The effect of elastic edge restraints was also investigated[12], and it was shown that very little elastic restraint is sufficient to obtain buckling loads close to the values quoted above. Although the critical load is obtained as half that of the classical load in two cases of simple support (S2 and S4), the condition that the edges of the shell be free to move in the tangential direction is seldom realized in practice. Hence in actual test conditions, the effects of edge restraint and prebuckling deformations account for only 10 to 15% reduction in the theoretical load, still leaving a large gap between theory and experiment.

* Strictly speaking, these conditions are for incremental quantities; similar conditions are employed in the prebuckling situation also.

2.2 Large Deflection Analysis

A major breakthrough in understanding the buckling phenomenon was achieved when Von Kármán and Tsien[13], using equations similar to Donnell's and a deflection function that roughly approximated the diamond buckling pattern observed in experiments, extended the analysis to the post-buckling regime. Their investigations indicated the presence of post-buckling equilibrium states at loads far below the critical load, which were connected to the prebuckling linear path by steeply ascending curves forming very sharp cusps at the bifurcation point (see the curve corresponding to U = 0 in Figure 2.1, page 14). It was immediately recognized that the presence of initial imperfections, or that of external disturbances, would cause the shell to jump to these lower equilibrium positions before reaching the maximum theoretical load. On this basis, it was proposed that the minimum post-buckling load could be taken as the safe design load. Several researchers[14-17] refined the approach of Von Kármán and Tsien, by increasing the number of terms used to express the deflection, and minimizing the total potential energy with respect to the aspect ratio as well as the wave number parameter, in an attempt to find the "true" minimum. This resulted in producing lower and lower values of the minimum post-buckling load, until Hoff, Madsen and Mayers[18] showed that as the number of terms is increased indefinitely, the minimum load required to maintain the post-buckled state approaches zero, the thickness to radius ratio of the shell tends to zero, and the deflection pattern approaches the exact Yoshimura pattern.

2.3 The Yoshimura Pattern

The physical explanation for the presence of postbuckling equilibrium states with lower energy than the prebuckled state became apparent when Yoshimura[19] showed that the buckled surface of the cylindrical shell in axial compression is a near developable surface. He suggested that the observed buckling pattern can be approximated by a concave polyhedron made up of triangular facets (this has come to be known as the Yoshimura pattern - see Figure 2.3, page 21) which can be obtained by an inextensional transformation from the original cylindrical surface. Although the intermediate stages in this transformation would involve stretching of the middle surface, the fact that the final buckled state is almost inextensional (in contrast to the buckling of a flat plate) means that the total strain energy of the shell in its buckled configuration mostly consists of the bending strain energy required to form the ridges between the triangular facets. Since the stiffness of the shell is proportional to the cube of its thickness, for a thin shell, the energy involved in bending is small and hence the total strain energy in the buckled configuration much smaller than the extensional strain energy in the compressed state just before buckling. This explains the sudden snapping with loud report caused by the release of energy and the small value of the load required to maintain the buckled configuration. Of course if the thickness were vanishingly small, the resistance to bending would be negligible; hence the shell would assume the exact Yoshimura pattern, and no load would be required to maintain this shape.

2.4 Experiments on Near Perfect Shells

Meanwhile considerable advances were made in experimental techniques. With sophisticated testing equipment it was possible to subject the shell to uniform loading conditions without the problems of misalignment and eccentricity. Improved methods of fixing the shell to the end plates ensured almost complete circularity of the ends of the shell. At the same time using advanced manufacturing techniques like electroplating[20,21] and spincasting[22-24], shells with almost perfect cylindrical shape and minimum variations in thickness (of the order of 2 to 5%) could be made. Tests conducted on these near perfect shells have yielded buckling loads within 10 to 20% of the classical load, i.e., in close agreement with the reduced theoretical value taking into account the edge restraints and prebuckling bending deformations. While these experiments proved that the theory is indeed valid for perfect cylindrical shells, they also showed that initial imperfections are the main culprits in reducing the buckling load in normal test conditions. It became clear that external disturbances present during usual test conditions are hardly of any consequence to warrant scrutiny; although some experimenters[25-27] have shown that by deliberately imposing such disturbances (like applying lateral forces on the shell), the shell can be made to buckle prematurely.

2.5 Effect of Initial Imperfections

The effect of initial geometric imperfections on the buckling behaviour of axially compressed cylindrical shells has been

the subject of many investigations in the past several decades. The first successful attempt in this regard, using the non-linear approach, was that of Donnell and Wan[28]. Improving upon Donnell's earlier work[2], they considered an initial deviation of the same shape as the assumed normal deflection of the shell, and showed that with increasing amplitude of the initial deviations the peak of the load deflection curve dropped drastically (see Figure 2.1, taken from ref.28). Expressing the amplitude of initial deviation in terms of a constant "Unevenness parameter" U, and the square of the radius to thickness ratio, they showed that a small value of 0.00015 for the constant U was sufficient to explain most of the discrepancy observed between theory and experiment.

The quantitative results of Donnell and Wan are only approximate in nature, and are seldom used for design purposes. Also it has often been criticized on the grounds that the imperfection considered does not have any definite shape. However the significance of their work lies in the fact that it showed, at least qualitatively, the degrading effect of initial imperfections and at the same time laid the foundations for the non-linear approach to imperfection analysis. Improvements to this work were first attempted by Lee[29] as well as Lu and Nash[30]. Babcock and Sechler[20], using the non-linear equations of Donnell, studied the effect of initial deviations of constant curvature and in the form of a half sine curve extending over the whole length of the shell. They also conducted experimental studies on shells of the same shape manufactured by electroforming. Dym and Hoff[31], using a perturbation approach to solve the non-linear

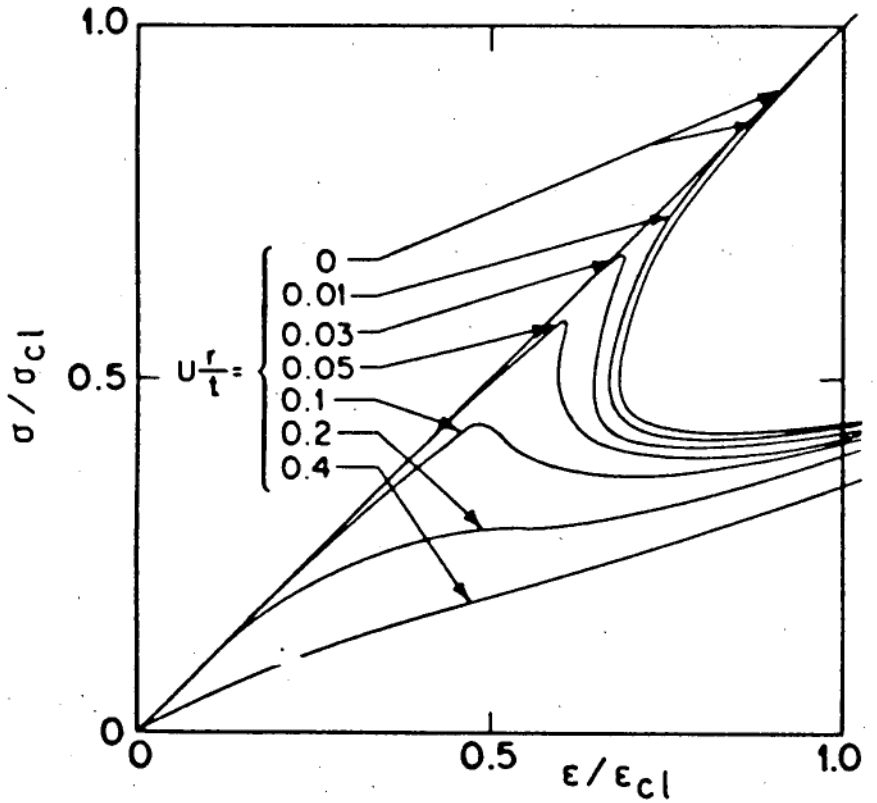

Figure 2.1
Effect of Imperfections on
the Load - Deflection Curves
(Source Donnell & Wan, Ref.28)

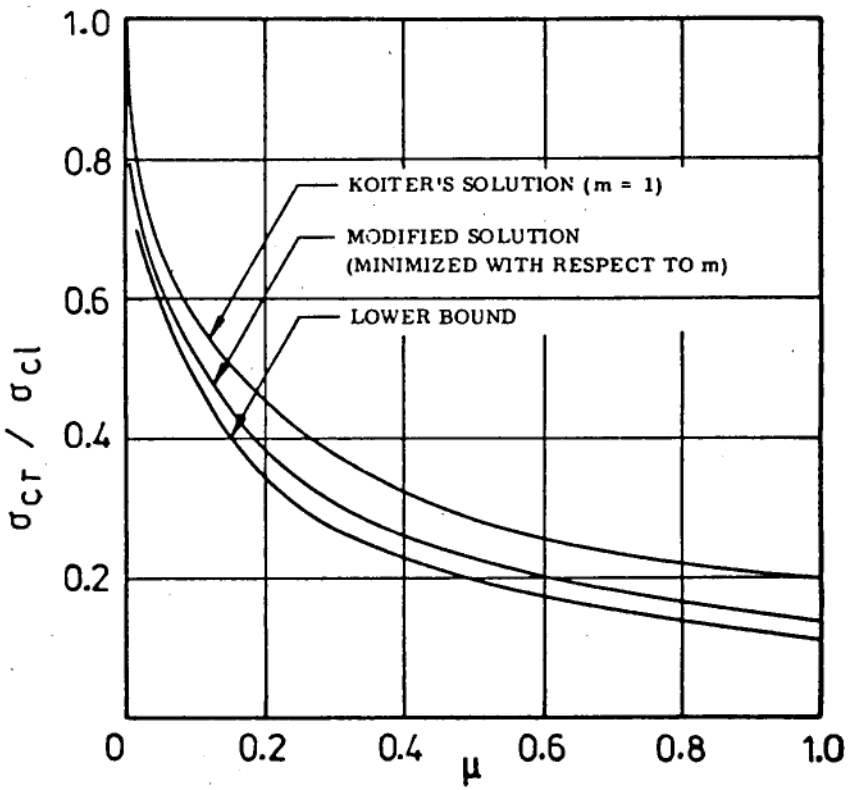

Figure 2.2
Buckling of Long Cylinders with
Periodic Initial Imperfections of
Amplitude μt. (Source Almroth, Ref.12)

equations of Donnell for simply supported shells of finite length, showed that effect of imperfections in the shape of the buckling mode is nearly the same as that obtained for the infinitely long shell. The effect of prismatic imperfections in the shape of flat spots extending over the full length of the cylinder was investigated by Bhatia and Babcock[32].

A large number of theoretical investigations on the effect of initial imperfections are based on the asymptotic theory of initial post-buckling behaviour developed by Koiter[33,34]. Classifying the bifurcation point into three types, asymmetric, stable symmetric and unstable symmetric, Koiter showed that the imperfection sensitivity of a structure depends on the type of bifurcation point associated with it. In particular, for the cylindrical shell in axial compression, he showed that small imperfections in the shape of the classical axisymmetric buckling mode can significantly reduce the buckling load and obtained an asymptotic solution for small but finite values of the imperfection amplitude. Almroth[12] modified Koiter's approximate analysis by including the effect of boundary conditions and non-linear prebuckling deformations and assuming a more general buckling pattern, to obtain results which predicted slightly lower buckling loads. Figure 2.2 showing the results of Koiter and Almroth is from ref.12.

Experimental verification of Koiter's predictions on the effect of axisymmetric imperfections was obtained by Tennyson and Muggeridge[35], who conducted an extensive testing program on accurately made spun-cast acrylic shells containing various types of axisymmetric

imperfections. Extending Koiter's theory to cover axisymmetric imperfections of different wavelengths they obtained results which were in close agreement with the observed buckling loads. These studies indicated that the minimum buckling load is obtained when the wavelength of the axisymmetric imperfection is equal to that of the classical axisymmetric buckling mode. The effects of random and localized axisymmetric imperfections were also investigated[36-38]. Theoretical investigations on the effect of random axisymmetric imperfections were conducted by Amazigo[39] and Van Slooten et al[40], using a probabilistic approach. Using the same approach, Hansen[41,42] has extended Koiter's asymptotic theory to the case of general random imperfections. Hansen's studies have indicated that non-axisymmetric and general random imperfections can have a greater degrading effect than axisymmetric imperfections, on the buckling of axially loaded cylindrical shells.

The effect of actual imperfections present on shells was first investigated by Arbocz and Babcock[43]. By carrying out surveys of imperfect shell models and obtaining Fourier series representations of the actual initial deviations of the shell wall, they made theoretical predictions for the buckling load which were in reasonable agreement with the observed test values. This analysis was extended to consider the effects of end conditions and prebuckling deformations by Arbocz and Sechler[44]. Improving on these works, sophisticated measurement techniques as well as computer programs have now been developed for the evaluation of buckling loads for stiffened and unstiffened shells based on actual imperfection measurements[45-47].

While a variety of imperfection shapes have thus been investigated, a notable omission in this regard is that of specific local deformations. It may also be pointed out that while the theoretical studies using the asymptotic approach is strictly restricted to small initial deviations, the applicability of the non-linear approach using Donnell's equations for local deformations of large amplitude is also doubtful, owing to the shallow shell approximations involved.

The effect of diamond-shaped local dents (of the type considered in this study) on the ultimate strength of thick tubular members have been previously investigated[48-50]. However failure in these tubes is caused by yielding, and bears no resemblance to the elastic buckling of thin cylindrical shells.

Experimental studies on the effect of concentrated lateral loads on the buckling of axially loaded cylindrical shells have been conducted by Ricardo[26,27] and Babcock. (The latter's work is mentioned by Okubo et al[51]., who studied the influence of lateral loads on the stability of cylindrical shells in bending). Since the lateral load produces a local deformation of the shell wall, this work is of some relevance to the present study, and will be discussed in greater detail when the results of the current experimental work are presented.

2.6 Buckling and Post-buckling Modes

According to classical theory, the buckling mode for the non-axisymmetric case is not uniquely defined. The minimum value of the buckling load is obtained by using the condition[1]

$$N^2 + q^2 - q\, q_0 = 0 \qquad (2.2)$$

where N is the number of circumferential waves, q is the axial wavenumber*; and q_0 is the critical wave number for axisymmetric buckling given by

$$q_0 = \left[12\,(1 - \nu^2)\, R^2 / t^2 \right]^{1/4} \qquad (2.3)$$

Thus any combination of N and q which satisfies equation (2.2) is admissible. However, on assuming a square wave formation, i.e., that the wavelengths in the axial and circumferential directions are equal, which gives N = q, eqn.2.2 yields the "classical" value of N as†

$$N_{cl} = \left[\frac{3}{4}\,(1 - \nu^2)\, R^2 / t^2 \right]^{1/4} \qquad (2.4)$$

Non-linear theory, considering the effects of edge restraints and prebuckling deformations, predicts critical values for N which are only 5 to 10% smaller than the above value (see Table 2.1).

The actual number of circumferential lobes observed after the shell has buckled, however, is much smaller than that predicted by

* The axial wavenumber $q = m\pi R/L$, where m is the number of half-waves in the axial direction, R and L the radius and length of the shell.

† The same result may also be derived by putting $dN/dq = 0$ in eqn.2.2 which gives $N = q = q_0/2$.

theory, though the buckles are more or less square. (This discrepancy was also first pointed out by Donnell[2]). While the discrepancy in the buckling loads has been successfully attributed to the presence of initial deviations, imperfections cannot account for the reduction in N, since the latter is observed even in near perfect shells.

Several investigators[22,23,25,52-54] have attempted to determine the initial buckling modes by using high speed photography to record the growth of the deflection pattern during the process of buckling. These studies have shown that in the initial post-buckling stage, the number of circumferential lobes is much higher (close to the value predicted by theory) than that observed at the final stage. On the basis of comparisons between the 45° isoclinics observed on shells made of photo-elastic plastic and those predicted by theory, Tennyson[54] has reported the observation of the classical mode at the inception of buckling. He further states that this initial mode rapidly degenerates into the diamond buckling pattern, and that in the final stage (which is reached within a few milli-seconds) the observed isoclinics bear no resemblance to those predicted, indicating that the theory is valid only in the initial post-buckling stages.

The transition from the buckling mode to the post-buckling mode (the stable configuration observed at the final stage) occurs simply due to the fact that the initial mode is unstable, which is predicted by the theory. What the theory does not predict, or explain, is the reduction in the number of circumferential lobes that occurs during this transition.

Esslinger and Geier[25] have suggested that in the final stage the shell assumes the mode corresponding to the "characteristic curve"; the "characteristic curve" being defined as that curve in the theoretical post-buckling diagram (plotted for different values of N), which gives the minimum possible end-shortening for the shell under consideration. Although it has not been clarified as to why the shell should choose to stop at this particular curve; experimental evidence[11,25] indicates that the number of circumferential lobes actually present in the stable buckled state of the cylinder is much closer to the N corresponding to the characteristic curve than it is to the classical value of N.

De Neufville and Connors[55] as well as Hoff[56] have observed that the post-buckled N depends not only on the radius to thickness ratio but also on the length to radius ratio, and have hence developed empirical formulae relating N to both these quantities. (These relations will be examined in greater detail in Chapter 6).

Finally it may be pointed out that although in theoretical analyses it is generally assumed that the Yoshimura pattern extends over the whole cylinder, the buckle pattern actually observed in controlled end-shortening tests is either the "one tier" pattern, containing only one row of buckles, or the "two tier" pattern, containing two rows of staggered buckles (Figure 2.4). On the basis of the nature of symmetry of the deformations with respect to the middle section of the shell, these two patterns have respectively been labelled as "symmetric" and "antisymmetric" patterns by Yamaki[11].

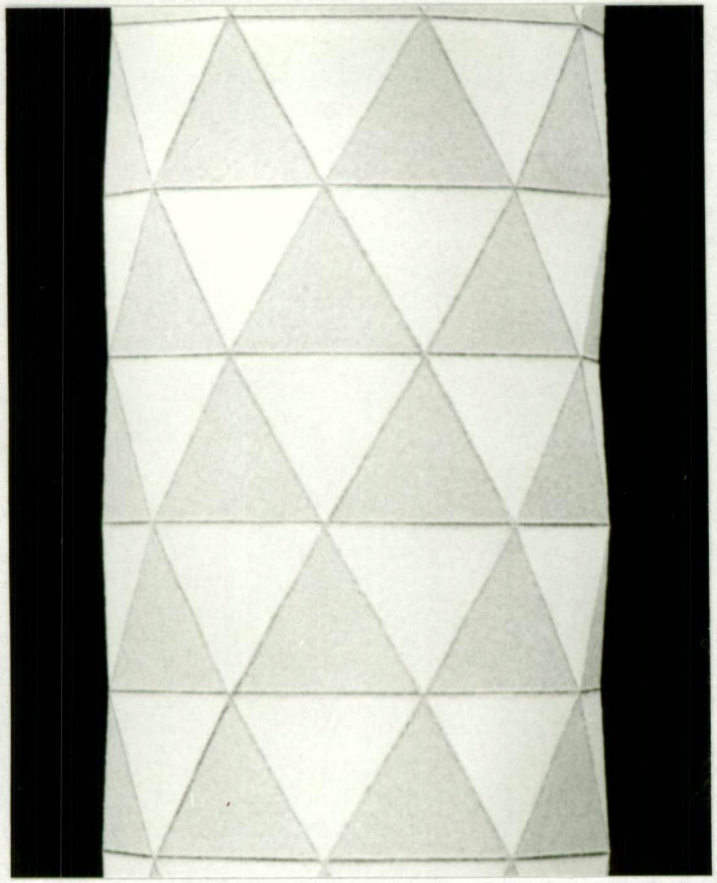

Figure 2.3
The Yoshimura Pattern

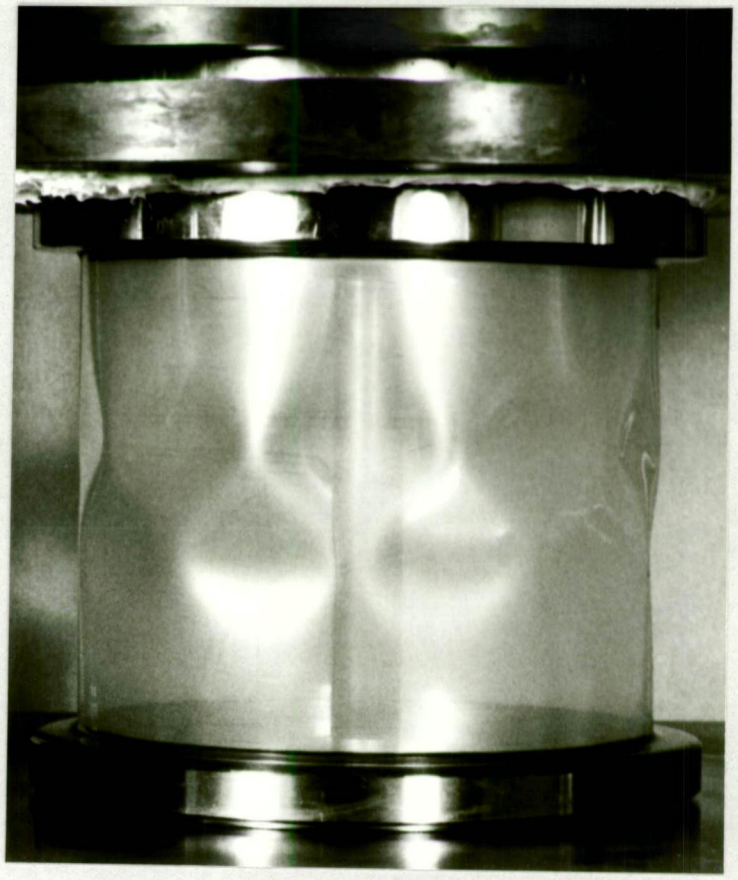

Figure 2.4
Observed Buckle Pattern
(Two Tier)

He further observes that long thin shells with values of the Batdorf parameter* Z greater than or equal to 200 buckled naturally into the two tier pattern, although in the advanced post-buckling stages even the one tier pattern could be realized in these shells by adjusting the deformed shell wall appropriately with the fingertips; whereas in shells with values of Z less than or equal to 100 only the one tier pattern could be realized.

2.7 Secondary Buckling

Many researchers[57,55,11,25] have experimentally investigated the behaviour of the cylindrical shell after it has buckled under axial compression. In these controlled end-shortening experiments, it has been found that on subjecting the shell to further end-shortening after it has buckled, the load gradually rises, until at some specific value of the load, the shell suddenly undergoes a second collapse, snapping through into a new mode which has one circumferential lobe less than the previous configuration. This second mode is also a stable one, so that further end-shortening again raises the load and results in yet another collapse in which the circumferential number of lobes is further reduced by one. The post-buckling behaviour of the axially compressed cylindrical shell is thus characterized by a series of secondary collapses, each one producing a successive reduction in the value of N (see Figure 2.5).

* The Batdorf parameter is given by $Z = \sqrt{(1-\nu^2)}\, L^2/Rt$.

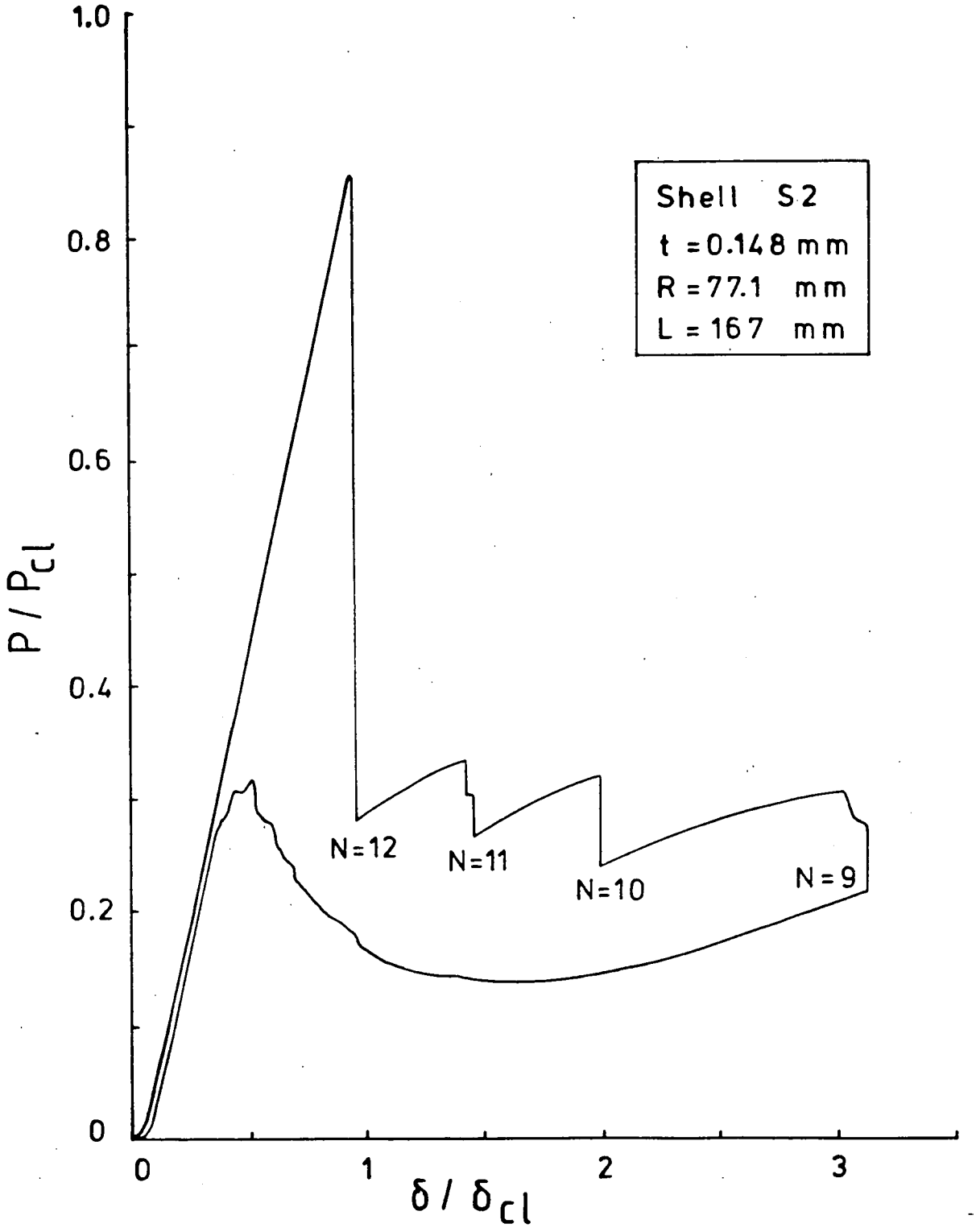

Figure 2.5
Post-Buckling Behaviour of Axially
Compressed Cylindrical Shells

Yamaki (Ref.11, page 223) has reported that only in shells which have buckled into the two tier pattern, the secondary buckling produces a reduction in N; the secondary collapse of shells which have buckled into the single tier pattern results in the formation of additional buckles initiating local torsional deformations. It may also be mentioned that with deflection functions representing the one and two tier patterns, using Donnell's non-linear equations, Yamaki obtained analytical post-buckling curves which were in reasonable agreement with the experimental ones for corresponding values of N. However, his analysis did not include an examination of the stability limits of these curves, hence the critical loads for the secondary collapses were not predicted.

In fact the author is not aware of any attempt that has been made to explain or predict the phenomenon of secondary buckling based on the traditional shell theory. The only explanation offered in this regard is the one that has been put forward by Foster based on the Space Frame Model. The original space frame theory, as proposed by Foster in his Doctoral thesis[58], is presented in the next chapter.

CHAPTER 3

SPACE FRAME THEORY

The space frame model is based on the geometry of the Yoshimura pattern. The theory was developed by Foster[24,58-62] on the basis of numerous studies conducted on paper models, and proposes what is essentially a new interpretation of the buckling behaviour of cylindrical shells, drawing on the similarities between the "concave polyhedron" (Yoshimura pattern) and the buckled cylindrical shell.

Paper models reveal several important aspects concerning the Yoshimura pattern. Firstly, that a thin rectangular sheet of paper can be folded into such a shape is itself proof of the fact that the Yoshimura form is a completely developable surface. Secondly, although the folds of the paper cannot support any transverse moment - so that the folds as well as the corners of the model are in effect hinged or pin-ended - it is seen that the model can support a substantial amount of axial load. Thirdly, since the plane sheets of paper forming the interior of the facets cannot carry much stress, owing to their flexibility, it can be deduced that the end load is mainly supported by internal stresses along the folds of the model. The concentration of the stresses to this region can be attributed to the local increase in effective stiffness along the folds of the Yoshimura model.

The increase in stiffness due to the development of a fold is easily demonstrated by the fact that while a thin sheet of paper

held vertically bends over itself, it can easily be made to stand upright and even support some weight on top by folding it laterally to form an angle (see Figure 3.1). The unfolded sheet buckles under its own weight because its stiffness is very small, being proportional to the cube of the sheet thickness. The bending stiffness of the folded sheet is considerably greater, owing to the redistribution of mass about the centroidal axis, as indicated by the term W^3 in the expression for the minimum moment of inertia of the thin angle section (see equation 3.11, page 42). It may however be observed that the greater section of each flange towards the free end of the folded paper tends to buckle under the load, and is thus ineffective, so that the weight is mainly supported by the two narrow strips of sheet immediately adjacent to the fold.

Although the illustration may sound trivial, it clearly demonstrates the fact that the axial load supported by the Yoshimura model, as well as the buckled cylindrical shell which it represents, is mainly supported by the folds between the facets, and that the central plane regions of the triangular facets are rather ineffective in this regard. These central panels may therefore be removed, leaving only the angular folds of the Yoshimura model, which becomes a space frame as shown in Figure 3.2. The members of the space frame are wide flanged angles, assumed to be pin-jointed so that they carry only axial load which is applied at the corners of the angles. The behaviour of the buckled cylindrical shell may now be studied in terms of this simple space frame model. In fact, as early as 1963, Cox[63] had suggested that such a space frame model could be used to conduct an

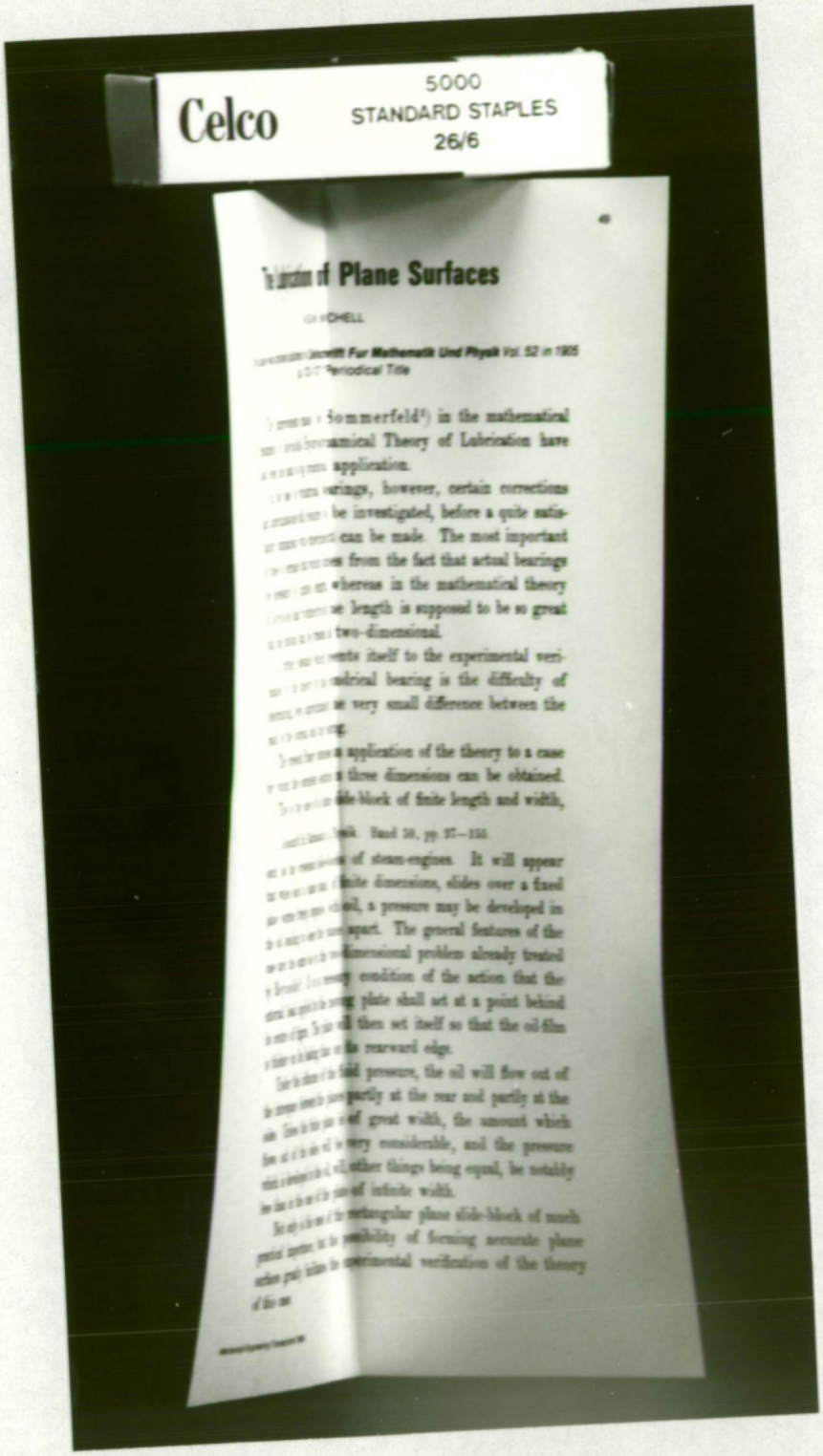

Figure 3.1
A Folded Sheet of Paper Supports
More Than its Own Weight

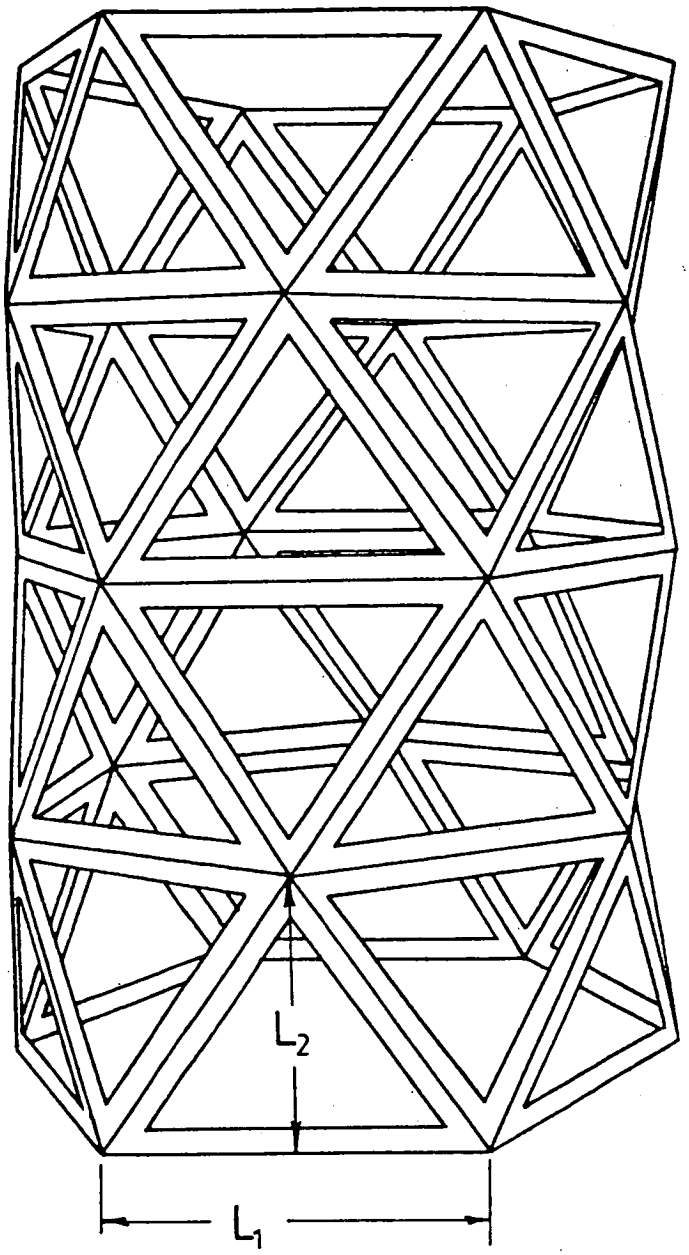

Figure 3.2
Space Frame Model
(Source Foster, Ref.61)

approximate analysis of the post-buckling characteristics of the axially compressed cylindrical shell. However he himself did not persue this suggestion, probably because the secondary buckling characteristics of cylindrical shells were not widely known at that time. It was Foster, who, arriving independently at the same conclusion, realized the potential of the analogy and developed the space frame theory to provide a physical interpretation as well as a mathematical model for the secondary collapse phenomenon.

3.1 Physical Model for Secondary Collapse

A compressive end load on the space frame model produces compression in its diagonal members and tension in the tangential members. Hence the failure of the model takes place due to the buckling of the diagonal members of the frame. It is therefore proposed that the secondary collapse of the buckled cylinder is caused by the buckling of diagonal folds of the Yoshimura pattern. Using a number of paper models for illustration, Foster[58,59] has convincingly described how such a collapse of the diagonal fold can lead to the reduction in the number of circumferential lobes of the buckled cylinder. The argument basically is as follows:

Suppose that the diagonal member AC (Figure 3.3) buckles. Then in its place a new member FB is formed while the other members more or less retain their original configuration. With the formation of the member FB, the folds AB and FC straighten out and the nodes A and C move inward, so that the four triangular panels HAB, ABC, ACF

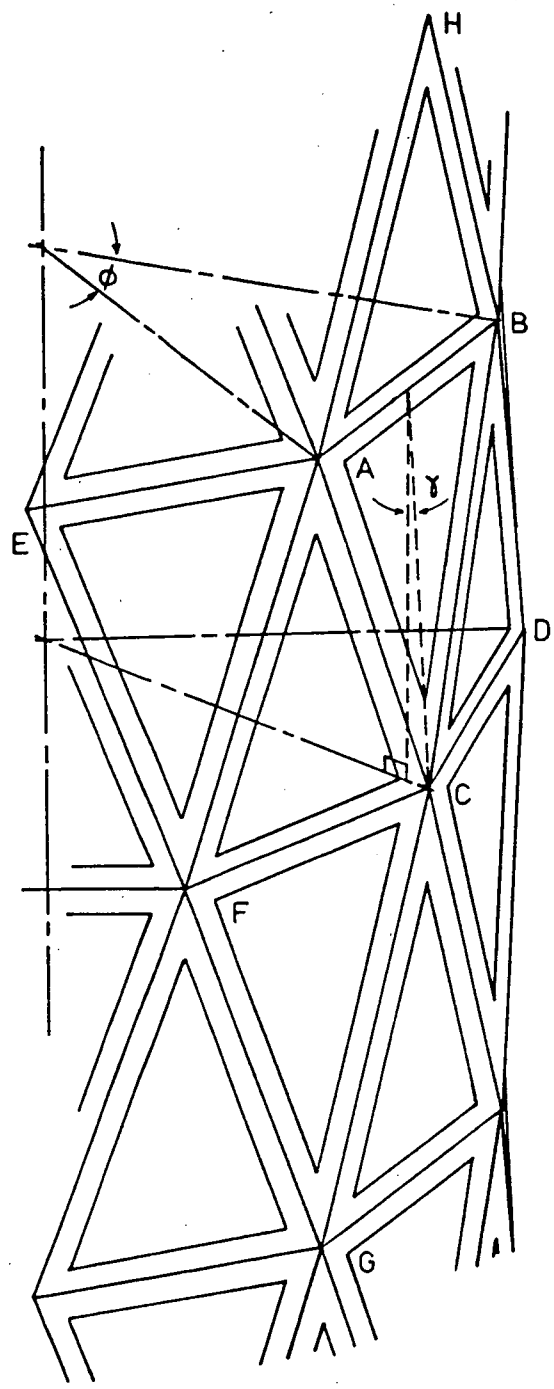

Figure 3.3
Exploded View of Space Frame

and FCG comprising the quadrilateral FHBG are replaced by two new triangular facets, namely FBH and FBG. The members HF and HB now carry compression while the new member FB is in tension. Thus a new pattern is formed in which the facets are not isosceles triangles, since the side HF is twice as long as the side HB. For the same reason, the larger member HF is likely to collapse, hence this pattern is quite unstable and is only an intermediate stage. When the member HF collapses, a new tension member EB is formed, which is tangential and has twice the length of AB. Owing to the straightening of the member EB, the three triangles below it, namely ABC, AFC and AFE, as well as the triangle CFG, will now together constitute a new larger triangular panel, namely EGB; while a similar large facet will be formed on top of EB. Thus in the final stage of collapse, a new Yoshimura pattern is formed with facets twice as long and twice as wide as the facets in the original configuration. Assuming that this occurs all round the circumference, the number of circumferential lobes in the second pattern will be half that of the first pattern. If the Yoshimura model had, say, 32 facets around the circumference to begin with, each successive collapse will reduce this number by half, to 16, 8 and so on, until for N = 2, the model becomes completely flat.

Of course, in the secondary collapse of the cylindrical shell, the circumferential number of lobes is reduced only by one, so the shell goes from, say, N = 12 to N = 11. Thus the final pattern observed in the secondary collapse of the axially loaded cylindrical shell is different from that obtained by the collapse of the Yoshimura model. This is because in a model the original facets as well as their

nodes are fixed in space. Hence the formation of the tension member FB is immediately followed by another collapse (of the member HF) resulting in the reduction of N by a factor of 2. Whereas, in a cylindrical shell which has collapsed elastically, the nodes of the facets are not fixed, and the buckles are free to move around. Hence when the member FB is formed due the collapse of the first diagonal member (see Figure 3.4), the tension in this member will pull the facets on either side together, which expand and move in to take up the position of the collapsed facet. At the same time all other facets around the circumference also expand slightly, thus the final pattern has slightly larger buckles, and only one circumferential number less than the previous pattern.

Thus, according to the proposed model, the secondary collapse is a local phenomenon, i.e., it is only one diagonal member and hence one facet that collapses, while the others merely grow and move sideways to occupy the space created. Since this whole process takes place within a very short period (a few microseconds), it is not normally visible to the eye. However, evidence of such movement by the neighbouring facets to occupy the space of the collapsed facet, can be seen in the photograph on the left of Figure 3.5, which was accidentally recorded by the author. It is perhaps necessary to explain first that the image seen in the photograph is that of the inner surface of the test shell, reflected on the surface of a conical mirror situated at the lower end. The wide inner ring is the top end ring on the shell, while the bottom end ring is seen as the outer rim. The lines in the photograph are the reflections of a cylindrical grid

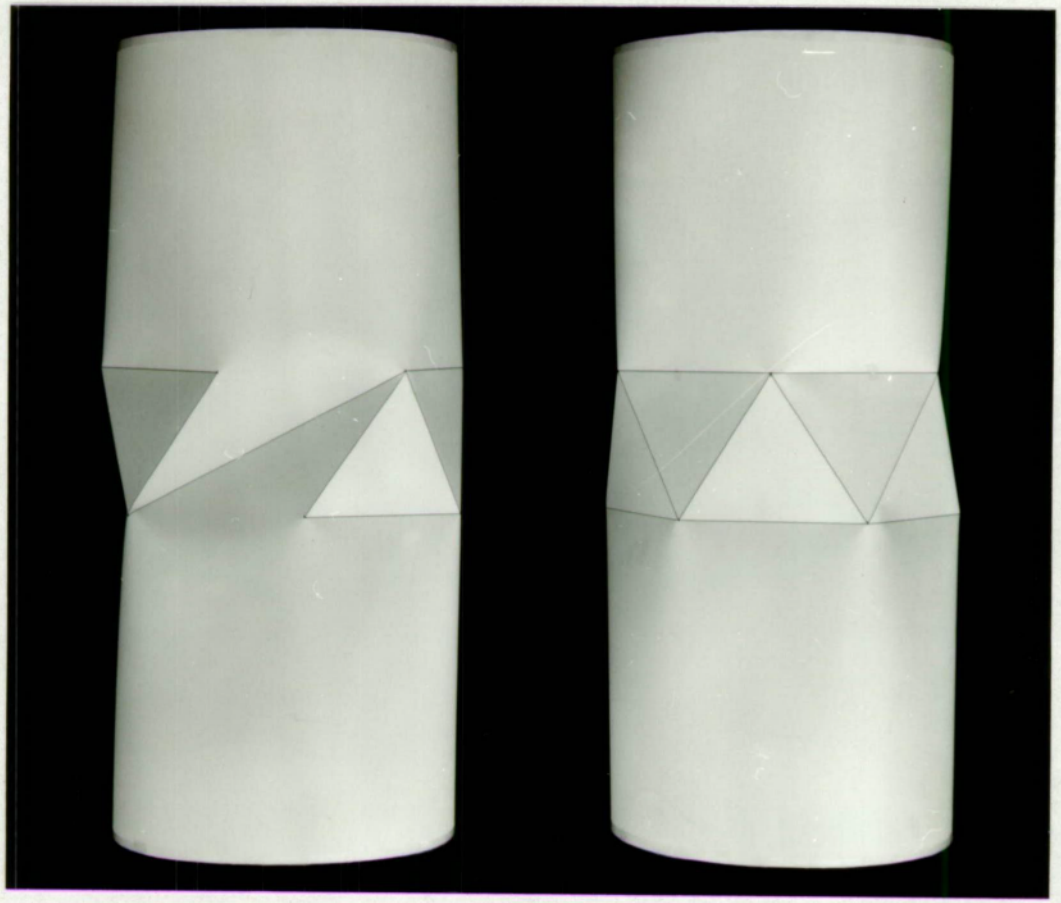

Figure 3.4
Paper Models of Secondary Collapse
(Source Foster, Ref.58)

Figure 3.5. (Shell S38)
Secondary Collapse Observed In Experiment

placed along the axis of the shell. (The optical system used to take these photographs is described in detail in Chapter 7.) The dark images in the middle are the facets of the two tier buckle pattern, the inner row being the top tier and the outer one the bottom tier. The photograph on the left was actually meant to record the first collapse mode which had thirteen lobes around the circumference. However, during the exposure (which takes about 8 seconds), the shell suddenly snapped through into the second mode (with twelve lobes); both these images got superposed on the same film. After this shot, another photograph of the second mode was taken, which is shown to the right, for comparison. It can be seen from the first photo, that the collapse occurred in a facet at about the twelve o'clock position. The movement of the adjacent buckles towards this position is clearly visible. The slight expansion of the neighbouring facets is also visible in the photograph. The buckles towards the bottom of the photograph seem more or less unaffected by the whole process. It may be mentioned that a similar superposed image, showing the lateral movement of the adjacent facets to occupy the position of the collapsed facet, was also obtained (again accidentally) in a test on another shell, S8, when it collapsed from a secondary mode of N = 10 to N = 9 while being photographed.

Thus it is seen that the space frame model provides a fairly accurate description of the physical process of secondary collapse in axially loaded cylindrical shells. The theoretical analysis developed by Foster[58,60] for predicting the collapse loads, is outlined in the following sections.

3.2 Basic Relations

Noting that the buckled shape is an inextensional form, for a cylinder of radius R, the length L_1 of the tangential members is given by

$$L_1 = 2\pi R/N \tag{3.1}$$

where N is the circumferential number of facets*. Denoting the height of the facets by L_2 (see Figure 3.2), the aspect ratio of the facet is defined as

$$\lambda = L_2 / L_1 \tag{3.2}$$

The length of the diagonal member $L_d = L_1 \left[\lambda^2 + \frac{1}{4}\right]^{1/2}$ (3.3)

From the geometry of the space frame (Figure 3.3), the angle θ between the facets adjacent to the diagonal member can be established as

$$\cos(\theta/2) = \sin(\varphi/4) \left[1 + (\frac{1}{2\lambda})^2\right]^{1/2} \tag{3.4}$$

where the angle subtended by the facet at the axis $\varphi = 2\pi/N$. The inclination of the facets to the vertical plane may be obtained as

$$\gamma = \sin^{-1}\left[\frac{1}{2\lambda} \tan(\varphi/4)\right] \tag{3.5}$$

For a given end load P acting on the space frame, by considering the axial equilibrium at the nodes, the force P_1 in the diagonal members

* The notations used are listed at the end of the chapter.

can be shown to be

$$P_1 = \frac{P}{2N}\left[\frac{4\lambda^2 + 1}{4\lambda^2 - \tan^2(\varphi/4)}\right]^{1/2} \qquad (3.6)$$

From radial equilibrium, the force P_2 in the tangential members is obtained as

$$P_2 = \frac{-P_1}{\left[1 + \cos(\varphi/2)\right]\left[\lambda^2 + \frac{1}{4}\right]^{1/2}} \qquad (3.7)$$

It may be pointed out that in this and the following discussion, the compressive force is taken to be positive, so that the negative sign in eqn.3.7 indicates tension in the tangential member. Since secondary collapse has been shown to be caused by the buckling of the diagonal member, the end load P at which secondary collapse occurs can be obtained from eqn.3.6, if the critical value of P_1 at which the diagonal member buckles can be established. However, at this stage some additional elements are introduced, so that the model considered by Foster for the buckling of the diagonal member is not that of a simple Euler column. This model is described below.

3.3 Model for collapse of Diagonal Member

In section 3.1, it was shown that the collapse of the member AC results in the formation of a new member FB. Although in the final stage this member is in tension, at the beginning of the collapse, the two halves of FB are in compression. Hence initially, the deflection of the diagonal member inwards is constrained by the forces in these

members. To account for this, Foster introduced springs on either side of the diagonal member[58,60], as shown in Figure 3.6. While these springs greatly enhance the buckling strength of the column, they also ensure that the buckling takes place only inwards, as it does in the Yoshimura model. To estimate the force in the springs, the strain in the member FN caused by the deflection MN at the midsection of the member AC is determined from the geometry of Figure 3.6. The strain due to the change in the geometry of the facet caused by loading is also taken into account.

From the geometrical relations evident in Figure 3.6, the altered length of the spring can be shown to be

$$FM = \frac{1}{2}\left[AF^2 + 2.AB^2 - 8.AB.MN.\sin(\varphi/4)\right]^{1/2}$$

while the original length is given by $FN = \frac{1}{2}\left[L_2{}^2 + (\frac{3L_1}{2})^2\right]^{1/2}$. The lengths AF and AB are respectively given by

$$AF = L_d.\left[1 - \frac{P_1}{2.E.W.t}\right] \quad \text{and} \quad AB = L_1.\left[1 - \frac{P_2}{2.E.W.t}\right]$$

where W is the width of the flanges and t is the thickness of the shell. Assuming, for simplicity, that the cross section area of the member FN is the same as that of the diagonal and tangential members, the compressive force in the spring is given by $P_3 = -2.E.W.t.\epsilon$, where ϵ is the strain in the member FN given by $\epsilon = FM/FN - 1$. Substituting for P_2 in terms of P_1 from eqn.3.7, and neglecting the second order terms, from the above relations P_3 is obtained as

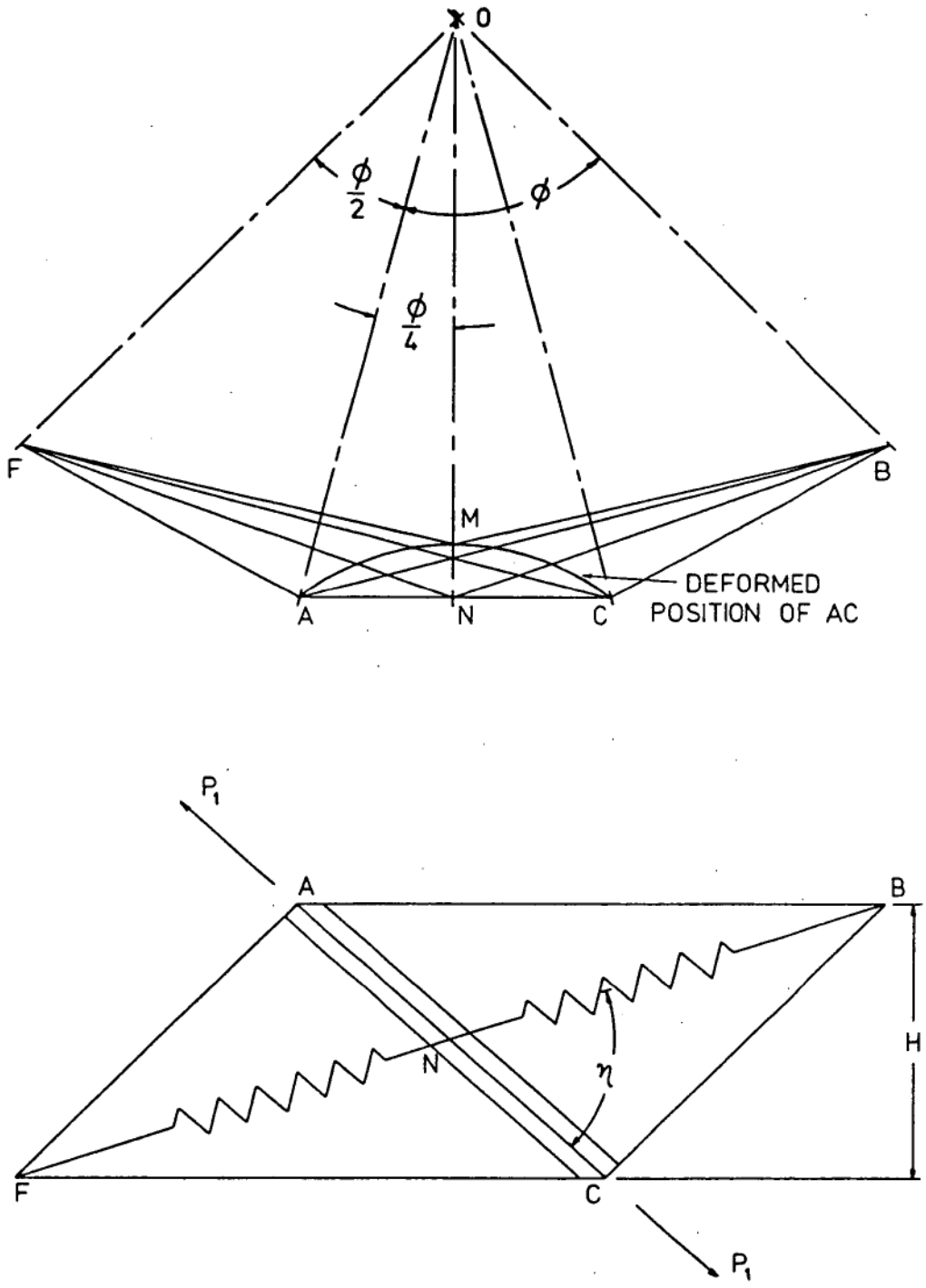

Figure 3.6
Model for Collapse of Diagonal Member
(Source Foster, Ref.58)

$$P_3 = MN.\left[\frac{8.L_1.E.W.t.\sin(\varphi/4)}{L_2^2 + 9L_1^2/4}\right]$$

$$+ P_1.\left[\frac{L_d^2 - \frac{2\,L_1^3}{(1 + \cos(\varphi/2)).L_d}}{L_2^2 + 9L_1^2/4}\right] \qquad (3.8)$$

The angle η between the restraining force and the column is given by

$$\cos\eta = \frac{3L_1^2/4 - L_2^2}{L_d.\left[L_2^2 + 9L_1^2/4\right]^{1/2}} \qquad (3.9)$$

3.4 Solution for the Buckling Load

Having determined the forces in the springs, the buckling of the diagonal member can now be treated as that of a pin-ended column, loaded at the corners and restrained by transverse forces in the middle as shown in Figure 3.7. The governing differential equation is obtained as

$$EI\frac{d^2y}{dx^2} = -P_1\left[y + \frac{W}{2}\cos(\theta/2)\right] + P_3\sin\eta\cos(\theta/2)\left[\frac{L_d}{2} - x\right]$$

whose solution is given by

$$y = C_1\sin(Jx) + C_2\cos(Jx) - \frac{W}{2}\cos(\theta/2)$$

$$+ \frac{P_3}{P_1}\sin\eta\cos(\theta/2)\left[\frac{L_d}{2} - x\right] \qquad (3.10)$$

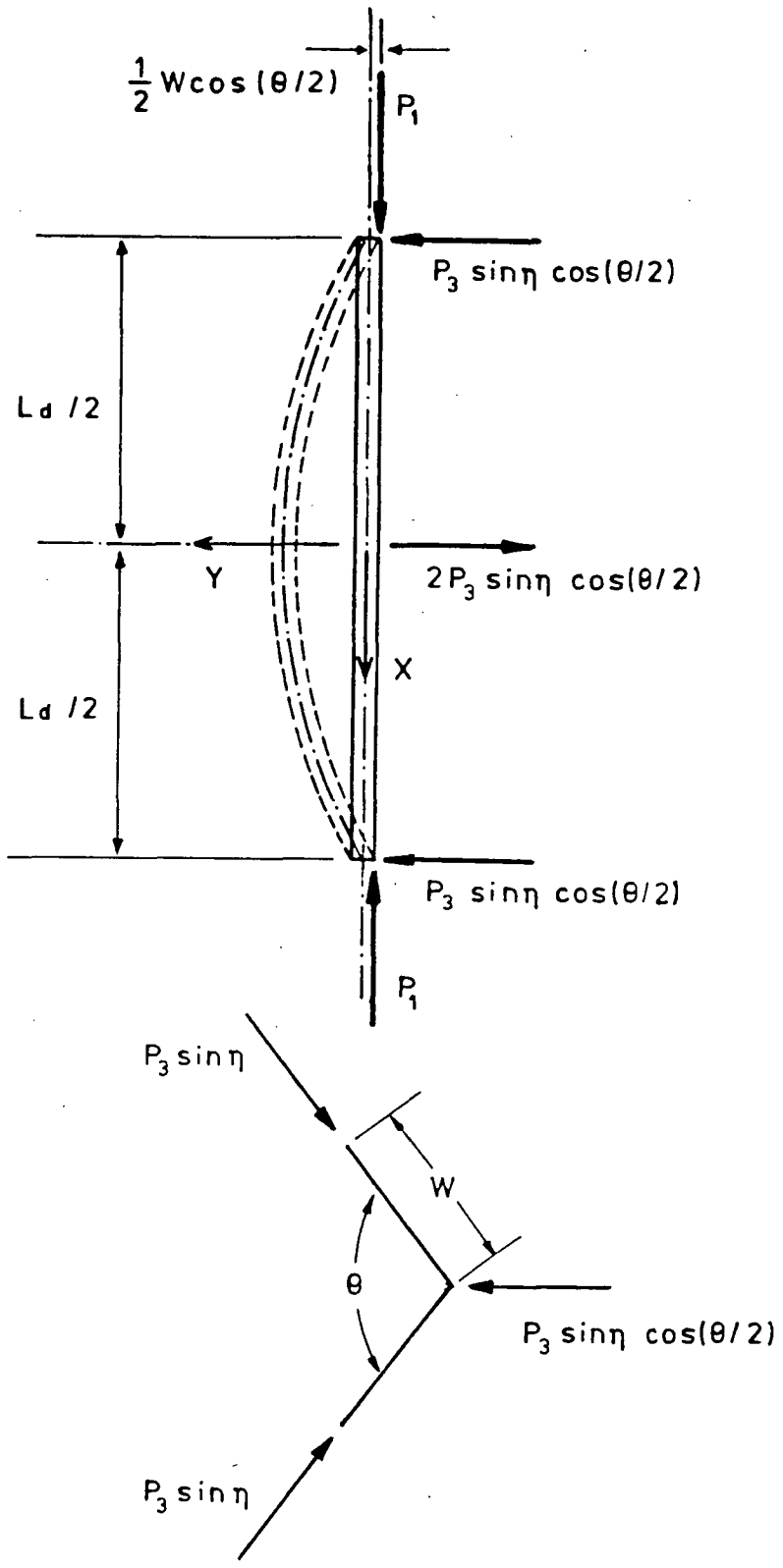

Figure 3.7
Loading System on Column Member

where $J = \sqrt{P_1/EI}$; the moment of inertia I being taken approximately as

$$I = \frac{1}{6} W^3.t.\cos^2(\theta/2) \qquad (3.11)$$

Using the boundary conditions $y = 0$ at $x = L_d/2$ and $\frac{dy}{dx} = 0$ at $x = 0$, the constants C_1 and C_2 may be obtained as

$$C_1 = \frac{P_3 \sin\eta \cos(\theta/2)}{P_1.J} \; ; \; C_2 = \frac{1}{2} \frac{W \cos(\theta/2)}{\cos(JL_d/2)} - C_1 \tan(JL_d/2) \qquad (3.12)$$

The deflection at the centre of the column is given by

$$MN = C_2 - \frac{W}{2} \cos(\theta/2) + \frac{P_3}{P_1} \sin\eta \cos(\theta/2)\left[\frac{L_d}{2}\right] \qquad (3.13)$$

Substituting for P_3 from eqn.3.8 and for C_2 from eqn.3.12 in eqn.3.13, we finally obtain

$$MN.\left[1 - \frac{8.L_1.E.W.t.\sin(\varphi/4)}{P_1.\left[L_2^2 + 9L_1^2/4\right]}.\sin\eta.\cos(\theta/2).\left[L_d/2 - \frac{1}{J}\tan(JL_d/2)\right]\right]$$

$$= \left[\frac{L_d^2 - \frac{2\,L_1^3}{(1 + \cos(\varphi/2)).L_d}}{L_2^2 + 9L_1^2/4}\right].\sin\eta.\cos(\theta/2).\left[L_d/2 - \frac{1}{J}\tan(JL_d/2)\right]$$

$$+ \frac{W}{2}.\cos(\theta/2).\left[\frac{1}{\cos(JL_d/2)} - 1\right] \qquad (3.14)$$

When the deflections grow very large, the term in the parentheses on the left hand side of eqn.3.14 vanishes, hence the critical load is given by the minimum value of P_1 which satisfies the equation

$$1 - \frac{8.L_1.E.W.t.\sin(\varphi/4)}{P_1.\left[L_2^2 + 9L_1^2/4\right]}.\sin\eta.\cos(\theta/2).\left[L_d/2 - \frac{1}{J}\tan(JL_d/2)\right] = 0 \quad (3.15)$$

By substituting for $\cos(\theta/2)$ and $\sin\eta$ from eqns.(3.4) and (3.9), the above equation may be rewritten as

$$P_1.(\lambda^2 + 9/4)^{3/2} - \frac{16EWt}{L_1}\sin^2(\varphi/4)\left[L_d/2 - \frac{1}{J}\tan(JL_d/2)\right] = 0 \quad (3.16)$$

It may be pointed out that eqns.3.15 and 3.16 are identical to the ones used in ref.58, except for a change in sign in the second terms on the left hand side, which is due to the fact that in the original work tensile forces were considered positive whereas in the current work the compressive force is taken as positive.

3.5 Determination of Aspect Ratio and Effective Width

Equation 3.16 can be solved using an iterative approach to yield the critical value of P_1 corresponding to any given value of N, provided the values of the aspect ratio λ and the effective width W are determined; the critical value for the end load on the shell is then given by eqn.3.6. Assuming a reasonable value of 0.7 initially for the aspect ratio, Foster used the secondary buckling data obtained in a test by Esslinger and Geier[25] to determine the effective width as well as to check the validity of the analytical formulation. The secondary buckling loads observed by Esslinger et al., for values of N ranging from 15 to 10 are presented in the second column of Table 3.1.

Matching the theoretical buckling load with one of these values Foster determined the effective width as 21 times the thickness of the shell. The secondary buckling loads obtained from the solution of eqn.3.16 using λ = 0.7 and W/t = 21 for the corresponding values of N are shown in the third column of the table. It can be seen that the agreement between theory and experiment is very good.

Two further modifications were subsequently introduced by Foster. The first was the determination of the aspect ratio on an empirical basis[58]. For this purpose several Melinex cylinders were buckled under axial compression and measurements of the buckle dimensions were taken. The measured values of aspect ratio are shown in Figure 3.8a (from ref.58). Although the values show some variation with the circumferential number of buckles, this was attributed to the scatter of the results and a least square fit was obtained for the variation of the aspect ratio with the radius to thickness ratio as shown in Figure 3.8b. On this basis the empirical relation for the aspect ratio was established as

$$\lambda = 1.606 - 0.121 \ln(R/t) \qquad (3.17)$$

Using this relation, the aspect ratio for the shell tested by Esslinger and Geier (R/t = 526) is obtained as λ = 0.848, hence the effective width ratio was changed to 23.5 to fit their experimental data. The theoretical buckling loads evaluated with W/t = 23.5 and λ from eqn.3.17 is shown in the fourth column of Table 3.1.

Table 3.1

Comparison of Secondary Buckling Loads Predicted by Space Frame Theory with Esslinger and Geier's experimental data.

N	$^{*}P_{exp.}$	$^{1}P_{th.}$	$^{2}P_{th.}$	$^{3}P_{th.}$	$^{4}P_{th.}$
15	275	271	275	308	280
14	260	254	257	284	258
13	235	236	239	261	237
12	215	218	221	238	216
11	200	200	203	216	195
10	185	181	184	194	175

Shell Data : R = 100 mm, t = 0.19 mm , E = 5.5 Gpa, ν = 0.35

P_{exp}(primary) $\simeq$ 520 N, P_{cl} = 769 N, $P_{exp}/P_{cl} \simeq 0.68$

* Experimental secondary buckling loads observed by Esslinger and Geier (quoted from Ref.58 - wherein they were obtained by reading from a graph in Ref.25)

[1] Using W/t = 21, λ = 0.7, and approximate M.I. (eqn.3.11)

[2] Using W/t = 23.5, λ = 0.85 (eqn.3.17) and approx. M.I.

[3] Using W/t = 23.5, λ = 0.85, and exact M.I. (eqn.3.18)

[4] Using W/t = 22.7, λ = 0.85, and exact Moment of Inertia

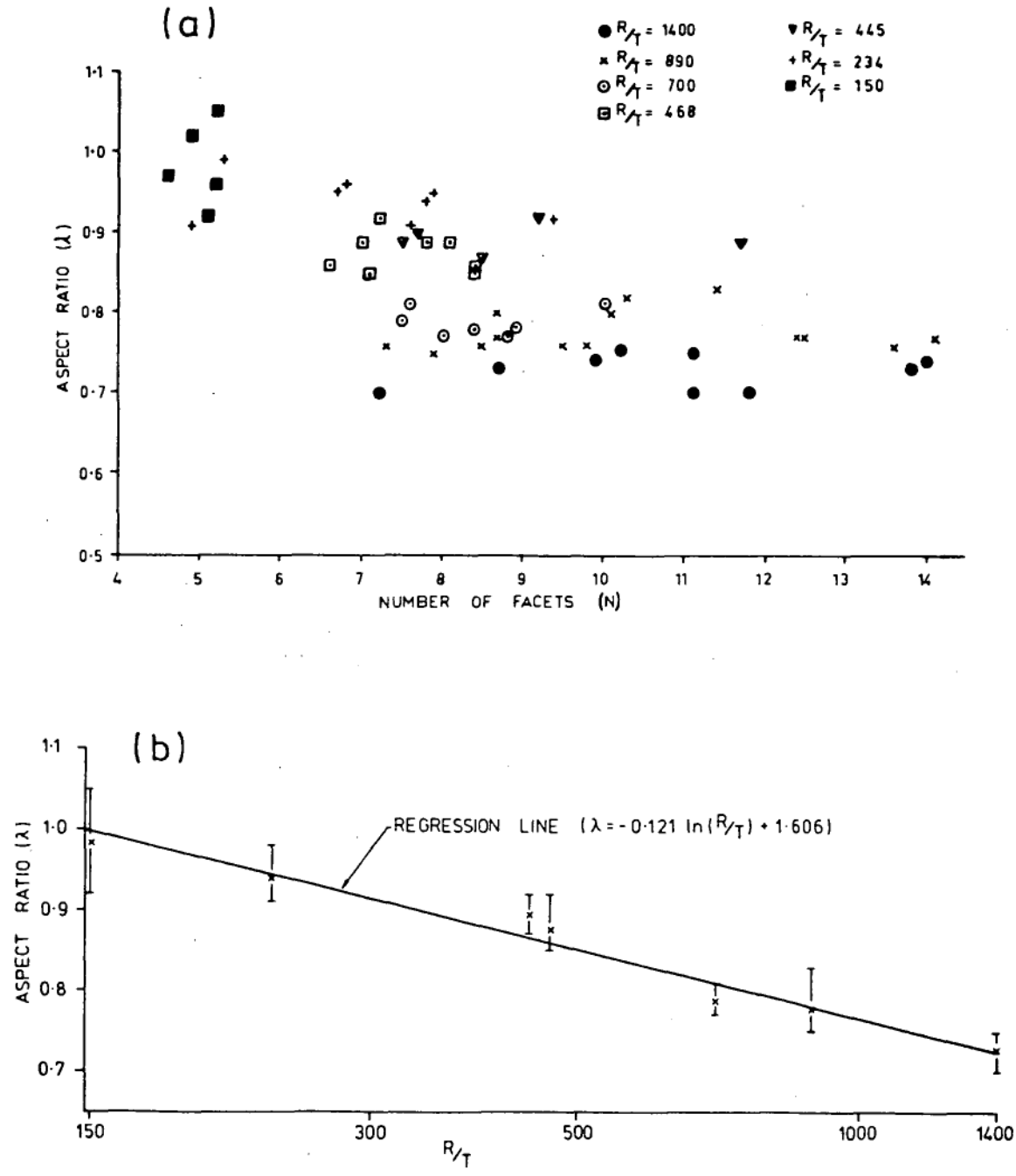

Figure 3.8
(a) Aspect Ratio of Buckled Cylinders
(b) Empirical Relation for Aspect Ratio
(Source Foster, Ref.58)

The second improvement is the use of a more exact expression for the moment of inertia of the diagonal member. For a thin wide wide flanged angle section the moment of inertia is actually given by

$$I = \frac{1}{6} W^3 t \cos^2(\theta/2) + \frac{1}{6} W t^3 \sin^2(\theta/2) \qquad (3.18)$$

Previously, neglecting the second term on the basis that W/t is very large, the moment of inertia was approximated to that given by the first term (see eqn.3.11). However as θ approaches 180° the error due to such an approximation becomes very large, as can be seen by the fact that for $\theta = 180^\circ$, I is obtained as zero from eqn.3.11. In the space frame the angle θ between the facets is large and gets close to 180° as N increases; hence the second term cannot be neglected. To illustrate the importance of the second term, the buckling loads obtained using the correct moment of inertia for W/t = 23.5 and λ = 0.848 are shown in the fifth column of Table 3.1. It can be seen that these values are significantly greater than those in the fourth column which were obtained by neglecting the second term. It was found that with this correct moment of inertia, the theoretical values match the secondary buckling loads obtained by Esslinger and Geier, if the effective width ratio W/t is taken to be 22.7. These values are shown in the last column in Table 3.1; it can be seen that they too agree quite well with the experimental values in column one.

The secondary buckling loads predicted by eqn.3.16, using W/t = 22.7 and the aspect ratio given by eqn.3.17 (and the exact moment of inertia), are plotted for various values of N for R/t

ranging from 100 to 4000 in Figure 3.9. In the figure, the ordinate is the ratio of the calculated buckling load to the classical buckling load. The latter was calculated using a value of ν = 0.34, this being the value determined for the Poisson's ratio ν of the epoxy material of the shells tested in the current experimental program.

3.6 Hypothesis for the Buckling Load of Imperfect Shells

Although the space frame model was developed on the basis of secondary collapse behaviour, one of the major emphases of Foster's work is on the application of the theory to the prediction of the primary buckling loads for imperfect circular cylindrical shells in axial compression[58,61,62,24]. The extension of the space frame theory to the primary collapse behaviour of imperfect cylindrical shells may be argued as follows:

While the Yoshimura pattern represents the buckled shape of the axially compressed shell, the straight cylindrical form of the perfect unbuckled shell may be perceived as a Yoshimura model with infinitely small facets extending over the whole of its surface. In practice, however, all cylinders are more or less imperfect, so that small deviations from the true cylindrical shape are bound to exist. These initial deviations in geometry may be conceived of as diamond shaped facets of finite size existing on the Yoshimura model of the otherwise true cylinder, and the primary collapse of the imperfect cylinder may be attributed to the collapse of the diagonal member in one of these facets. Noting that the collapse of the diagonal fold

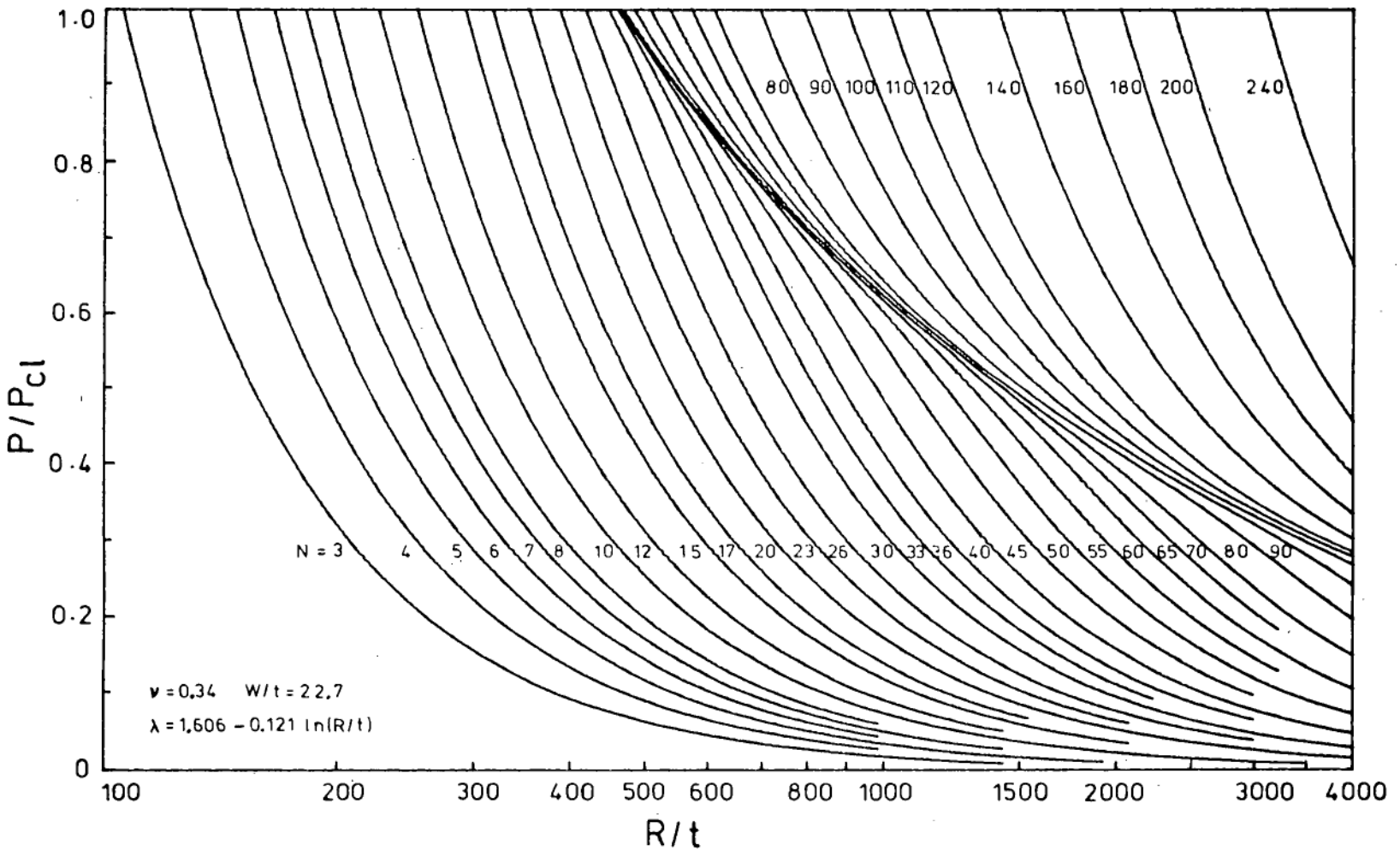

Figure 3.9. Secondary Collapse Loads Predicted by Original Space Frame Model

between two facets is more or less independent of the facets elsewhere in the space frame, and also that facets of larger size (smaller N) have smaller buckling loads, the primary buckling load of the cylindrical shell is taken to be that predicted by the theory for the largest facet on the model, i.e., the one corresponding to the largest defect on the shell. If the N corresponding to the largest defect on the shell is greater than the N for which the space frame theory predicts a knockdown factor equal to 1 (for example, if the largest defect on a shell with an R/t of 400 has a value of N greater than 25) then the shell will buckle at the classical buckling load. For larger defects the shell will buckle at the load given by the corresponding N in Figure 3.9. (The figure also indicates that a defect of the same size will have greater detrimental effect on shells of larger R/t).

Thus it is postulated by Foster that the primary buckling load of an axially compressed imperfect shell can be predicted in terms of the largest value of the measured circumferential lengths of its defects, using the space frame theory. Experimental evidence to support this hypothesis has been presented by Foster in references 58, 61 and 24, in which the knockdown factors predicted with measured defect sizes are compared with the experimental values. Of particular interest are the results of eight tests presented in ref.24, four of which had imposed defects of specific size, while in the other four the measurements were taken off defects naturally present in the shells. The largest discrepancy between the quoted theoretical predictions and observed knockdown factors for these eight shells is of the order of 0.03, i.e., within four percent. Results were also

presented for six conical shells, with reasonable agreement between experiment and theory.

3.7 Basis of the Present Work

The author's present work was motivated by the encouraging results of the initial tests conducted by Foster. In the majority of these tests (except for the four mentioned above) the imperfections were unintended, i.e., they were caused by factors like improper fixing, presence of the seam and so on. Moreover, except for those mentioned in ref.24, these tests were conducted on shells of rather poor quality in a loading frame with somewhat insufficient rigidity[73]. It was therefore decided to conduct a systematic testing program on shells of high quality with imposed defects of different specific sizes, and obtain experimental data over a wider range of shell geometry, in order to check the validity of the hypothesis concerning the applicability of the space frame theory for shells with local defects. A new rigid loading machine was designed and built for this purpose. It was also observed that the theoretical formulations of the space frame model for the secondary collapse loads had only been compared to the results of one test by Esslinger and Geier (since no other data was available at that time), hence the experimental program was extended to include observation of secondary buckling loads, to check the validity of the basic premise of the space frame theory.

One of the main reasons for continuing the investigations into the space frame theory was the perceived shortcomings in the

original theory. Foster[73] regarded the buckling curves (Figure 3.9) as being too steep in the low R/t region. It was felt that the constant value determined for the effective width might not be applicable over the whole range. For this reason, the theoretical investigations in the current work are mostly devoted to establishing the effective width on an analytical basis. It was also considered desirable to investigate further on the subject of the aspect ratio, since the data for the empirical relation employed by Foster was obtained in tests which were subject to the same shortcomings as those indicated earlier. It may however be mentioned that neither the experimental nor the theoretical investigations produced the anticipated results.

The first attempt to establish the effective width of the sides of the triangular facets was made along the lines of the effective width concept proposed by Von Kármán (Ref.1, page 418) for the sides of the rectangular plate. This concept is based on the fact that while the buckled plate is capable of carrying a much higher load, the stresses supporting this load are basically concentrated along the edges of the plate, which are supported. Hence it may be considered that only the strips of the plate along either edge is effective in carrying the load, and the ratio of the combined widths of these strips to the total width of the plate is obtained simply as the ratio of the average stress to the maximum stress in the plate. However, in order to determine these stresses in the buckled panel it is necessary to resort to a large deflection analysis. Hence a large deflection analysis of the simply supported isosceles triangular panel is conducted, which is presented in the next chapter.

NOTATIONS

E : Young's Modulus

I : Moment of Inertia

$J = \sqrt{P_1/EI}$

L_1 : Length of the facet in the circumferential direction

L_2 : Height of the triangular facet, in its own plane

L_d : Length of the diagonal member

N : Circumferential number of facets

P : Axial load on the cylinder

P_1 : Axial load in diagonal member

P_2 : Axial load in tangential member

P_3 : Load in member being formed

R : Radius of the shell

W : Effective width of flange on angle member

t : Thickness of the shell

x,y : Co-ordinate axes on column member (see Figure 3.7)

ϵ : Strain in member being formed

φ : Angle subtended at the axis of the cylinder by each facet

γ : Angle of inclination of the facet to the axial plane

η : Angle between the collapsing diagonal member and the new member being formed

λ : Aspect ratio of the triangular facet = L_2/L_1

ν : Poisson's ratio

θ : Angle between facets adjacent to the diagonal member

CHAPTER 4

FINITE DEFLECTION ANALYSIS OF SIMPLY SUPPORTED ISOSCELES TRIANGULAR PLATES

For the analysis of the behaviour of plates when subjected to loads higher than the critical load at which buckling first occurs, the strains in the middle plane of the plate have to be taken into account. The application of the general equations of large deflection theory becomes rather complicated in this case and approximate analytical solutions are usually obtained using the principle of stationary potential energy. However earlier solutions of this nature have mostly been restricted to rectangular and circular plates, for which the boundary conditions can be easily satisfied.

In investigating the bending of triangular plates, the main problem is that of representing the out of plane deflection by a function which satisfies the boundary conditions. In one of the earliest works, Woinowsky-Krieger (Ref.1, page 393) used a polynomial function to obtain an exact solution for the buckling of an equilateral triangular plate. Subsequently, combinations of double trigonometric series were used by Klitchielf[64] and Wakasugi[65] for the right isosceles, and by the latter for the equilateral triangular plate[66]. Only for these particular cases of the isosceles triangle, the out of plane deflection has been represented by functions which satisfy the boundary conditions completely.

Solution to the buckling of the general isosceles triangle has been obtained by satisfying the boundary conditions approximately, by a collocation method[67] and by the modified Galerkin's approach[68]. Of particular interest is the latter approach, which makes use of the fact that the boundary conditions are implicit in the principle of stationary potential energy, and therefore the Galerkin's equation, which is derived from it, can be generalized to include minimization of the errors due to the unsatisfied boundary conditions.

In the present analysis, an approach similar to that of Ref.68 is employed. The out of plane deflection is first represented by functions that satisfy only the geometric boundary condition; the error due to the moment boundary condition not being satisfied is then minimized by using the stationary potential energy principle. The finite deflection analysis is conducted in a manner similar to that used by Timoshenko and Gere for the rectangular plate[1], namely, that of satisfying the boundary conditions and determining the amplitude parameters of the deformations by minimizing the total strain energy of the plate.

Although, theoretically, it is possible to solve for the amplitude parameters of all the terms representing the deformations of the plate simultaneously, the computational work involved becomes enormous as one takes more and more terms. This is especially so since the final set of equations contains cubic terms in the coefficients of the out of plane deflection. It is however found that the ratios of the coefficients of the deflection obtained by the solution of these

equations are the same as those obtained by the buckling analysis. (This was verified by the author by first using only two terms in the function representing the out of plane deflection). That is, unlike the cylindrical shell, the post-buckling mode of the plate is the same as the buckling mode; only the amplitude of the deflection increases with further loading. (The possibility of the plate going into a higher mode when the second critical load is exceeded is also investigated). It is therefore found expedient to conduct the analysis in two stages: in the first stage the buckling modes are determined using small deflection theory; the out of plane deflection is then represented in terms of these modes, so that only its amplitude remains to be evaluated. In the second stage, the large deflection theory is used to determine the amplitude of the out of plane deflection as well as the coefficients of the in-plane displacements.

4.1 Loading Conditions

The dimensions of the isosceles triangular plate and the co-ordinate system adopted are shown in Figure 4.1. For the analysis two types of loading are considered. In the first case, the triangular panel is subjected to normal compressive loads on all three edges; and in the second, the compressive load on the base of the triangle is resisted by shear loads on the equal sides of the plate (see Figure 4.2). The pre-buckling plane stress conditions for the two loading cases are shown in Figure 4.3. It may be observed that the triangular facets in the space frame are subjected to loading conditions similar to that of the second case; hence this case is of the most relevance

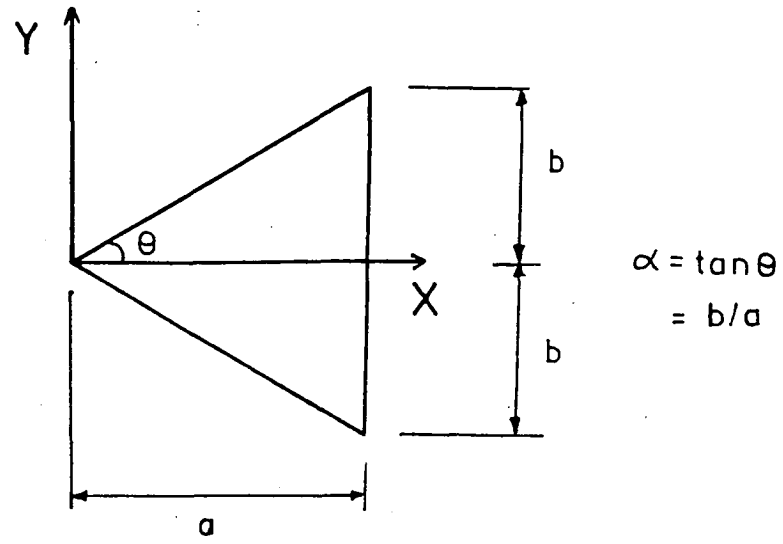

Figure 4.1
Dimensions and Co-ordinate System

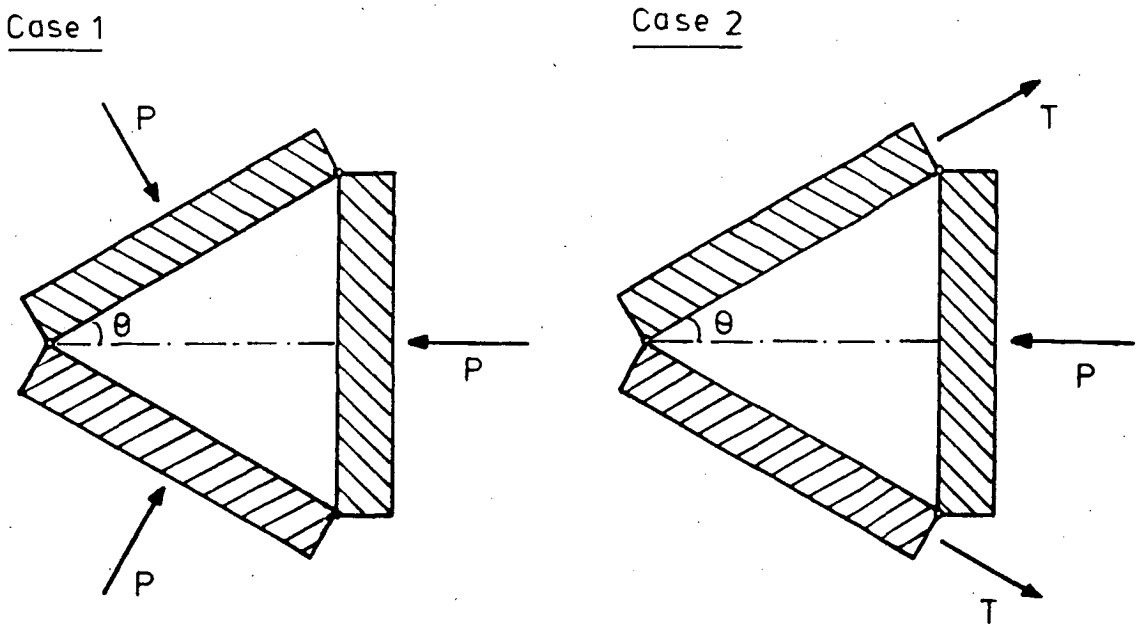

Figure 4.2
Loading Conditions

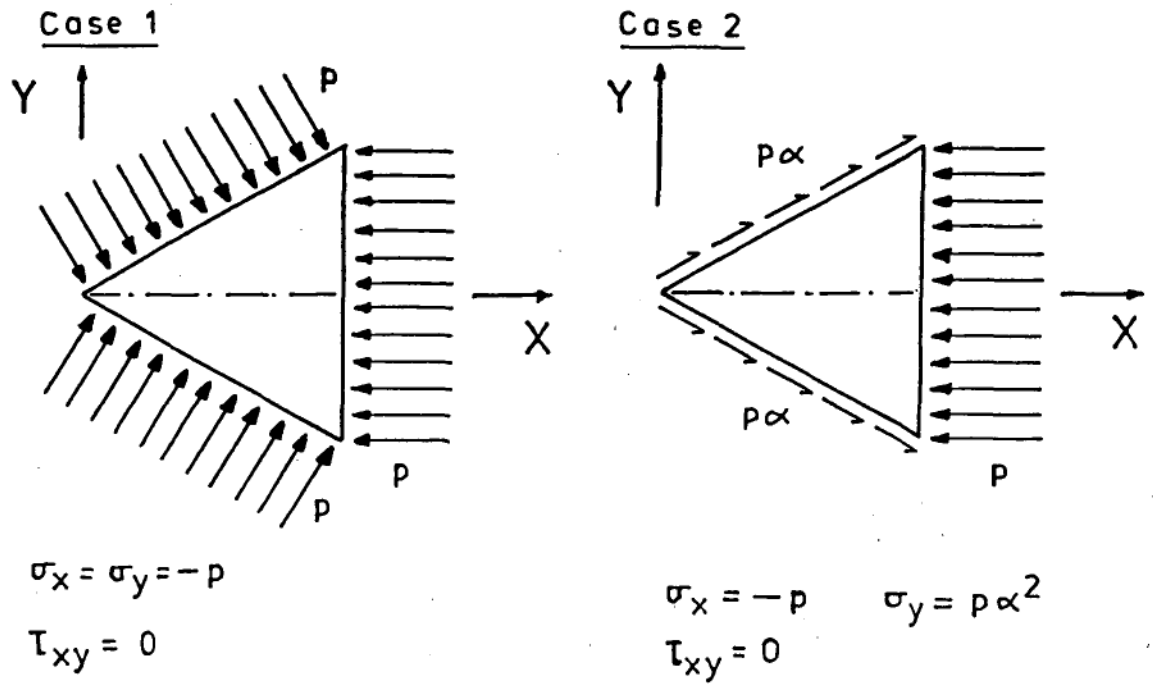

Figure 4.3
Plane Stress Conditions

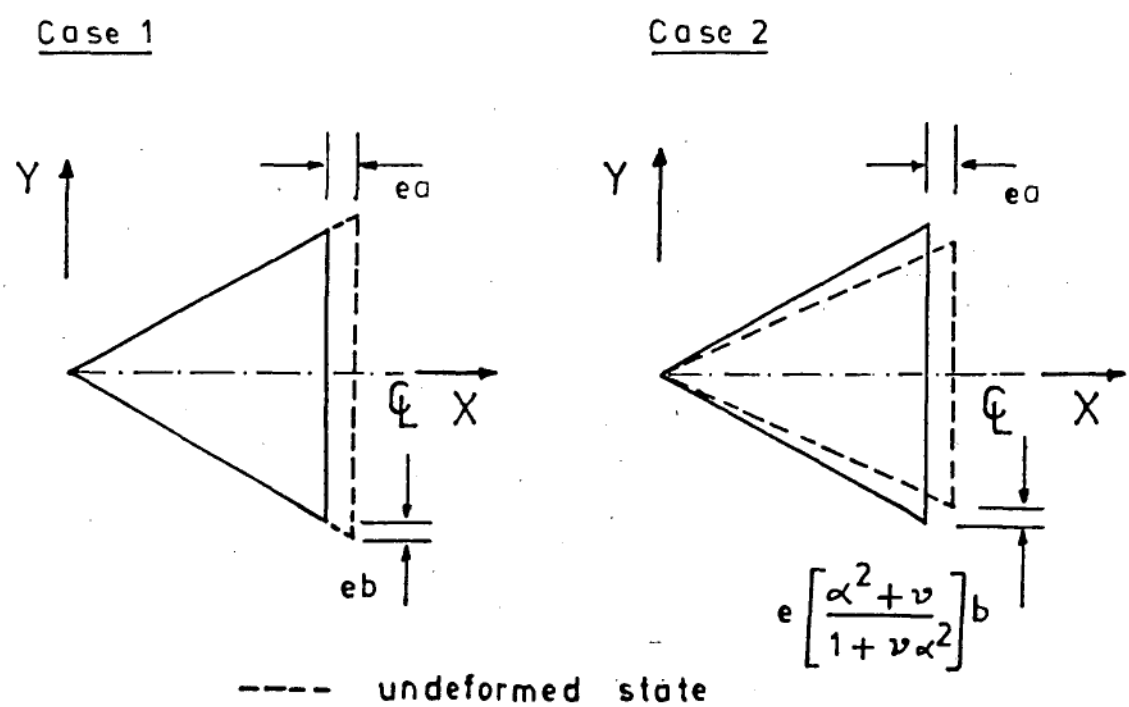

Figure 4.4
Displacement of the Edges

here, while the first case, which is simpler, has only been included for the purposes of comparison. For both cases, the edges of the plate are considered to be simply supported, simulating the edge conditions of the panel in the space frame. Further it is assumed that the edges of the plate are constrained to remain straight even after buckling; this is necessary to maintain the conditions of symmetry (between neighbouring panels) in the space frame. Figure 4.4 shows the in-plane displacements along the edges of the plate, for the two cases considered, for an applied strain, or unit displacement, "e" normal to the base of the plate.

It may also be pointed out that, unlike the rectangular plate, which can have arbitrary loads along its adjacent sides, the triangular plate can be loaded only in a fixed proportion, due to the restriction of statics. The in-plane displacements of the edges, or the linear components of the strains in the X and Y directions are thus constrained to retain the same proportion as that of the plane stress condition in the pre-buckling stage.

4.2 Expressions for the Displacements

The displacements u, v, and w for the plate, in the X, Y, and Z directions respectively, are expressed in the following form:

$$u = \sum_i C_{1i} g_i(x,y) - ex \; ; \quad v = \sum_i C_{2i} h_i(x,y) + t_0 ey \qquad \text{for } i = 0 \text{ to } N$$

$$\text{and} \quad w = A\, f(x,y) = A \sum_i r_i\, f_i(x,y) \tag{4.1}$$

where,

$$g_i(x,y) = \cos(k_i\pi x/2a)\cos(l_i\pi y/2b) - \cos(l_i\pi x/2a)\cos(k_i\pi y/2b)$$

$$h_i(x,y) = \sin(k_i\pi x/2a)\sin(l_i\pi y/2b) - \sin(l_i\pi x/2a)\sin(k_i\pi y/2b)$$

$$f_i(x,y) = \cos(m_i\pi x/2a)\cos(n_i\pi y/2b) - \cos(n_i\pi x/2a)\cos(m_i\pi y/2b) \qquad (4.2)$$

In these expressions k_i, l_i, m_i and n_i are odd integers such that $k_i \neq l_i$ and $m_i \neq n_i$. The ratio of the linear strain component in the Y direction to that in the X direction, t_0, is obtained by plane stress analysis in the pre-buckling stage, for case 1 & 2 respectively, as,

$$t_0 = -1 \quad \text{and} \quad t_0 = (\alpha^2 + \nu) / (1 + \nu\,\alpha^2) \qquad (4.3)$$

where $\alpha = \tan\theta = b/a$ and ν is the Poisson's ratio, taken to be 0.3.

The functions g, h and f are chosen so that they vanish along the boundary of the plate. Although h is zero at the points (a,0), (a,±b), and its integral over the edge x = a vanishes, it has non-zero values at the intermediate points; so that the condition of v being linear along this edge is only approximately satisfied. Apart from this, the functions u, v and w completely satisfy the geometric boundary conditions, namely that w should vanish and the in-plane displacements be linear along the edges of the plate. It may be mentioned that the functions $f_i(x,y)$ used for the lateral deflection w, are essentially of the same form as that used by Wakasugi for the right isosceles triangular plate[65], in which case, they satisfy both the boundary conditions of simple support exactly. A similar function is used in Ref.68 also.

4.3 Strains and Stresses in the Middle Plane

The strains and stresses in the middle plane of the plate are given by,

$$\epsilon_x = u_{,x} + \frac{1}{2} w_{,x}^2 \qquad \sigma_x = \frac{E}{(1-\nu^2)} \left[\epsilon_x + \nu\, \epsilon_y\right]$$

$$\epsilon_y = v_{,y} + \frac{1}{2} w_{,y}^2 \qquad \sigma_y = \frac{E}{(1-\nu^2)} \left[\epsilon_y + \nu\, \epsilon_x\right]$$

$$\gamma_{xy} = u_{,y} + v_{,x} + w_{,x}\, w_{,y} \qquad \tau_{xy} = \frac{E}{2(1+\nu)}\, \gamma_{xy}$$

The normal and shear stresses along the edges $x = \pm\, a$ y , are given by,

$$\sigma_n = \sigma_y \cos^2\theta + \sigma_x \sin^2\theta \mp 2\, \tau_{xy} \cos\theta \sin\theta$$

$$\tau_{sn} = \left[\sigma_y - \sigma_x\right] \cos\theta \sin\theta \pm \tau_{xy} \left[\cos^2\theta - \sin^2\theta\right]$$

The boundary conditions to be satisfied by the stresses in the middle plane, for cases 1 and 2 are respectively as follows:

Case 1

(i) Shear is zero along the three edges of the plate.

(ii) The sum of the X components of the normal stresses along the equal sides of the plate is equal to the sum of the normal stresses along the base of the triangle.

Case 2

(i) Shear stress along the base and the normal stresses along the equal edges of the plate are zero.

(ii) The X component of the sum of the shear stresses along the equal edges and the sum of the normal stresses along the base of the triangular plate should add up to zero.

Noting that the functions chosen for u , v and w are such that the shear stresses are always zero along the base and that the functions are symmetric about the X axis, these boundary conditions may be expressed as follows:

Case 1

$$\text{(i)} \quad \int_0^a \tau_{sn}\Big|_{y=\alpha x} dx = 0 \qquad \text{(ii)} \quad \int_0^b \sigma_x\Big|_{x=a} dy - \tan\theta \int_0^a \sigma_n\Big|_{y=\alpha x} dx = 0$$

Case 2

$$\text{(i)} \quad \int_0^a \sigma_n\Big|_{y=\alpha x} dx = 0 \qquad \text{(ii)} \quad \int_0^b \sigma_x\Big|_{x=a} dy + \int_0^a \tau_{sn}\Big|_{y=\alpha x} dx = 0$$

4.4 Determination of Buckling Modes

The change in the potential energy of the plate when it buckles may be expressed as $V = U_b - W$, where U_b is the strain energy due to bending of the plate, given by

$$U_b = \frac{D}{2} \iint \left[\left[w_{,xx} + w_{,yy} \right]^2 - 2(1-\nu) \left[w_{,xx}\, w_{,yy} - w_{,xy}^2 \right] \right] dx\, dy \qquad (4.4)$$

and W is the work done by the stresses in the middle plane, or alternatively, the energy associated with the stretching of the middle plane during buckling, which is given by

$$W = -\frac{t}{2}\iint \left[\sigma_x\, w_{,x}^2 + \sigma_y\, w_{,y}^2\right] dx\, dy \qquad (4.5)$$

In eqn.4.4, the modulus of rigidity of the plate $D = Et^3/12(1 - \nu^2)$. Expressing the lateral deflection of the plate as $w = \sum A_i\, f_i(x,y)$, where the functions $f_i(x,y)$ are given by the third of eqns.4.2, the total change in potential energy is obtained as,

$$V = \frac{D}{2}\iint \sum_i\sum_j A_iA_j\left[f_{,xx} + f_{,yy}\right]_i\left[f_{,xx} + f_{,yy}\right]_j dx\, dy$$

$$+ \frac{t}{2}\iint \sum_i\sum_j A_iA_j\left[\sigma_x\, f_{,xi}\, f_{,xj} + \sigma_y\, f_{,yi}\, f_{,yj}\right] dx\, dy$$

It may be pointed out that the terms $\iint f_{,xxi} f_{,yyj} dxdy$ and $\iint f_{,xyi} f_{,xyj} dxdy$ cancel out and therefore do not appear in the bending energy term. Minimizing V w.r.t. the amplitude parameters A_i we get,

$$\frac{\partial V}{\partial A_i} = D\sum_j A_j \iint \left[f_{,xx} + f_{,yy}\right]_i\left[f_{,xx} + f_{,yy}\right]_j dx\, dy$$

$$+ t\sum_j A_j \iint \left[\sigma_x\, f_{,xi}\, f_{,xj} + \sigma_y\, f_{,yi} f_{,yj}\right] dx\, dy = 0 \qquad (4.6)$$

In the above set of equations the stresses σ_x and σ_y are given by the plane stress relations $\sigma_x = -p$ and $\sigma_x/\sigma_y = (\nu - t_0)/(1 - \nu t_0)$, which are applicable to both the loading cases considered. Expression 4.6 thus represents a system of homogeneous equations for the solutions of A_j, which can be treated as an eigen value problem. The eigen values represent the buckling stresses and the corresponding eigen vectors the buckling modes.

It may be observed that the functions $f_i(x,y)$ representing the deflection w do not satisfy the moment boundary condition of simple support, namely that $w_{,xx} + w_{,yy} = 0$, along the edges of the isosceles triangle. (This condition is satisfied exactly only for the particular case of the right isosceles triangular plate.) However minimization of the potential energy of the plate, represented by eqns.4.6, determines the buckling mode for the triangle such that this second boundary condition is approximately satisfied. This may easily be observed by looking at eqns.4.6 in its variational form. Noting that the function w as well as its derivatives in the tangential direction vanish along the boundary, we may write the variation of the potential energy V in its expanded form (Ref.69, pages 88-91) as

$$\delta V = D \iint \left[w_{,xxxx} + 2w_{,xxyy} + w_{,yyyy} \right] \delta w \, dx dy - t \iint \left[\sigma_x \, w_{,xx} + \sigma_y \, w_{,yy} \right] \delta w \, dx dy$$

$$+ D \int \left[w_{,xx} + w_{,yy} \right] \delta \left[\frac{\partial w}{\partial n} \right] ds = 0 \qquad (4.7)$$

Eqn.4.7 represents the generalized Galerkin's equation for an isotropic plate. The first two integrals represent minimization of the error in satisfying the governing equation over the entire area of the plate. The third, which is to be integrated along the boundary, represents minimization of the error due to the unsatisfied boundary condition with respect to variations in the slope ($\partial w/\partial n$) normal to the boundary of the plate. Eqn.4.7 is essentially the same as eqn.4.6, since they are both expressions of the same principle. Both yield the same results, and in either case the buckling modes are determined so as to satisfy the moment condition approximately along the boundary of

the plate. Thus the critical stress values obtained by the solution of eqn.4.6 for Case 1 in this study are identical to those obtained by solving eqn.4.7 in Ref.68 for isotropic isosceles triangular plates under uniform compression.

For the present analysis, the deflection w of the triangular plate was represented by six terms of the functions $f_i(x,y)$, with values of (m,n) = (1,3),(1,5),(3,5),(1,7),(3,7) and (5,7). The primary buckling stresses obtained by the solution of eqns.4.6 are plotted (in solid lines) in Figure 4.5 as a function of a/b, for the two loading cases. The ordinate of the figure is the non-dimensionalized buckling coefficient p_0 which is given by the relation

$$p_0 = \frac{ta^2}{\pi^2 D} p_{cr} = \frac{t\,b^2}{\pi^2 \alpha^2 D} p_{cr} \qquad (4.8)$$

Also indicated with crosses in the figure, for comparison, are the results obtained using the exact deflection functions of Wakasugi[65,66] for the right isosceles and the equilateral triangle. The broken lines in the figure are the plots of the buckling coefficients corresponding to the second buckling mode. It may be observed that the latter values are at least two times higher than those of the primary mode.

To indicate the convergence of the solutions obtained, the values of p_0 for the second loading case obtained by the addition of each successive term are tabulated in *Table 4.1, for two types of

* The tables are presented at the end of the chapter (page 89).

triangles: the right isosceles ($\alpha = 1$) and the equilateral ($\alpha = 1/\sqrt{3}$). It may be observed that the degree of convergence is much higher for the right isosceles triangle (wherein the functions used for w satisfy both boundary conditions exactly) than for the equilateral triangle.

The critical compressive strain e_{cr} is given by

$$e_{cr} = \frac{(1 - \nu^2)}{E(1 - \nu t_0)} p_{cr} \tag{4.9}$$

which may be expressed in non-dimensional form as

$$e_0 = \frac{1}{\pi^2} \left[\frac{a}{t}\right]^2 e_{cr} \tag{4.10}$$

The numerical values of p_0 and the non-dimensional critical strain e_0 corresponding to the primary buckling mode are presented in the first two columns under case 1 and 2 in Table 4.3 for reference.

4.5 Evaluation of the Amplitude Parameters of the Buckled Plate

The deflection modes corresponding to the primary critical load, determined by the buckling analysis conducted in the preceding section, are presented in Tables 4.4 and 4.5 for the loading cases 1 and 2, respectively. For the large deflection analysis, these values are used for the constants r_i (see eqn.4.1) in the function f(x,y) for the lateral deflection w. The amplitude A of this deflection and the coefficients C_{1i} and C_{2i} for the in-plane displacements are evaluated

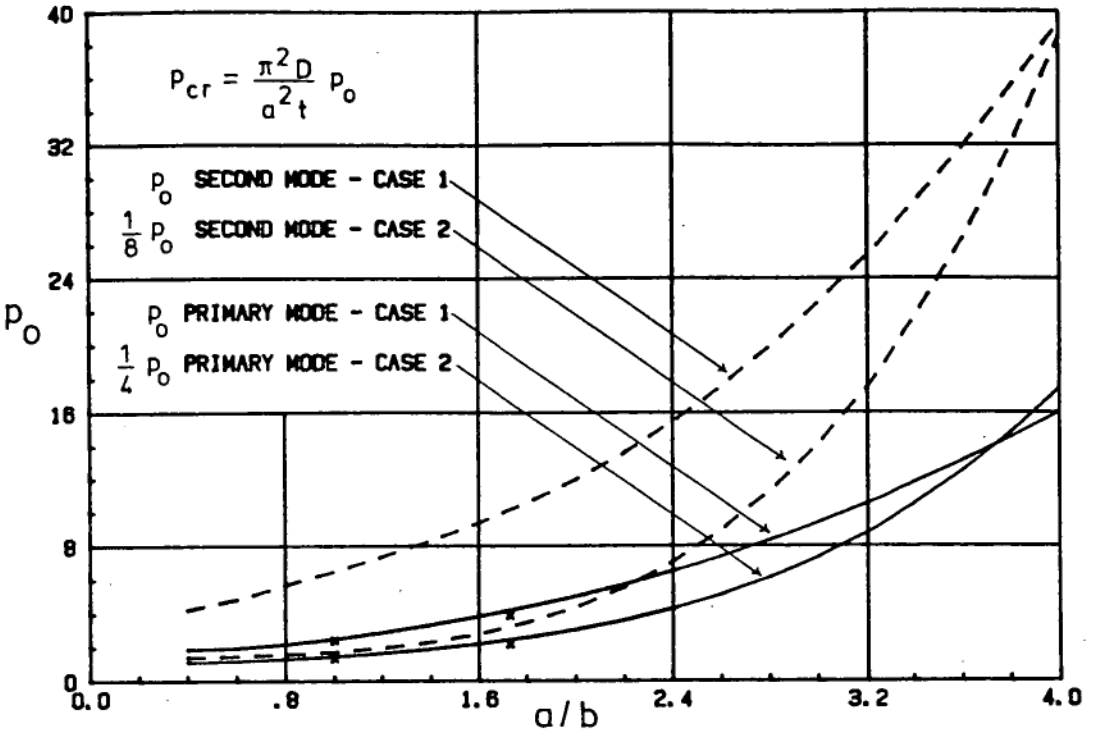

Figure 4.5. Buckling Coefficients for the Isosceles Triangular Plate

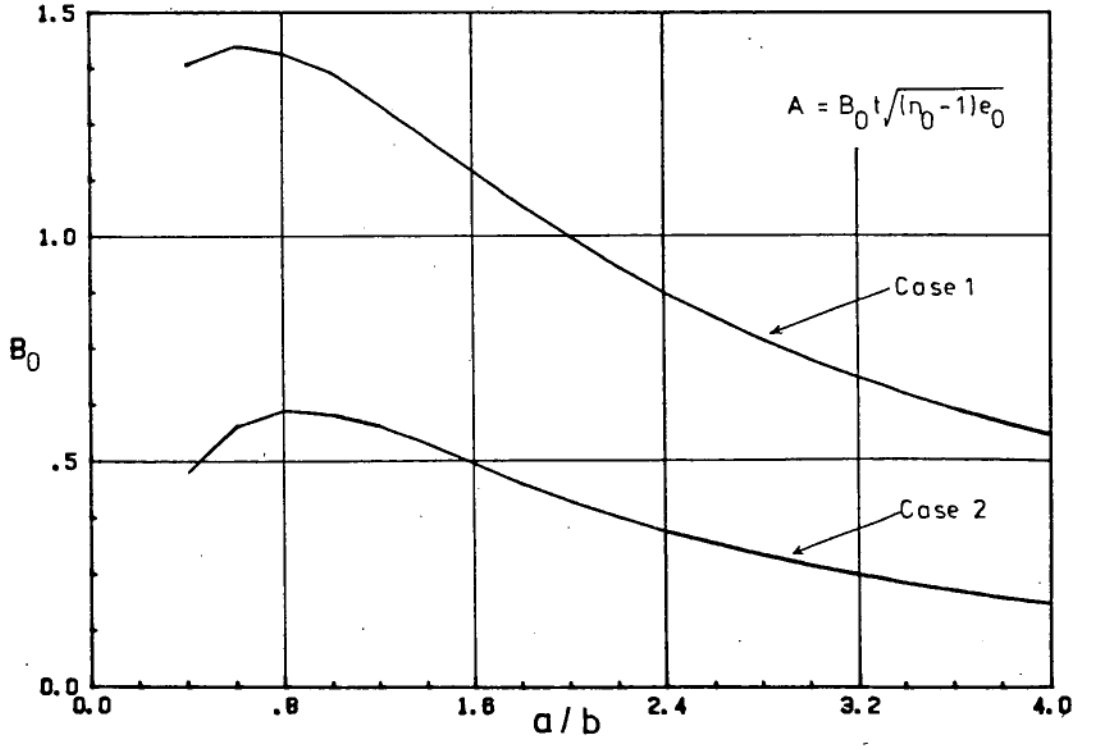

Figure 4.6. Constant B_0 for the Amplitude of Lateral Deflection

in the following manner.

The middle plane stresses (see secn.4.3) are first expressed in terms of the functions representing the displacements u, v and w (eqns. 4.1 and 4.2). Then by satisfying the boundary conditions (i) and (ii) for the middle plane stresses, the first constants C_{10} and C_{20}, in the functions u and v respectively, are obtained in terms of the remaining 2N constants in those functions and the amplitude A of the lateral deflection. They may thus be expressed as

$$C_{10} = b_{01}\left[\frac{\pi}{a}\right]A^2 + \sum_i b_{1,1,i}\, C_{1i} + \sum_i b_{1,2,i}\, C_{2i}$$

and

$$C_{20} = b_{02}\left[\frac{\pi}{a}\right]A^2 + \sum_i b_{2,1,i}\, C_{1i} + \sum_i b_{2,2,i}\, C_{2i} \qquad (4.11)$$

In eqns.4.11, i takes values from 1 to N only. b_{01}, b_{02}, $b_{1,1,i}$, $b_{1,2,i}$, $b_{2,1,i}$ & $b_{2,2,i}$ are constants obtained by integration. The amplitude A and the 2N unknown coefficients C_{1i}, C_{2i} are determined by minimizing the total strain energy of the plate with respect to these unknown quantities. The total strain energy of the plate is given by $U_0 = U_b + U_m$, where U_b is the bending strain energy, given by eqn.4.4, and U_m is the energy due to the strains in the middle plane, which may be expressed as

$$U_m = \frac{E\,t}{2(1-\nu^2)}\iint \left[\epsilon_x^2 + \epsilon_y^2 + 2\nu\,\epsilon_x\epsilon_y + \frac{(1-\nu)}{2}\,\gamma_{xy}^2\right] dx\, dy \qquad (4.12)$$

Expressing U_b and U_m in terms of the displacement functions

u, v and w, in which the relations 4.11 are substituted, the partial derivatives of the total strain energy U_0 w.r.t the coefficients C_{1i} and C_{2i} are equated to zero to yield a system of 2N linear equations of the form:

$$\begin{bmatrix} X_{11} & X_{12} \\ X_{21} & X_{22} \end{bmatrix} \begin{bmatrix} C_1 \\ C_2 \end{bmatrix} + \left[\frac{\pi}{a}\right] A^2 \begin{bmatrix} Y_1 \\ Y_2 \end{bmatrix} = 0 \qquad (4.13)$$

In the above expression, X_{11}, X_{12}, X_{21} and X_{22} are N×N matrices whose elements are constants depending on a/b, obtained by integration over the whole area of the plate. Y_1 and Y_2 are column vectors, each having N elements, which are also constants. C_1 and C_2 are column vectors of the unknown coefficients C_{1i} and C_{2i} respectively. Solving eqns.4.13 for C_{1i} and C_{2i} (for i = 1 to N), and using the relations 4.11 for the first coefficients C_{10} and C_{20}, all the 2(N+1) constants in the functions u and v can be expressed in terms of A^2 as,

$$C_{1i} = t_{1i} \left[\frac{\pi}{a}\right] A^2 \quad ; \quad C_{2i} = t_{2i} \left[\frac{\pi}{a}\right] A^2 \qquad (4.14)$$

The partial derivative of the total energy U_0 with respect to A, when equated to zero, results in an equation of the form:

$$\left[X_1 e - X_2 \left[\frac{\pi}{a}\right]^2 t^2 + X_3 \left[\frac{\pi}{a}\right]^2 A^2 + 2\left[\frac{\pi}{a}\right] \sum_i \left[C_{1i} Y_{1i} + C_{2i} Y_{2i}\right]\right] A = 0 \qquad (4.15)$$

In eqn.4.15, the summation is to be taken from i = 1 to N only. X_1, X_2, X_3, Y_{1i} and Y_{2i} are again constants depending only on a/b; the

last two having the same values as the elements of the vectors Y_1 and Y_2 in eqn.(4.13). Substituting for C_{1i}, C_{2i} from eqns.4.14, eqn.4.15 is reduced to:

$$A.\left[X_0\left[\frac{\pi}{a}\right]^2 A^2 - \left[X_1 e - X_2\left[\frac{\pi}{a}\right]^2 t^2\right]\right] = 0$$

that is, A = 0, or

$$A = \frac{1}{\sqrt{X_0}}\left[\frac{a}{\pi}\right]\sqrt{X_1 e - X_2\left[\frac{\pi}{a}\right]^2 t^2} \qquad (4.16)$$

Hence the critical strain is given by,

$$e_{cr} = e_0\left[\frac{\pi}{a}\right]^2 t^2 = \frac{X_2}{X_1}\left[\frac{\pi}{a}\right]^2 t^2 \qquad (4.17)$$

The values of e_0, given by X_2/X_1, are found to be the same as those obtained by the buckling analysis in the preceding section. This is of course due to the fact that the values of the constants r_i in the deflection function are taken to be those given by the buckling mode. One could alternatively have considered the constants r_i to be unknowns, and minimized the energy with respect to these terms also, to obtain the same buckling strain and the buckling modes obtained in the preceding section. However by conducting the analysis in two separate stages, a tremendous saving is achieved in terms of computational work.

For an applied compressive strain $e = n_0\, e_{cr}$, eqn.4.16 may be rewritten to give the amplitude A for the lateral deflection as

$$A = B_0 \left[\frac{a}{\pi}\right] \sqrt{(n_0 - 1)e_{cr}} = B_0\, t \sqrt{(n_0 - 1)e_0} \qquad (4.18)$$

where $B_0 = \sqrt{X_1/X_0}$. The stresses in the X and Y directions may now be expressed as:

$$\sigma_x = - n_0 p_{cr} \left[1 - \frac{1}{(1-\nu t_0)} \left[1 - \frac{1}{n_0}\right] B_0^2 \left[\frac{a}{\pi}\right]^2 \left[\frac{1}{2} f_{,x}^2 + \frac{\nu}{2} f_{,y}^2 \right.\right.$$

$$\left.\left. + \left[\frac{\pi}{a}\right] \sum_i \left[t_{1i}\, g_{,xi} + \nu t_{2i}\, h_{,yi} \right] \right] \right]$$

and

$$\sigma_y = \frac{n_0 p_{cr}}{(1-\nu t_0)} \left[(t_0 - \nu) + \left[1 - \frac{1}{n_0}\right] B_0^2 \left[\frac{a}{\pi}\right]^2 \left[\frac{\nu}{2} f_{,x}^2 + \frac{1}{2} f_{,y}^2 \right.\right.$$

$$\left.\left. + \left[\frac{\pi}{a}\right] \sum_i \left[\nu t_{1i}\, g_{,xi} + t_{2i}\, h_{,yi} \right] \right] \right] \qquad (4.19)$$

In the present analysis, computations for the amplitude parameters of the buckled plate were carried out using seven terms of the trigonometric functions $g_i(x,y)$ and $h_i(x,y)$ for the displacements u and v (see eqns.4.1 and 4.2). The values of the integers k_i and l_i used in these functions, for i = 0 to 6, are listed in Table 4.2. Also presented in the next two columns of the table, are the values of e_0 and B_0 obtained by the addition of each successive term (with all six terms of the deflection w) for the right isosceles triangle subjected to the second loading condition. It may be observed that the values of B_0, which is the constant for the amplitude of the lateral deflection of the plate, converge to within 5% when all the seven terms are included. The values obtained for the constants t_{1i} and t_{2i}, which relate the coefficients C_{1i} and C_{2i} to the amplitude A of the lateral

deflection (see eqn.4.14) are given in Tables 4.6 to 4.9 for the two loading cases. The amplitude parameter B_0 is plotted against a/b in Figure 4.6 and its numerical values presented in Table 4.3. For a physical appreciation of the magnitudes of these values, the deflections along the centre-line of a right isosceles triangle are plotted for the two cases in Figure 4.7 for an applied strain equal to 10 times the critical strain. The maximum values of the deflection, again for a value of n_0 = 10, are plotted in Figure 4.8 as a function of a/b. Finally, for the same value of n_0, the stress distribution along the edges of a right isosceles triangular plate are shown in Figure 4.9 for the two loading cases. It may be noticed that while the stresses are of the same magnitude as the "applied stress" (10 times p_{cr}) at the corners of the plate, the stresses normal to the edge show a drastic reduction in magnitude as one moves towards the middle of each side, particularly in the first loading case. It may also be observed that in the second case, the tangential stresses show only a reduction of about 20% towards the middle of the plate.

4.6 Load End-Shortening Relations

The total load P, given by the sum of the normal stresses σ_x acting on the unequal edge of the isosceles triangular plate, may be expressed as,

$$P = (2bt)(n_0 p_{cr})C_0 \tag{4.20}$$

where

$$C_0 = \left[R_0 + \frac{(1 - R_0)}{n_0} \right] \tag{4.21}$$

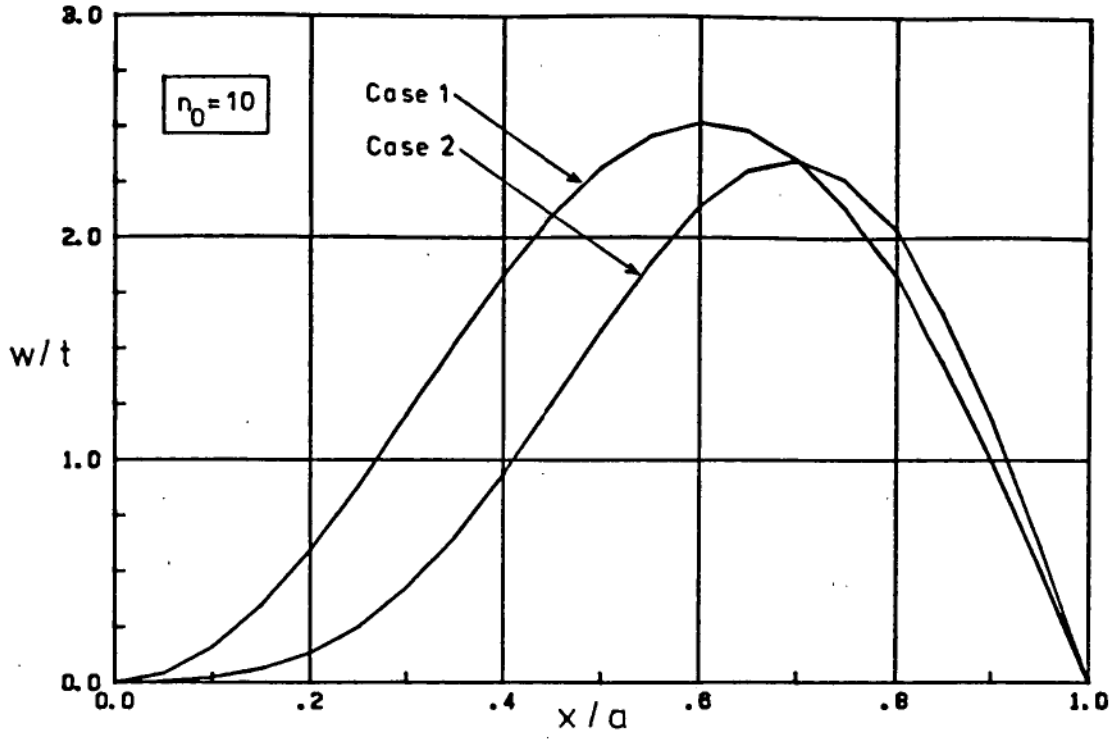

Figure 4.7. Deflections along the Centre-Line of the Right Isosceles Triangular Plate

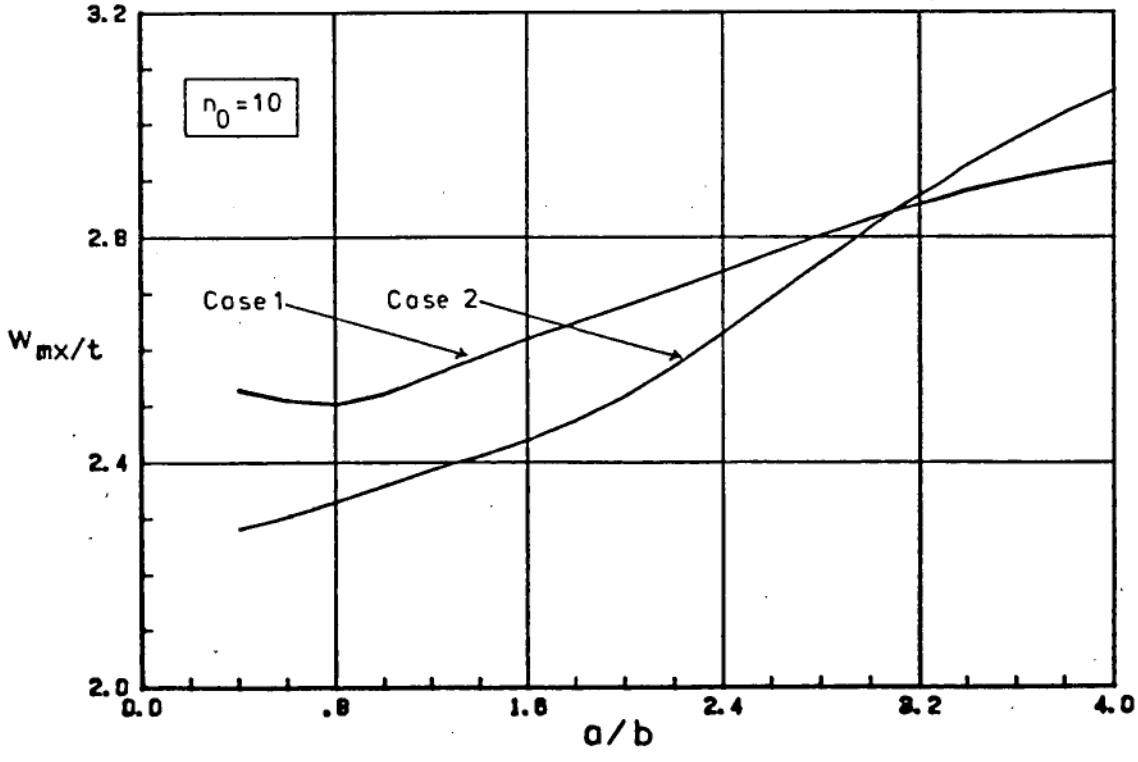

Figure 4.8. Maximum Deflections

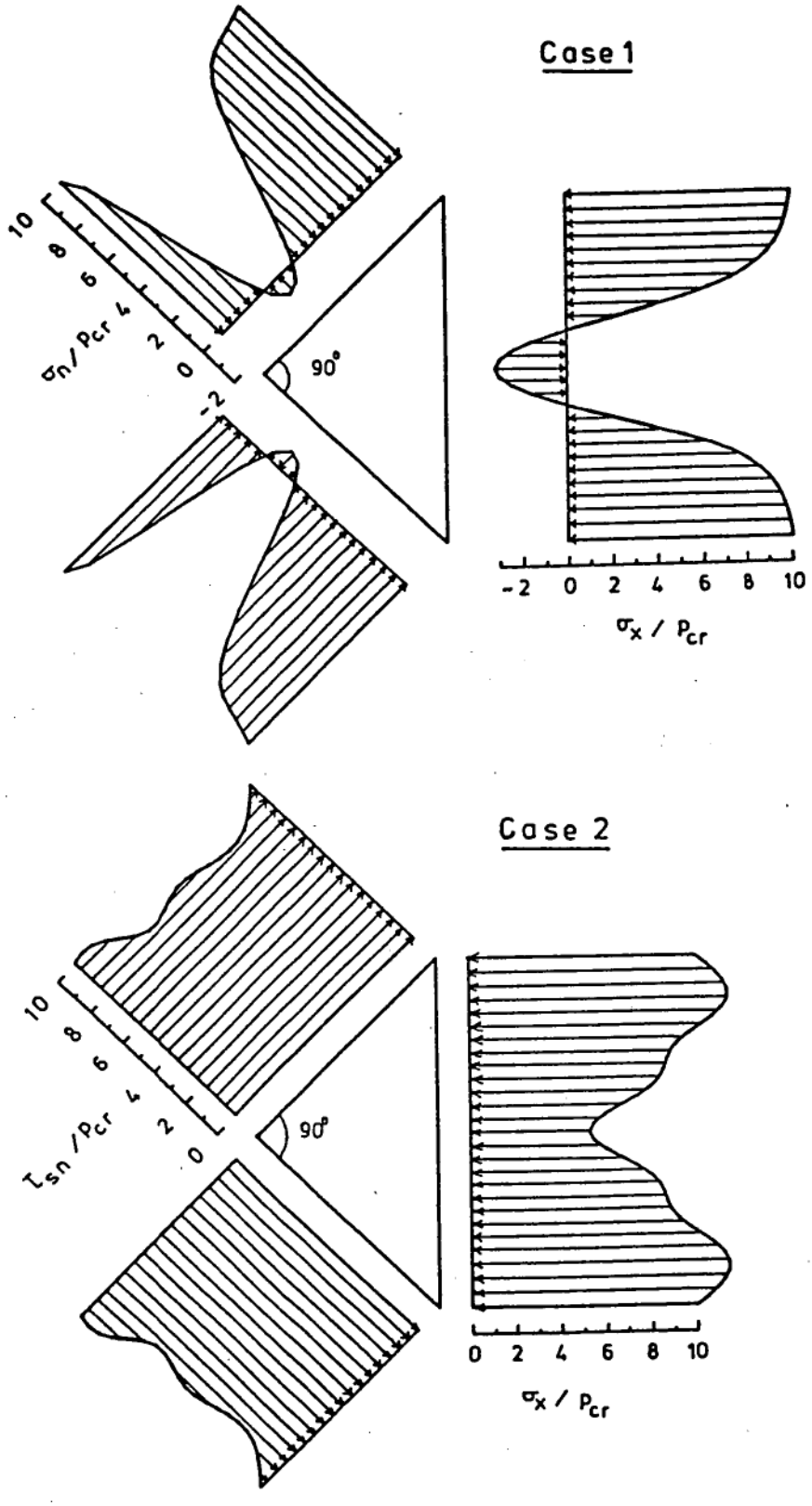

Figure 4.9. Stress Distribution along the Edges of the Right Isosceles Triangular Plate

In eqn.4.21, R_0 is a constant for a fixed a/b ratio obtained as,

$$R_0 = 1 - \frac{B_0^2}{(1-\nu t_0)b}\left[\frac{a}{\pi}\right]^2 \int_0^b \left[\frac{1}{2} f_{,x}^2 + \frac{\nu}{2} f_{,y}^2 + \left[\frac{\pi}{a}\right]\sum_i \left[t_{1i} g_{,xi} + \nu t_{2i} h_{,yi}\right]\right]_{x=a} dy \qquad (4.22)$$

For the unbuckled plate, the relation between the total load P acting on the base and the end-shortening in the X direction (normal to the base), may be expressed in non-dimensionalized form as

$$\eta = n_0 \qquad (4.23)$$

where η is the normalized load given by $\eta = P/(2btp_{cr})$ and n_0 is the normalized end-shortening, given by the relation $n_0 = e/e_{cr}$. It may be noted that e is the linear component of the strain, and hence the end-shortening per unit height "a" of the isosceles triangular plate. The terms p_{cr} and e_{cr} are respectively the critical stress and strain corresponding to the primary buckling mode. From eqns.4.20 and 4.21, the relation between the load and end-shortening (in normalized terms) for the plate which buckles into the primary mode, is obtained as

$$\eta = (1 - R_0) + R_0\, n_0 \qquad (4.24)$$

Eqn.4.24 indicates that the post-buckling path is linear, and that its slope is given by the value of R_0. The values of R_0 obtained from eqn.4.22 are tabulated in the last columns under Case 1 and 2 in Table 4.3, and also plotted (in solid lines) in Figure 4.10.

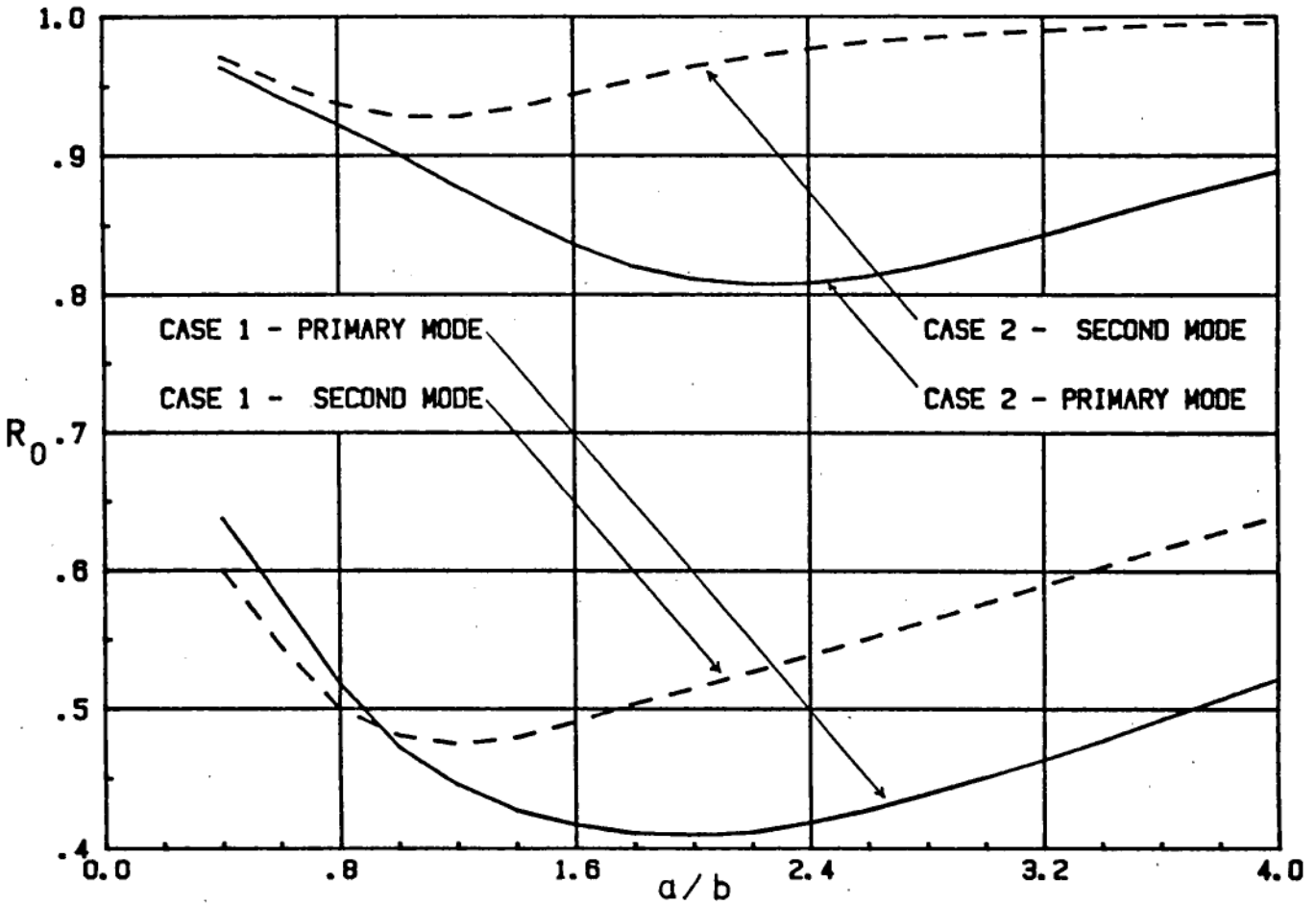

Figure 4.10. Constant R_0
for the Total Load on the Plate

In order to investigate the possibility of the deflection pattern of the plate changing into a higher mode when the loading is continued after primary buckling has occurred, the foregoing large deflection analysis was repeated using the values of the second buckling mode for the deflection function w. The values of R_0 thus obtained for the second mode are shown in broken lines for the two loading cases in Figure 4.10. Denoting the values of R_0 for the second mode by R_{02}, and the buckling coefficients for the first and second modes respectively by P_{01} and P_{02}, the relation between load and end shortening for the second mode may be expressed as

$$\eta = (1 - R_{02})(p_{02}/p_{01}) + R_{02}\, n_0 \tag{4.25}$$

where η and n_0 still represent the load and the end-shortening non-dimensionalized with respect to the buckling stress and strain corresponding to the primary mode. Hence R_{02} represents the slope of the post-buckling path for the second buckling mode. As seen in Figure 4.10, the difference between the values of R_0 for the two modes is only about 10%. Further, for most of the values of a/b considered, the slope of the second post-buckling path is greater than that of the primary mode. Thus the intersection of these two paths, according to the present analysis, is only a remote possibility. To illustrate this the load vs. end-shortening diagram of the right isosceles triangular plate is shown in Figure 4.11, for the first loading condition.

It may be added that the repetition of the analysis using the second buckling mode and the investigation of the possibility of

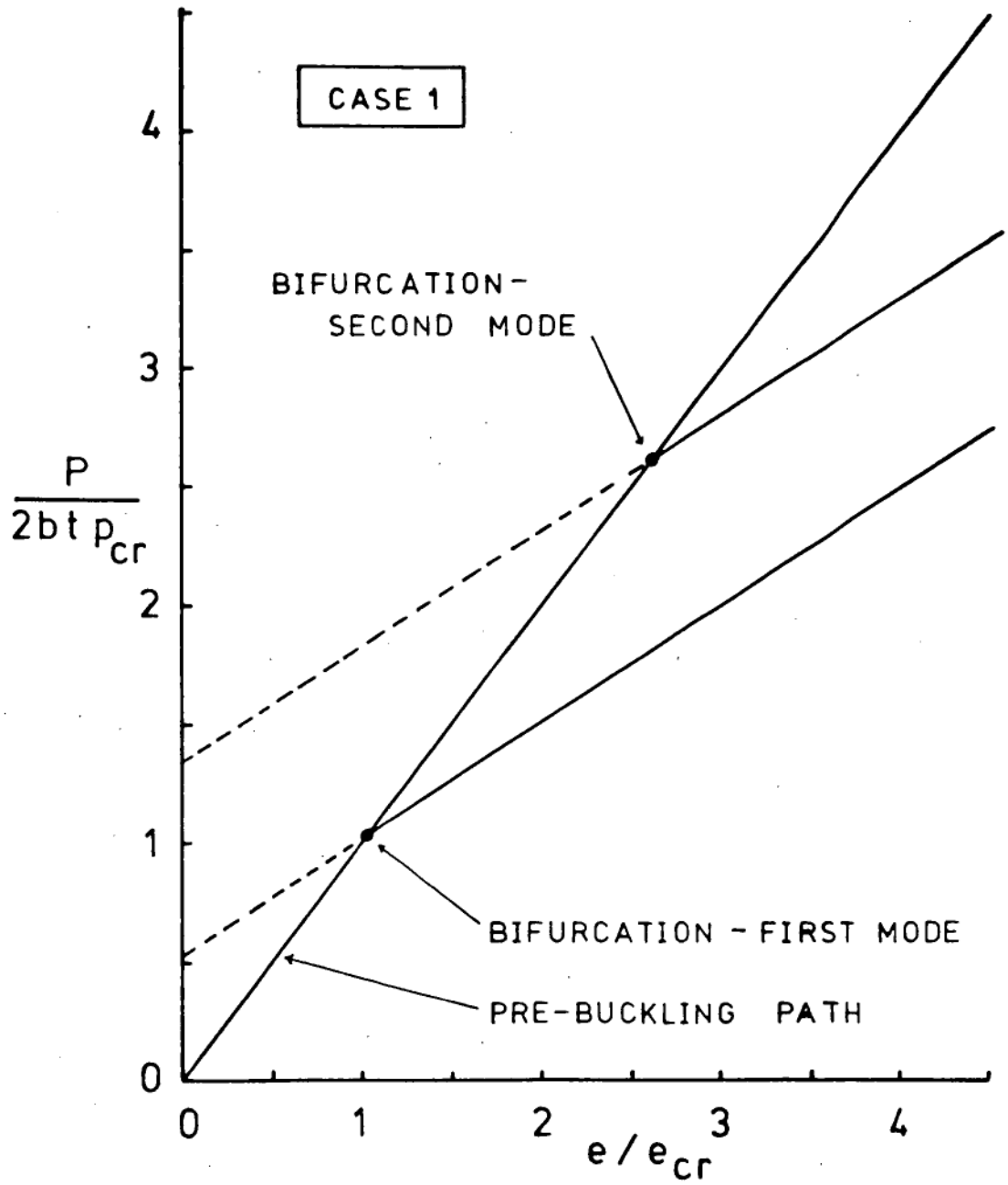

Figure 4.11. Load End-Shortening Diagram for the Right Isosceles Triangular Plate

its occurrence was conducted only because it had been pointed out to the author that the results obtained using the primary mode may not be valid in the advanced post-buckling region, owing to the possibility of a change in the deflection mode. However it is obvious from the foregoing discussion that, a plate with negligible imperfections, which buckles into the primary mode when the load reaches its first critical value and follows the post-buckling path for the first mode, continues to remain in this mode even when the load is increased beyond its second critical value, since it can go into the second mode only when the two post-buckling paths intersect. The present study being restricted to the perfect isosceles triangular plate, it is thus safe to assume that the buckled plate retains the primary mode to the limit of its load carrying capacity.

4.7 Effective width

For the rectangular plate subjected to compression in only one direction, the load may be considered to be supported by two strips along the unloaded sides of the plate, where the ratio of the combined widths of these strips to the width of the loaded edges is given by the ratio of the average of the non-uniform stresses to the maximum stress in the buckled plate. Such an approximation was first suggested by Von Kármán (Ref.1, page 418) and simplifies the determination of the ultimate strength of the plate considerably. Thus as far as the load carrying capacity is concerned, we may replace the rectangular panel by these two strips along the edges of the plate.

The analogous situation for a triangular plate would be its replacement by a triangular frame, whose three members have the same thickness as that of the plate, and widths equal to the effective widths of the sides of the triangular plate. This idealization has already been made in order to replace the Yoshimura model of the buckled cylindrical shell with a simpler space frame model, which has facilitated the development of a theory to predict the secondary buckling behaviour observed in axially loaded cylindrical shells. The key to the idealization, however, is the effective widths of the sides of the triangular panel, and the analysis outlined in the preceding sections has been conducted with the aim of estimating these effective widths.

Following the approach used for the rectangular plate, the non-uniform stress distribution on the base of the buckled triangular plate may be replaced by an equivalent uniform distribution of stress, of magnitude ($n_0 p_{cr}$), acting over a length of $C_0 b$ at either end, where the value of C_0 is given by eqn.4.21. It may be noted from eqn.4.20 that the summation of this stress over the area upon which it acts ($2btC_0$) is equal to the total load acting on the base of the plate. Thus, the load carried by the triangular panel may be considered to be supported entirely by two strips along the equal edges of the plate, spanning a length equal to $C_0 b$ at each end of the base. The widths of these strips, by geometry, is given by

$$w_s = C_0 b \cos \theta \qquad (4.26)$$

where θ is the semi-vertex angle of the plate. Assuming that the third

member, along the base of the triangle, has a width equal to $C_0 a$, we may replace the panel by an equivalent triangular frame as shown in Figure 4.12a.

Using the maximum value of $C_0 = 1$, we see that the strips along the equal sides of the equivalent frame replacing an unbuckled (or, just buckled) panel have widths such that each covers half the base; and the strip along the base has a width equal to the height of the triangle. Hence this idealization, although it may be applicable for small values of C_0 (which requires that R_0 be small and n_0 be large), would seem unreasonable for large values of R_0(as in case 2) or for small values of n_0 (in both cases).

A better idealization may be made by using the following approach: Since the base length of the buckled plate is effectively reduced by a factor of C_0, and since the maximum deflections occur in the vicinity of the centre of the plate, a small region at the centre of the plate may be considered as ineffective in supporting the load. This region is assumed to be a similar isosceles triangle, whose base length is $2(1-C_0)b$ and height equal to $(1-C_0)a$, as shown with broken lines in Figure 4.12b. The strips of the panel surrounding this region is assumed to constitute the equivalent isosceles triangular frame. In this case the effective width of the member along the base of the triangle becomes equal to $C_0 a/2$; and the width of the members along the equal sides is obtained from geometry as,

$$w_s = \frac{1}{2} C_0 b \cos \theta \qquad (4.27)$$

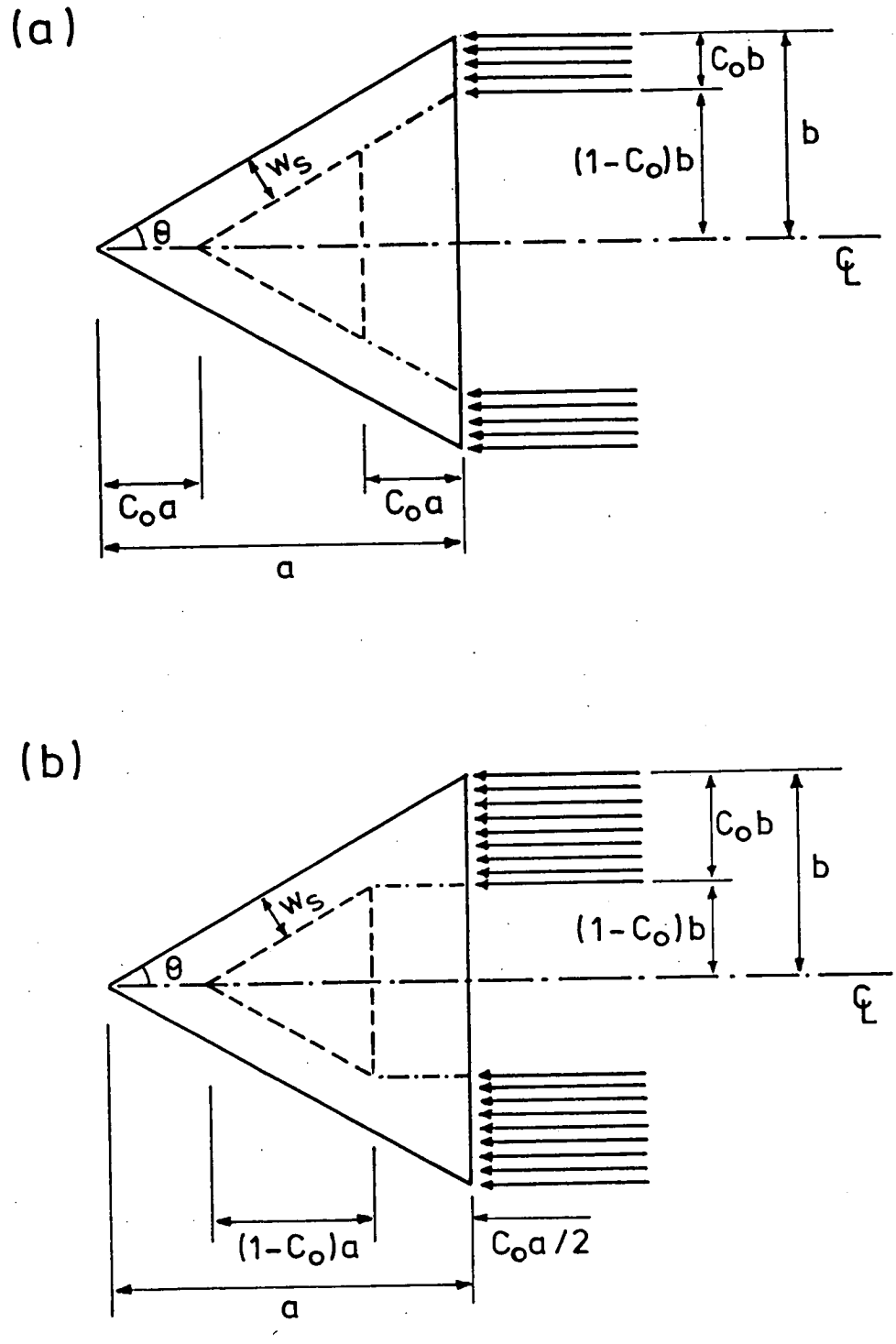

Figure 4.12
Idealizations for Effective Width

Thus the values obtained by this approach for the effective widths of all the three members are half of those given by the first. For the unbuckled plate, the equal members have widths covering only a quarter of the base, and the strip along the base has a width equal to half the height of the triangle; hence this idealization seems more reasonable. Whichever idealization is employed, the ratio of the effective width of each member to its maximum width is obtained as

$$\frac{w_s}{w_{s\ max}} = C_0 \tag{4.28}$$

and its minimum value

$$\frac{w_{s\ min}}{w_{s\ max}} = R_0 \tag{4.29}$$

Having determined the values of R_0 by means of the analysis conducted in the preceding sections, it is now seen that the actual value of the effective width depends on the value of w_{smax}, which is basically the effective width of the sides of the unbuckled plate. In the case of the rectangular plate it is readily seen that the value of w_{smax} should be half the total width of the plate. However, for the triangular plate, the matter of interpreting as to what constitutes the width of each edge of the unbuckled plate is not so easy. The two idealizations presented above, one by considering what portion of the base of the plate is effective in supporting the load, and the other by looking at what may be considered to be the ineffective region of the plate*, may thus be looked upon as two different interpretations

* It is interesting to note that both these approaches lead to the same result for the rectangular plate.

regarding the widths of the sides of the unloaded plate. In the first approach the equal edges of the unbuckled plate are found to span over half the length of the base, while in the second case, these sides are taken to be only half as wide.

In comparing the two cases of loading considered it is found that the values of R_0 are much higher in the second case than in the first (see Figure 4.10). This is of course due to the fact that the variation in the stress distribution along the edges (Figure 4.9) is much smaller in the second case than in the first. (It is also to be noted that only the variation in the stresses along the base has been considered in developing the two idealizations for the effective width). The high values of R_0 imply two things: firstly, that the plate is stiffer in the post-buckled state under the second loading condition than under the first, and secondly that a greater portion of the total area of the plate is effective in resisting the load acting on it. Thus the analysis indicates that the plate is more effective in its buckled condition in case 2 than in case 1.

4.8 Application to the Space Frame Model

For the second loading case, which approximates the condition on the triangular panels in the Yoshimura model, the minimum value of R_0 obtained is about 0.81 (for a/b = 2.2, see Figure 4.10). Also the values obtained for the second mode are all higher than those of the primary mode in this case. Further, from Table 4.2, it can be seen that the values of R_0 hardly vary with the addition of successive

terms in u and v. Thus it is found that the values of the minimum effective width ratio cannot be reduced any further either by increasing the number of terms in the analysis or by considering deflections in the higher modes.

Considering the example of the shell tested by Esslinger and Geier*, it is seen that the first secondary collapse, from N = 15 to N = 14 occurred at 275N. The average axial stress in the shell for this load is obtained as

$$p_{av} = 275/(2\pi Rt) = 2.30 \text{ Mpa}$$

Taking $\lambda = 0.7$ (i.e., a/b = 1.4, where $b = \pi R/N$) for the aspect ratio, which gives a value of $p_0 = 7.59$ (from Table 4.3), the buckling stress for the panel is found to be

$$p_{cr} = \pi^2 D p_0/(ta^2) = 1.64 \text{ Mpa}$$

which gives an approximate value for $n_0 \simeq p_{av} / p_{cr} = 1.4$. Using this value of n_0, and $R_0 = 0.856$ (for a/b = 1.4 from Table 4.3), the value of C_0 is obtained as 0.96. *Thus it is found that when secondary buckling occurs in the shell, the facets of the buckle pattern are loaded only about 50% in excess of their buckling load, and the reduction in the effective width of the sides of the panel is within 5%.* Using the second idealization - which predicts only half as much as the effective widths predicted by the first idealization - the maximum value for the effective widths of the diagonal members is

* R = 100 mm, t = 0.19 mm, E = 5.5 Gpa, $\nu = 0.35$.

obtained as $$w_{smax}/t = \frac{\pi R}{N t} \frac{\lambda}{\sqrt{4\lambda^2 + 1}} = 44.85$$

Using the values of $C_0 = 0.96$, and $R_0 = 0.856$, the actual effective width and its minimum value are respectively obtained as

$$w_s = 43.1\ t \quad \text{and} \quad w_{smin} = 38.4\ t$$

Noting that the moment of inertia and hence the buckling load is approximately proportional to the cube of the flange width, even if the minimum value of W = 38.4t is employed, the secondary buckling load predicted for N = 15 would be about 6 times higher than the observed value. The effective width given by the first idealization would result in predictions that are a further 8 times higher.

It is therefore clear that - even assuming that the two idealizations are valid for the second loading case - neither of them yields the values for the flange width of the diagonal members of the space frame that have been used in the analysis in chapter 3. It is also obvious that while the question of what constitute the widths of the sides of an unloaded triangular plate remains unresolved, the present method cannot be employed to determine the effective width.

4.9 Concluding Remarks

While the approach using the large deflection analysis of isosceles triangular plates has thus been unsuccessful as far as the determination of the effective flange widths of the members of the

space frame is concerned, several significant aspects have been revealed by the study which are noteworthy.

Firstly it is seen that the concept of effective width which has been successfully employed in the analysis of the rectangular plate cannot be easily extended to the case of the triangular plate. The concept may still be applicable where only the proportionate reduction in the effective area of the plate is required, as in the estimation of the ultimate strength of the plate; but where the actual values of the widths of the sides are required, the problem arises in the definition of the initial widths of the sides of the unloaded triangular plate, which is open to different interpretations.

Secondly, the analysis has been conducted on the assumption of rigid supports along the edges of the plate. Such an analysis would thereby be appropriate to situations wherein the panels are supported by strong members along the edges, as in the case of a triangular stiffening construction*. In the present context, however, it is seen that the whole frame including the supports and the panels, collapses at an average stress that is only about 50% higher than the buckling stress of the panels. In fact in the model of the buckled cylinder, there are no separate supports, the support is provided by the panels themselves or by similar panels in the neighborhood. In this case, the strength of the panels and the strength of the supports are

* In view of the new interest in triangular stiffening construction[68], the results of the present analysis have been used to estimate the ultimate strength of the isosceles triangular panel, which, not being directly relevant to the current investigation on cylindrical shells, is presented at the end of the thesis, in Appendix A.

interdependent. Hence it is realized, in hindsight, that it would perhaps be more appropriate to investigate the supports and the panels simultaneously, that is, to consider the buckling of the folds as columns and that of the flanges as wide panels under axial compression, in conjunction. Such an approach is used - more successfully - in the next chapter to determine the effective widths of the flanges of the diagonal members of the space frame.

Perhaps the most significant aspect revealed by the study, is that - as long as the supports do not fail - a large proportion of the interior of the triangular panel is effective in resisting the load acting on it. This is indicated by the relatively low variation in the stress distribution along the edges as well as by the high values of R_0 obtained, for the second loading case. Although the quantitative evaluations of the widths of the equal members of the panel are suspect, owing to the uncertainty regarding the definition of the initial widths; the analysis definitely indicates that the widths of the flanges of the diagonal members of the space frame could be large, and need not necessarily be restricted to the values that have been used in the space frame theory developed in the preceding chapter.

Table 4.1. Effect of Increasing the Number of Terms in w on the Buckling Coefficient

Case 2			p_0	
i	m	n	$\alpha = 1$	$\alpha = 1/\sqrt{3}$
1	1	3	8.67467	30.2628
2	1	5	5.86397	12.0712
3	3	5	5.85063	11.5484
4	1	7	5.82554	9.81455
5	3	7	5.78267	9.80271
6	5	7	5.78239	9.771

Table 4.2 Effect of Increasing the Number of Terms in u and v (α = a/b = 1, Case 2)

i	k	l	e_0	B_0	R_0
0	1	3	0.688381	0.302054	0.925626
1	1	5	0.688381	0.390538	0.946053
2	3	5	0.688381	0.458544	0.902273
3	1	7	0.688381	0.536108	0.902124
4	3	7	0.688381	0.542901	0.895983
5	1	9	0.688381	0.585716	0.917947
6	5	7	0.688381	0.605485	0.90105

Table 4.3 Basic Parameters Obtained by the Analysis

	Case 1				Case 2			
a/b	p_0	e_0	B_0	R_0	p_0	e_0	B_0	R_0
0.4	1.8822	.12070	1.3952	.63816	4.4385	1.1686	.47323	.96345
0.6	1.9707	.12641	1.4191	.57853	4.7168	.79191	.57388	.94244
0.8	2.1841	.14010	1.4073	.51846	5.1605	.69410	.60921	.92242
1.0	2.5000	.16034	1.3613	.47322	5.7824	.68838	.60549	.90105
1.2	2.8872	.18513	1.2945	.44468	6.5883	.72901	.57853	.87826
1.4	3.3301	.21350	1.2191	.42748	7.5905	.80150	.53883	.85566
1.6	3.8292	.24548	1.1425	.41679	8.8166	.90200	.49446	.83570
1.8	4.3900	.28142	1.0681	.41093	10.314	1.0319	.45109	.82048
2.0	5.0188	.32172	.99748	.40958	12.148	1.1958	.41154	.81099
2.2	5.7219	.36679	.93194	.41240	14.396	1.4000	.37646	.80716
2.4	6.5048	.41698	.87211	.41869	17.146	1.6519	.34545	.80828
2.6	7.3728	.47261	.81805	.42765	20.491	1.9597	.31785	.81340
2.8	8.3298	.53396	.76936	.43857	24.531	2.3324	.29306	.82148
3.0	9.3786	.60119	.72545	.45091	29.372	2.7794	.27061	.83158
3.2	10.521	.67443	.68571	.46425	35.127	3.3110	.25019	.84287
3.4	11.758	.75371	.64956	.47823	41.915	3.9380	.23155	.85468
3.6	13.089	.83904	.61656	.49258	49.863	4.6719	.21451	.86652
3.8	14.515	.93042	.58630	.50706	59.106	5.5251	.19894	.87803
4.0	16.034	1.0278	.55849	.52150	69.784	6.5103	.18470	.88897

Table 4.4 Buckling Modes for Case 1

m,n	1,3	1,5	3,5	1,7	3,7	5,7
a/b	r_1	r_2	r_3	r_4	r_5	r_6
0.4	1	0.155481	-.090060	0.045192	-.011065	-.011971
0.6	1	0.119313	-.048714	0.030970	0.001005	-.008755
0.8	1	0.063823	-.016378	0.013665	0.005370	-.003721
1.0	1	-.000007	-.000006	-.000008	-.000005	-.000002
1.2	1	-.063435	0.004790	-.006442	-.009633	0.000903
1.4	1	-.121474	0.002917	-.005278	-.018310	-.000235
1.6	1	-.172831	-.002757	0.001687	-.023825	-.002150
1.8	1	-.217702	-.010596	0.012057	-.026153	-.004043
2.0	1	-.256384	-.019431	0.023733	-.026137	-.005595
2.2	1	-.289083	-.028354	0.035215	-.024727	-.006758
2.4	1	-.316148	-.036739	0.045627	-.022664	-.007592
2.6	1	-.338129	-.044241	0.054586	-.020433	-.008178
2.8	1	-.355717	-.050730	0.062033	-.018307	-.008589
3.0	1	-.369642	-.056218	0.068082	-.016410	-.008882
3.2	1	-.380588	-.060795	0.072923	-.014784	-.009094
3.4	1	-.389156	-.064578	0.076760	-.013424	-.009252
3.6	1	-.395847	-.067692	0.079782	-.012304	-.009374
3.8	1	-.401061	-.070249	0.082153	-.011391	-.009470
4.0	1	-.405125	-.072349	0.084009	-.010650	-.009548

Table 4.5 Buckling Modes for Case 2

m,n	1,3	1,5	3,5	1,7	3,7	5,7
a/b	r_1	r_2	r_3	r_4	r_5	r_6
0.4	1	-.165153	0.009925	-.006113	-.000278	0.000568
0.6	1	-.189196	0.004453	-.004023	-.004953	0.001002
0.8	1	-.228439	-.003540	0.001929	-.012304	0.000557
1.0	1	-.279397	-.014009	0.014400	-.018918	-.001161
1.2	1	-.336366	-.026984	0.034264	-.021872	-.003594
1.4	1	-.394575	-.042307	0.059658	-.020185	-.005894
1.6	1	-.450011	-.059151	0.087134	-.014815	-.007579
1.8	1	-.499520	-.076199	0.113434	-.007485	-.008589
2.0	1	-.541469	-.092261	0.136570	0.000310	-.009070
2.2	1	-.575745	-.106628	0.155863	0.007658	-.009207
2.4	1	-.603167	-.119058	0.171467	0.014151	-.009147
2.6	1	-.624901	-.129609	0.183903	0.019694	-.008988
2.8	1	-.642098	-.138481	0.193767	0.024344	-.008786
3.0	1	-.655755	-.145920	0.201602	0.028217	-.008576
3.2	1	-.666668	-.152163	0.207859	0.031439	-.008372
3.4	1	-.675459	-.157421	0.212891	0.034126	-.008183
3.6	1	-.682603	-.161869	0.216972	0.036377	-.008012
3.8	1	-.688460	-.165653	0.220309	0.038273	-.007858
4.0	1	-.693307	-.168892	0.223065	0.039880	-.007721

Table 4.6 Constants for the Coefficients of g(x,y) in u for Case 1

k,l	1,3	1,5	3,5	1,7	3,7	1,9	5,7
a/b	t_{10}	t_{11}	t_{12}	t_{13}	t_{14}	t_{15}	t_{16}
0.4	0.08317	-.12231	-.14203	0.05492	-.00953	0.01885	0.02192
0.6	0.03099	-.13690	-.12342	0.04581	-.00374	0.01470	0.01434
0.8	-.00023	-.13559	-.11205	0.05120	0.00440	0.01245	0.00809
1.0	-.01231	-.12458	-.10458	0.06594	0.01557	0.00858	0.00395
1.2	-.01495	-.11301	-.09877	0.08300	0.02830	0.00016	0.00157
1.4	-.01398	-.10539	-.09456	0.09853	0.04070	-.01256	0.00080
1.6	-.01140	-.10171	-.09192	0.11167	0.05179	-.02760	0.00130
1.8	-.00869	-.10023	-.09029	0.12266	0.06135	-.04287	0.00263
2.0	-.00789	-.09913	-.08899	0.13166	0.06941	-.05670	0.00448
2.2	-.01089	-.09693	-.08744	0.13853	0.07615	-.06803	0.00670
2.4	-.01872	-.09261	-.08535	0.14306	0.08178	-.07634	0.00927
2.6	-.03149	-.08562	-.08260	0.14509	0.08649	-.08158	0.01215
2.8	-.04865	-.07574	-.07921	0.14456	0.09043	-.08397	0.01532
3.0	-.06932	-.06303	-.07528	0.14152	0.09372	-.08389	0.01870
3.2	-.09258	-.04770	-.07091	0.13611	0.09643	-.08174	0.02225
3.4	-.11760	-.03005	-.06618	0.12850	0.09861	-.07789	0.02590
3.6	-.14368	-.01037	-.06119	0.11890	0.10030	-.07267	0.02959
3.8	-.17031	0.01103	-.05600	0.10749	0.10153	-.06633	0.03329
4.0	-.19709	0.03386	-.05068	0.09448	0.10233	-.05910	0.03695

Table 4.7 Constants for the Coefficients of g(x,y) in u for Case 2

k,l	1,3	1,5	3,5	1,7	3,7	1,9	5,7
a/b	t_{10}	t_{11}	t_{12}	t_{13}	t_{14}	t_{15}	t_{16}
0.4	0.27126	-.13266	-.19363	0.16449	0.01065	-.06872	-.05716
0.6	0.27116	-.14012	-.16486	0.16303	0.02207	-.07386	-.04190
0.8	0.27951	-.15063	-.14181	0.16846	0.03500	-.08760	-.03003
1.0	0.30418	-.16375	-.12356	0.17958	0.04836	-.10940	-.01925
1.2	0.34630	-.18015	-.10905	0.19419	0.06114	-.13728	-.00826
1.4	0.40104	-.19851	-.09681	0.21076	0.07270	-.16764	0.00318
1.6	0.45799	-.21597	-.08547	0.22775	0.08269	-.19613	0.01462
1.8	0.50551	-.22988	-.07456	0.24336	0.09106	-.21929	0.02530
2.0	0.53602	-.23877	-.06436	0.25611	0.09799	-.23550	0.03466
2.2	0.54753	-.24235	-.05534	0.26525	0.10376	-.24486	0.04246
2.4	0.54208	-.24108	-.04774	0.27067	0.10863	-.24846	0.04874
2.6	0.52338	-.23571	-.04159	0.27266	0.11280	-.24764	0.05371
2.8	0.49528	-.22704	-.03671	0.27167	0.11637	-.24364	0.05762
3.0	0.46109	-.21577	-.03289	0.26818	0.11943	-.23745	0.06070
3.2	0.42334	-.20250	-.02988	0.26262	0.12203	-.22981	0.06314
3.4	0.38388	-.18770	-.02749	0.25537	0.12421	-.22124	0.06510
3.6	0.34400	-.17178	-.02555	0.24674	0.12598	-.21212	0.06670
3.8	0.30456	-.15504	-.02392	0.23700	0.12739	-.20270	0.06802
4.0	0.26611	-.13772	-.02252	0.22638	0.12846	-.19317	0.06913

Table 4.8 Constants for the Coefficients of h(x,y) in v for Case 1

k,l	1,3	1,5	3,5	1,7	3,7	1,9	5,7
a/b	t_{20}	t_{21}	t_{22}	t_{23}	t_{24}	t_{25}	t_{26}
0.4	-.04974	0.01209	0.05649	0.02197	0.01445	0.01233	-.00419
0.6	-.04283	0.03943	0.07479	0.02925	0.02224	0.01115	0.00183
0.8	-.02383	0.06685	0.08964	0.02757	0.02419	0.00627	0.00668
1.0	-.00341	0.08874	0.10141	0.01959	0.02024	0.00200	0.00753
1.2	0.01582	0.10460	0.10978	0.00836	0.01247	0.00011	0.00590
1.4	0.03409	0.11649	0.11561	-.00402	0.00288	0.00049	0.00361
1.6	0.05136	0.12666	0.12000	-.01660	-.00746	0.00237	0.00125
1.8	0.06734	0.13667	0.12378	-.02897	-.01806	0.00505	-.00112
2.0	0.08201	0.14735	0.12762	-.04089	-.02857	0.00801	-.00344
2.2	0.09570	0.15900	0.13203	-.05212	-.03871	0.01093	-.00554
2.4	0.10889	0.17160	0.13734	-.06253	-.04830	0.01365	-.00726
2.6	0.12200	0.18497	0.14367	-.07207	-.05727	0.01607	-.00849
2.8	0.13537	0.19891	0.15104	-.08079	-.06562	0.01819	-.00923
3.0	0.14917	0.21320	0.15935	-.08876	-.07342	0.02004	-.00950
3.2	0.16350	0.22768	0.16850	-.09608	-.08075	0.02164	-.00937
3.4	0.17840	0.24223	0.17836	-.10288	-.08769	0.02303	-.00890
3.6	0.19384	0.25675	0.18883	-.10922	-.09431	0.02425	-.00815
3.8	0.20981	0.27121	0.19981	-.11519	-.10068	0.02533	-.00716
4.0	0.22626	0.28555	0.21121	-.12085	-.10684	0.02628	-.00597

Table 4.9 Constants for the Coefficients of h(x,y) in v for Case 2

k,l	1,3	1,5	3,5	1,7	3,7	1,9	5,7
a/b	t_{20}	t_{21}	t_{22}	t_{23}	t_{24}	t_{25}	t_{26}
0.6	0.26936	0.02630	0.13531	0.01824	-.03006	-.01511	0.06063
0.8	0.26511	0.03220	0.15448	0.01020	-.03262	-.01606	0.06387
1.0	0.27291	0.03883	0.16954	0.00073	-.03826	-.01484	0.06816
1.2	0.29018	0.04498	0.18229	-.01026	-.04669	-.01186	0.07380
1.4	0.31222	0.05184	0.19414	-.02246	-.05711	-.00773	0.08026
1.6	0.33464	0.06101	0.20580	-.03536	-.06861	-.00309	0.08672
1.8	0.35472	0.07341	0.21718	-.04842	-.08036	0.00157	0.09247
2.0	0.37175	0.08898	0.22792	-.06115	-.09179	0.00598	0.09713
2.2	0.38633	0.10703	0.23784	-.07327	-.10266	0.00999	0.10069
2.4	0.39959	0.12671	0.24700	-.08464	-.11296	0.01356	0.10337
2.6	0.41253	0.14729	0.25561	-.09528	-.12275	0.01673	0.10547
2.8	0.42588	0.16824	0.26392	-.10524	-.13216	0.01952	0.10723
3.0	0.44007	0.18921	0.27212	-.11461	-.14128	0.02199	0.10884
3.2	0.45531	0.21000	0.28036	-.12350	-.15020	0.02419	0.11043
3.4	0.47165	0.23050	0.28874	-.13197	-.15897	0.02617	0.11208
3.6	0.48906	0.25065	0.29731	-.14011	-.16764	0.02797	0.11385
3.8	0.50749	0.27044	0.30611	-.14796	-.17625	0.02961	0.11575
4.0	0.52683	0.28988	0.31513	-.15559	-.18480	0.03112	0.11779

NOTATIONS

a : Height of the isosceles triangle

b : Half-length of the base (the unequal side) of the triangle

e : Linear component of strain in the X direction

e_{cr} : Critical value of the strain e

e_0 : Non-dimensional value of e_{cr} (see eqn.4.10)

$f_i(x,y)$: Functions representing the lateral deflection w

$g_i(x,y)$: Functions representing the non-linear component of u

$h_i(x,y)$: Functions representing the non-linear component of v

k_i, l_i : Odd integer constants used in $g_i(x,y)$ and $h_i(x,y)$

m_i, n_i : Odd integer constants used in $f_i(x,y)$

n_0 : Ratio of the applied strain to the critical strain = e/e_{cr}

p : Normal compressive stress along the base

p_{cr} : Critical value of p - Buckling stress

p_0 : Non-dimensional buckling coefficient (see eqn.4.8)

r_i : The buckling mode - relative amplitudes of $f_i(x,y)$

t : Thickness of the plate

t_0 : Ratio of linear strains in X and Y directions (see eqn.4.3)

t_{1i}, t_{2i} : Constants relating C_{1i}, C_{2i} to the amplitude A of w

u, v : Displacements in X and Y directions respectively

w : Out of plane displacement of the plate

w_s : Effective widths of the equal sides of the plate

A : Amplitude of the out of plane deflection

B_0 : Parameter for the amplitude A (see eqn.4.18)

C_0 : Factor for total load on the buckled plate (see eqn.4.20)

C_{1i}, C_{2i} : Coefficients for $g_i(x,y)$ and $h_i(x,y)$ respectively

D : Modulus of rigidity of the plate = $Et^3/12(1-\nu^2)$

E : Young's Modulus

P : Total load carried by the plate

R_0 : Slope of the (non-dimensional) post-buckling path

U_b, U_m : Bending and membrane strain energies of the plate

U_0 : Total strain energy

V : Change in potential energy due to buckling

W : Work done by the middle plane stresses during buckling

α : Measure of the aspect ratio = $\tan\theta$ = b/a = $1/(2\lambda)$

ν : Poisson's ratio

θ : Semi-vertex angle of the isosceles triangular plate

ϵ_x, ϵ_y : Strains in X and Y directions respectively

γ_{xy} : Shear strain

σ_x, σ_y : Stresses in X and Y directions

τ_{xy} : Shear stress

σ_n, τ_{xy} : Normal and shear stress components along the equal edges of the plate

CHAPTER 5

MODIFICATIONS TO THE SPACE FRAME THEORY

The attempt made in the previous chapter to establish the effective width was based on the fundamental premise of the Von Kármán hypothesis, according to which the total load on the buckled plate is considered to be supported by a uniform stress of intensity equal to the maximum stress distributed over a width equal to the effective width of the buckled plate, which gives rise to the relation

$$b_e / b = \sigma_{av} / \sigma_0 \qquad (5.1)$$

σ_{av} and σ_0 are respectively the average and the maximum stresses in the buckled plate of width b, and b_e is the effective width, or the width of an equivalent unbuckled plate, which can in effect replace the buckled plate for considerations of its load carrying capacity. The above equation, however, is seldom used to establish the effective width (the attempt made in the previous chapter not withstanding). Since it is only the minimum effective width corresponding to the maximum load that is of practical interest, this width is usually established by simpler means using other criteria.

For example, for determining the ultimate strength of the rectangular plate, the maximum value of σ_0, which is taken to be the buckling stress of the equivalent plate with the minimum effective width, is equated to the yield stress σ_{yp} of the material (this method

was also suggested by Von Kármán - Ref.1, page 418) to give the relations

$$(\sigma_0)_{max} = \sigma_{yp} = K\,E\,t^2/(b_e)^2_{min} \tag{5.2}$$

where K is the buckling coefficient depending on the edge conditions of the plate and the Poisson's ratio ν. Noting that for the original plate the critical stress $\sigma_{cr} = KEt^2/b^2$, the minimum effective width may be expressed as

$$\frac{(b_e)_{min}}{b} = \sqrt{\frac{\sigma_{cr}}{\sigma_{yp}}} \tag{5.3}$$

or as

$$\frac{(b_e)_{min}}{t} = \sqrt{\frac{KE}{\sigma_{yp}}} \tag{5.4}$$

the latter equation being directly obtainable from eqn.5.2. The above relations are often used for design purposes, particularly in Civil Engineering[70]. It is interesting to note (from eqn.5.4) that this approach provides the minimum value of the effective width independent of the initial width of the plate.

5.1 Effective Width for the Flanges of an Euler Column

Eqn.5.4 is not suitable for determining the effective width of the flanges of a thin angle member in compression. This is because the equation is derived on the assumption that the maximum stress in the panel is given by the yield stress of the material. In the case of a wide-flanged column, the maximum stress is limited by the column buckling stress, which can have any value, depending on the geometry

of the angle member (the length and the angle between the flanges, in addition to the width). Thus in this case it would be more appropriate to determine the effective width by equating the flange buckling stress to the column buckling stress, as shown by the intersection of the curves in Figure 5.1. The minimum effective width obtained by using the yield criterion (eqn.5.4) is given by the intersection of the flange buckling curve with the horizontal line at $y = \sigma_{yp}/E$, as shown in the figure.

The hypothesis of effective width is based on the increasing load bearing capacity of the buckled plate. The effective width of the plate however reduces with increasing load; so that a wide plate, which buckles at a comparatively low value of the applied stress, can be considered to follow the plate buckling curve (such as the flange buckling curve in Figure 5.1) as the post-buckling load increases. The rationale behind this assumption is that at any given value of the maximum stress, if the effective width is higher the equivalent plate would buckle, and if it is smaller, then an increase in the load has to increase either the maximum stress or the effective width, both of which take the equivalent plate closer to its buckling point. In the case of a wide rectangular plate considered in isolation, the increase in loading and the consequent reduction in the effective width can be carried on till the material yields, thus the minimum effective width, as proposed by Von Kármán and predicted by eqn.5.4, is given by the intersection of the flange buckling curve with the horizontal line drawn at $y = \sigma_{yp}/E$. In the case of an angle column the reduction in the effective width stops at the intersection of the two buckling

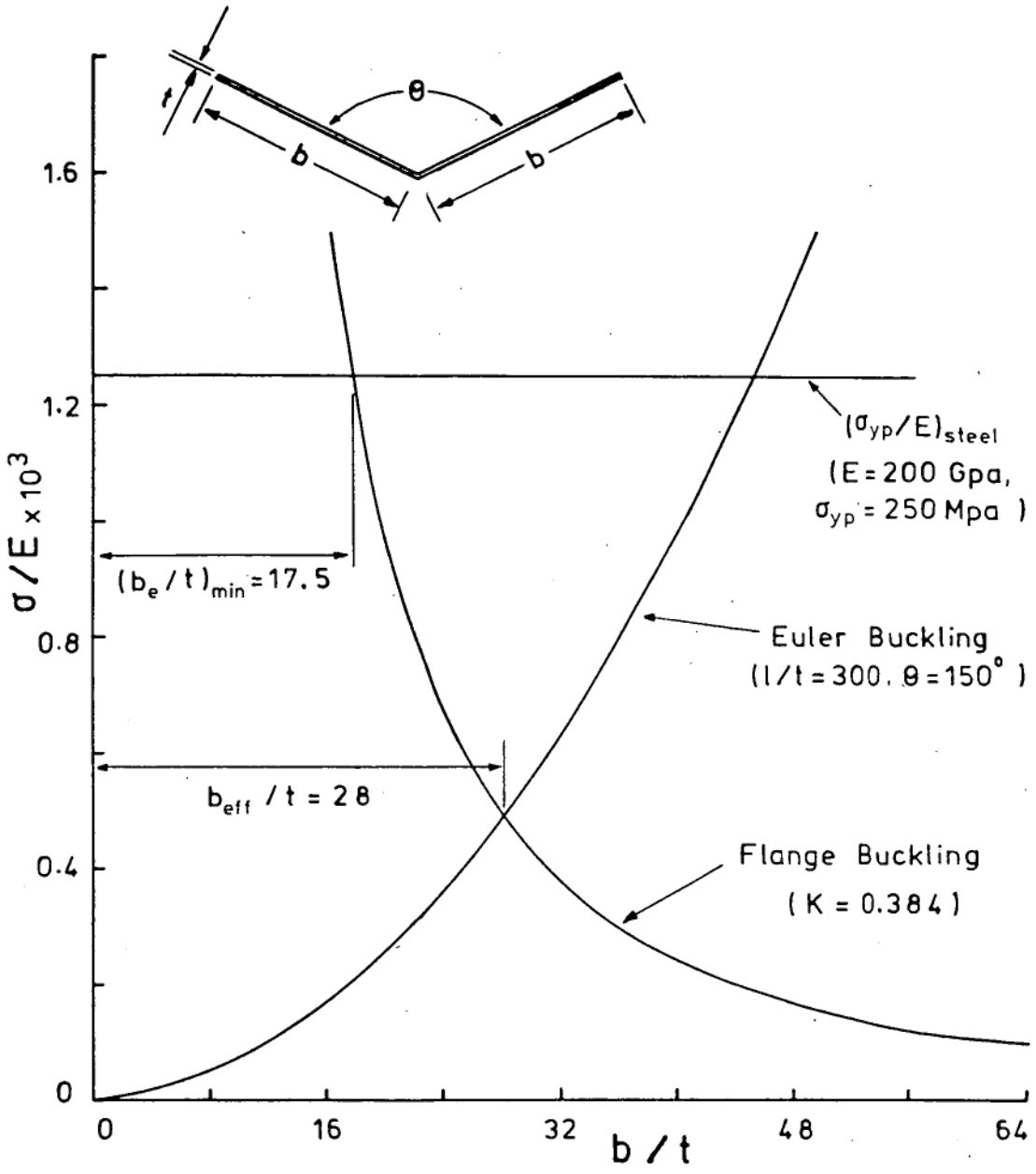

Figure 5.1
Effective Width for Euler Column

curves since the maximum stress is limited by the buckling of the column.

On this basis, the effective width of the flanges of the diagonal members in the space frame is established by equating the flange buckling stress to the buckling stress of the diagonal members. It may be mentioned that the same approach is used in optimum design, and that several investigators have shown that structures based on optimum design tend to be imperfection sensitive[47]. However the effect of imperfections is not considered in the present context, since the investigation is only concerned with developing a model for the secondary buckling of the axially compressed cylindrical shell.

5.2 Application to the Space Frame Model

The flange buckling curve in Figure 5.1 was drawn using a value of K = 0.384, which is the theoretical value (for ν = 0.3) for a rectangular plate with three sides simply supported and the fourth edge free. For the rectangular plate simply supported on all edges, the buckling coefficient for ν = 0.3 is obtained as 3.62. The panels in the Yoshimura model are considered to be simply supported on all sides. Hence, for the flanges of the diagonal members in the space frame, which are taken to be rectangular for simplicity, it can be expected that the flange buckling coefficient will be higher than 0.384, although it is unlikely that it will be as high as 3.62.

To investigate the applicability of the above approach of determining the effective width by equating the flange and the column

buckling stresses to the space frame model, the experimental values observed in the test by Esslinger and Geier were again utilized. By trial and error it was found that secondary buckling loads comparable to these observed values can be obtained from the space frame theory, if a value of K = 0.61 is used to determine the effective width. The secondary buckling loads thus obtained and the corresponding effective widths are shown in Table 5.1 along with the experimental loads and the values predicted originally using a constant width of W = 22.7 t.

Table 5.1

Secondary Buckling Loads for Esslinger and Geier's Shell

N	Observed critical load(N)	Original Sp.Frame (W/t=22.7, λ=0.85) Critical load(N)	Current Values (K=0.61, λ=0.85)	
			P (N)	W / t
15	275	280	277	22.59
14	260	258	257	22.67
13	235	237	238	22.75
12	215	216	219	22.82
11	200	195	200	22.89
10	185	175	181	22.95

It can be seen that the agreement is quite good. It may also be noted that the flange width to thickness ratio increases gradually with the decrease in the number of circumferential lobes, and that the average of these values is about the same as that used previously.

5.3 Modified Space Frame Theory

To include the procedure adopted for determining the width of the flanges of the compression members in the space frame model, the theory developed in the third chapter is modified as follows:

The buckling equation for the diagonal member was previously obtained as

$$P_1.(\lambda^2 + 9/4)^{3/2} - \frac{16EWt}{L_1} \sin^2(\varphi/4)\left[L_d/2 - \frac{1}{J}\tan(JL_d/2)\right] = 0 \qquad (3.16)$$

Using the non-dimensional quantities,

$$B = W/t \qquad (5.5) \qquad\qquad R_0 = R/t \qquad (5.6)$$

$$\rho = P_1/Et^2 \qquad (5.7) \qquad\qquad \phi = JL_d/2 \qquad (5.8)$$

eqn.3.16 can be expressed in non-dimensionalized form as

$$f(\phi) = C\,\phi^3 + \tan\phi - \phi = 0 \qquad (5.9)$$

where

$$C = \frac{I_0\,N^2}{8B\pi^2 R_0{}^2 \sin^2(\varphi/4)} \left[\frac{\lambda^2 + 9/4}{\lambda^2 + 1/4}\right]^{3/2} \qquad (5.10)$$

In eqn.5.10 I_0 is the non-dimensionalized moment of inertia obtained by substituting for $\cos(\theta/2)$ in eqn.3.18, as

$$I_0 = I/t^4 = \frac{B}{6}\left[\left[B^2 - 1\right](1 + 1/4/\lambda^2)\sin^2(\varphi/4) + 1\right] \qquad (5.11)$$

whereas the approximate moment of inertia represented by eqn.3.11 is obtained as

$$I_{01} = \frac{1}{6} B^3 (1 + 1/4/\lambda^2) \sin^2(\varphi/4) \qquad (5.12)$$

Noting that $J^2 = P_1/EI$, the relation between ρ and ϕ is given by

$$\rho = \frac{I_0 N^2}{\pi^2 R_0{}^2(\lambda^2 + 1/4)} \phi^2 \qquad (5.13)$$

The load on the diagonal member corresponding to the flange buckling stress $\sigma = KE/B^2$ is

$$\rho_f = 2K/B \qquad (5.14)$$

The above equations are solved using an iterative procedure, starting with an assumed initial value for B. Substituting for B in eqns.5.11 and 5.10, the value of C is determined, which is used in eqn.5.9 to obtain the value of ϕ. If the column buckling load obtained by substituting for ϕ in eqn.5.13 is less than the flange buckling load given by eqn.5.14, then a higher value of B is used. This procedure is repeated until two values of B on either side of the intersection point are obtained. Using an averaging procedure, the iteration is now conducted between these two widths, until the two values of ρ converge to the specified degree. The total load on the space frame is obtained from

$$\xi = P/Et^2 = 2N\rho \left[\frac{4\lambda^2 - \tan^2(\varphi/4)}{4\lambda^2 + 1} \right]^{1/2} \qquad (5.15)$$

The ratio of the secondary buckling load to the classical load may be expressed as

$$\eta = P / P_{cl} = \xi / \xi_{cl} \qquad (5.16)$$

where ξ_{cl} is given by

$$\xi_{cl} = \frac{2\pi}{\sqrt{3(1-\nu^2)}} \qquad (5.17)$$

5.4 An Approximate Solution for the Column Buckling Load

Eqn.5.9 does not yield an explicit solution for the buckling load of the column. To solve this equation the Newton Raphson method was employed which gives the relation

$$\phi_2 = \phi_1 - f(\phi_1) \,/\, (df/d\phi)\Big|_{\phi_1} \quad \text{where } df/d\phi = 3C\phi^2 + 1/\cos^2\phi - 1$$

Trying different initial values for ϕ_1, it was found that convergence is very quickly obtained if the iteration is begun with the solution of the equation

$$\tan\phi - \phi = 0 \tag{5.18}$$

which is given by

$$\phi = \phi_0 = 4.4934 \tag{5.19}$$

In fact the final solution obtained is very close to the value of ϕ_0. For example, using B = 22.7 and N = 15, for Esslinger and Geier's shell, the final value of ϕ is obtained as 4.4562, which differs from initial value by less than 1%. Further examination revealed that the value of C in eqn.5.9 is very small (as long as N is not excessively large). For the above case of N = 15, C has a value of only 0.0072. If the first term in eqn.5.9 is neglected, its solution is given by ϕ_0, from which the buckling load of the diagonal member is obtained as

$$\rho = 4\phi_0^2 I_0/(L_d/t)^2 \tag{5.20}$$

that is

$$P_{1_{cr}} = 8.183\ \pi^2 EI/L_d^2 \tag{5.21}$$

Using eqn.5.21 instead of the exact solution of eqn.3.16, for B = 22.7 and λ = 0.85, the secondary buckling loads for Esslinger and Geier's shell are obtained as follows:

	N	15	14	13	12	11	10
Eqn.3.16	P(N)	280	258	237	216	195	175
Eqn.5.21	P(N)	285	262	239	218	197	176

It may be observed that the values obtained are quite close, and that the error due to the above approximation is much less than that introduced by using the approximate moment of inertia (see Table 3.1).

5.5 The Significance of the Modification for Flange Width

The ratio of the secondary buckling loads to the classical load, obtained by the solution of eqn.5.9, are plotted in Figure 5.2 against R/t for different values of N. It may be observed that the variation of the critical loads with the radius to thickness ratio of the shell is much more gradual in this figure than that indicated by the steep curves obtained from the original space frame theory (Figure 3.9). The difference in the nature of the two plots is not so much due to the values used for λ and K in this figure*, but due to the fact that in the present case the flange buckling coefficient has been assigned a constant value whereas in the previous theory the flange width to thickness ratio was assumed to be constant.

* The reasons for using K = 0.78 and the constant value of λ = 0.5 to obtain the curves in Figure 5.2 will be explained subsequently.

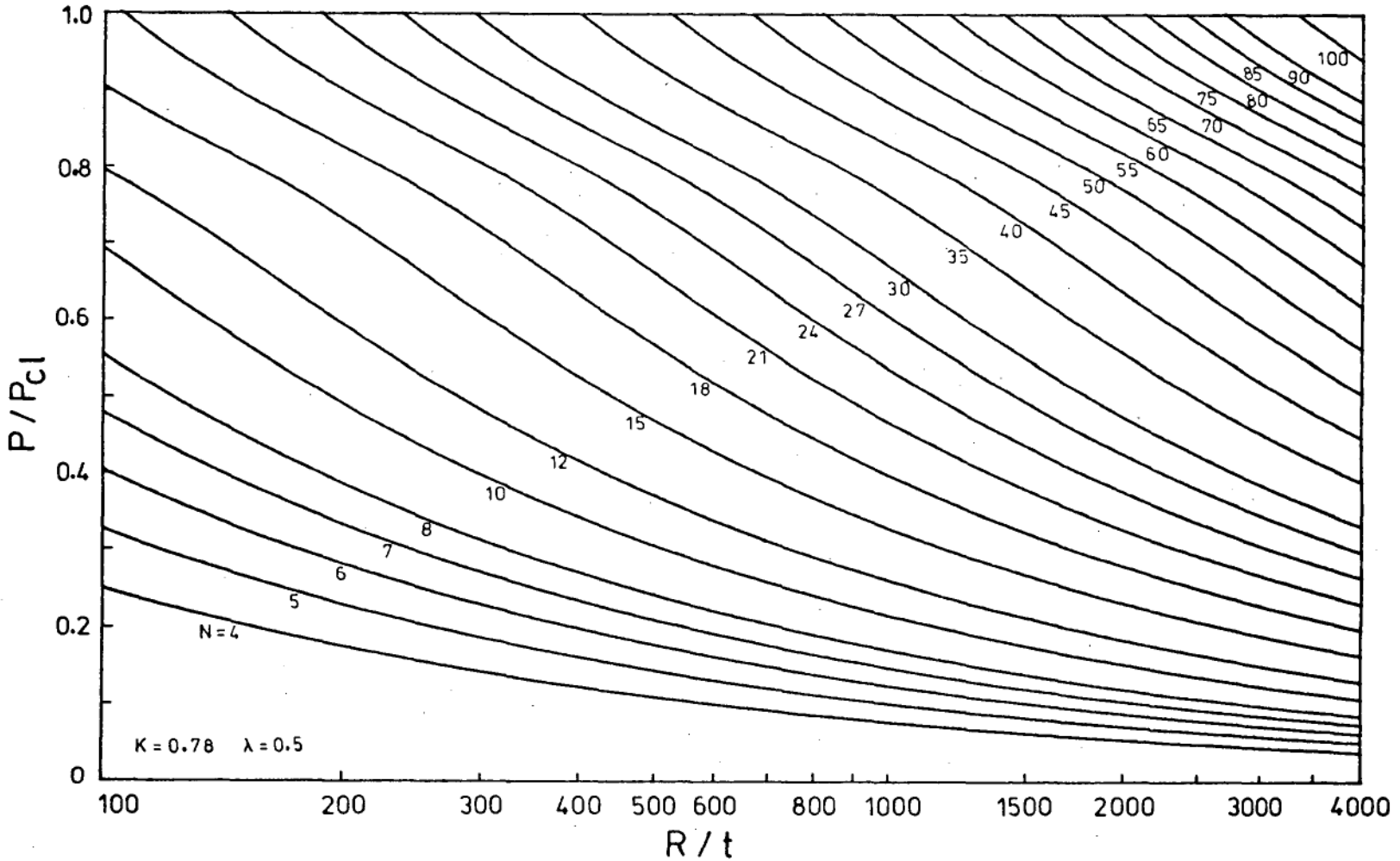

Figure 5.2. Secondary Collapse Loads
Predicted by Modified Space Frame with Spring

The significance of the modification introduced by using a constant flange buckling coefficient K instead of a constant width ratio can be gauged by an approximate estimation of the variation of the secondary collapse load with R/t. By substituting for L_d and I_0 in eqn.5.20, using the approximate moment of inertia (eqn.5.12) for the latter, we get

$$\rho \simeq \frac{B^3}{6} \left[\frac{\psi_0 \, N \sin(\varphi/4)}{\pi \, \lambda \, R_0}\right]^2 \tag{5.22}$$

Equating eqns.5.22 and 5.14, the value for the flange width ratio B is obtained as

$$B \simeq (12K)^{1/4} \left[\frac{\pi \, \lambda \, R_0}{\psi_0 \, N \sin(\varphi/4)}\right]^{1/2} \tag{5.23}$$

Substituting the above value of B in eqn.5.22 or eqn.5.14 gives

$$\rho \simeq \left[\frac{4}{3} K^3\right]^{1/4} \left[\frac{\psi_0 \, N \sin(\varphi/4)}{\pi \, \lambda \, R_0}\right]^{1/2} \tag{5.24}$$

Noting from eqn.5.15 that the relation between the total load ξ and ρ is independent of R_0, the above relation indicates that if N and λ are held constant the secondary buckling load varies in inverse proportion to the square root of R_0. Whereas, if instead of equating the flange buckling stress to the column buckling stress, the value of B is taken to be constant, then the secondary buckling load will be inversely proportional to the square of R_0, as indicated by eqn.5.22. Although the assumed variation of the aspect ratio with R_0 (eqn.3.17) slightly mitigates this effect (since a reduction in λ increases the secondary buckling load slightly), the contribution of the variation in λ is small, as can be seen from the steepness of the curves in Figure 3.9.

Thus the modification for the effective width of the flanges introduces a major change in the predicted variation of the secondary buckling loads with the radius to thickness of the shell, the validity of which is to be borne out by the results of the secondary buckling tests described in Chapter 8.

5.6 Aspect Ratio at Secondary Collapse

The secondary buckling loads of the cylindrical shell are evaluated in the the present work using a constant value of $\lambda = 0.5$ for the aspect ratio of the triangular facets in the space frame, instead of the empirical relation obtained by Foster (eqn.3.17). The reasons for introducing this change are as follows:

In the experiments conducted for the present work, over a hundred measurements of the aspect ratio of the facets of the buckle pattern were taken, from photographs recording the immediate stable post-buckled configuration of the test cylinders. By far the majority of these values are below those predicted by the empirical formula (eqn.3.17) for the respective values of R/t, although the amount of scatter observed (see Figures 8.14 a, b) is about the same as that seen in Figure 3.8a. Further the values of the aspect ratio observed after primary collapse, plotted in Figure 8.14b, do not indicate any reduction with increasing R/t as suggested by the relation 3.17. The discrepancy may perhaps be due to the difference in the material of the shells tested (Foster's shells were of Melinex while those in the current work are made from epoxy). It could also be due to the fact

that the majority of the shells tested by Foster developed buckles only over a part of the circumference owing to their poor quality and the presence of seams in them[58,73]. It is felt that the scatter in the plots of the measured values of the aspect ratio is to a large extent due to the influence of factors other than R/t, such as the length of the shell and the circumferential number of facets, which were not considered in obtaining eqn.3.17. It is to be admitted that even with the data collected in the present work the effects of the various factors in determining the aspect ratio of the facets formed in the initial stable buckled state of the cylinder could not be determined.

It has, however, been established that whatever be the value of the aspect ratio in the initial post-buckled state, it reduces as the end-shortening on the shell is increased further. The reduction in the axial height of the facets is much greater than that due to the increase in the membrane strain in the facets, and arises mainly from an inextensional response to continued end-shortening of the shell*. Due to this reduction, the aspect ratio of the facets in the shell at the occurrence of secondary collapse is much lower than that observed in the initial buckled condition. It may be mentioned that Foster was aware of the possibility of such a variation in aspect ratio with the post-buckling load, but could not establish it quantitatively due to the limitations of the equipment available at the time[73].

As part of the current work, photographs of the buckled shells were taken at various stages of end-shortening to record the

* The reduction in the axial height of the facets with increasing end-shortening is discussed at greater length in the next chapter.

changes in the axial height and hence the aspect ratio of the facets (see Figure 6.4). Measurements taken from photographs recorded at loads near the secondary buckling load (these values are presented in Chapter 8) indicate that the value of the aspect ratio reduces to within 0.5 and 0.4 at the time of collapse. Although the exact value at the onset of collapse and the possible effect on it of factors like the shell length and the number of facets have not been established, from the practical point of view this was not essential, since changes in the aspect ratio within the small range of 0.4 to 0.5 have very little effect on the magnitude of the secondary buckling load. It was therefore considered expedient to regard the aspect ratio at the occurrence of secondary collapse as a constant and to use the value of the traditional "square wave" buckles, namely that of $\lambda = 0.5$, for the determination of secondary buckling loads for the cylindrical shell.

5.7 Some Anomalies in the Space Frame Model with Spring

In section 5.4 it was shown that the buckling load for the diagonal member of the space frame is very close to the value given by the solution of the equation $\tan\psi - \psi = 0$ (eqn.5.18), where $\psi = JL_d/2$. This equation is exactly the same as that representing the buckling of a column of length equal to $L_d/2$, with one end built in and the other simply supported (Ref.1, page 53). In other words, the critical load determined for the diagonal member is nearly the same as that which would have been obtained if it was assumed to be fixed in the middle.

To check whether the similarity extended to the assumed

deflection pattern also, sample calculations were made for the value of N = 15, for the geometry corresponding to Esslinger and Geier's shell. It may be noted that owing to the eccentricity of the end loads as well as the presence of the transverse loads, the buckling of the diagonal member in the space frame is of the non-linear type, not of the bifurcation type. That is, the column starts deflecting as soon as the loading is begun, and when the critical load is approached these deflections become indefinitely large. It is therefore possible to calculate the magnitude of the deflections for any value of the load less than the critical load. For N = 15 in this case, the critical load in the diagonal member was estimated as $P_{1_{cr}}$ = 10.84N. Hence choosing a value of P_1 = 10 Newtons, eqns. 3.14, 3.8 and 3.12 were successively employed to obtain the values of the central deflection MN, the load P_3 in the spring and the constants C_1 and C_2 for the deflection function y (eqn. 3.10). The deflection pattern determined in this manner is shown in Figure 5.3; it is obviously similar to that of a column fixed in the middle, except that in this case the spring allows some lateral displacement (= MN) at the centre.

To assume deflections of this form for the diagonal folds of the Yoshimura pattern will be somewhat unrealistic and contrary to the behaviour observed in models. Further, it is seen that the force in the springs required to maintain this shape is, relatively speaking, very large. For instance, considering the member FN - which the spring represents - to be rectangular in cross-section*, for the dimensions considered above, its Euler buckling load is found to be 0.206 N. In

* It may be recollected that in developing the theory in Chapter 3, the thickness of the member FN was taken to be that of the shell and its width equal to twice the flange width of the diagonal members.

R=100mm . t=0.19mm . E=5.5 Gpa . W/t=22.7 . λ = 0.85 .

N=15 : P_{cr} = 280N P_{1cr} = 10.84 N .

Deflections for P_1 = 10N (MN = $y_{|(x=0)}$ = 0.32 mm , P_3 = 9.65 N).

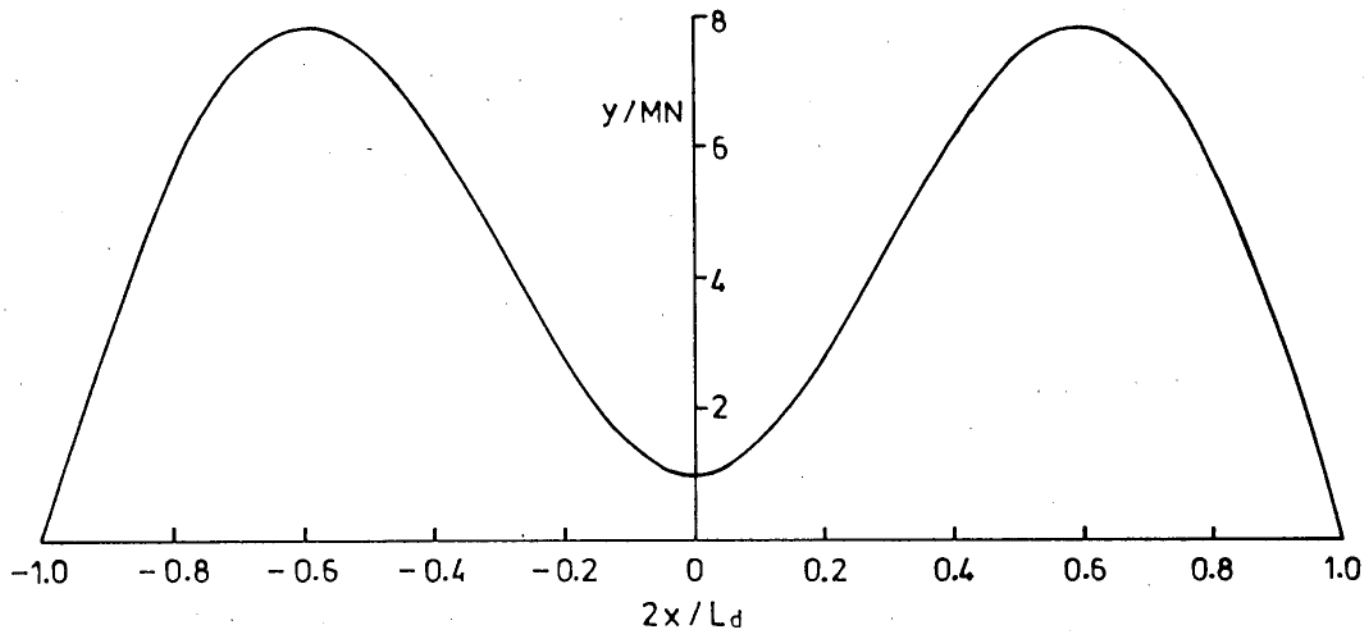

Figure 5.3.
Deflections of the Diagonal Member
in the Space Frame with Spring

the calculations used for plotting the deflections in Figure 5.3, the load P_3 in the member FN was obtained as 9.65N, more than 40 times its buckling load! The magnitude of P_3 reaches its critical value (0.206N) when the load P_1 in the diagonal member is about 1.26N, which is only about an eighth of the value used in the calculations. Of course, the difficulties presented by these figures may be overcome by presuming that the member FN is not allowed to buckle, which is perhaps implied in its representation by the spring. However, the fact that even in the prebuckling situation* the magnitude of lateral forces provided by the springs is relatively large, runs counter to the basic premise upon which the space frame theory was developed by Foster, namely that the Yoshimura model is not capable of sustaining forces of appreciable magnitude in the direction normal to the folds of the pattern[58,59]. It is to be mentioned that Foster[73] had suggested that when the diagonal member, say AC, deflects the adjacent nodes F and B (see Figure 3.3) move radially outward, probably causing a reduction in the compressive force in the the newly formed member FB. However his attempts to accommodate this in the theory were not successful.

In view of the foregoing observations, the inclusion of the springs in the space frame model appears to be undesirable. Removing the springs would result in a model that is simpler and at the same time more consistent. Hence in the following section a new theory is developed for the space frame model, without the springs, in which the effective width of the flanges is determined in the same manner as presented in section 5.1.

* On approaching the critical load of the column, the spring force P_3 becomes indefinitely large, being proportional to MN (see eqn.3.8).

5.8 Space Frame without Springs

If the springs are eliminated, the diagonal member of the space frame buckles in the Euler mode, at a load that is about an eighth of the buckling load obtained with the springs (see eqn.5.21). Noting that the strength of the column is roughly proportional to the cube of the flange width, the same load can be achieved without the springs by increasing the width to about twice the value that was used previously. For instance, using a value of B = 46.7 in the model without spring gives nearly the same secondary buckling loads for the shell tested by Esslinger and Geier as was obtained previously with B = 22.7. Normally, an increase of this order for the flange width would have been considered unacceptable; however in view of the conclusions obtained in Chapter 4, it seems plausible, and even likely, that the effective width of the diagonal folds in the Yoshimura model is of such magnitudes. It may be noted, though, that the assumption of a constant width to thickness ratio of this magnitude will lead to serious difficulties; for, as the circumferential number increases, the size of the triangular facet reduces, and may eventually, for some value of N, become even smaller than the assumed width of the flange. As to whether such a possibility can arise in the present model will be investigated subsequently; but first, the determination of the collapse loads for the space frame is presented.

The Euler buckling load for the diagonal member is given by

$$P_{1_{cr}} = \pi^2 E I_0 t^4 / L_d^2$$

This load may be expressed in non-dimensional form, by substituting for L_d and I_0, as

$$\rho = \frac{B}{24}\left[\frac{N}{R_0\lambda}\right]^2\left[[B^2 - 1]\sin^2(\varphi/4) + \frac{1}{(1 + 1/4/\lambda^2)}\right] \qquad (5.25)$$

Equating this ρ to the flange buckling load given by eqn.5.14 as ρ_f = 2K/B yields a fourth order equation in B of the form

$$B^4 + 2X_1.B^2 - X_2 = 0 \qquad (5.26)$$

which gives

$$B = \sqrt{- X_1 + \sqrt{X_1^2 + X_2}} \qquad (5.27)$$

as the smaller of the two solutions for the effective width ratio. The terms X_1 and X_2 in the above equations are obtained as

$$X_1 = \frac{1}{2}\left[\frac{1}{(1 + 1/4/\lambda^2)\sin^2(\varphi/4)} - 1\right] \; ; \; X2 = 48K\left[\frac{R_0\,\lambda}{N\,\sin(\varphi/4)}\right]^2 \qquad (5.28)$$

The effective width B and the critical load ρ can be determined explicitly from eqns 5.28, 5.27 and 5.14. The secondary collapse loads are then given by eqn.5.15. For comparison, the values obtained for Esslinger and Geier's shell using K = 1.25 (and λ = 0.85) are given below. It may be noted that the buckling loads agree closely with those in Table 5.1.

N	15	14	13	12	11	10
P(N)	275	256	237	219	200	182
B	46.60	46.65	46.70	46.75	46.80	46.85

5.9 Value of the Flange Buckling Coefficient K

The physical as well as the mathematical simplicity of the new space frame model - without springs - makes it quite attractive. However, unless it is ascertained that the flanges of the diagonal members are not excessively large, the validity of the model remains in question. (It may be noted that the width of the tangential members does not enter the mathematical formulation). Of course, as mentioned earlier, it is not the actual magnitude of the width, but only its proportion to the size of the facet that is of main concern here. A reasonable upper limit for the flange width would be half the perpendicular distance from either of the flanges to the opposite corner in the triangular facet, as shown in Figure 5.4. This width is given by $W_{max} = \frac{1}{2} L_1 \cos\beta$. Substituting for L_1 from eqn.3.1 and for the semi-vertex angle β in terms of λ, we get

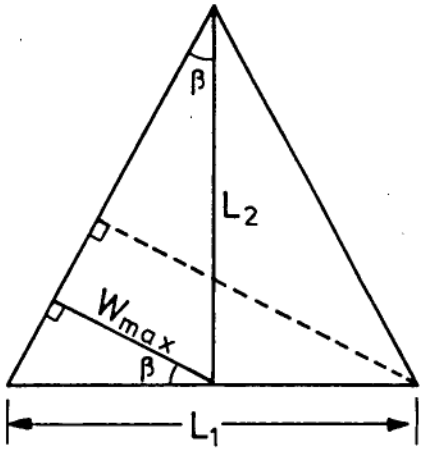

Figure 5.4

$$B_{max} = \frac{\pi R_0}{N} \frac{\lambda}{(\lambda^2 + 1/4)^{1/2}} \qquad (5.29)$$

Introducing the notation

$$\omega = B / B_{max} \qquad (5.30)$$

the relationship between ω and K is investigated below, with a view to determining the limiting value of K for which ω is restricted to less than or equal to one. It may be noted that the inverse relationship between B_{max} and N expressed by eqn.5.29 is much more severe than the

gradual variation of the effective width B with N observed in the data presented in the foregoing section. Hence the ratio B/B_{max} is directly proportional to N. Since the secondary collapse load is also directly proportional to N, the value of ω increases with increasing value of the load ξ. Therefore to restrict the maximum value of ω, it is only necessary to examine its variation with K at the maximum value of the load, which is taken to be the classical buckling load.

The secondary buckling load reaches the classical value only at high values of N. Hence in this region, the angle φ subtended by the facet at the axis of the cylinder is small, and $\varphi/4$ even smaller. In Figure 5.2, the least value of N corresponding to $P = P_{cl}$ is seen to be about 15, which gives a maximum value for $\varphi/4 = 6^{\circ}$. For such small angles, the following approximation is quite valid.

$$\sin^2(\varphi/4) \simeq (\varphi/4)^2 = \left[\frac{\pi}{2\ N}\right]^2 \qquad (5.31)$$

Further, at high values of N, the semi-angle $\theta/2$ between the flanges of the diagonal members gets close to 90° (it may be recollected that it was for this reason that the term containing $\sin^2(\theta/2)$ was included to obtain the exact relation for moment of inertia), hence $\sin^2(\theta/2)$ in eqn.3.18 may be approximated to unity. For N = 15, using $\lambda = 0.5$, the value of $\sin^2(\theta/2)$ is obtained as 0.978; hence for higher values of N the error in using this approximation is less than 2%.

Introducing these two approximations and using $\lambda = 0.5$, eqn.5.25 simplifies to

$$\rho = \frac{B\,N^2}{12\,R_0^2}\left[\frac{\pi^2 B^2}{2\,N^2} + 1\right] \tag{5.32}$$

Noting that $B_{max} = \frac{\pi\,R_0}{\sqrt{2}\,N}$ for $\lambda = 0.5$, replacing B with ωB_{max} in this equation gives

$$\rho = \frac{\omega\,\pi\,N}{12\,\sqrt{2}\,R_0}\left[\frac{\omega^2\pi^4 R_0^2}{4\,N^4} + 1\right] \tag{5.33}$$

and the relation $\rho_f = 2K/B$ for the flange buckling load becomes

$$\rho_f = \frac{2\sqrt{2}\,N\,K}{\omega\,\pi\,R_0} \tag{5.34}$$

Neglecting the term $\tan^2(\varphi/4)$ in comparison with unity in eqn.5.15, for $\lambda = 0.5$ the value of ρ corresponding to the classical load ξ_{cl} is obtained as

$$\rho_0 = \frac{\xi_{cl}}{\sqrt{2}\,N} \tag{5.35}$$

Substituting for ρ in eqn.5.34 from eqn.5.35 yields

$$K = \frac{1}{4}\,\pi\,\omega\,\xi_{cl} \;/\; (N^2/R_0) \tag{5.36}$$

Similarly, using $\rho = \rho_0$ in eqn.5.33 we obtain

$$\left[\frac{N^2}{R_0}\right]^2 - \frac{12\,\xi_{cl}}{\omega\,\pi}\cdot\left[\frac{N^2}{R_0}\right] + \frac{\omega^2\,\pi^4}{4} = 0$$

which gives

$$\left[\frac{N^2}{R_0}\right] = \frac{6\,\xi_{cl}}{\pi\,\omega}\left[1 \pm \sqrt{1 - \left[\frac{\pi^3\,\omega^2}{12\,\xi_{cl}}\right]^2}\right] \tag{5.37}$$

In eqn.5.37, only the solution given by the negative sign on the right hand side (which gives lower values for N) is applicable. Substituting for ξ_{c1} from eqn.5.17, and using this solution for (N^2/R_0) in eqn.5.36 the expression for K is obtained as

$$K = \frac{\pi^2 \omega^2}{24.\left[1 - \sqrt{1 - \pi^4\omega^4(1 - \nu^2)/192}\right]} \qquad (5.38)$$

Eqn.(5.38) represents the relation between K and ω at the classical load, which is found to be independent of the values of N and R_0, owing to the approximations used which are valid at high values of N. On substituting $\omega = 1$ and the value of $\nu = 0.34$ in this equation, the value of K is obtained as

$$K = 1.597 \qquad (5.39)$$

On examination it is found that the relation between K and ω represented by eqn.5.38 is of an inverse nature, i.e., the value of ω increases as K decreases. Thus the value of K = 1.6 obtained above is the minimum value required to ensure that the effective width used in the model does not, under any circumstance, exceed the limit specified by B_{max}. (It may be mentioned that if the root given by the positive sign on the right hand side of eqn.5.37 is employed, the relationship between ω and K becomes direct and the value of K corresponding to ω = 1 is obtained as 0.236. Thus theoretically B/B_{max} can be maintained below unity by using values of K less than 0.236 also. However noting that even for a flange with one side completely free the buckling coefficient is about 0.38, this latter solution is ignored.)

To verify the validity of the assumptions used in obtaining the above minimum value of K, calculations were performed using the exact relations developed in section 5.8. Choosing constant values for K and N, the value of R_0 required to obtain the classical load was determined from these equations by iteration. The values of ω obtained in this manner for different values of N and K are shown in Table 5.2. It may be observed that the ratios B/B_{max} and N^2/R_0 are nearly constant for constant values of K, as predicted by the relations 5.38 and 5.37. The maximum deviation in these values occurs at the minimum N used as expected. Further it is seen that the value of ω decreases as K is increased and that for K = 1.6, B/B_{max} is equal to unity.

The value of 1.6 for the flange buckling coefficient is the minimum value required to satisfy the condition that the effective width used in the model does not exceed the maximum width specified even when the secondary collapse load reaches the classical buckling value. Thus higher values for K can be used. It may further be argued that even lower values are admissible, firstly because the variation in ω with K is not very drastic, and secondly on the grounds that in practice the secondary collapse loads of cylindrical shells seldom reach the classical value. While these arguments are irrefutable, it is found that if the value of K = 1.6 is used, the collapse loads predicted by the model agree well with those observed in the tests performed under the current experimental program (the comparison of the experimental and theoretical results are presented in Chapter 8). Hence the value of the buckling coefficient K was fixed at 1.6 for the space frame model without springs.

Table 5.2

Variation of Width Ratio with the Buckling Coefficient K at the Classical Load

K	N	R_0	N^2/R_0	B/B_{max}	P/P_{cl}
1.0	15	63.5	3.545	1.164	1.000
	25	177.9	3.513	1.157	1.000
	40	456.8	3.502	1.155	1.000
	60	1029.0	3.499	1.154	1.000
	80	1830.0	3.497	1.154	1.000
1.6	15	117.3	1.918	1.007	1.000
	25	328.7	1.901	1.002	1.000
	40	844.0	1.896	1.000	1.000
	60	1901.0	1.894	1.000	1.000
	80	3380.7	1.893	1.000	1.000
2.4	15	207.8	1.083	0.853	1.000
	25	582.0	1.074	0.849	1.000
	40	1494.3	1.071	0.848	1.000
	60	3365.6	1.070	0.847	1.000
	80	5985.4	1.069	0.847	1.000

It may be recalled that to fit the experimental data of Esslinger and Geier a value of K = 1.25 was employed earlier (with λ = 0.85) in the space frame model without springs. When the values of K = 1.6 and λ = 0.5 are employed in this model, the experimental values of Esslinger and Geier are found to be about 20% lower than the loads predicted by the theory. It appears that the observed lower values in this particular case were probably caused by the presence of the seam and other possible imperfections in the shell tested by Esslinger and Geier. Even the primary buckling load of this shell was only about 70% of the classical value. Hence the results of this particular test are considered to be in the lower range of the experimental scatter and not representative of the expected secondary buckling loads of axially loaded cylindrical shells. On the other hand the secondary collapse loads observed in tests conducted on over thirty near-perfect shells in the current program are found to be in reasonable agreement with the estimates using the value of K = 1.6 and λ = 0.5; for this reason the value of the flange buckling coefficient has been retained at K = 1.6 in the proposed space frame model without spring.

The buckling loads predicted by the new model (using K = 1.6 and λ = 0.5) are plotted against R/t for various values of N in Figure 5.5. For the modified space frame model with springs (Figure 5.2), the value of K = 0.78 was determined so as to give the same collapse loads as predicted by the present model in the region of R/t = 500. It may be noted that the secondary buckling loads predicted by the two models have practically the same values over almost the entire range of R/t considered for the small values of N (from 6 to 15) which are observed

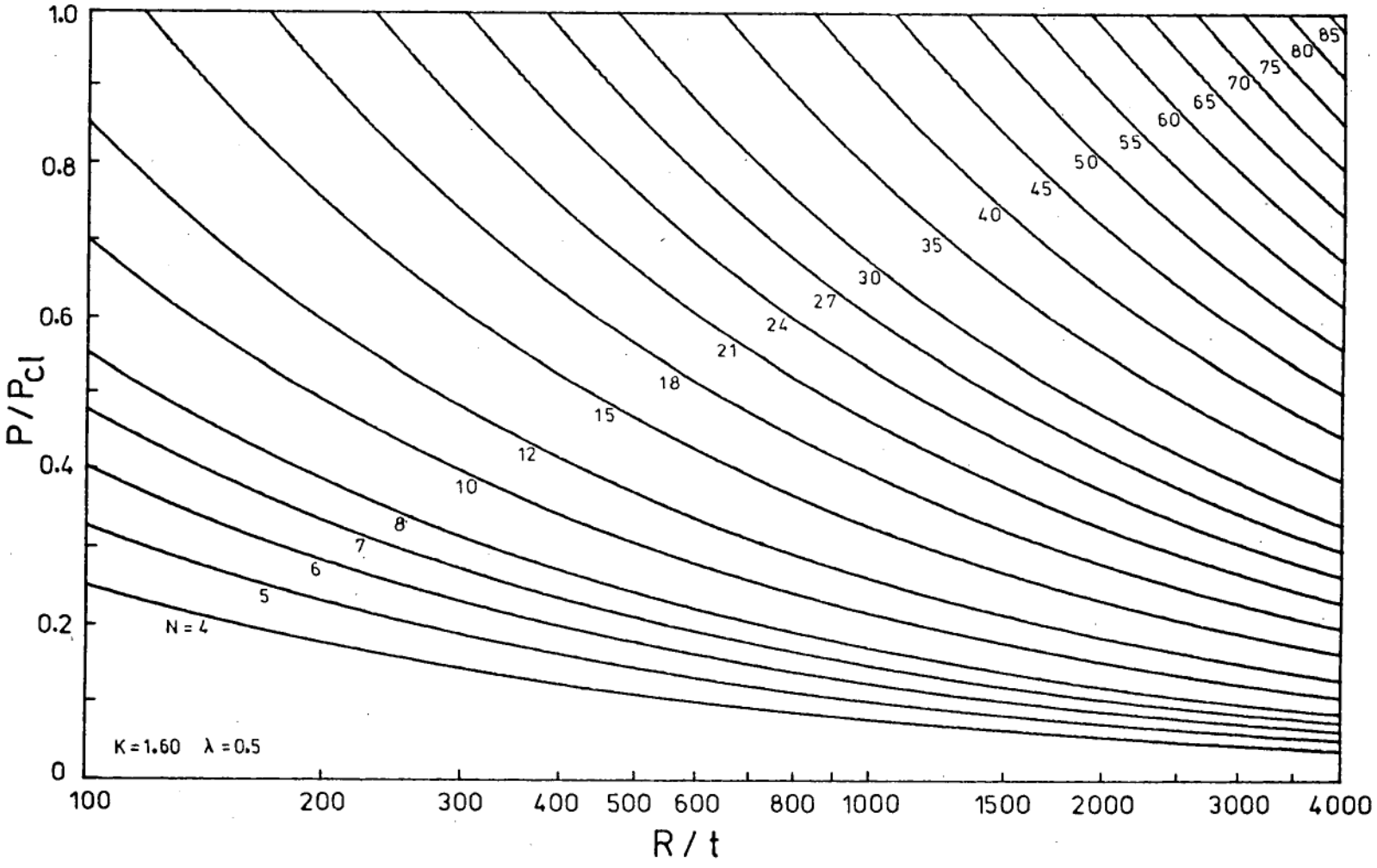

Figure 5.5. Secondary Collapse Loads
Predicted by Space Frame without Spring

in practice. (The plots have been drawn for all values of N up to the classical load mainly for the purpose of investigating the applicability of the models in predicting the primary collapse loads of imperfect cylindrical shells). Thus for the estimation of secondary buckling loads either of the models can be used. However, owing to the inconsistencies arising from the inclusion of the spring, which were pointed out earlier, the latter model of the simple space frame appears to be more appropriate for the physical representation of secondary collapse behaviour of circular cylindrical shells in axial compression.

NOTATIONS

B : Flange-width to thickness ratio = W/t

B_{max} : Maximum value of B specified as $B_{max} = \frac{1}{2} L_1 . \cos\beta / t$

C : Constant in the buckling function (see eqns.5.9, 5.10)

E : Young's Modulus

I_0 : Non-dimensionalized moment of inertia = I/t^4 (see eqn.5.11)

I_{01} : Approximate non-dimensional moment of inertia (eqn.5.12)

K : Flange buckling coefficient

R_0 : Radius to thickness ratio

X_1, X_2 : Constants (see eqns.5.28)

b : Width of rectangular plate

b_e : Effective width of rectangular plate

$f(\phi)$: Function for buckling of the diagonal member (see eqn.5.9)

t : Thickness of the plate, shell

β : Semi-vertex angle of the triangular facet (see Figure 5.4)

η : Ratio of secondary buckling load to classical load = P/P_{cl}

ξ : Non-dimensionalized secondary buckling load = $P/(Et^2)$

ξ_{cl} : Non-dimensionalized classical buckling load = $P_{cl}/(Et^2)$

ρ : Non-dimensional buckling load of diagonal member = $P_1/(Et^2)$

ρ_f : Non-dimensional flange buckling load

σ_{av} : Average stress on the buckled rectangular plate

σ_0 : Maximum stress on the buckled rectangular plate

σ_{yp} : Yield stress

ϕ = $J.L_d/2$

ω : Ratio of effective width to maximum width = B/B_{max}

Note : The remaining symbols are the same as those used in Chapter 3.

CHAPTER 6

GEOMETRIC CONSIDERATIONS OF THE BUCKLED CYLINDRICAL SHELL

The Yoshimura model is an idealization which is very useful in understanding the collapse behaviour of axially loaded cylindrical shells. Strictly speaking the model is applicable only to a cylinder of infinite length. This is because it does not satisfy even the basic geometric requirement of circularity at the ends of the shell. While the violation of end conditions may be ignored, the fact remains that the Yoshimura model considers the buckles to be spread over the entire length of the cylinder, whereas in tests performed under controlled end-shortening conditions the buckles observed are mainly confined to the middle section of the shell. In fact this difference was first pointed out by Yoshimura himself[19], who attempted to analyse them separately in terms of general and local buckling phenomena. Further, in the Yoshimura representation of a finite cylinder, the axial height of the facets becomes a discrete variable since the number of facets along the length of the shell can be assigned only integer values (unless the end facets are taken to be incomplete or the facets are assumed to vary in size). These limitations are of course applicable to the space frame model also.

The investigations presented in this chapter are based on the geometry of models of the actual two tier and one tier patterns observed in controlled end-shortening tests (see Figure 6.1). The nomenclature one tier and two tier refers to the number of rows of

circumferential folds in the patterns. The model of the two tier pattern has in the middle a double band of alternating triangular panels which is similar to a single row of triangular facets in the Yoshimura pattern. The sections of the shell above and below this band are not sharply folded, which is how they appear in the actual shell. However for the purpose of definition they may be regarded as made up of alternating long triangular panels and conic sections as suggested by Hoff et al.[71], who pointed out that such a model can also be obtained by a near inextensional transformation from the cylindrical form of the shell. (It may be noted that the axial height of the facets in this model is a continuous variable). In the first model of the one tier pattern (Figure 6.1b), there is a single row of diamond shaped facets or two rows of opposing triangular facets which are also confined to the middle section of the shell as seen in the tests. For simplicity this model may be idealized to the form shown in Figure 6.1c, which has alternating triangular and conic sections connecting the folds in the middle to either end of the shell.

Based on these models two aspects of the post-buckling behaviour of axially loaded cylindrical shells are investigated in the following sections. The first is regarding the variation in the aspect ratio or the axial height of the facets. This discussion is purely qualitative. The second is with regard to the circumferential number of facets in the buckled cylinder. In this case limiting relationships are established between the number of facets and the end-shortening of the cylinder, which provide simple expressions for predicting the number of facets observed on primary collapse.

(a) Two Tier Pattern

(b) One Tier Pattern

(c) Idealized
One Tier Pattern

Figure 6.1. Models of Observed Buckle Patterns

6.1 Observations From Plane Geometry

Before considering the geometry of the buckled shell, some basic relations from plane geometry are reviewed here, which will be used in the discussions to follow. These relations are based on the theorem that for a given height and base-length of a triangle, the sum of the lengths of the other two sides is least when those two sides are equal, i.e., when the triangle is isosceles. This is shown in Figure 6.2a. It can easily be proved mathematically that the sum of the sides of any other triangle (such as those shown by the broken lines in the figure) is greater than the sum of the lengths AB and BC (solid lines) formed by the triangle with its vertex over the midpoint of the base AC. Conversely, if the height of the triangle and the sum of the lengths AB + BC are fixed, then the length of the base AC is maximum for the isosceles triangle. In other words, if we start with a straight bar of length say L_0, and fold it at the point B (so that the sum of lengths AB + BC = L_0), then the end deflection δ attains its minimum value when the fold B is at the mid-point of the bar (see Figure 6.2b). Further, it can be shown that the total angle of the folds, i.e., the sum of the angles $\theta 1+\theta 2+\theta 3$ (Figure 6.2a) is also a minimum when the triangle is isosceles (this may be seen from the fact that the included angle $A\hat{B}C$ is maximum for the isosceles triangle).

The above relations may easily be extended to the case when there are two folds in opposite directions (see Figure 6.3). If the lateral deflections w in opposite directions are equal, the minimum value of the combined lengths AB+BC+CD is obtained when B and C occur

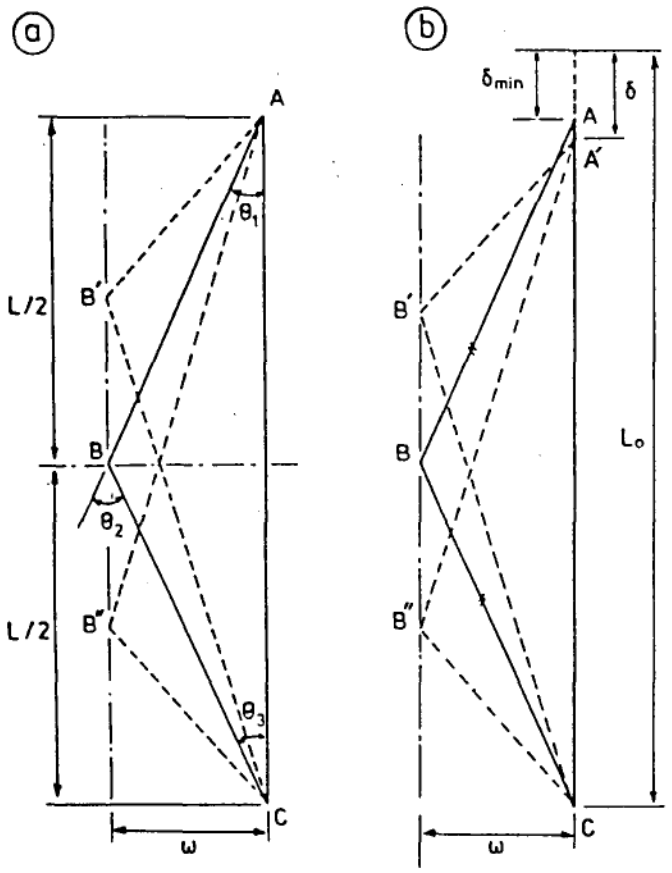

Figure 6.2.
Geometry of a Single Fold

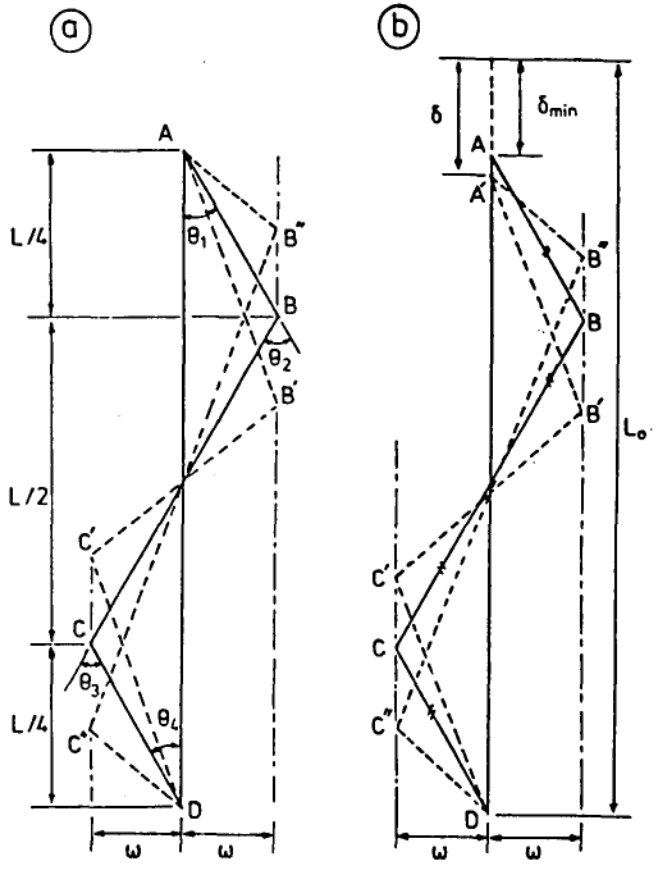

Figure 6.3.
Geometry of Two Folds

at the mid-points of each half of the length AC, that is, when the axial length H of the middle segment BC is equal to L/2 (Figure 6.3a). Hence, in the case of a rod of fixed length L_0 (Figure 6.3b), the minimum value of the end-shortening δ is obtained when the axial length H = L/2, i.e., when the length BC of the middle segment is equal to half the full length L_0. Again as before, the total angle θ_0 of the folds also reaches its minimum when H = L/2.

6.2 Aspect Ratio and Post-Buckling Load

A longitudinal section passing through one of the nodes of the two tier pattern shown in Figure 6.1a will look similar* to the doubly folded elements in Figure 6.3. The points B and C in the figure correspond to the vertex and the mid-point of the base of the triangular facets in the middle of the two tier pattern. It may be noted that since the buckled form of the cylindrical shell is near developable, its overall folded length will be almost equal to the original (unloaded) length of the shell. When the end shortening on the shell is increased, if the points B and C remain stationary, then obviously the compressive strain and hence the membrane strain energy of the shell will be considerably increased. However if the shell has undergone only elastic buckling, so that its nodes are free to move along the length of the shell, then it is likely the points B and C will move towards each other so as to retain the original length of the shell as far as possible, as illustrated in Figure 6.3b. Of course

* For the buckled shell the inward and outward radial displacements at the two folds are actually unequal; however this difference may be ignored for the present qualitative discussion.

in doing so the total angle θ_0 by which the shell has folded will increase, thereby increasing the bending energy of the shell. Hence the final length of the segment BC will be determined by a balance between the reduction in membrane strain energy obtained by the decrease in the axial height of the facets and the corresponding increase in bending energy caused by the same*. Since the stiffness of the shell in bending is comparatively small, it is obvious that such a balance will result in considerably less increase in the total strain energy than that which would have resulted if all the end-shortening had been absorbed solely by compression. It is to be noted that had the shell not offered any resistance to bending, the end-shortening could have been accommodated in a purely inextensional manner and there would have been no increase in the load acting on the shell. (In fact if not for the bending resistance, the initial post-buckling load would have been zero). In the actual shell however, such completely inextensional end-shortening is not possible; along with the increase in the bending strain, the membrane strain also rises resulting in an increase in the axial load. Without taking the bending into account it would be impossible to determine the variation in the post-buckling load with increasing end-shortening. However in predicting the maximum load - based on the assumption that this load is transmitted along the folds and hence it is limited by the strength of the diagonal folds - it is not necessary to know how the load varies. Hence neglect of the bending at the corners does not affect the applicability of the space frame model in predicting the secondary collapse loads of the shell.

* Geometrically, the same effect can be achieved if the axial height increases to a value beyond L/2; however the shell being subjected to compression, such an increase is not practically feasible.

It thus appears that a shell which has buckled elastically into the two tier pattern can accommodate further end-shortening by changing the axial height or the aspect ratio of the facets, retaining its near inextensibility to a considerable extent. In order to verify the above hypothesis photographs of several buckled shells were taken at various stages of end-shortening. Measurements from the photographs as well as direct measurements of the height of the facets confirm the variation in the aspect ratio. (These values are presented in Chapter 8). For illustration, the photographs of shell S18 taken immediately after it buckled, and on further loading are shown in Figures 6.4a and 6.4b. The flattening of the facets due to further loading is quite apparent in the latter. Although in terms of the length of the shell the reduction in axial height appears to be small, in terms of aspect ratio this variation is quite significant, resulting in as much as 50% reduction from the initial to the fully loaded state. The increase in axial height of the facets on unloading is much more noticeable, in Figure 6.4c. It may be mentioned that the elongation of the facets in the axial direction on unloading was noted earlier by Yoshimura[19].

6.3 Secondary Collapse of One Tier Pattern

Interesting observations arise when the possibility of a similar mechanism in the one tier pattern is investigated. If the longitudinal section passing through the vertices of two opposing triangular facets in the model shown in Figure 6.1b is considered, it is obvious that when the end-shortening is increased, this section can retain its original length by moving these two vertices towards each

(a) Immediately after collapse :

Δ = 125
η = 0.184
H/L = 0.246
λ = 0.78

(b) On further loading :

Δ = 512
η = 0.304
H/L = 0.149
λ = 0.47

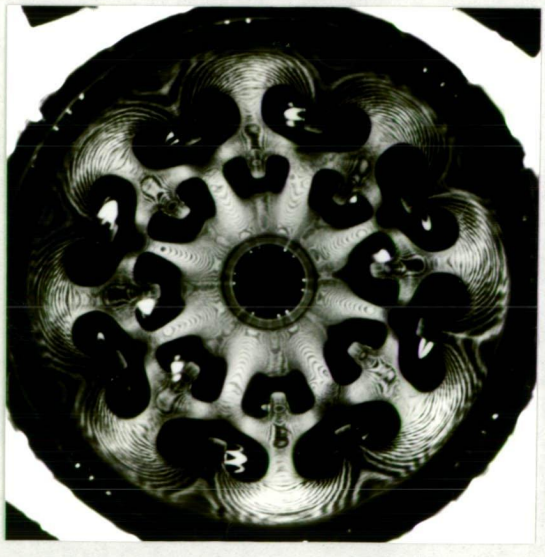

(c) On partial unloading :

Δ = 80.3
η = 0.186
H/L = 0.274
λ = 0.87

Figure 6.4. (Shell S18, N = 8)
Changes in Facet Size with End-Shortening

other. However a section taken through one of the nodes between the tangential folds consists of only two straight line segments, hence such a mechanism is not possible at this section. Therefore when the buckled shell is subjected to further end-shortening, the regions over the buckles will remain relatively unstressed, while the sections in between will develop high compressive stress. The collapse of these sections will form additional buckles in between the original ones. Unfortunately the author did not test any shell short enough to buckle into the one tier pattern. However, an illustration is provided from Foster[58] (Figure 6.5), showing the small secondary buckles appearing in between the main buckles of the one tier pattern. It thus appears that the secondary collapse mechanism of the one tier pattern does not involve the collapse of the diagonal folds of the buckle pattern. This also explains why the circumferential number of facets does not reduce in the case of the one tier pattern, as was observed by Yamaki[11].

It may therefore be noted that the space frame theory, which is based on the buckling of the diagonal members, is not applicable to the one tier pattern but only to the secondary collapse of shells which have buckled into the two tier pattern.

6.4 Minimum End-Shortening for Two Tier Pattern

A cross-section through the tangential folds of the models in Figure 6.1 (which is similar to the cross-section of the Yoshimura pattern) is shown in Figure 6.6. The radius of the shell is denoted by R and that of the circumscribing circle by R' in the figure. From

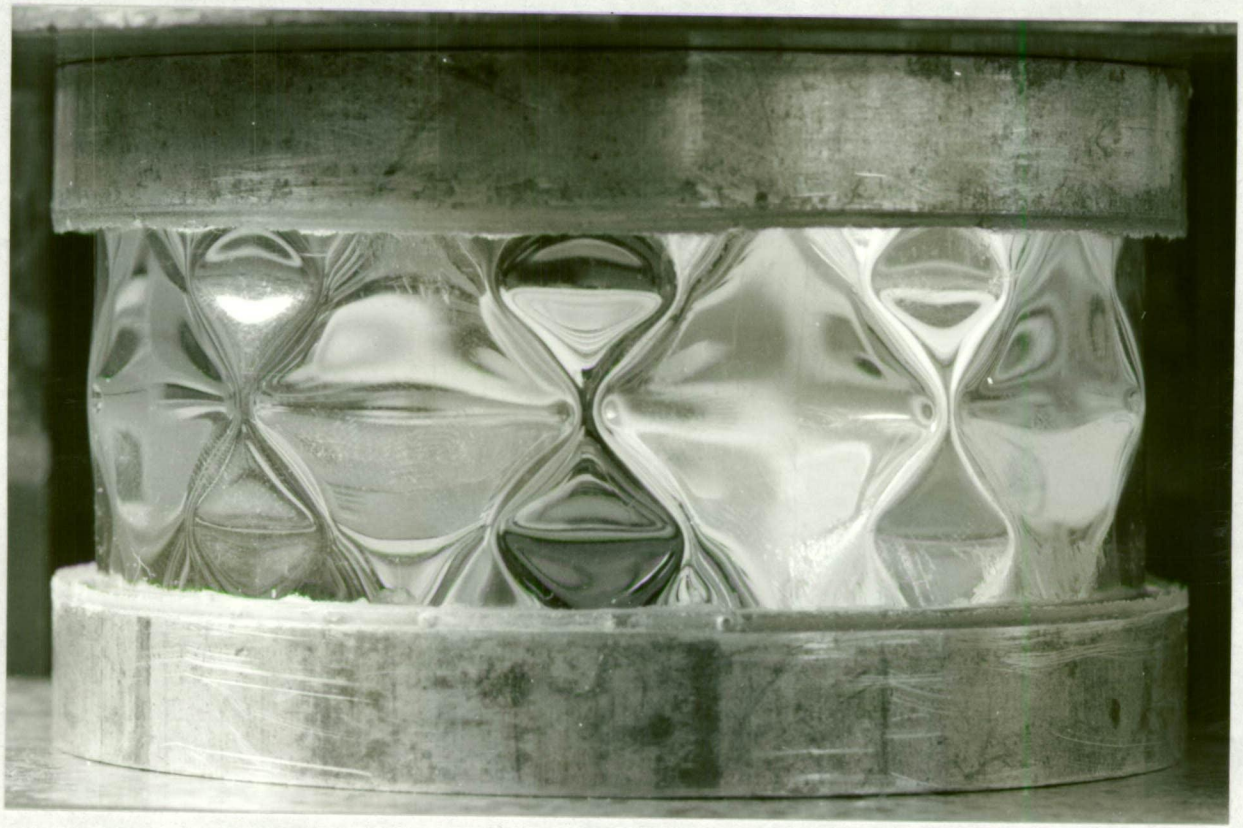

Figure 6.5
Single Tier Pattern Observed in Experiment
(Source Foster, Ref.58)

geometry the outward and inward deflections at the corner and the mid-point of the circumferential fold are respectively given by

$$\omega_0 = R' - R = R\left[\frac{\pi}{N}\,\mathrm{cosec}(\pi/N) - 1\right]$$

$$\omega_i = R - R'\cos(\varphi/2) = R\left[1 - \frac{\pi}{N}\cot(\pi/N)\right]$$

Using the relations $\mathrm{cosec}(\theta) \simeq 1/\theta + \theta/6$ and $\cot(\theta) \simeq 1/\theta - \theta/3$, the above relations may be simplified to*

$$\omega_0 = \frac{1}{6}\pi^2 R/N^2 \quad \text{and} \quad \omega_i = \frac{1}{3}\pi^2 R/N^2 \qquad (6.1)$$

The above approximations introduce less than 1% error for values of N greater than 4. It is to be noted that the inward deflection at the tangential fold is about twice the outward displacement at the nodes and that both are inversely proportional to N^2.

The minimum end-shortening required to form any specified number of facets around the circumference of the two tier pattern can be determined from the geometry of the longitudinal section of the two tier model shown in Figure 6.7. (That such a minimum exists is obvious from the geometrical considerations in section 6.1). In the figure the radial displacements of the points B and C - representing the inward fold at the vertex and the outward fold at the mid-point of the base of a triangular facet, respectively - are given by eqn.6.1. The axial height of the facet is given by H = h.L, where L is the length of the

* These simplified expressions were first obtained by Yoshimura[19].

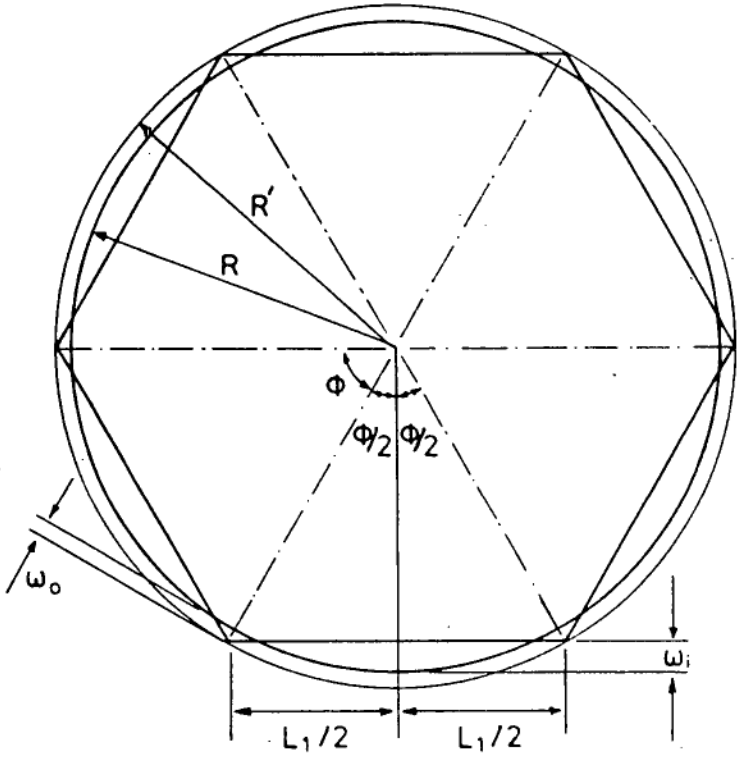

$$\Phi = 2\pi/N \qquad L_1 = 2\pi R/N$$

$$R' = \frac{L_1}{2\sin(\Phi/2)} = \frac{\pi R}{N\sin(\pi/N)}$$

Figure 6.6
Radial Displacements at the Folds

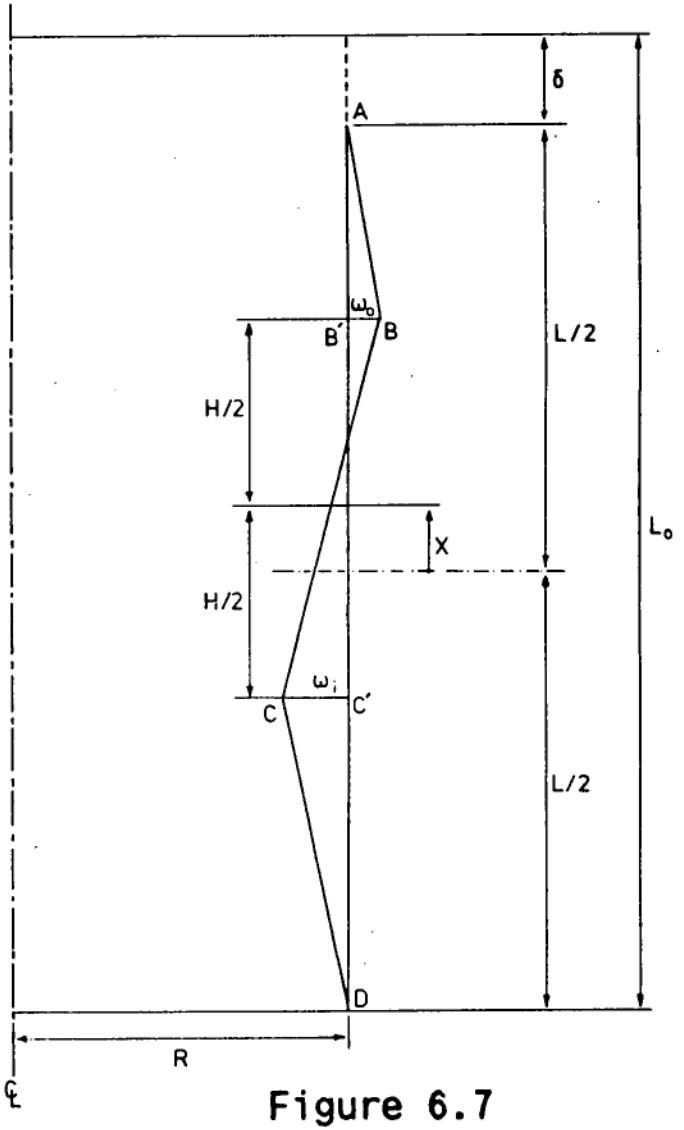

Figure 6.7
Longitudinal Section
of the Two Tier Model

buckled shell. For generality, the facets are considered to be formed away from the midsection; hence the mid-point of the facets is at a distance X = x.L from the origin, which is taken at the mid-section of the buckled shell. It may be noted that the end load on the shell is taken to be zero, hence the total length of the folded segments AB, BC and CD is equal to the original length L_0 of the unloaded shell. The end-shortening δ is therefore given by

$$\delta = L_0 - L = (AB - AB') + (BC - B'C') + (CD - C'D)$$

Using approximations that are valid for the small angles through which the shell is folded, the end-shortening may be expressed as

$$\delta = \frac{1}{L_0} \left\{ \frac{\omega_0^2}{(1-2x-h)} + \frac{(\omega_0+\omega_i)^2}{2h} + \frac{\omega_i^2}{(1+2x-h)} \right\}$$

Substituting for ω_0 and ω_i from eqn.6.1 we get

$$\delta = \frac{\pi^4 R^2}{36 N^4 L_0} \left\{ \frac{1}{(1-2x-h)} + \frac{9}{2\ h} + \frac{4}{(1+2x-h)} \right\} \qquad (6.2)$$

It may be noted that the above relation is obtained for a section passing through a node in the positive X direction. If the section is taken through a tangential fold in the positive X direction, i.e., if the node occurs in the negative X direction this relation is changed to

$$\delta = \frac{\pi^4 R^2}{36 N^4 L_0} \left\{ \frac{4}{(1-2x-h)} + \frac{9}{2\ h} + \frac{1}{(1+2x-h)} \right\} \qquad (6.3)$$

The difference between the two relations arises due to ω_0 and ω_i being unequal, and because the facets are considered to occur away from the mid-section of the shell. Eqns.6.2 and 6.3 were solved numerically to obtain the minimum value of δ for different values of x. The minimum values of the end-shortening thus obtained from the two relations and the corresponding values of h (at which the minimum δ occurs) are plotted against X/L in Figures 6.8a and 6.8b. It may be observed that the minima of the curves in Figure 6.8a occur at about x = $\pm$ 0.06 and not at x = 0. Noting that the curves represent the minimum deflections for two sections separated by an angle of $\varphi/2$, it is obvious that for the facets to develop all round the end-shortening corresponding to the upper of the two curves has to be present. Hence the minimum value of δ is actually given by the envelope of the two curves denoted by the solid line in Figure 6.8a, which it may be noted has its minimum value at x = 0. (The corresponding values for h are given by the sections of the curves in solid lines in Figure 6.8b).

Thus the least value of end-shortening is that which forms the facets at the midsection of the buckled shell. For x = 0, eqns.6.2 and 6.3 reduce to

$$\delta = \frac{\pi^4 R^2}{72 N^4 L_0} \left\{ \frac{h + 9}{h\,(1-h)} \right\} \qquad (6.4)$$

Minimizing δ w.r.t h gives $h^2 + 18h - 9 = 0$, whose positive solution is

$$h_0 = 3\sqrt{10} - 9 = 0.487 \qquad (6.5)$$

Substituting this value in eqn.6.4 the minimum end-shortening is obtained as

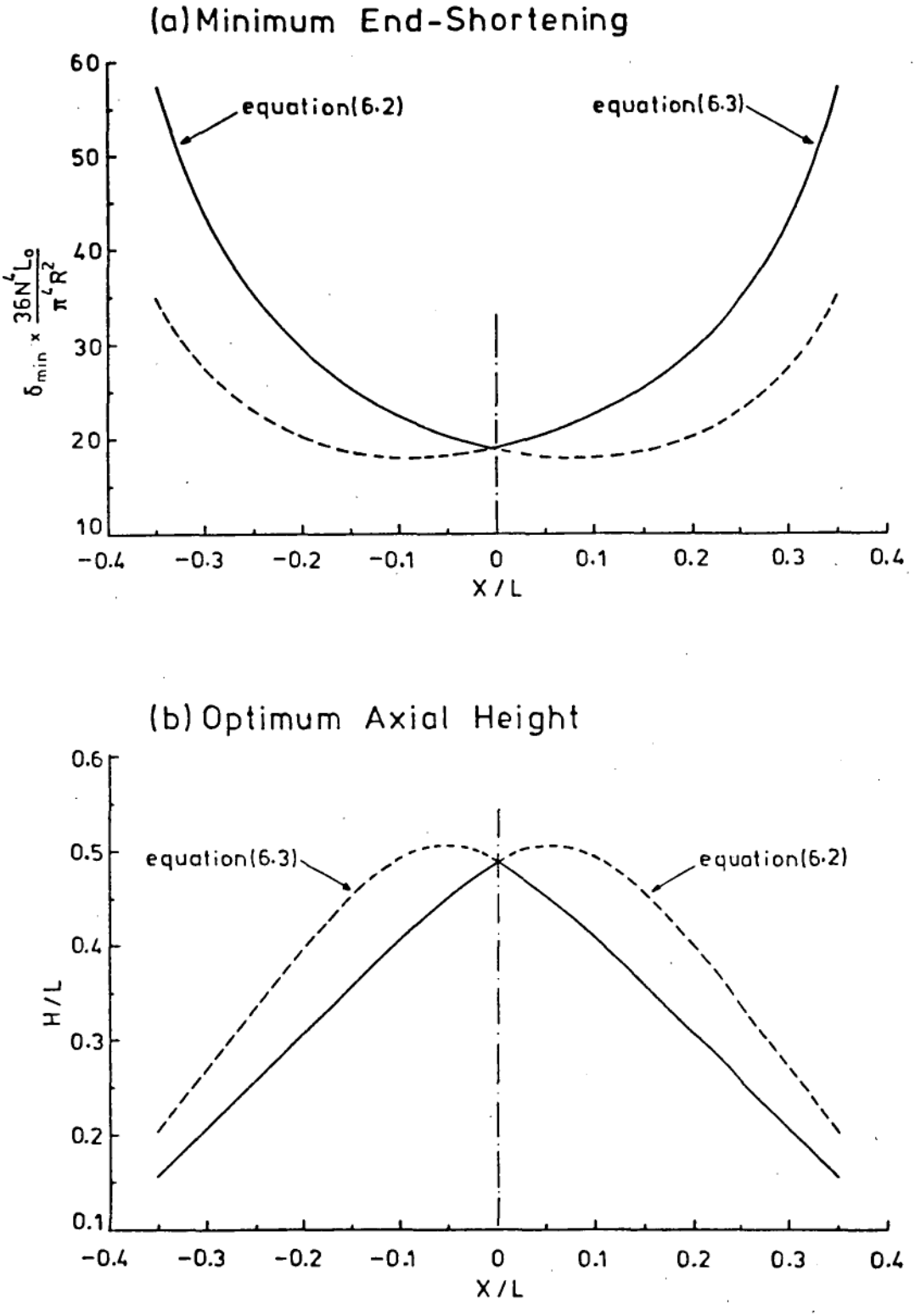

Figure 6.8. Effect of Axial Location of the Facets

$$\delta_{min} = 51.37 \frac{R^2}{L_o N^4} \qquad (6.6)$$

It may be recalled that in obtaining this relation the end load on the buckled shell has been neglected. The presence of a post buckling load of finite magnitude will introduce an axial strain so that the folded length of the generators in an actual shell will be less than their original length L_o. Hence the actual δ_{min} will tend to be higher than that given by eqn.6.6. Further any curvature of the segments AB, BC and CD which may be expected in the actual shell will again increase the required value of δ. Thirdly the formation of the facets anywhere else other than the midsection of the shell will also require a higher value of end-shortening, as shown by the curves in Figure 6.8. The only factor that has been ignored which reduces the required value of δ is the curvature at the two folds due to which the actual radial deflections will be less than the values of w_o and w_i considered. While the sharpness of the folds decreases with increasing shell thickness, the curvature elsewhere and the post-buckling load (owing to higher bending rigidity) would increase with the thickness, thus counteracting the error that is introduced by the neglect of the curvature at the folds. Hence the minimum end-shortening given by eqn.6.6 can be taken to be sufficiently accurate.

It is to be noted that the shell can form a <u>fully developed</u> two tier pattern with a particular number of circumferential facets only if it has been subjected to an end-shortening equal to or greater than that given by eqn.6.6. In other words, geometric requirements of the fully developed two tier pattern demand that at any given value of

end-shortening equal to δ_0, the circumferential number of facets in the buckled cylinder satisfy the relation

$$N \geq N_{min} = \left[\frac{51.37\ R^2}{L_0\ \delta_0} \right]^{1/4} \tag{6.7}$$

Thus in a controlled end-shortening situation while different values of N can be accommodated by appropriate variation in the axial height of the facets, there is a minimum number of facets required for the full development of the two tier pattern.

6.5 Minimum End-Shortening for One Tier Pattern

For the one tier pattern, the minimum end-shortening is easily obtained by considering a longitudinal section passing through the mid-point of a tangential fold in Figure 6.1c. When the folds are formed at the mid-section of the shell, the end-shortening is obtained as

$$\delta_{min} = 2\ \omega_i^2/L_0 = \frac{2}{9L_0}\ (\pi^4 R^2/N^4)$$

which gives

$$\delta_{min} = 21.65\ \frac{R^2}{L_0 N^4} \tag{6.8}$$

It is obvious that if the tangential folds develop elsewhere other than the mid-section of the shell, or if the buckles are smaller as in the model in Figure 6.1b, then higher values of end-shortening than that given by eqn.6.8 will be required. It may be noted that for a longitudinal section passing through the node, the lateral deflection at the fold would be ω_0 instead of ω_i, hence the δ required would be

only a quarter of that obtained above. However for the tangential fold to develop fully the end-shortening has to be at least that given by eqn.6.8. Hence, as before, it can be said that for a given value of the end-shortening equal to δ_0, the full development of the one tier pattern requires that the number of facets should be such that

$$N \geq N_{min} = \left[\frac{21.65\ R^2}{L_0\ \delta_0} \right]^{1/4} \tag{6.9}$$

It is to be noted that even when the end-shortening is just sufficient to allow the full development of the tangential folds, the generators along the nodes will be under substantial compression. In other words the one tier pattern is much less inextensional than the two tier pattern. At higher values of δ the axial stress will be even higher; for this reason one tier patterns observed in practice are usually accompanied by secondary buckles as seen in Figure 6.5.

6.6 Initial Stable Post-Buckling Mode of the Cylindrical Shell

In the foregoing sections it has been emphasized that the minimum N predicted is for the fully developed configurations. This is because theoretically even lower values of N are possible if the lateral displacements are taken to be smaller than those required for the full development of the buckle pattern. It is however to be noted that partially developed buckle patterns occur only in the unstable transition regions of the post-buckling regime, while the buckles of the observed stable configurations are invariably fully developed facets. Indeed the present discussion is intended to investigate only

the stable post-buckling configurations of the axially compressed cylindrical shell.

The relations represented by eqns.6.6 and 6.8 are plotted on a semi-log scale in Figure 6.9. The abscissa of the plots is the non-dimensional value of the end-shortening given by

$$\Delta = 10^4 \, \delta L/R^2 \qquad (6.10)$$

These plots may be used to determine the minimum N that can be formed at any value of end-shortening of the buckled shell. It is to be noted that since only integer values are admissible for the number of facets around the circumference, the minimum N is given by the nearest integer greater than or equal to the N_{min} predicted by eqns.6.7 and 6.9. Hence in the figure the points immediately to the left of the vertical line passing through the given Δ are to be used. For example, for a value of $\Delta = 40$ the minimum number of facets that can be found in the one tier pattern is equal to 9, while in the two tier pattern the circumferential number of facets will be greater than or equal to 11. As to which of these patterns - the one tier or the two tier - will be formed, is apparently determined by the Batdorf parameter Z, as discussed in the next section.

The number of circumferential lobes observed after the primary collapse of the perfect cylinder, can be predicted from these geometrical relations in terms of the end-shortening corresponding to the classical load, which is given by

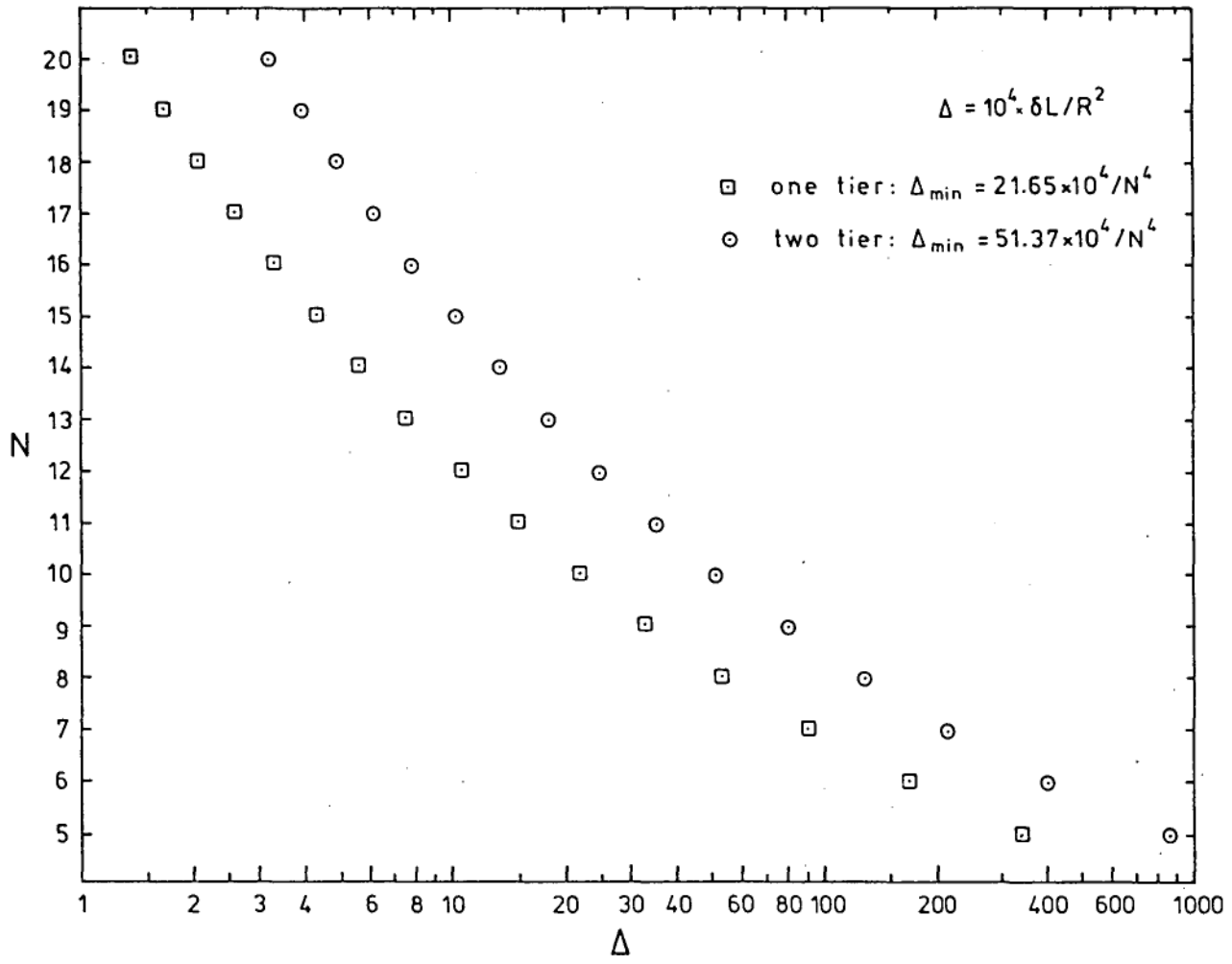

Figure 6.9. Values of Minimum End-Shortening for the One and Two Tier Patterns

$$\delta_{cl} = \frac{(tL/R)}{\sqrt{3\ (1-\nu^2)}} \tag{6.11}$$

Substituting this value in eqns.6.7 and 6.9, the minimum value of N observed after primary collapse is obtained as*

$$N_{min} = C^{1/4}[3.(1-\nu^2)]^{1/8}.(R/L)^{1/2}.(R/t)^{1/4} \tag{6.12}$$

where C takes values of 21.65 and 51.37 for the one and two tier patterns respectively. For a Poisson's ratio ν = 0.34, which applies to the material of the shells tested in the current work, the minimum values of N for the one tier and two tier patterns are respectively given by

$$N_{min} = 2.44\ (R/L)^{1/2}(R/t)^{1/4} \tag{6.14}$$

and

$$N_{min} = 3.02\ (R/L)^{1/2}(R/t)^{1/4} \tag{6.15}$$

While the above relations based on geometric considerations determine only the minimum value for the number of facets around the circumference, empirical evidence indicates that the shell generally tries to attain this minimum value on buckling. The reason for such behaviour is that lower values of N are associated with lower energy levels. This is evidenced by the fact that the post-buckling curves - those obtained experimentally (see Figures 8.1, 8.2) as well as those predicted by non-linear theory - get lower and lower as the value of N decreases. While the present geometric considerations based only on a

* It may be noted that the subscript has been dropped from the length L_0 of the cylinder, since it is no longer necessary.

longitudinal section of the shell cannot conclusively prove that the total energy of the shell increases with increasing N, they do provide some physical explanations for such an increase. In the case of the two tier pattern, the increase in total energy is seen to arise from the increase in the total angle through which the shell folds, which is associated with the reduction in the axial height of the facets necessary to accommodate higher values of N. The increase in energy in the one tier pattern may be directly attributed to the increase in the axial strain in the sections over the corners of the tangential folds.

Hence, on the premise that the buckled shell tries to attain the stable configuration associated with the minimum strain energy, it is proposed that the number of circumferential facets observed on primary collapse is given by the minimum value predicted by eqn.6.14 or 6.15, whichever is applicable.

6.7 Geometric Criterion for the Formation of Two Tier Pattern

The buckling modes possible at the onset of collapse at the critical load corresponding to the classical value are given by the relation $N^2 + q^2 - q.q_0 = 0$ (eqn.2.2) which represents a semi-circle for the positive values of N as shown in Figure 6.10a. (This circle, attributed to Koiter - Ref.33, page 266 - is sometimes referred to as the Koiter circle). The classical value of N, obtained by equating the derivative of N w.r.t. q in eqn.2.2 to zero, hence represents the maximum number of circumferential facets that can be formed at the occurrence of primary collapse. This maximum value, which is given by

eqn.2.4 as $$N_{cl} = \left[\frac{3}{4} (1 - \nu^2) R^2/t^2 \right]^{1/4} \qquad (2.4)$$

may be expressed in terms of the Batdorf parameter $Z = \sqrt{(1-\nu^2)} \frac{L^2}{Rt}$ as

$$N_{cl} = (3/4)^{1/4} (R/L) Z^{1/2} \qquad (6.16)$$

The minimum number of circumferential facets geometrically possible in the stable post-buckled configuration, given by eqn.6.12 may also be expressed in terms of the Batdorf parameter Z as

$$N_{min} = 3^{1/8} C^{1/4} (R/L) Z^{1/4} \qquad (6.17)$$

The relations expressed by eqns.6.16 and 6.17 are plotted in Figure 6.10b. The two curves indicated by solid lines in the figure, corresponding to the minimum value of N in the stable post-buckled two tier pattern and the maximum (classical) value of N, intersect at Z = 119. For values of Z greater than this value the buckling mode has a higher number of facets, so that after collapse it is possible for the shell to settle into a stable two tier mode with a lower value of N (close to the N_{min} indicated by the curve). However for values of Z less than 119, the maximum number of facets that can possibly form at collapse (according to the linear theory) is less than the minimum required for the two tier configuration, so that the development of a stable two tier post-buckling mode is geometrically not possible. (It may be observed that the non-linear theory taking into consideration the clamped end conditions of the cylinder predicts a value of N at collapse that is 5% less than the classical value, which gives a

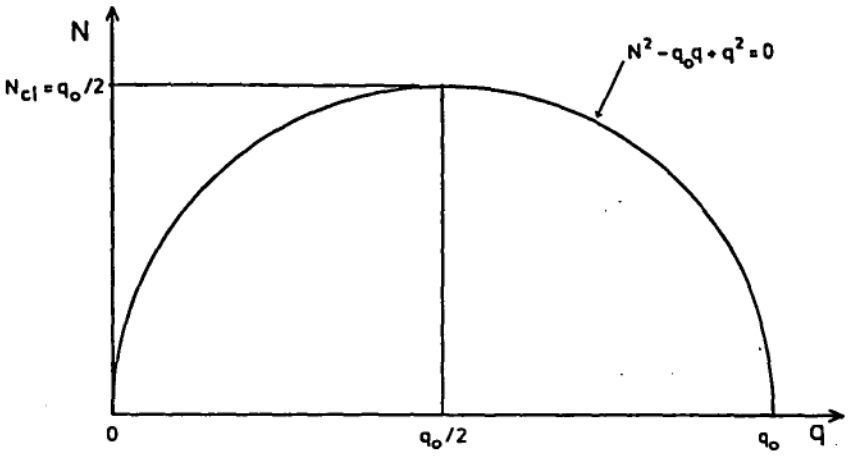

Figure 6.10a. Koiter Circle

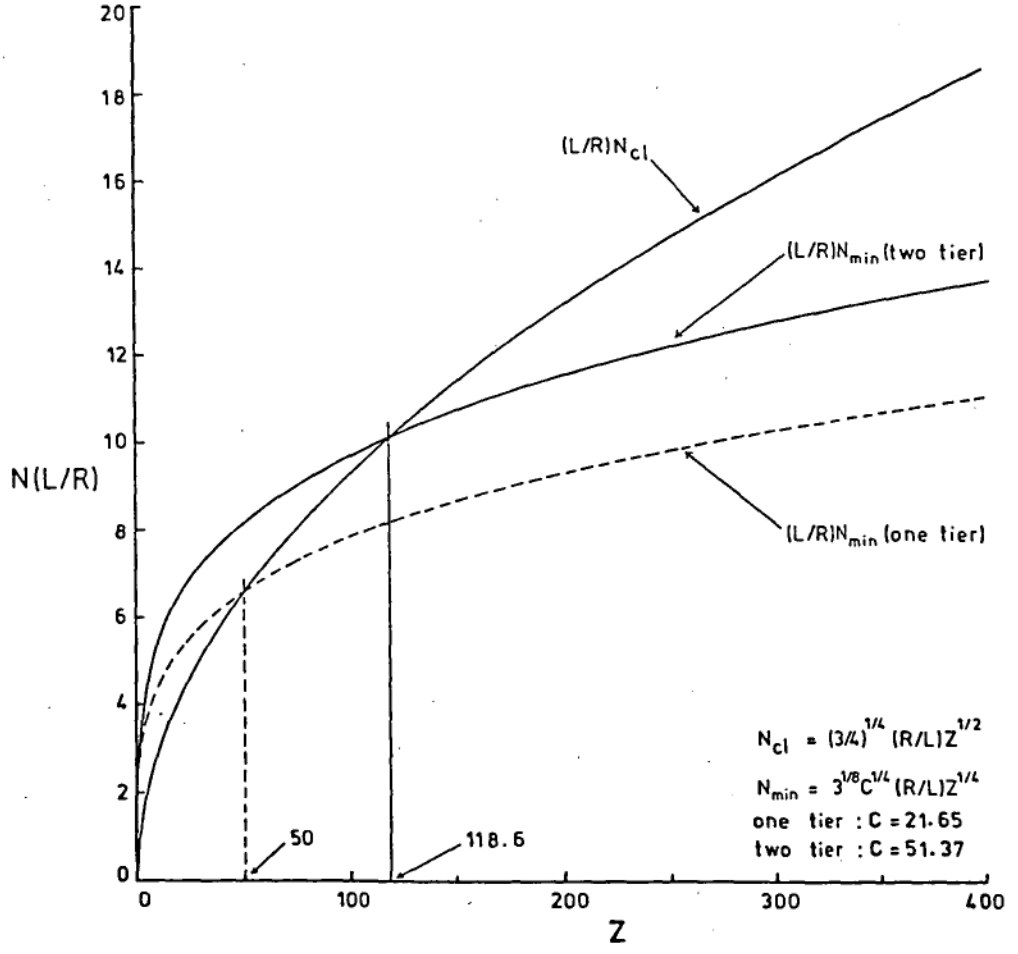

Figure 6.10b. Effect of the Parameter Z on the Circumferential Number of Facets

limiting value of Z of about 146). It thus appears that the minimum value of Z required for the formation of the two tier pattern on primary collapse is given by Z = 119. This value is in agreement with the observations by Yamaki (Ref.11, page 223) that the two tier pattern could not be realized in shells with values of less than or equal to 100, while shells with values of $Z \geq 200$ readily buckled into the two tier pattern. The fact that the longer shells buckle into the two tier pattern even though both modes are geometrically possible indicates that for long shells the two tier mode is a state of lower energy than the corresponding one tier pattern. It is to be noted that Yamaki was able to realize the one tier modes also in the longer shells ($Z \geq 200$) by adjusting the shell wall with the finger tips, with a consequent reduction in the number of circumferential facets.

The intersection of the curve corresponding to the classical N with the curve representing the minimum N required for the one tier pattern in Figure 6.10b occurs at Z = 50. Thus for values of Z between 50 and 119, it is seen that the shell can readily go into the one tier pattern. Although the plots indicate that the formation of the one tier pattern at values of Z less than 50 is not possible, experimental evidence points to the contrary. In the same work Yamaki has reported the development of the one tier pattern in a shell with Z = 20. This apparent discrepancy is probably due to the fact that the classical relations regarding the buckling load and the number of facets do not hold good at such low values of Z (although the geometric relations may still be valid). For instance, the shell with Z = 20 tested by Yamaki (Ref.11, page 250) appears to have developed 18 facets around

the circumference in the initial deformed state while the predicted maximum value of N was only 12, with a theoretical buckling load of about 1.2 times the classical load. It is therefore to be noted that the lower limit of Z for the formation of the one tier pattern cannot be established by the above considerations, while they have provided the criterion for establishing the value of Z above which the two tier pattern may be expected to occur.

6.8 Comparison with Existing Formulae for the Number of Facets

The relations developed in previous works for predicting the number of circumferential facets observed on primary collapse do not generally differentiate between the one tier and two tier patterns. Whereas, the foregoing geometrical considerations indicate that for the same value of end-shortening the two tier pattern requires a higher number of circumferential facets than the one tier pattern.

The formula proposed by Hoff[56], based on tests conducted on shells with R/t in the range of 530 to 760, and L/R between 1/2 and 10, is as follows:

$$b = 11\ (L/R)^{0.36}\ (R.t)^{1/2}$$

Substituting for the circumferential wave-length $b = 2\pi R/N$, this may be rewritten as

$$N = 0.57\ (R/L)^{0.36}\ (R/t)^{1/2} \qquad (6.18)$$

The indices of both R/L and R/t in this equation differ considerably

from those obtained in the current work. Much better agreement is seen to exist between the present relations and the semi-empirical formula proposed by De Neufville and Connor[55], which is as follows:

$$N = 2.7\ (R/L)^{1/2}\ (R/t)^{1/4} \qquad (6.19)$$

It may be noted that while the indices are exactly the same, the coefficient has a value that is in between the values of the two equations 6.14 and 6.15. This formula was derived in a rather curious manner. While the classical value of N is obtained by putting N = q, or (dN/dq) = 0 in eqn.2.2 (see previous section), De Neufville and Connor neglected the term q^2 in the above relation, to obtain* $N^2 = q.q_0$. The rationale for doing so was that the number of half waves m observed in practice is always small (one or two). Substituting $q = m\pi R/L$ and for q_0 from eqn.2.3, this gives

$$N = m^{1/2}.\left[\ 12.\pi^4(1 - \nu^2)\right]^{1/8}(R/L)^{1/2}(R/t)^{1/4}$$

For ν = 0.34, using m = 1 and m = 2 in the above equation the values of N for the one and two tier are respectively obtained as

$$N = 2.38\ (R/L)^{1/2}\ (R/t)^{1/4} \qquad (6.20)$$

and

$$N = 3.37\ (R/L)^{1/2}\ (R/t)^{1/4} \qquad (6.21)$$

It may be noted that even for ν = 0, the coefficient obtained for

* This is expressed by the authors as $N^8 = 12(1 - \nu^2)[R/t]^2\ q^4$.

m = 1 (eqn.6.20) is only 2.42. It thus appears that the value of 2.7 in eqn.6.19 (quoted from Ref.55) has been determined empirically, and is perhaps the result of not differentiating between the one and two tier patterns. It is interesting to note that the difference between the coefficients in eqn.6.20 and the eqn.6.14, which was obtained from the geometry of the one tier pattern is less than 3%, while in the case of the two tier pattern (eqns.6.15 and 6.21) the difference is of the order of 10%.

Noting that the observed number of facets varies with the post-buckling load, Pflügger proposed that the constant coefficient in the expression for the classical value of N (eqn.2.4) be replaced with a factor which varies with the ratio of the post-buckling load to the classical load (reported in Ref.72). Approximating the curves of Pflügger for this factor by a linear relation, Kollár and Dulácska[72] give the following formula for the number of facets observed after collapse*:

$$N = 0.93\ (1 - \nu^2)^{1/4}(R/t)^{1/2}.(P/P_{cl}) \qquad (6.22)$$

Equating this value of N to the minimum N (given by eqn.6.12) expected to occur after primary collapse in the two tier pattern (C = 51.37), the ratio of the post-buckling load to the classical load is obtained as

$$P/P_{cl} = 3.3\ Z^{-1/4} \qquad (6.23)$$

where Z is the Batdorf parameter. It may be noted that experimental

* There is some doubt regarding the value of 0.93 quoted (from Ref.72) for the constant in eqn.6.22, which will be discussed in Chapter 8.

investigations by Yamaki[11] have already shown that the post-buckling load decreases with increasing Z. To verify whether this relation can be expressed in such a simple form as that given by eqn.6.23, the values from the above formula are compared with the experimentally obtained initial post-buckling loads in Chapter 8. The predictions of the various formulae for N are also compared with the number of facets observed in the tests.

6.9 Concluding Remarks

The foregoing geometric considerations show that the minimum number of circumferential facets in the buckled shell is determined by the magnitude of the end-shortening that the shell has undergone after it has buckled. In developing the relations the curvature at the folds has been ignored; however the error due to this is expected to be very small, particularly for thin shells. Hence for all practical purposes the inequalities represented by eqns. 6.7 and 6.9 should hold good. The suggested use of eqns.6.14 and 6.15 for predicting the number of facets observed on primary collapse is based on the premise that the shell attempts to attain the minimum energy level by developing the stable configuration with the minimum number of circumferential facets. While this premise is reasonable, there are other assumptions involved in the use of these equations which do not always hold good.

The first such assumption is that the buckles are formed at the mid-section of the shell. The second is that the end-shortening of the buckled shell is that corresponding to the classical load. These

assumptions are valid only for the perfect shell. The presence of imperfections can cause a shell to buckle well before the classical value of the end-shortening is reached; it can also induce the buckles to form away from the mid-section of the shell. In either case the observed value of N will be higher than the predicted minimum value.

There is another major assumption implicit in the derivation of eqns.6.14 and 6.15, which is in relation to the rigidity of the loading machine. In equating the end-shortening in the post-buckled state to that at the occurrence of collapse, the flexibility of the machine has been ignored. In an actual controlled end-shortening test, the release of the load on the machine when the shell buckles causes the distance between the platens to reduce, owing to the flexibility of the loading device. Hence the end-shortening on the buckled shell will always be greater than that at the onset of buckling. The extent to which the end-shortening increases on buckling depends on the flexibility of the machine so that with increasing flexibility the circumferential number of facets can be expected to reduce. In fact, such reduction in the number of facets with decreasing rigidity of the loading machine has been reported by Yoshimura[19]. It may however be noted that the effect of the flexibility of the loading device and that of the imperfections in the shell somewhat counteract each other, so that for a reasonably good shell tested in a fairly rigid testing machine the number of facets observed on primary collapse can still be expected to be reasonably close to the values predicted by equations 6.14 and 6.15.

CHAPTER 7

EXPERIMENTAL SET UP

7.1 The Loading Frame

The apparatus used for testing the cylindrical shells in axial compression is shown in Figure 7.1. The rigid loading frame, having a capacity of 20 KN, was designed specially to accommodate the optical arrangement devised to monitor the presence and growth of defects in the shell*. The 30 mm thick cross-head is supported by linear bearings on two $1^1/_4$ inch diameter parallel guide rods fixed between the 30 mm thick base plate and the 20 mm thick top plate of the machine. The loading screws, with a diameter of $1^1/_4$ inch and having 5 square threads per inch, were driven by a hand wheel via a 50:1 worm reduction unit and a chain and sprocket arrangement. A motor was also attached to the hand wheel for quicker movement in raising and lowering the cross-head; however the loading of the shells was always done by manually turning the hand wheel.

The design of the load cells proved a challenging task. The first attempt, based on the measurement of compressive strains on a thin 150 mm diameter steel shell which was located in between the cross-head and the top end-ring of the test-shell, was abandoned when it was found that the calibration plot was non-linear and showed

* It is to be acknowledged that in designing the loading machine and developing the optical set up the author had considerable assistance from Foster. The latter in particular is based on a previous optical arrangement set up by Foster for monitoring defects in shells.

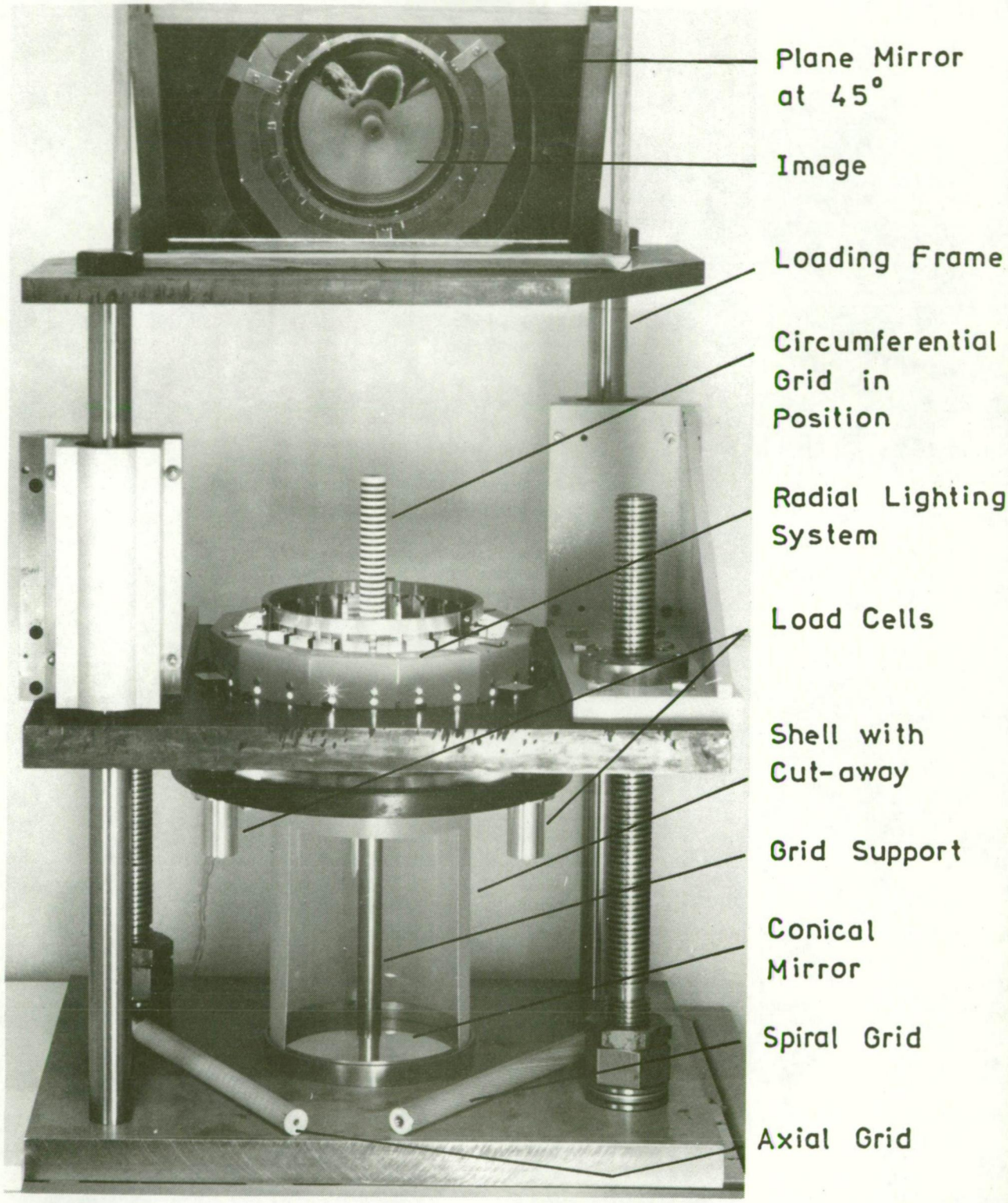

Figure 7.1. The Experimental Set-up

substantial variation from test to test. This was attributed to the thin-ness of the load cell and the presence of cut-outs in it which were necessary to provide the required sensitivity. Subsequently the present load cells were designed consisting of thin (0.4 mm thick) Aluminium tubes which develop tension when the compressive load is transferred from the cross-head to the circular loading plate below it by means of steel loading pins passing through them (see Figure 7.2). The three equi-spaced load cells provide a three point contact between the cross-head and the loading plate; however the thickness of the loading plate and the presence of the end-rings on the shell ensure uniform distribution of load around the circumference of the shell. In each load cell four active elements are used, two for the measurement of axial strain and two for the transverse strain. A bridge circuit was used to eliminate the bending strains in each load cell and to maximize the sensitivity by adding the output from the three load cells. The strains were measured on a Brüel and Kjær Strain Indicator Type 1526. These load cells were designed for a capacity of 2.5 KN (the maximum load required to buckle the shells tested was only about 1.5 KN) and provided a sensitivity of 0.5042 $\mu\epsilon$ per Newton with the gauge factor on the instrument set at 1.00. The calibration plot for the load-measurement system is shown in Figure 7.3.

The end-shortening was measured by means of a Differential Current Displacement Transducer (Hewlett Packard 24 DCDT-250) with a calibration factor of 27.2 Volts per inch. The outputs from the Strain Indicator and the DCDT were fed directly into an X-Y plotter (Hewlett Packard 7004 B) to record the load deflection curves during the tests.

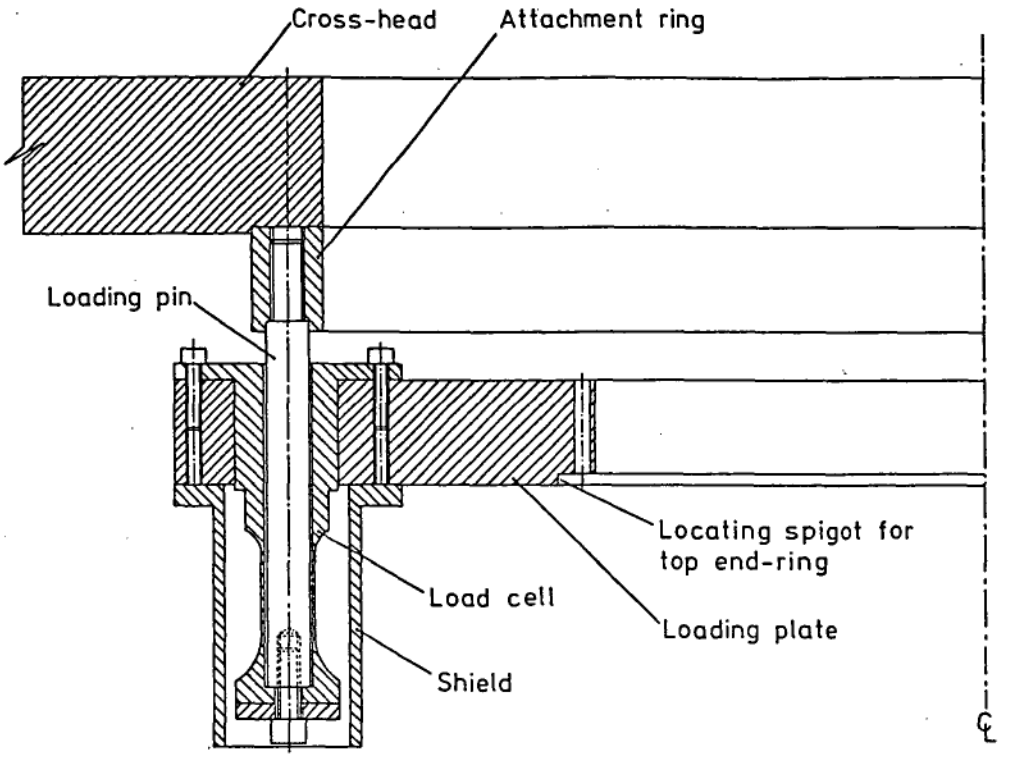

Figure 7.2. Load Cell Assembly

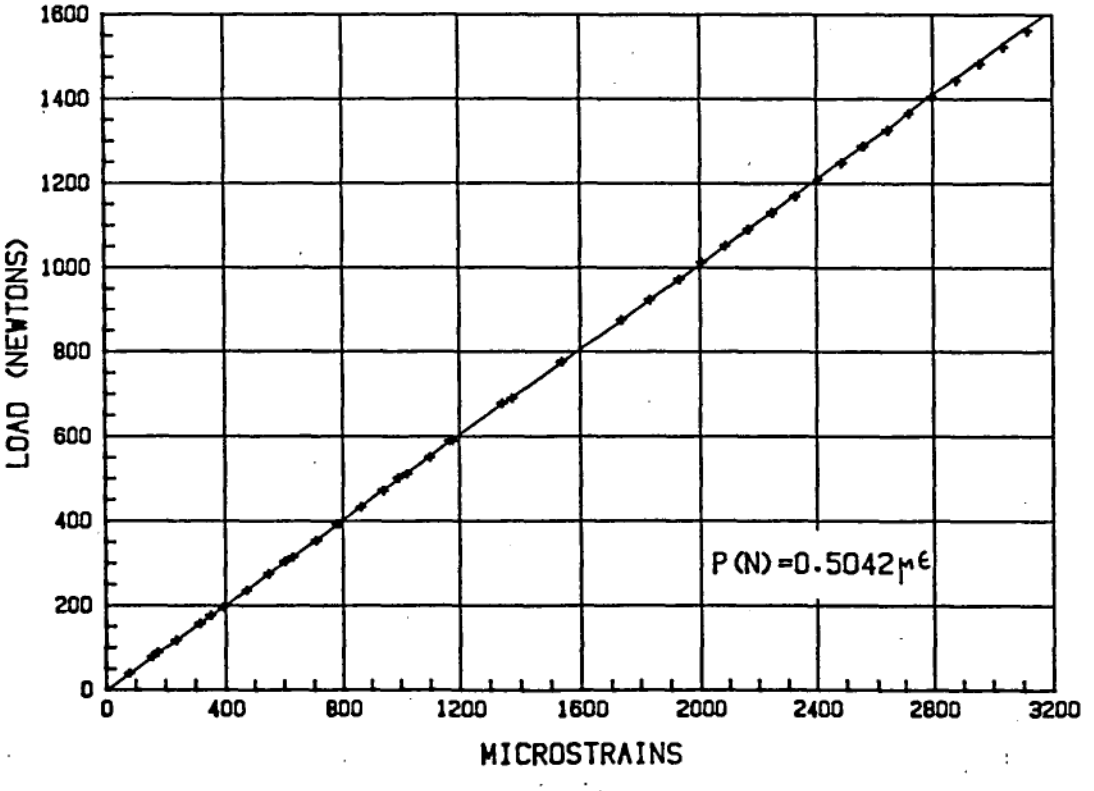

Figure 7.3. Load Cell - 2.5 KN Calibration Plot

7.2 Manufacture of Shells

The shells for the experimental work were manufactured by a spin-casting technique from Araldite LC 261 mixed with hardener LC 249 in the ratio of 10:3 by weight. The method of spin-casting shells for experimental purposes was developed by Tennyson[22,54], who employed the technique successfully to manufacture near perfect shells with buckling loads close to the theoretical value. The equipment used in the present work is an improvement over that used by Tennyson and was developed by Foster[25]. (Comparison between the two techniques of spin-casting is given in Ref.25). A photograph of this equipment is shown in Figure 7.4. It consists of a steel former with an open end cantilevered from a rotating shaft supported on a rigid structure in bearings in which the backlash was eliminated (similar to those of a machine lathe). The shaft was rotated at a speed of about 1000 rpm. An aerosol PTFE spray was used as release agent. The mixture of the epoxy resin and hardener was pre-warmed to about 65° before pouring it into the former. A liner was cast first to eliminate the irregularities on the inner surface of the former and to provide a smooth cylindrical surface concentric with the bearing axis. Once the liner was cured sufficiently, the release agent was again sprayed and the required amount of the epoxy mix was injected with a syringe (which provided access to the inner end of the former) and spread evenly by means of a brass spreader. The former was allowed to spin for about 10 to 12 hours with heat supplied from a fan heater during the first three or four hours to speed up the curing process. The shells manufactured by this technique had a smooth highly reflective inner surface.

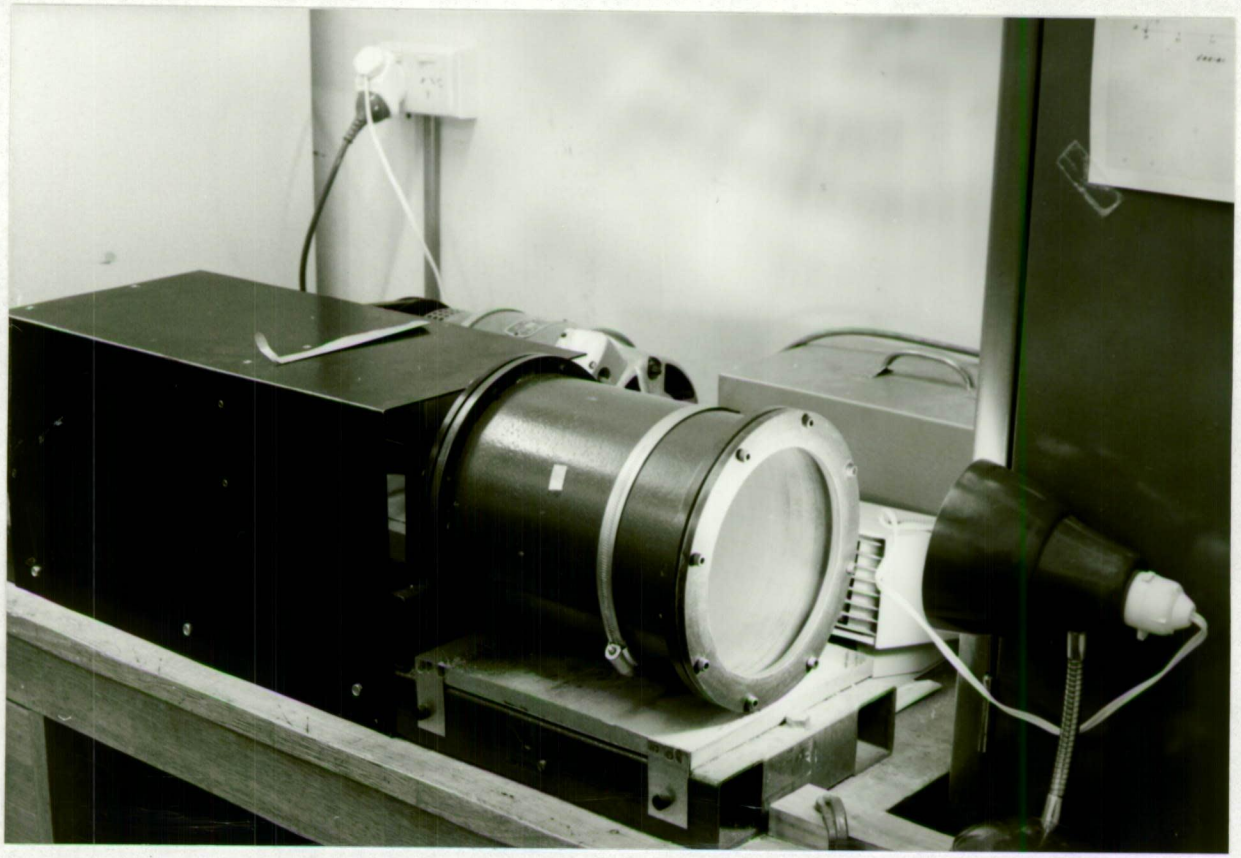

Figure 7.4. Spin-Casting Equipment

The former used for the manufacture of the shells had a diameter of about 154 mm. The actual inner diameter of the shell was measured with vernier callipers before it was removed from the former. For measuring the wall thickness, the shell was placed on a machined steel mandrel attached with a dial gauge with a least count of 0.001 mm. By rotating the shell over the mandrel and moving it along the axis, thickness measurements were taken over the entire surface of the shell. Many of the shells manufactured had a thickness variation of less than 0.002 mm, although shells with a maximum variation of up to 0.008 mm were used in the tests. The average wall thicknesses ranged between 0.13 and 0.39 mm providing a range of R/t from 200 to 600.

7.3 Mounting the shells

The ends of the shells were set into rings with circular grooves using the same LC 261/249 epoxy mixture as that used for making the shells. The tapered guide spigot of the end-ring provides intimate contact between the shell and the surface of the spigot on which it is mounted (see Figure 7.5). This system of end-support is similar to that proposed by Sendelbeck and Hoff[21], and maintains good circularity at the ends. To ensure parallelism between the ends of the shell the following procedure was adopted : With the end-rings fitted the shell was first placed upside down in the loading frame, i.e., with the top end-ring resting on the base plate. After aligning the shell properly, the end of the shell was "potted" into this end-ring using the epoxy mix. When the epoxy was cured the shell was inverted and the top end-ring secured to the loading plate below the cross-head

using a set of eight equi-spaced locating screws. The cross-head was then lowered and the seating of the bottom end-ring on the base plate with complete contact all round ascertained before the lower end of the shell was potted in. In this manner the alignment of the shell along the axis of the loading frame and the uniformity of loading around its circumference could be ensured. It may be mentioned that complete curing of the epoxy in the end-rings, which took place at room temperature, required a period of about 30 to 36 hours.

After the tests were completed on each shell the epoxy from the grooves of the end-rings was machined out, and further cleaning done by hand before using them again on the next shell. After testing a few shells, it was found that due to the repeated cleaning process the outer diameter of the guide spigots on the first two pairs of end-rings was reduced so that they fitted loosely on the ends of the shell. Further, since they were made from Aluminium and were rather thin, due to repeated mounting on the lathe they had lost their perfect circular shape. For this reason the next three pairs of end-rings were made thicker and from mild steel, whose performance remained satisfactory till the completion of the testing program.

The weight of the Aluminium end-rings was 441 and 235 grams each, top and bottom respectively; while the steel end-rings weighed 936 grams (top) and 810 grams (bottom). It is to be noted that when the cross-head is raised with the shell suspended from the loading plate, the shell is subjected to a tension equal to the weight of the bottom end-ring. Since the Strain Indicator was set to zero at this

point, the weight of the bottom end-ring has been subtracted from all registered load readings to get the actual load values presented in the tables in the next two chapters.

7.4 The Optical System

The optical system incorporated in the experimental set up is based on the well known grid reflection technique, which makes use of the significant distortions produced in the reflected image by small variations in slope on the reflecting surface to monitor the deformations of the reflective surface. Reflection of grids or an array of lights replacing the grid has often been used in the past for the study of shell buckling[52,53,74]. However in those studies the outer surface of the shell was utilized for reflection, and the field of view was restricted to a portion of the circumference. A whole field optical technique for the measurement of radial deformations over the entire surface of the cylindrical shell was developed by Foster[58,75]. Central to the technique is the use of a conical mirror which provides a complete view of the inner surface of the shell. The reflection of the grid on the inner surface of the shell wall is viewed through this conical mirror, which essentially transforms the cylindrical surface of the shell to a plane surface in the image suitable for photographic recording. Foster employed the inner surface of a large hollow cone to view the inside of the shell. The technique used in the current work is a modification of Foster's earlier method, replacing the large hollow cone by a compact solid cone whose outer surface is used for reflecting the shell wall.

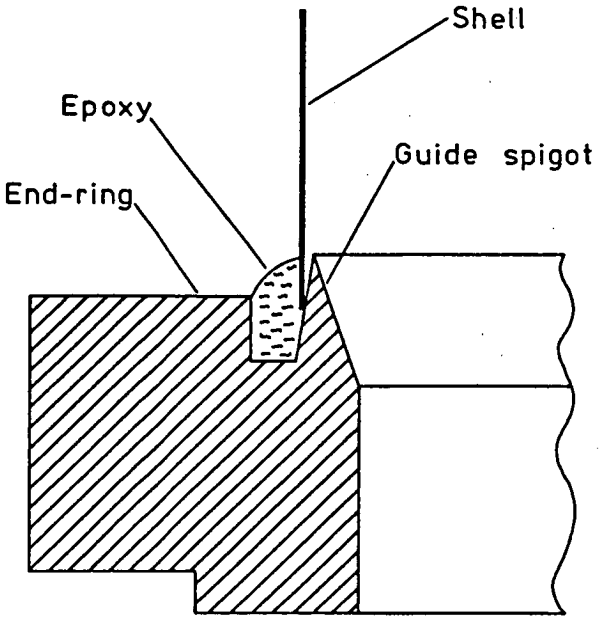

Figure 7.5. Shell Mounting

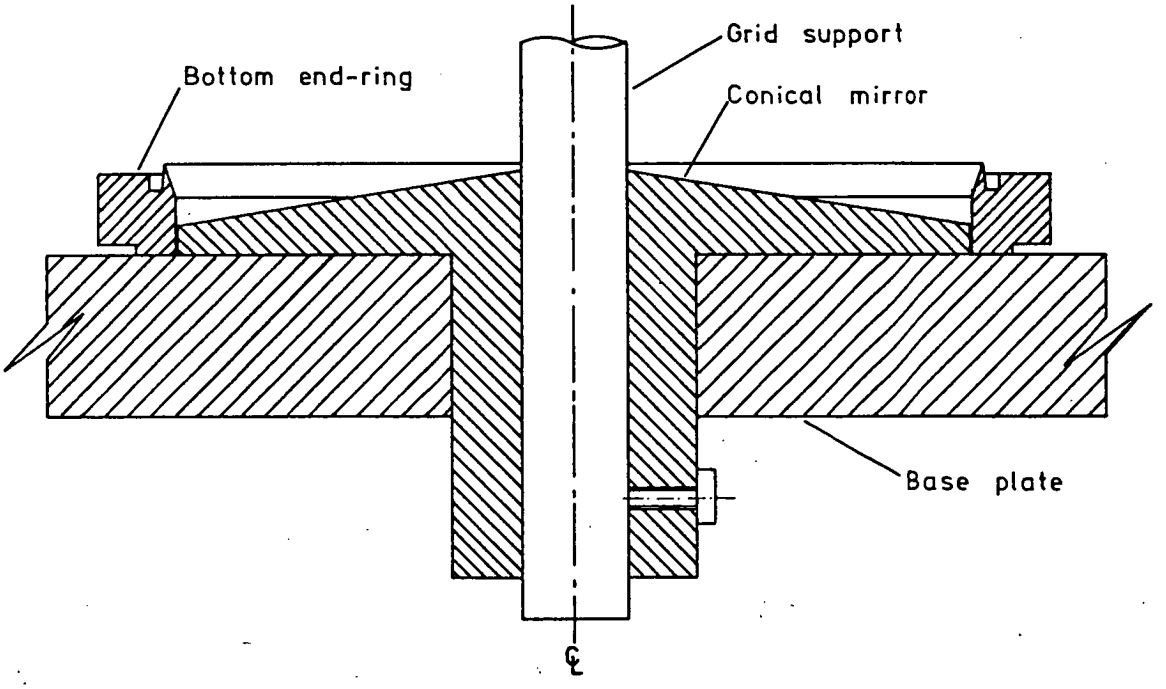

Figure 7.6
Alignment of the Optical System

The lines on the grid placed along the axis of the shell are reflected by the shell's inner surface onto the conical mirror (Figure 7.1). The image formed in the conical mirror is viewed by the camera via a plane mirror positioned at the top at 45° to the grid axis. The conical mirror, made from Aluminium NO.2011, has a diameter of 149 mm and a base angle of 9°. The height from the base is less than 17 mm. In comparison, the hollow cone used previously by Foster required a length nearly twice that of the shell and a minimum diameter of about one-third the length of the shell. The manufacture of this hollow cone and the polishing of its inner surface required considerable time and effort. The machining of the present conical mirror and the polishing of its outer surface to mirror finish was relatively easy.

The main advantage of the new conical mirror is that it facilitates ready alignment of the components of the optical system. In the old set up the hollow conical mirror was located some distance away from the shell at the opposite end to the grid, which made the task of aligning the grid and the mirror with the shell axis rather difficult. In the new system, the grid is supported on a cylindrical rod situated along the axis of the conical mirror, the latter being positioned flat on the base plate at its centre (see Figure 7.6). The bottom end-ring has a clearance fit to the outside edge of the conical mirror. Thus the axes of the shell, the grid and the conical mirror are automatically aligned in the modified arrangement.

Three different types of grids were used in the present work: a circumferential grid consisting of equi-spaced circles with a

pitch p_c = 5.85 mm, an axial grid with longitudinal lines with a pitch p_a = 1.206 mm, and a spiral grid with equi-spaced helical lines having a normal pitch p_s = 1.184 mm and a helix angle α = 79°. The grid with circumferential lines produces an image of concentric circles and the helical lines on the spiral grid appear as spiral lines on the image plane, while the axial grid is transformed to a set of radial lines. The axial grid responds only to slope changes in the circumferential direction on the shell surface, while the circumferential grid is sensitive mainly to slope changes in the axial direction with some dependence on the circumferential slope. The spiral grid is sensitive to slope variations in both the directions, effectively combining the qualities of the other two. The grids were made by painting black lines (a lathe was used for this purpose) on a white background on the surface of Aluminium cylindrical rods. All three grids were of the same size with a radius R_g = 9.6 mm.

The grid (on the axis of the shell) is illuminated by a circular array of lights positioned on the cross-head of the loading frame. Inside the circle of light sources is an array of Aluminium panels which prevent the light from illuminating the shell directly. Vertical slits in these panels in front of the light sources direct their beams radially towards the grid at the centre, so that the shell is illuminated only by the light scattered from the cylindrical grid surface. This arrangement provided very good contrast, making the grid lines sharp and clear in the photographs. It was later found necessary to include another array of lights on top (not shown in Figure 7.1) to obtain even illumination on long cylindrical shells.

A Pentax K1000 camera (35 mm format) with a 400 mm focal length telephoto lens attached was used to photograph the image reflected by the plane mirror at the top of the loading frame. The camera was placed at a distance of about $11^1/_2$ feet from the machine providing an overall distance of 14 ft (4267 mm) from the lens to the base of the conical mirror. The photographs were recorded on 35 mm black and white film - Kodak Technical Pan 2415 (125 ASA) - using F22 aperture and an exposure period of 8 seconds. The negatives were developed for $4^1/_2$ minutes using Kodak D-19 developer and fixed with Kodak liquid X-ray fixer (4 minutes).

The reason for using such a large distance between the camera and the object is that the view from the camera is a conical field giving rise to non-linearities in the axial direction. In the previous arrangement used by Foster (which was set up for 4" diameter shells) this difficulty was overcome by introducing a long focal length convex lens in the optical path which provided a collimated field. This however could not be done for the present set up since a large diameter (more than 6") lens with long focal length was not readily available. Even with the camera placed at 14 feet, the maximum angle of convergence at the aperture of the camera is about 1°, which is not small compared to the 9° base angle of the conical mirror. Unfortunately the camera could not be moved back any further due to the limited size of the room in which the experimental set up was located. It may however be noted that these non-linearities do not in any way restrict the utility of the optical system in detecting defects or monitoring their growth.

7.5 Geometry of the Optical System

Owing to the finite distance between the camera and the loading frame, the view from the camera is a diverging conical field, which, as mentioned earlier, introduces non-linearities in the transformation from the object plane to the image plane. To consider this effect, the rays from the conical mirror are taken to converge to a point on the optical axis at the aperture of the camera. The angle of convergence γ of a ray arriving at the aperture will depend on the radial position r of the point at which it gets reflected from the conical mirror as well as the distance D between the aperture and the base of the conical mirror (see Figure 7.7). This angle is given by

$$\text{Tan}\gamma = \frac{r}{D_0 + r\,\tan\theta} \tag{7.1}$$

where

$$D_0 = D - R_m\tan\theta \tag{7.2}$$

R_m being the radius of the conical mirror and θ its base angle. For a given geometry of the conical mirror and shell radius R_s, the highest section of the shell that could possibly be viewed in the conical mirror is that which would be reflected from the apex of the conical mirror. This height is denoted by Z_0 in the figure and is given by

$$Z_0 = R_m\tan\theta + R_s\cot 2\theta \tag{7.3}$$

It may be noted that for a ray to arrive at the aperture with an angle γ it has to leave the grid at an angle $(2\theta+\gamma)$, and be reflected from

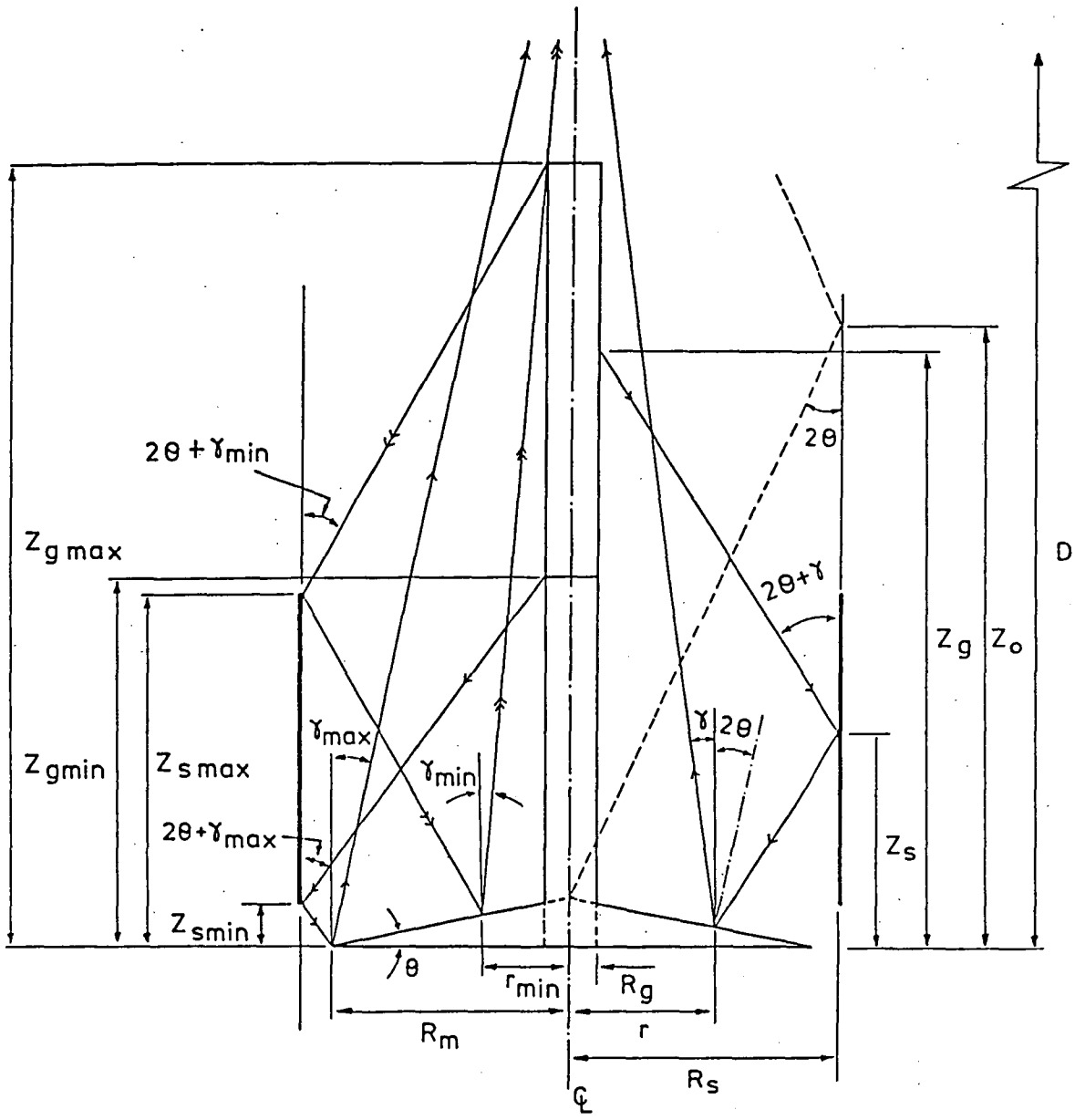

Figure 7.7
Geometry of the Optical System

the surface of the shell at the same angle, which gives rise to the relations,

$$\tan(2\theta+\gamma) = \frac{R_s - r}{Z_s - (R_m - r)\tan\theta} \tag{7.4}$$

and

$$Z_g = Z_s + (R_s - R_g)\cot(2\theta+\gamma) \tag{7.5}$$

where Z_s and Z_g respectively denote the distances from the base of the conical mirror to the position at which the ray gets reflected on the shell and the point of incidence of the ray on the grid surface. By substituting for $\tan\gamma$ from eqn.7.1 in the trigonometric expansion $\tan(2\theta+\gamma) = (\tan2\theta + \tan\gamma)/(1 - \tan2\theta.\tan\gamma)$, it can be shown that

$$\cot(2\theta+\gamma) = \cot2\theta - \frac{r}{\sin2\theta(r + D_0\sin2\theta)} \tag{7.6}$$

Substituting eqn.7.6 in eqns.7.4 and 7.5 gives rise to the following relations

$$r = \frac{(Z_0 - Z_s)\sin2\theta}{1 + [Z_s + (R_s - R_m)\tan\theta]/D_0} \tag{7.7}$$

$$Z_s = Z_0 - \frac{r}{\sin2\theta}\left[1 + \frac{R_s - r}{r + D_0\sin2\theta}\right] \tag{7.8}$$

and

$$Z_g = Z_0 + (R_s - R_g)\cot2\theta - \frac{r}{\sin2\theta}\left[1 + \frac{2R_s - R_g - r}{r + D_0\sin2\theta}\right] \tag{7.9}$$

If the optical arrangement is modified so that only rays parallel to its optical axis are utilized, in which case $\gamma = 0$, or if the distance D between the camera and the conical mirror is very large compared to the radius of the mirror so that γ is negligibly small,

then the terms containing D_0 in the denominator in the above relations vanish and they become linear to give

$$Z_s = Z_0 - r/\sin 2\theta \qquad \text{and} \qquad Z_g = Z_s + (R_s - R_g)\cot 2\theta.$$

The cylindrical co-ordinates (Z_g, φ) and (Z_s, φ) of the grid and shell surfaces are transformed into flat polar co-ordinates (r, φ) on the image plane. While there is no change in the angular co-ordinate φ, the relationships between r and Z_g, Z_s are given by eqns.7.7 to 7.9. The relation between the pitch p_c of the lines on the circumferential grid and that of the corresponding concentric circles (p_{ci}) on the image plane is obtained by differentiating the expression for Z_g with respect to r and neglecting the second order terms, as

$$p_c \,/\, p_{ci} = \frac{1}{\sin 2\theta}\left[\,1 + \frac{2R_s - R_g - 2r}{r + D_0 \sin 2\theta}\,\right]$$

The effect of the finite value of the distance D_0 is to increase the pitch of the concentric circles in the image plane with increasing radius. However if D_0 is very large, or if γ is equal to zero, then the two pitches are related by the constant term $\sin 2\theta$.

The lines on the axial grid appear as radial lines on the image plane whose pitch p_{ai} is a function of r and is related to the pitch P_a of the axial grid by

$$p_a \,/\, p_{ai} = R_g \,/\, r$$

Noting that the pitches in the axial and circumferential

directions of the lines on the spiral grid are respectively equal to $p_s/\cos\alpha$ and $p_s/\sin\alpha$, where p_s is the normal pitch of the spiral lines and α the helix angle; by using the transformations for the pitches in these two directions, the normal pitch p_{si} of the lines in the image of the spiral grid may be obtained as

$$p_s / p_{si} = \frac{1}{r \sin 2\theta} \sqrt{R_g^2 \sin^2(2\theta)\sin^2\alpha + \beta^2 r^2 \cos^2\alpha}$$

$$\text{where } \beta = \left[1 + \frac{2R_s - R_g - 2r}{r + D_0 \sin 2\theta}\right]$$

7.6 Maximum Shell and Grid Lengths

The maximum value of γ is given by $\gamma_{max} = \tan^{-1}(R_m/D)$. The minimum height of the shell and the corresponding minimum grid height are given by

$$Z_{smin} = (R_s - R_m)\cot(2\theta + \gamma_{max})$$

and

$$Z_{gmin} = (2R_s - R_m - R_g)\cot(2\theta + \gamma_{max})$$

Since the view from the camera is a diverging conical field, a small section of the conical mirror around the base of the grid is hidden from the view of the camera by the top of the grid. When the shell height is increased, the height of the grid also has to be correspondingly increased. While the former moves the image of the top section of the shell closer to the axis of the grid, the increase in the grid height obstructs a greater portion of the mirror around the

base of the grid from the view of the camera. Hence the maximum shell height and the corresponding height of the grid are obtained from the limiting condition that the rays illuminating the top section of the shell, after reflection from the circle of minimum radius (r_{min}) on the conical mirror, travel towards the camera along lines that are tangent to their points of incidence at the top of the grid (shown on the left hand side in Figure 7.7). The angle of convergence of these rays at the camera is the minimum value of γ (γ_{min}) ; hence we get

$$Tan\gamma_{min} = \frac{R_g}{D-Z_{gmax}} = \frac{r_{min}}{D_0+r_{min}tan\theta}$$

Substituting eqn.7.9 into these relations provides the values of r_{min} and γ_{min} and hence the values of Z_{smax} and Z_{gmax}, the maximum shell height and the corresponding grid height. The maximum length of the shell whose image can be seen through the optical system and the corresponding length required for the grid are then given by

$$L_s = Z_{smax} - Z_{smin} \quad \text{and} \quad L_g = Z_{gmax} - Z_{gmin}$$

If the effect of the convergence angle γ is ignored, then the maximum shell length depends only on the geometry of the conical mirror and the radius of the grid and is given by

$$L_s = L_g = (R_m - R_g)/sin2\theta$$

Thus longer shells can be accommodated by having flatter conical mirrors (smaller values of θ), which is another advantage of the

present optical setup. The effect of the finite distance between the camera and the conical mirror is to reduce the length of the shell that can be tested and to increase the required length of the grid by small amounts. For example, for a distance of D = 4267 mm (14 feet) the maximum length of the shell is reduced from 210 to 205 mm and the grid-length required is increased to 215 mm.

7.7 Use of the Optical System

The conical mirror provides a whole field view of the entire inner surface of the cylindrical shell reflecting the lines on the grid placed along the axis of the shell. When reflected by a perfectly cylindrical surface, the image of the grid in the plane mirror at the top of the loading frame appears as a regular pattern of smooth curves - circular, radial or spiral lines, depending on the grid employed. Any small deviation of the shell wall from its true cylindrical shape is immediately indicated by the distortion of the grid-lines in the image. In the course of the current experimental work it soon became apparent that a major source of imperfections (and hence lower load carrying capacity) is non-uniform geometry at the ends of the cylinder. Although very little elastic restraint is sufficient to produce high buckling loads for the perfect cylinder (as was shown by Almroth[12]), deviations from the cylindrical shape at the ends of the shell can be highly detrimental. This is all the more so for thin flexible shells (as those used in the current work) whose cylindrical shape is mainly maintained by the presence of the supports provided at the ends. Thus great care has to be taken in mounting the shell into

the end-rings, and in this regard the optical system incorporated in the experimental set up was extremely useful. The large number of high buckling loads obtained in the current testing program would not have been possible without such a sensitive system to facilitate the mounting of the shells. In spite of this facility, it may be added, it has not been possible to achieve perfect end conditions for all the shells tested. In many cases, although wrinkling at the edges or some other form of non-circularity was visible in the grid image, it could not be corrected. Some of the imperfections at the ends of the shells tested occurred during the setting of the Araldite mix in the grooves of the end-rings, while some others were caused by non-circularity of the end-rings themselves.

One of the main applications of the optical system has thus been to record the presence of initial imperfections in the shell. The location of the imperfection as well as its size, i.e., that of the area on the shell surface covered by the imperfection, could easily be gauged from the extent of the distortion of the lines in the recorded photographs. By taking photographs of the grid pattern at various intervals of loading it was possible to monitor the growth of these imperfections in the pre-buckling stage. It may be noted that the deformation in the facets of the buckled cylinder were so large that the shell surface no longer reflected the grid, hence these facets appeared as dark regions in the image plane.

The photographs in the pre-buckling stage were taken with all three grids employed one after another (some times in different

tests) in the optical system. This is because each grid, in general, is more sensitive to deformations normal to the orientation of its grid lines, so that not all imperfections show up to the same extent if only one particular grid is employed. For example, the axial grid is insensitive to axisymmetric deformations, while it is extremely sensitive to slope variations in the circumferential direction. Though the circumferential grid is sensitive to axisymmetric deformations, the variations in the pitch of its lines in the image caused by the bending deformations in the pre-buckling stage is hardly noticeable, whereas these axisymmetric deformations show up very well in the image of the spiral grid.

The optical system also facilitated photographic recording of the buckle patterns over the entire surface of the collapsed shell. From these photographs the number of facets around the circumference as well as the size and regularity of the facets could be noted. Photographs taken at various stages of loading and unloading in the collapsed condition provided measurements of the variations in the aspect ratio of the facets.

In the tests conducted on the shells with imposed defects photographs of the shell were taken in the unloaded condition for the precise measurement of the size of the defects, and subsequently at various stages of end-shortening in the pre-buckling stage to record the growth of the defects and the deformations of the shell surface in the vicinity of the imposed defect. The frequent partial collapse of these cylinders precipitated by the formation of facets in the regions

adjacent to the imposed defect and the development of the complete buckle pattern by the formation of additional facets by subsequent collapses could also be recorded.

The optical system was thus extremely useful in observing and recording the presence and growth of imperfections as well as imposed defects, the geometry of the buckled configuration of the shell and the changes produced in it by continued end-shortening in the post-buckling regime. On an average about fifty photographs were taken for each of the shells tested, covering its complete loading history, from the unloaded state to the advanced post-buckling stage, without and with the imposed defects. The axial compression tests on these shells conducted before imposing the defects are discussed in the next chapter. The introduction of the defects and the results of the ensuing tests are presented in Chapter 9.

7.8 Moiré Application of the Optical System

In the experimental work on axially compressed cylindrical shells the optical system has been employed only as a grid reflection technique. The presence of local deformations and the extent of their spread on the surface of the shell could readily be gauged in this case from the distortion of the grid lines in the image plane. For the measurement of the actual magnitudes of the radial deformations in a cylindrical shell, however, it would often be more convenient to employ the system as a photo-reflective moiré technique. The moiré fringes, obtained by the superposition of the images of the grid

reflected by the deformed and the undeformed shell surfaces, represent contours of constant changes in slope on the shell surface, and can hence readily be employed to determine the radial deformations of the shell wall. The development of the theory for the moiré application of the optical system as well as its verification by means of experiments performed on a cylinder subjected to rigid body rotation is presented in Appendix B. Practical application of this moiré method to shell bending problems is also illustrated by determining the deflections of a cantilevered cylindrical shell subjected to a concentrated lateral load at the free end.

NOTATIONS

D : Distance of the camera from the base of the conical mirror

D_0 = $D - R_m \tan(\theta)$

L_s : Maximum shell height

L_g : Length of the grid required for a shell of length L_s

p_a : Pitch of the lines on the axial grid (= 1.206 mm)

p_c : Pitch of the lines on the circumferential grid (= 5.85 mm)

p_s : Normal pitch of the lines on the spiral grid (= 1.184 mm)

p_{ai} : Pitch of the lines on the image of the axial grid

p_{ci} : Pitch of the lines on the image of the circumferential grid

p_{si} : Pitch of the lines on the image of the spiral grid

R_g : Radius of the cylindrical grids (= 9.6 mm)

R_m : Base radius of the conical mirror (= 74.5 mm)

R_s : Inner radius of the shell

r : Radial distance of the point of reflection on the conical mirror

Z_g : Height of the incident point on the grid from the base of conical mirror

Z_s : Height of the point of reflection on the shell from the base of the conical mirror

Z_0 : Theoretical maximum height for the shell that can be viewed in the conical mirror (eqn.7.3)

α : Helix angle of the lines on the spiral grid (= 79°)

φ : Angular Displacement

γ : convergence angle of the ray arriving at the camera

θ : Base angle of the conical mirror (= 9°)

CHAPTER 8

TESTS ON SHELLS BEFORE INTRODUCING DEFECTS

Axial compression tests were carried out on forty six epoxy shells manufactured and mounted into end-rings as described in Chapter 7. Typical buckling and post-buckling behaviour of two good shells is illustrated in Figures 8.1 and 8.2. The ordinate of the plots is the ratio of the axial load to the classical load and the abscissa is the non-dimensional value of the end-shortening given by $\Delta = 10^4 \delta L/R^2$. In each figure the load deflection plots from different tests conducted on the particular shell are superposed to provide a comprehensive view. In successive tests the shell was allowed to undergo one collapse more than in the previous test before unloading was done so as to obtain the loading and unloading paths corresponding to each of the modes observed in either shell. It may be noted that the pre-buckling paths are quite linear and from their slopes the modulus of elasticity of the shells could be easily determined. The initial tensile value of the axial load (due to the weight of the lower end-ring as explained in Chapter 7) is indicated in the figures as η_t. The primary buckling loads observed in different tests on each shell are very close (the pre-buckling paths practically overlap each other and are hence not shown independently) except for one test in which the shell S4 (Figure 8.2) buckled at a lower load forming 13 facets around the circumference. It may be observed that the secondary buckling loads obtained as well as the post-buckling paths followed in different tests are also reasonably consistent. Of particular interest

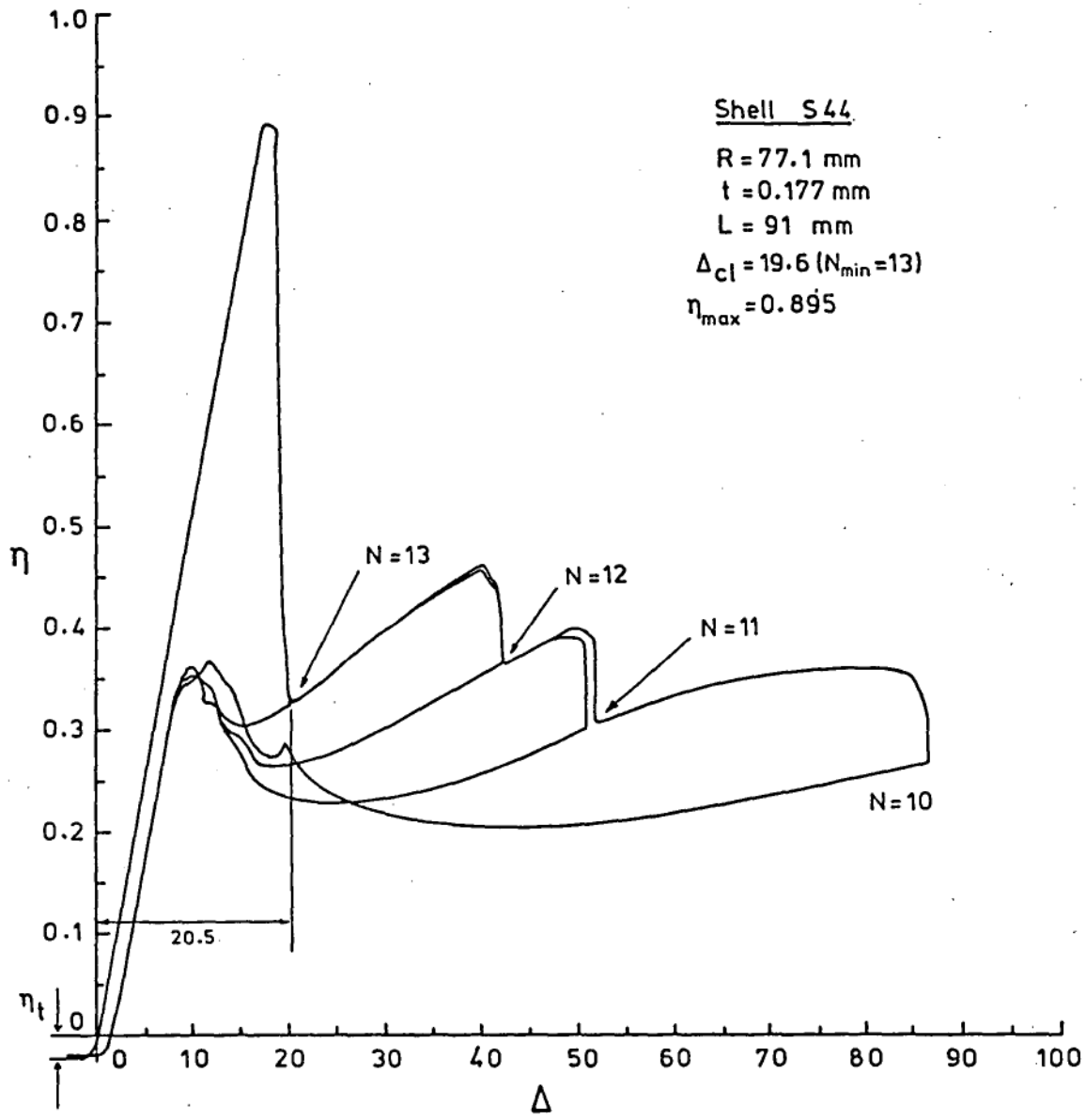

Figure 8.1
Load Deflection Diagram for Test Shell S44

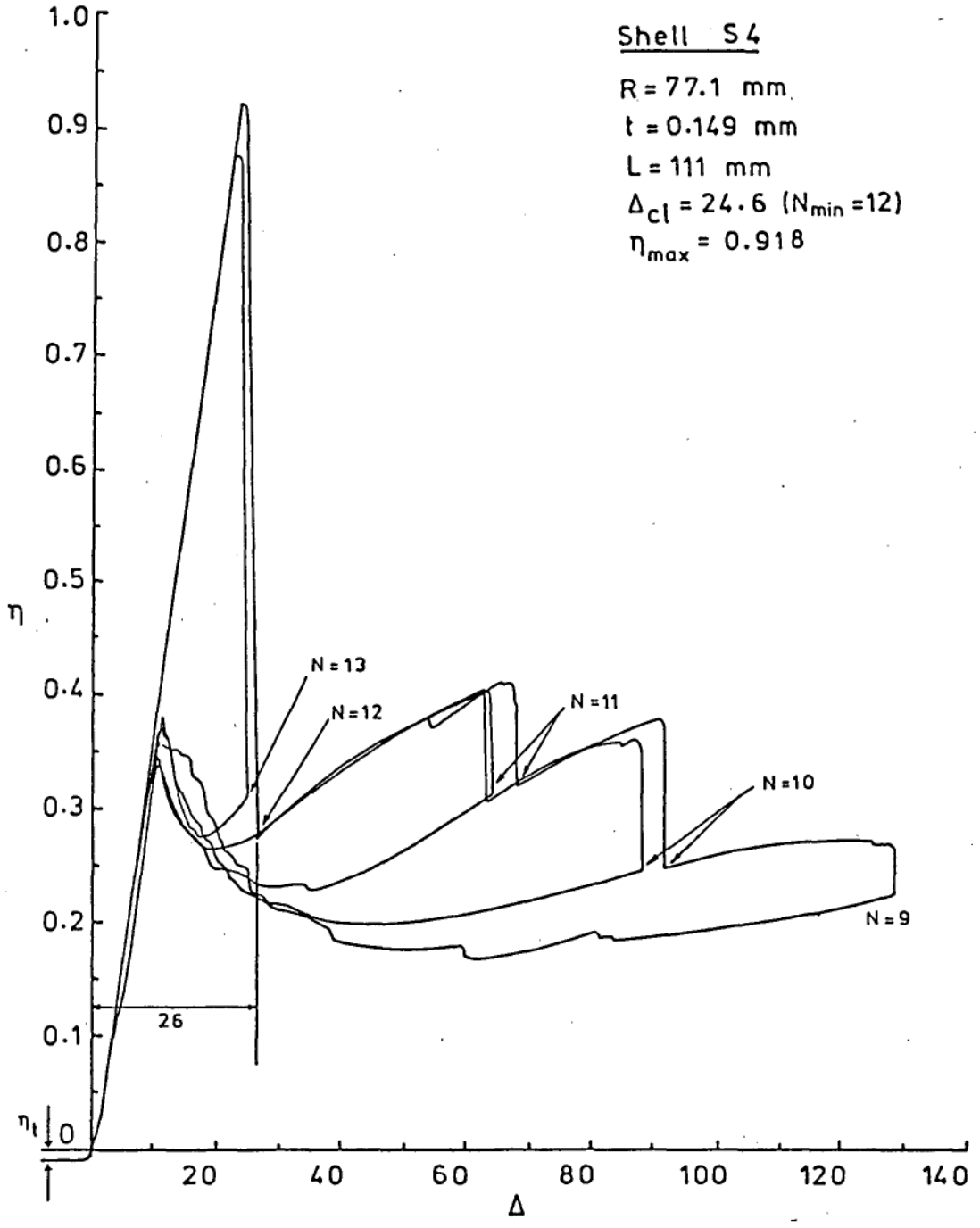

Figure 8.2
Load Deflection Diagram for Test Shell S4

is the fact that return paths of the secondary collapse modes in both cases (except for that of N = 12 in shell S44) have negative slopes at the value of end-shortening corresponding to the stable post-buckling state after primary collapse, indicating that these modes are unstable at that stage. This could be attributed to the geometrical constraints restricting the full development of the facets in buckle patterns with values of N lower than the N_{min}, as observed in chapter 6; although it is to be noted that the geometric relations, which do not consider the bending effects, can indicate the stability limits only approximately.

The geometric data of the shells tested is presented in Table 8.1. The shells are numbered in the chronological order in which they were tested, i.e., shell S1 was tested first and S46 was tested last. The radius to thickness ratios vary from about 200 to 600 and length to radius ratios from 0.93 to about 2.5. The Batdorf parameter Z ranges between 230 and 2800. The parameter $(R/L)^{1/2}(R/t)^{1/4}$ which determines the number of facets formed on primary collapse is given in the last column. The maximum deviation of the wall thickness from its average value is tabulated in the fourth column. Except for four shells - S1, S5, S21 and S28 - the deviation in wall thickness is limited to 5%; nearly two-thirds of all the shells tested had a thickness uniformity of within 2%. The first shell S1 which had 25% variation in thickness was tested merely as a trial run to test the apparatus. Shell S5 had uniform thickness elsewhere except for one region where a local thinning occurred resulting in a small hole at the centre. This shell was tested just out of curiosity, to see what effect such an imperfection would have on the buckling behaviour.

Table 8.1 Geometric Data of Shells Tested

Shell	R(mm)	t(mm)	Max. ($\Delta t/t$)	L(mm)	L/R	R/t	Z	$\left[\frac{R}{L}\right]^{\frac{1}{2}}\left[\frac{R}{t}\right]^{\frac{1}{4}}$
S1	77.12	0.152	25%	166	2.15	507	2211	3.24
S2	77.11	0.148	1.5%	167	2.17	521	2298	3.24
S3	77.07	0.147	1.0%	176	2.28	524	2571	3.17
S4	77.09	0.149	1.0%	111	1.44	517	1009	3.97
S5	77.11	0.179	*1.0%	142	1.84	431	1374	3.36
S6	77.05	0.148	1.5%	100	1.30	521	825	4.19
S7	77.07	0.187	1.0%	191	2.48	412	2381	2.86
S8	77.10	0.138	1.5%	166	2.15	559	2435	3.32
S9	77.03	0.158	2.0%	153	1.99	488	1809	3.33
S10	77.06	0.170	1.5%	131.5	1.71	453	1241	3.53
S11	77.05	0.167	1.5%	153.5	1.99	461	1722	3.28
S12	77.09	0.188	1.5%	160	2.08	410	1661	3.12
S13	77.06	0.158	1.0%	161.5	2.10	488	2015	3.24
S14	77.08	0.159	5.0%	101	1.31	485	783	4.10
S15	77.08	0.167	3.0%	104	1.35	462	790	3.99
S16	77.12	0.181	4.5%	114	1.48	426	876	3.73
S17	77.10	0.148	5.0%	112	1.45	521	1034	3.97
S18	77.13	0.243	2.0%	191	2.48	317	1830	2.68
S19	77.16	0.339	1.0%	190	2.46	228	1298	2.48
S20	77.08	0.189	2.5%	152	1.97	408	1491	3.20
S21	77.09	0.130	9.5%	80	1.04	593	601	4.84
S22	77.13	0.240	2.0%	155	2.01	321	1221	2.99
S23	77.11	0.188	3.0%	158	2.05	410	1619	3.14

*Thickness uniform within 1% except in one localized region in Shell S5.

Table 8.1 Geometric Data (Continued)

Shell	R(mm)	t(mm)	Max. ($\Delta t/t$)	L(mm)	L/R	R/t	Z	$\left[\frac{R}{L}\right]^{\frac{1}{2}}\left[\frac{R}{t}\right]^{\frac{1}{4}}$
S24	77.16	0.288	2.0%	157.5	2.04	268	1050	2.83
S25	77.24	0.390	1.5%	86.5	1.12	198	234	3.54
S26	77.24	0.389	1.0%	89	1.15	199	248	3.50
S27	77.09	0.177	3.5%	101	1.31	436	703	3.99
S28	77.13	0.132	6.0%	162.5	2.11	584	2439	3.38
S29	77.09	0.149	1.5%	157	2.04	517	2018	3.34
S30	77.10	0.129	1.0%	90.5	1.17	598	774	4.57
S31	77.10	0.133	2.5%	72	0.93	580	475	5.09
S32	77.10	0.151	3.5%	152.5	1.98	511	1879	3.38
S33	77.11	0.160	4.0%	191	2.48	482	2781	2.98
S34	77.17	0.288	1.5%	139	1.80	268	818	3.02
S35	77.18	0.312	1.5%	157	2.03	247	963	2.78
S36	77.21	0.385	1.5%	156.5	2.03	201	775	2.64
S37	77.09	0.170	1.5%	142	1.84	453	1447	3.40
S38	77.10	0.190	1.0%	124	1.61	406	987	3.54
S39	77.16	0.261	1.5%	121.5	1.57	296	689	3.31
S40	77.14	0.218	1.5%	77	1.00	354	332	4.34
S41	77.20	0.339	1.5%	190	2.46	228	1297	2.48
S42	77.14	0.217	1.0%	76	0.99	356	325	4.37
S43	77.21	0.363	1.5%	178.5	2.31	213	1069	2.51
S44	77.11	0.177	3.5%	91	1.18	436	571	4.21
S45	77.08	0.190	3.0%	157	2.04	406	1583	3.14
S46	77.18	0.366	3.0%	140	1.81	211	653	2.83

8.1 Primary Collapse

The observed primary critical loads are plotted in Figure 8.3 and the numerical data presented in Tables 8.2a and 8.2b. (The numerical data of all the tests including the secondary collapse values is assembled in Table C1 in Appendix C). The shells have been classified into four groups, A, B, C and D, on the basis of their performance. The first group A consists of shells that may be called near-perfect; the shells in this category reached within 13% of the classical load, that is within 5% of the theoretical buckling load ($0.92*P_{cl}$) for shells with clamped end constraints. Most of these shells had very little variation in wall thickness and only minor imperfections were detectable from the reflection of the grid-lines. The shells in group B are reasonably good shells which attained buckling loads between 85 and 75% of the classical load and developed complete two tier patterns on collapse. Most of the shells in group C also reached maximum loads close to those in group B (above 70% of the classical load). However the primary collapses in these shells were only partial, that is the buckles were formed only over a part of the circumference; complete two tier patterns were realized only in subsequent collapses. Hence the shells in Group C are not considered as good as those in Group B, although their performance may still be considered acceptable. The poor quality shells are classified as Group D; their critical loads range between 55 and 71% of the classical load. An effort has been made to indicate the nature of the initial imperfection observed on each of the shells in the last columns of the tables 8.2; a more detailed description of the imperfections will be

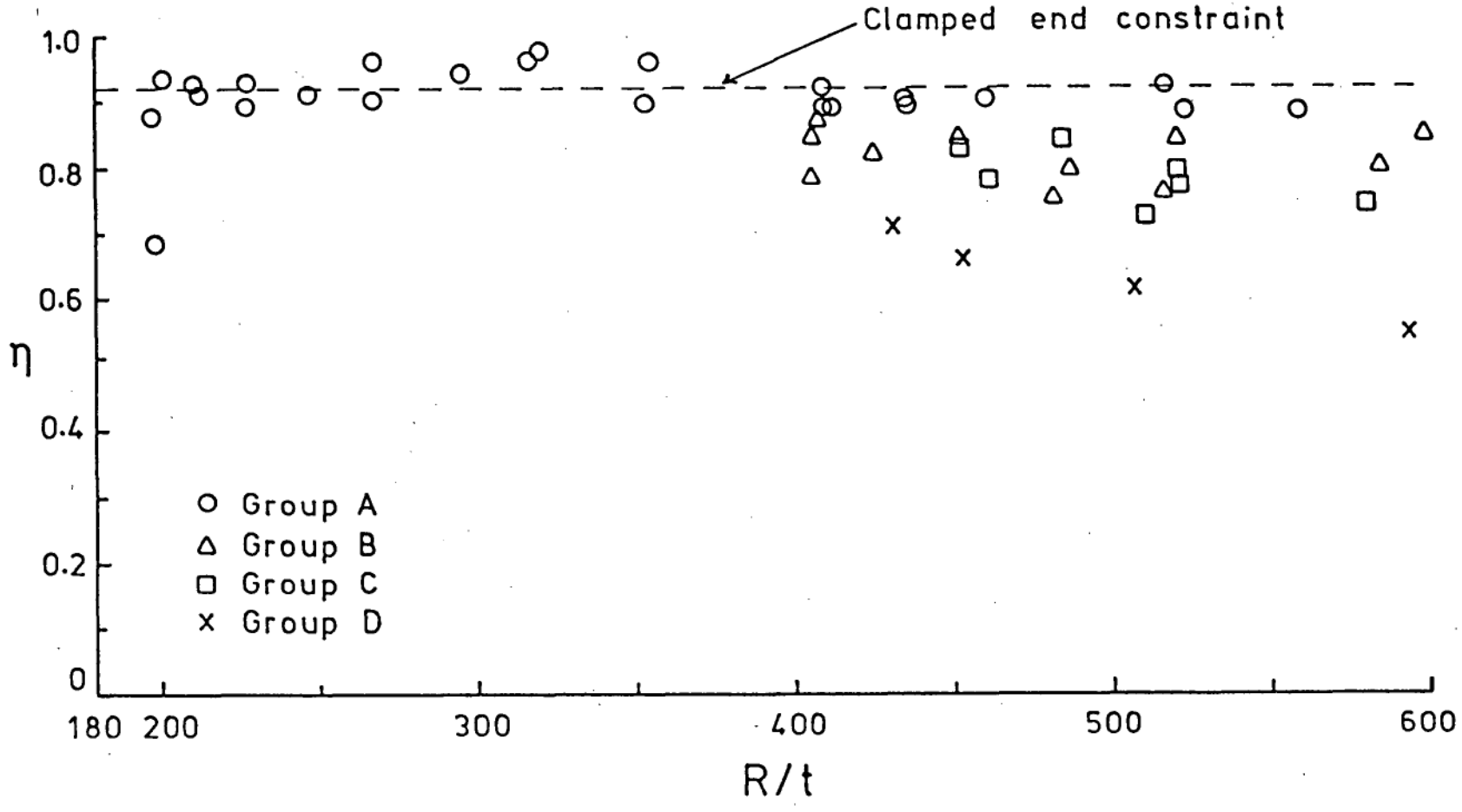

Figure 8.3
Observed Primary Buckling Loads

Table 8.2a Primary Buckling Data (Group A)

Sr. No.	Shell	Max. $\Delta t/t$	E(Gpa)	P_{cr}/P_{cl}	N	Remarks
1	S3	1.0%	3.12	0.883	10	
2	S4	1.0%	3.17	0.918	12	
3	S7	1.0%	3.20	0.887	10	Wrinkling along the periphery
4	S8	1.5%	3.05	0.879	11	
5	S11	1.5%	3.10	0.902	10	
6	S12	1.5%	2.91	0.916	10	
7	S18	2.0%	3.02	0.958	8	
8	S19	1.0%	2.91	0.926	8	
9	S22	2.0%	3.12	0.975	9	
10	S23	3.0%	3.14	0.890	10	
11	S24	2.0%	2.98	0.964	8	
12	S25	1.5%	3.05	0.874	10	
13	S27	3.5%	2.98	0.902	13	
14	S34	1.5%	2.89	0.902	9	
15	S35	1.5%	2.97	0.910	9	
16	S36	1.5%	2.90	0.936	8	
17	S39	1.5%	2.98	0.938	10	
18	S40	1.5%	3.00	0.907	13	
19	S41	1.5%	2.91	0.892	8	
20	S42	1.0%	3.04	0.960	13	
21	S43	1.5%	3.13	0.908	8	
22	S44	3.5%	3.07	0.895	13	
23	S46	3.0%	2.86	0.927	9	
24	S26	1.0%	3.05	0.687	I-8p	Tilted due to epoxy overflow

Note: All observed modes were complete two tier patterns except those indicated otherwise. p - partial ; I - one tier.

Table 8.2b Primary Buckling Data (Groups B,C and D)

Group	Sr. No.	Shell	Max. $\Delta t/t$	E(Gpa)	P_{cr}/P_{cl}	N	Remarks
B	1	S20	2.5%	3.00	0.867	11	Minor Imperfections
B	2	S30	1.0%	3.19	0.849	15	Minor Imperfections
B	3	S37	1.5%	3.17	0.840	11	Minor Imperfections
B	4	S45	3.0%	3.12	0.845	11	No detectable imperfections
B	5	S2	1.5%	2.98	0.837	12	Localized bulging at one end
B	6	S13	1.0%	2.98	0.797	11	Ends out of round
B	7	S16	4.5%	3.05	0.822	12	Localized bulging at one end
B	8	S28	6.0%	3.11	0.801	11	Localized bulging at one end
B	9	S29	1.5%	3.21	0.763	12	Localized bulging at one end
B	10	S33	4.0%	3.18	0.747	11	Wrinkling along the periphery
B	11	S38	1.0%	3.25	0.785	12	Slight bulge at one end
C	1	S6	1.5%	3.12	0.793	13p	Slightly twisted fixing
C	2	S10	1.5%	2.99	0.827	11p	End-ring improperly seated
C	3	S14	5.0%	2.96	0.837	12p	Ends out of round
C	4	S15	3.0%	3.01	0.784	12p	Ends out of round
C	5	S17	5.0%	3.18	0.774	13p	Localized bulging at one end
C	6	S31	2.5%	3.03	0.737	14p	Localized bulging at one end
C	7	S32	3.5%	3.25	0.719	12p	Ends out of round
D	1	S1	25%	3.05	0.614	I12p	Loading plates not parallel
D	2	S5	1.0%	3.14	0.710	I-9p	Local thinning with a hole
D	3	S9	2.0%	2.95	0.661	10p	End-ring slightly damaged
D	4	S21	9.5%	3.05	0.552	13p	Localized bulges on one side

presented later. It may be observed from Figure 8.3 that the shells in the last three groups are confined to the upper half of the range of R/t, although the group A shells cover the whole range. It is thus evident that as the shells become thinner they are more likely to have imperfections, those which arise from end fixity as well as those due to thickness variations, although with sufficient care either may be avoided. There is one exception in Group A which is the last shell listed, namely S26. This particular shell collapsed at about 69% of the classical load forming only one tier buckles over a part of the circumference. The reason for this poor performance was discovered only later, after the shell was removed and the defect introduced in it. A thin film of epoxy (about 0.1 mm thick) was found stuck under the bottom end-ring, the material from the groove in the mounted end-ring having overflowed and trickled over the edge overnight. When this film of epoxy was removed the shell was found to perform very well (the knockdown factor with the imposed defect was 0.72). For this reason it is included in group A and its modulus of elasticity assumed to be the average of the values measured for all the other shells*.

The moduli of elasticity of the shells have been estimated from the linear pre-buckling paths of the load end-shortening plots. The value presented for each shell in Tables 8.2 is the average of the values obtained in a series of five or six tests, these values all being within 2 to 3% agreement in all cases. Values of the modulus of elasticity of the shell material measured from tensile tests on cast rectangular specimens earlier showed 10 to 15% variation. It was

* For the purpose of calculations in the next chapter, the initial knockdown factor for this shell (S26) has been assumed as 0.91.

therefore decided that measurements from the axial compression tests on each individual shell would be more reliable, and hence this method was adopted. It may be observed that the measured values of the modulus of elasticity range between +6% and -6% of the average value of 3.05 Gpa, which may be due to the variations in the curing periods and pre-heating temperatures employed in casting the shells. The tabulated values of E and the value of 0.34 for the Poisson's ratio - which was determined from the tensile tests - have been used to evaluate the classical buckling load and hence the knock-down factors of the shells tested.

8.2 Observed Imperfections

Variations in wall thickness, eccentricity in loading and deviations of the shell wall from the true cylindrical shape are three common forms of imperfections that can drastically reduce the load carrying capacity of the axially loaded cylinder. The first of these, which occurs during the manufacturing stage was carefully monitored by taking measurements of the wall thickness over the entire length and circumference of the shell before it was mounted. The testing machine was designed and manufactured with great care in order to eliminate all possibilities of misalignment and eccentricity in loading. Still when the first shell was mounted, with the end-ring at the top fastened to the loading plate, its axis was seen to be slightly tilted indicating that the platens were not exactly parallel. Careful height measurements revealed that the loading plate was tilted with respect to the base by about 0.2°. Re-adjustment of the lengths of the loading

pins reduced this tilt to about 0.025° which appeared satisfactory, since the remaining misalignment could easily be taken care of during the mounting of the end-rings.

Other than the first shell, only two shells appear to have suffered from any eccentricity in loading due to incomplete contact between the end-rings and the platens. The first of these, shell S10, was mounted on a new pair of end-rings, the top one of which was found (after the initial tests) to be a bit too large to be properly seated into the spigot in the loading plate. The second shell S26, was tilted due to a thin film of epoxy resin under the bottom ring as mentioned earlier. The fact that when this was rectified, the shell attained a higher buckling load even with a defect extending over a ninth of the circumference imposed on it indicates the sensitivity of the shell to non-uniform end-loading conditions.

Imperfections in the form of geometric deviations from the true cylindrical shape occur in thin shells - such as the ones tested - mainly from non-uniformities in the end conditions, that is, from imperfect mounting of the shell into the end-rings. The majority of the imperfections in the shells tested arose from this source, and while being most difficult to avoid, were mainly detected only due to the availability of the optical system employed. Although due to the sensitivity of the system some deviation of the reflected grid-lines could be observed in almost all the shells tested, the imperfections in most of the shells in group A were very small and confined only to the very edges of the shells.

Local imperfections due to end-fixity appear to arise mainly from the shell being a little loosely fitted on the guide spigot of the end-ring. This causes a small segment of the shell end to bulge out or wrinkle up in one local spot when the epoxy sets. Examples of such localized imperfections due to end-fitting are shown in Figure 8.4. The first figure 8.4a is that of shell S27 (Group A) in which the imperfection is confined to a small region close to the end at the 11 o'clock position. In shell S28 (Group B) shown in Figure 8.4b, the imperfection extends nearly over the whole length between the 11 and 12 o'clock positions. A small localized wrinkle can also be observed at the opposite end. The deformations due to end-fixity appear to be quite small in the unloaded photograph of Shell S6 of Group C (Figure 8.4c); however neighbouring wrinkles at the top and bottom ends give rise to a twisting effect which is very noticeable (at the 10 o'clock position) in the loaded photograph in Figure 8.4d. The local bulges seen in the last photograph (8.4e) along with the 9% variation in the wall thickness of shell S21 (Group D) caused it to fail at the lowest critical load ($0.55*P_{cl}$) obtained in the current testing program.

Figure 8.5a (shell S14) is an example of the ends becoming out of round causing overall deviations of the shell wall from its true cylindrical shape. Loose-fitting of the shell on the guide spigot of the end-ring some times gives rise to this type of imperfection instead of the local effects seen previously, although it is suspected that at least in some cases the non-circularity was caused by the end-ring itself being out of round. The distortion of the end-ring as well as the reduction in the diameter of the guide spigot resulting in

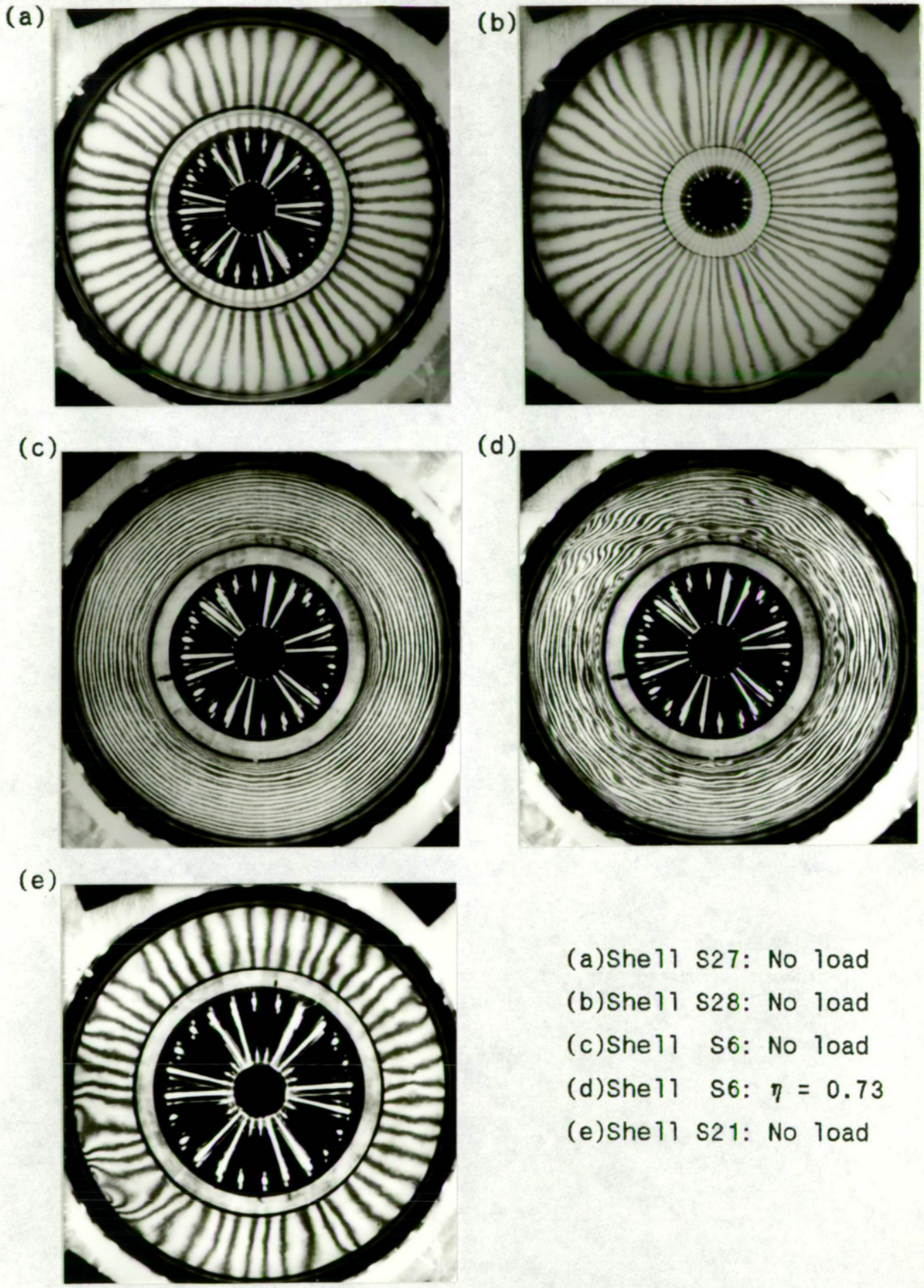

(a)Shell S27: No load
(b)Shell S28: No load
(c)Shell S6: No load
(d)Shell S6: η = 0.73
(e)Shell S21: No load

Figure 8.4. Local Imperfections due to Non-Uniform End-Fixity

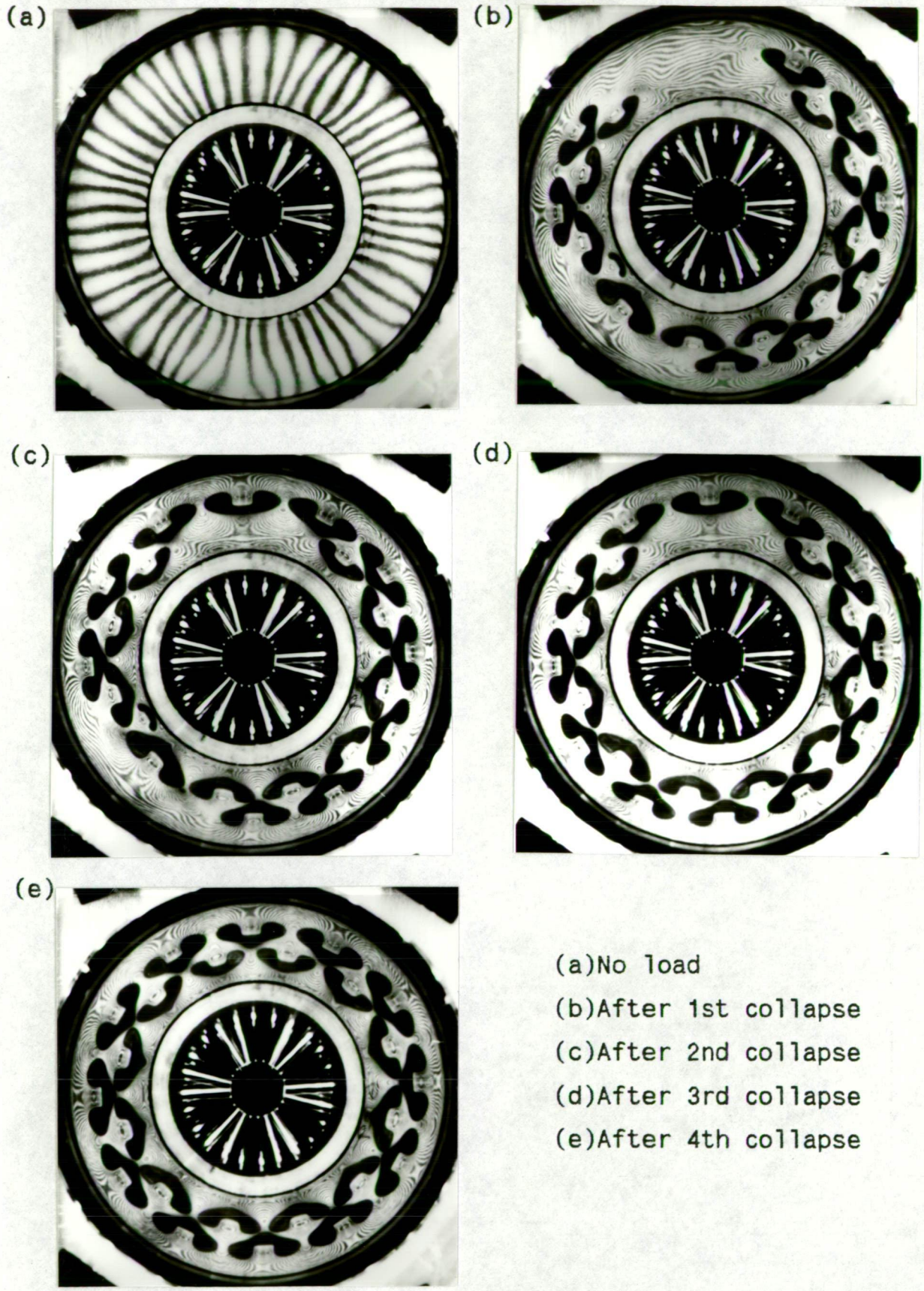

Figure 8.5. Effect of Non-Circularity at the ends (Shell S14)

a loose fit were both caused by repeated machining of the grooves of the end-rings on the lathe to remove the set epoxy. The partial pattern formed on primary collapse and the completion of the two tier pattern by subsequent collapses of the shell S14 are shown in the remaining photographs of Figure 8.5. The deformations seen at about the 9 o'clock position near the inner ring in Figure 8.6a were caused by an accidental dent - smaller than the size of a pin-head - on the guide spigot of the end-ring. The growth of the deformations in this region due to loading can be seen in the second photograph which eventually caused the shell to collapse prematurely forming one tier buckles in the same region. The two tier facets formed (in subsequent collapses) on the opposite side (Figure 8.6d) completing the buckle pattern indicate that had it not been for this imperfection shell S9 would have developed a two tier pattern. The photographs in Figure 8.7 are of shell S5 which had a thin region (extending over an eighth of the circumference and about a third of the length of the shell) with a small hole (nearly 1 mm in diameter) in the centre. The growth of the deformations around this hole (at the 6 o'clock position in the photographs) which led to the formation of a partial one tier pattern as well as the development of the complete pattern on subsequent collapses are also shown. The second collapse occurred when photograph 8.7c was being taken and shows the formation of the adjacent facets.

There is one more type of initial deformation which occurs during the shell mounting that is worth mentioning. This is a sort of wrinkling of the shell wall near the end-ring which occurs all around the circumference. Significant deformations of this type were noticed

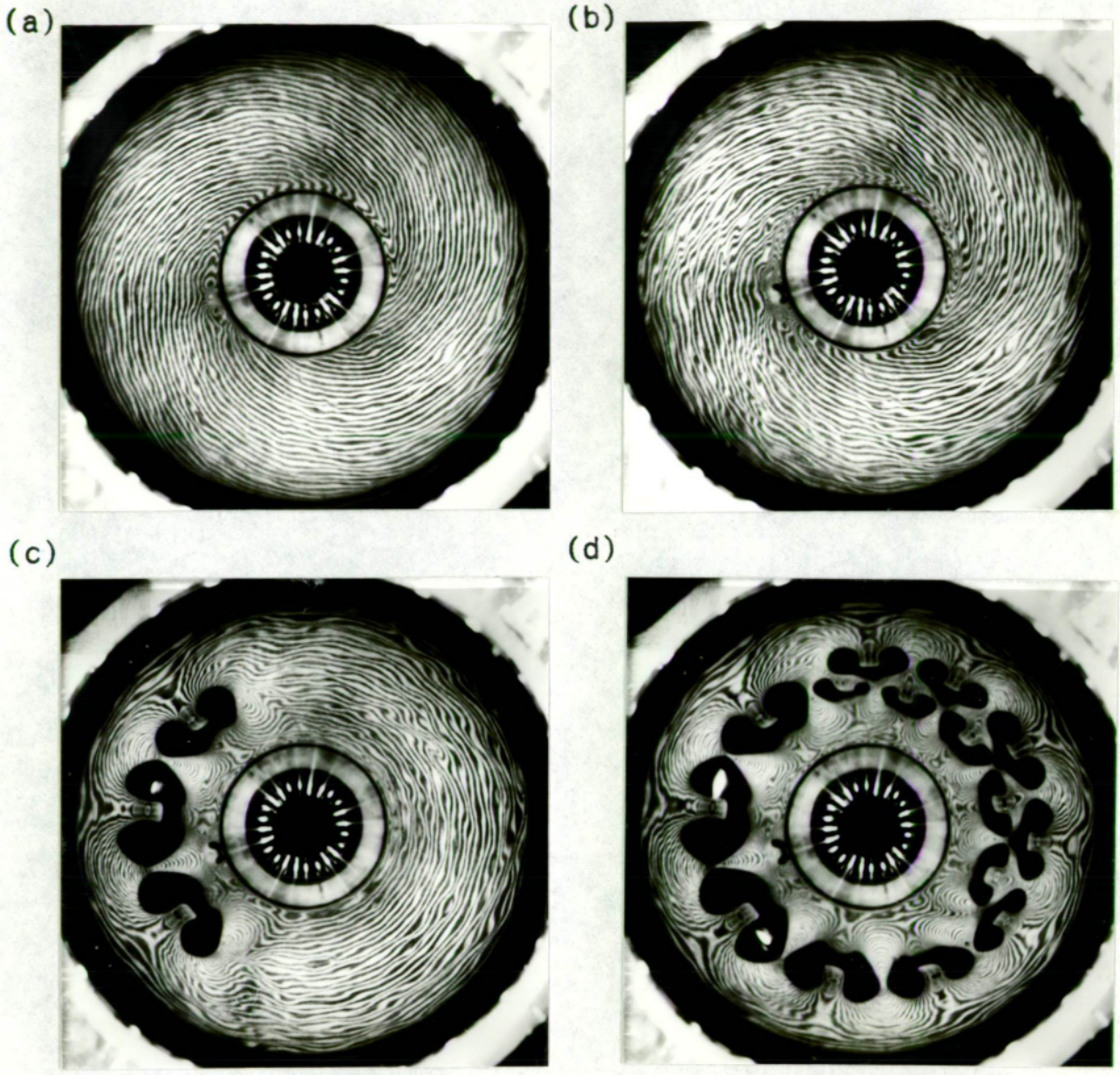

(a)No load

(b)Loaded (η = 0.532)

(c)After 1st collapse

(d)After three partial collapses

Figure 8.6. Deformations Caused by a Dent in the End-Ring (Shell S9)

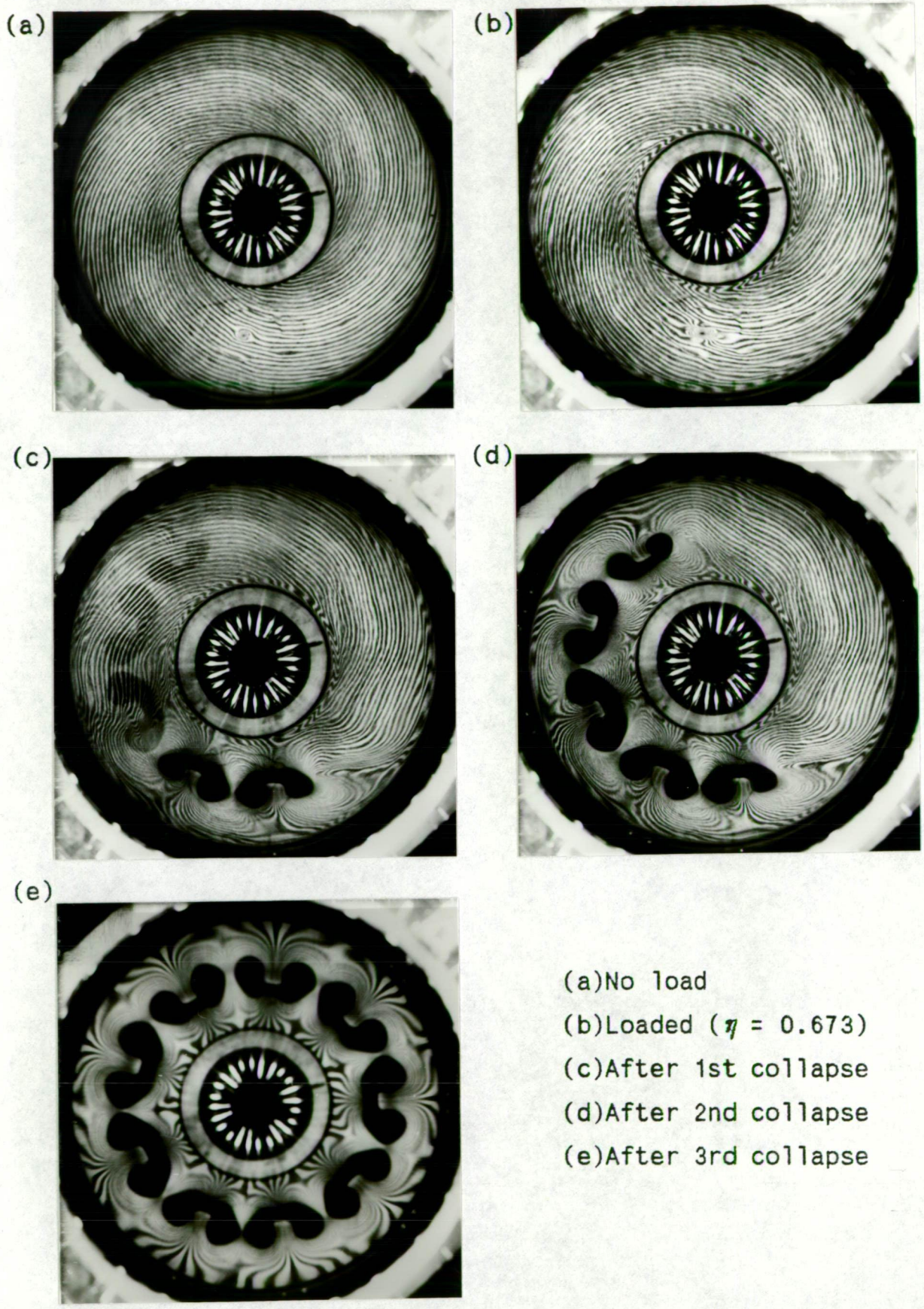

Figure 8.7. Effect of Local Thinning of the Shell Wall (Shell S5)

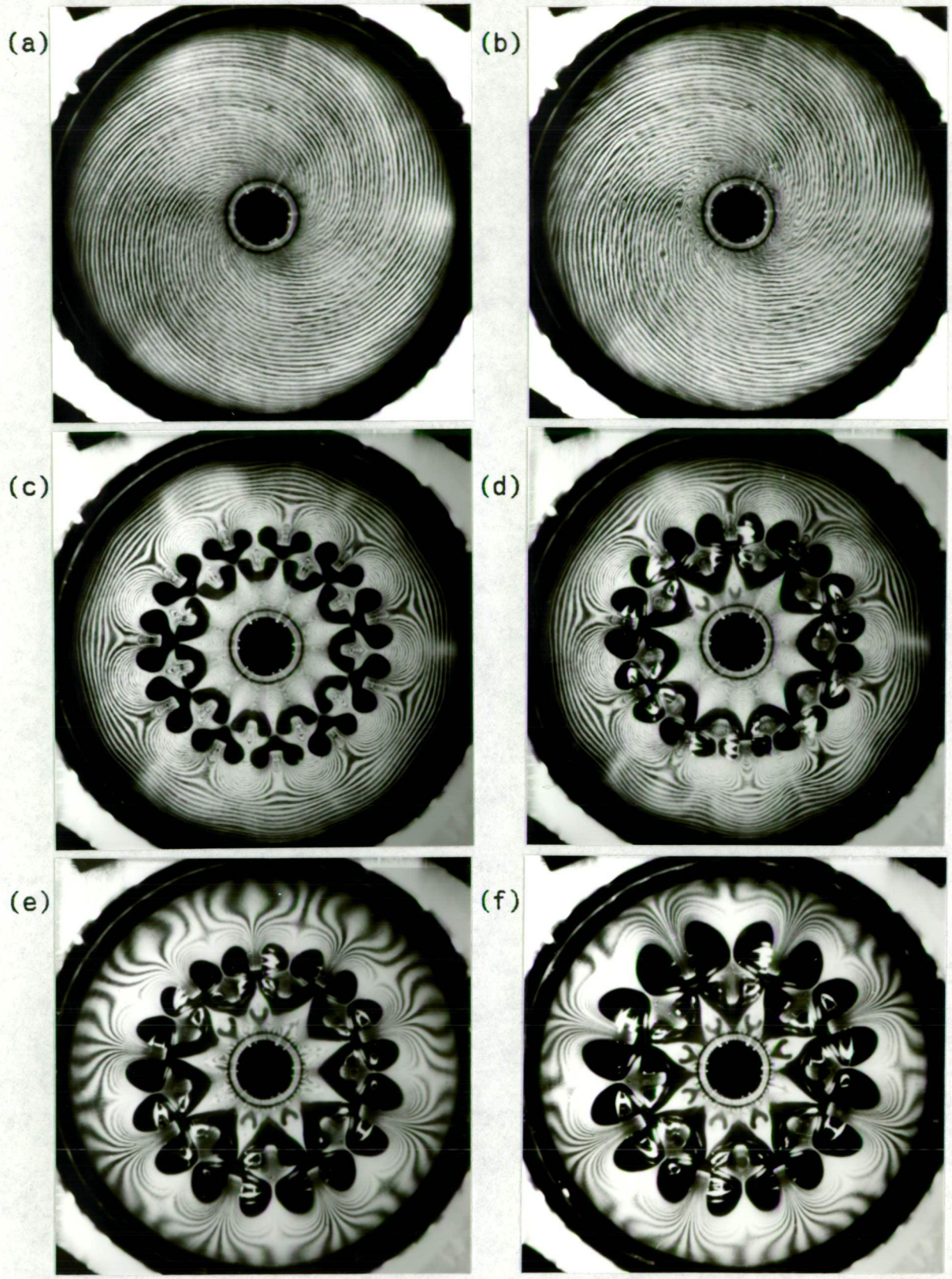

(a)No load (b)Loaded: η = 0.613 (c)Primary Mode (N = 11)
Secondary Modes : (d) N = 10 (e) N = 9 (f) N = 8

Figure 8.8. Displaced Buckle Formation due to Wrinkling along the Periphery (Shell S33)

in two of the shells tested, S7 and S33; the unloaded photograph of the latter is shown in Figure 8.8a. It appears that this imperfection, which probably occurs in the process of curing of the epoxy mix in the end-ring, does not cause a drastic reduction in the buckling load; it however causes the buckle pattern to occur closer to the affected end of the shell. It can be seen from Figures 8.8c to 8.8f that the primary buckling mode (N = 11) and the secondary buckling modes (N = 10 to 8) have all formed towards the upper half of the shell. The formation of small additional buckles above the two tier patterns of the secondary modes is also noteworthy.

8.3 Pre-Buckling Deformations due to End Restraint

The optical system employed, particularly the spiral grid, was extremely useful in observing the growth of the pre-buckling deformations caused by clamped end constraints. These deformations being essentially axisymmetric did not cause any distortions of the lines of the axial grid and caused only small changes in the pitch of the concentric circles in the image of the circumferential grid which could be noticed only on close inspection. However, in the images of the spiral grid the effect of pre-buckling deformations was readily noticeable as may be seen from the photographs shown in Figure 8.9. The first three photographs in the figure are of shell S24, the first one (8.9a) in the unloaded condition, the second and the third with loads equal to 52% and 84% of the classical load respectively. The growth of the pre-buckling bending deformations is clearly observable at both ends of the shell in the photographs 8.9b and 8.9c. It may be

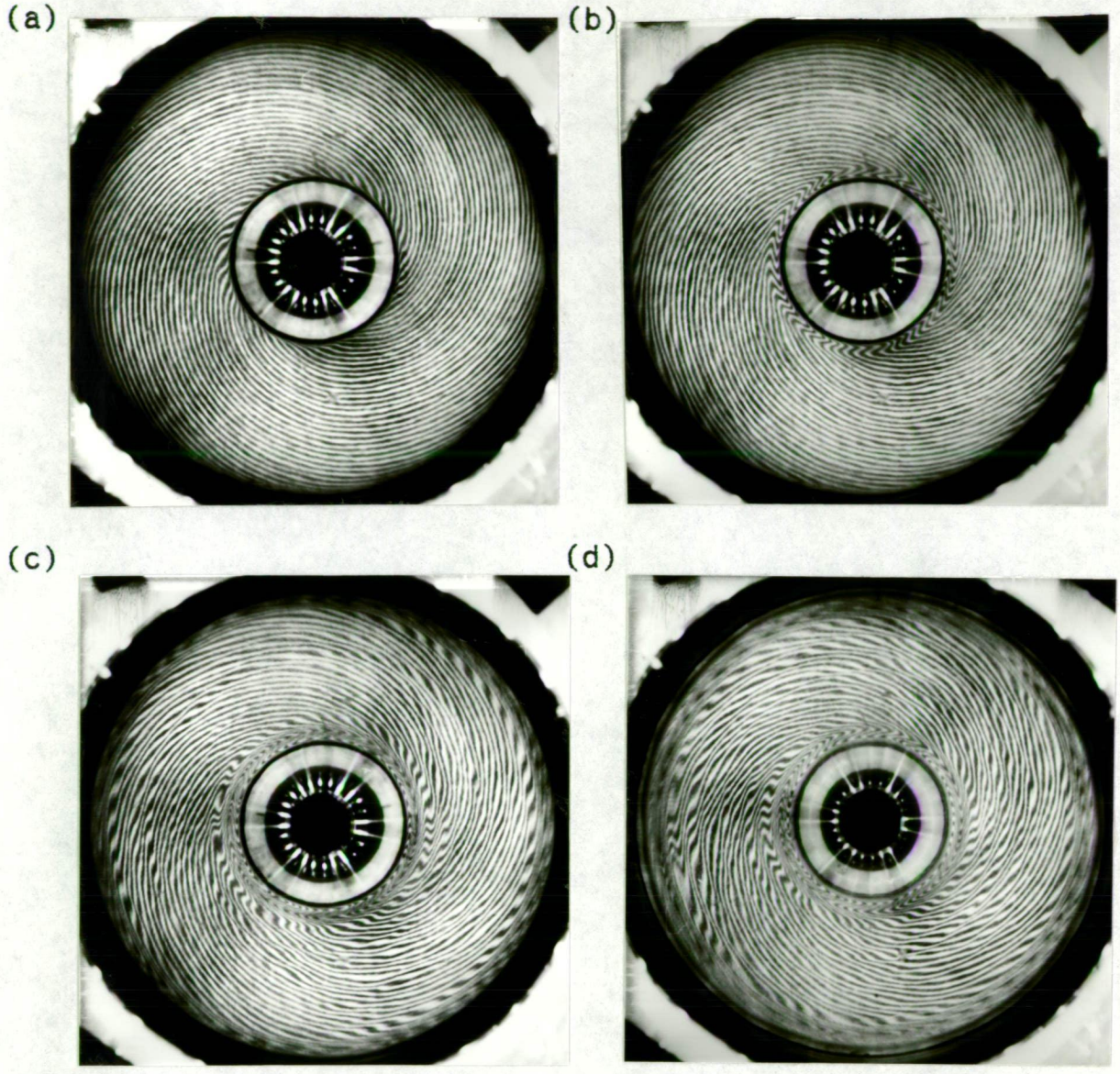

(a) Shell S24 : No load

(b) Shell S24 : Loaded (η = 0.52)

(c) Shell S24 : Loaded (η = 0.84)

(d) Shell S35 : Loaded (η = 0.85)

Figure 8.9
Pre-Buckling Deformations due to End Restraint

observed that although the spiral lines at the upper end (the inner ring) of the unloaded shell show some deviation, this is very little, and quite unlike the wrinkling at the periphery of shell S33 seen in Figure 8.8a. The photograph 8.9d is that of shell S35 loaded up to 85% of the classical load (the buckling load for this shell was $0.91*P_{cl}$). The axisymmetric bending deformations which are quite pronounced at the ends, can be seen to extend over the whole length of the shell, the spiral lines alternatively widening and closing in to produce bands of wide spaced spirals separated by thin apparently circular lines (these circles consist of segments of different spiral lines). While no special effort was made to record this phenomenon, it was found that the photographs taken in the advanced pre-buckling stages of nine of the thicker shells showed such axisymmetric deformations extending over the whole length of the cylinder.

The photograph of another shell, S34, with pre-buckling deformations extending over the whole length at a load of $0.735*P_{cl}$ is shown on the left in Figure 8.10. The shell buckled at 90% of the classical load. To the right is a plot of the deviations of the lines in the expected image of the spiral grid obtained analytically for an assumed axisymmetric sinusoidal deflection pattern of the shell wall. This plot was drawn from the linear theoretical relations (neglecting the effect of the diverging view of the camera) developed for the optical system (Appendix B) for a shell of the same dimensions as that of S34. The wavelength of the assumed deflection was taken to be a seventh of the shell length (it may be observed that there are about seven broad bands visible in the photograph on the left) and the

(a)

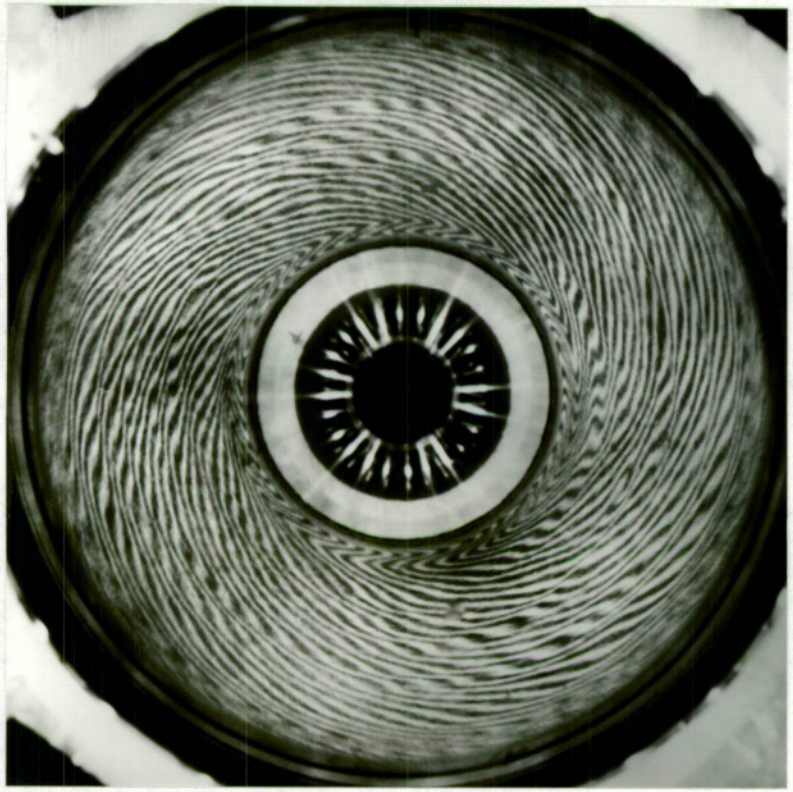

(b)

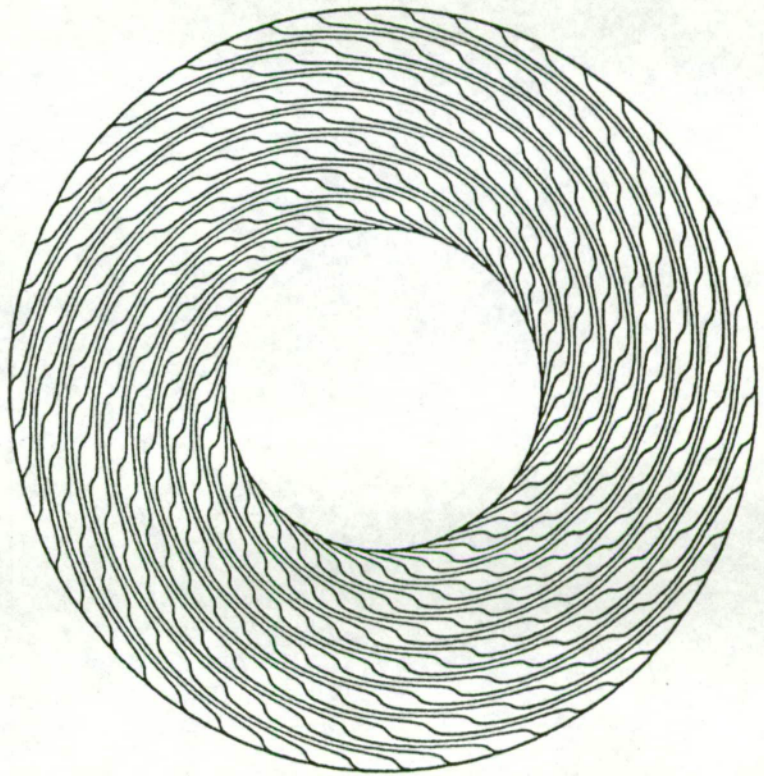

Figure 8.10. Axisymmetric Wave Pattern
in the Advanced Pre-Buckling Stage (Shell S34)

amplitude was taken as 0.006 mm (just over two percent of the wall thickness). The similarity between the theoretical plot (which ignores the clamped end conditions of the shell) and the recorded image of the deformations is striking. It is also interesting that the number of full waves given by theory for axisymmetric buckling (see eqn.2.3) for this shell is $8^1/_2$. Considering that the clamped end conditions of the actual shell could easily have suppressed over one full wave, the agreement between the number of waves observed in the pre-buckling stage with that predicted for axisymmetric buckling is surprising. In fact in all the nine shells in which such prebuckling deformations were recorded, the number of full waves observed over the whole length was close but below that predicted by the theory for axisymmetric buckling, as may be seen from the values tabulated below.

Table 8.3 Axisymmetric Waves Observed in Pre-buckling Stage

Shell	S22	S25	S34	S35	S37	S41	S43	S45	S46
Buckling load (η_{cr})	0.98	0.87	0.90	0.91	0.84	0.89	0.91	0.85	0.93
η at which axisymmetric waves were recorded	0.71	0.70	0.74	0.85	0.71	0.76	0.76	0.69	0.77
Number of waves observed in pre-buckling stage	9	4	7	8	10	9	8	9	6
Predicted no. of waves for axisym. buckling	10.4	4.5	8.5	9.2	11.3	10.7	9.7	11.8	7.6

It may be pointed out that Tennyson[54] has reported the observation of axisymmetric waves in the initial post-buckling stages in experiments conducted on photo-elastic shells using high speed

photographic equipment. The appearance of similar axisymmetric waves well before the onset of buckling does not seem to be previously reported, although Harris, et al.[79] mention that incipient buckling was often indicated by the formation of small circumferential ripples "similar to the shape of an axisymmetrical compression buckle".

8.4 Primary Buckling into Different Modes

Due to the thin-ness of the shells and the relatively high elastic limit of the epoxy material (about 70 Mpa) used for the manufacture of the test shells, several tests could be conducted on each shell with hardly any reduction in the observed critical loads. It was found that if a period of about three hours was allowed between the tests the shells would recover completely, and that the results of successive tests were usually consistent within 4 to 5%. In fact many shells seemed to improve with repeated testing and reached higher primary buckling loads in subsequent tests. Further, the majority of the shells which exhibited such improved performance collapsed in subsequent tests into buckling modes with lower values of N than observed previously. Once the highest value of the load and the least value of N was obtained, these values were maintained in further tests and the previously observed higher modes could not be realized any more. In Table C1 (Appendix C) the primary test data is presented as collapse from an initial value of N = 0 (denoting the pre-buckling state) to a final N of finite value. It may be observed that for those shells for which more than one primary buckling mode is reported, the lower value of N is usually associated with a higher buckling load.

(The underscored values indicate the highest buckling load and the lowest number of facets observed on complete primary collapse; only these have been presented in Tables 8.2a and 8.2b). It may also be observed that in these cases the lower primary buckling modes are associated with lower values of the initial post-buckling load, and higher values for the axial heights (H/L) of the facets. Both these observed phenomena are consistent with the geometrical considerations in Chapter 6, which showed that the same value of end-shortening can be accommodated by a lower value of N (provided it is greater than N_{min}) with a corresponding increase in the axial height of the facets; this being associated with smaller angles at the folds and hence lower values of bending energy, requiring smaller end-loads to sustain the stable buckled configuration.

Another interesting aspect associated with the different modes observed on primary collapse is that in many cases the pattern of the highest mode was formed away from the mid-section, whereas with the reduction in the number of facets on each subsequent collapse the buckles developed closer and closer to the mid-section of the shell. The primary collapse patterns of shell S12 with N = 12, 11 and 10 and those of S43 with N = 9 and 8 are shown in Figure 8.11. It can be seen that in both cases the buckles of the higher modes have formed towards the upper end, while the lowest modes are close to the mid-section of the shells. The measured values of the axial distances of the centre-line of the patterns from the bottom end, for those shells in which the buckles were observed to form away from the mid-section, are presented in the last column of Table C1. It may be pointed out that

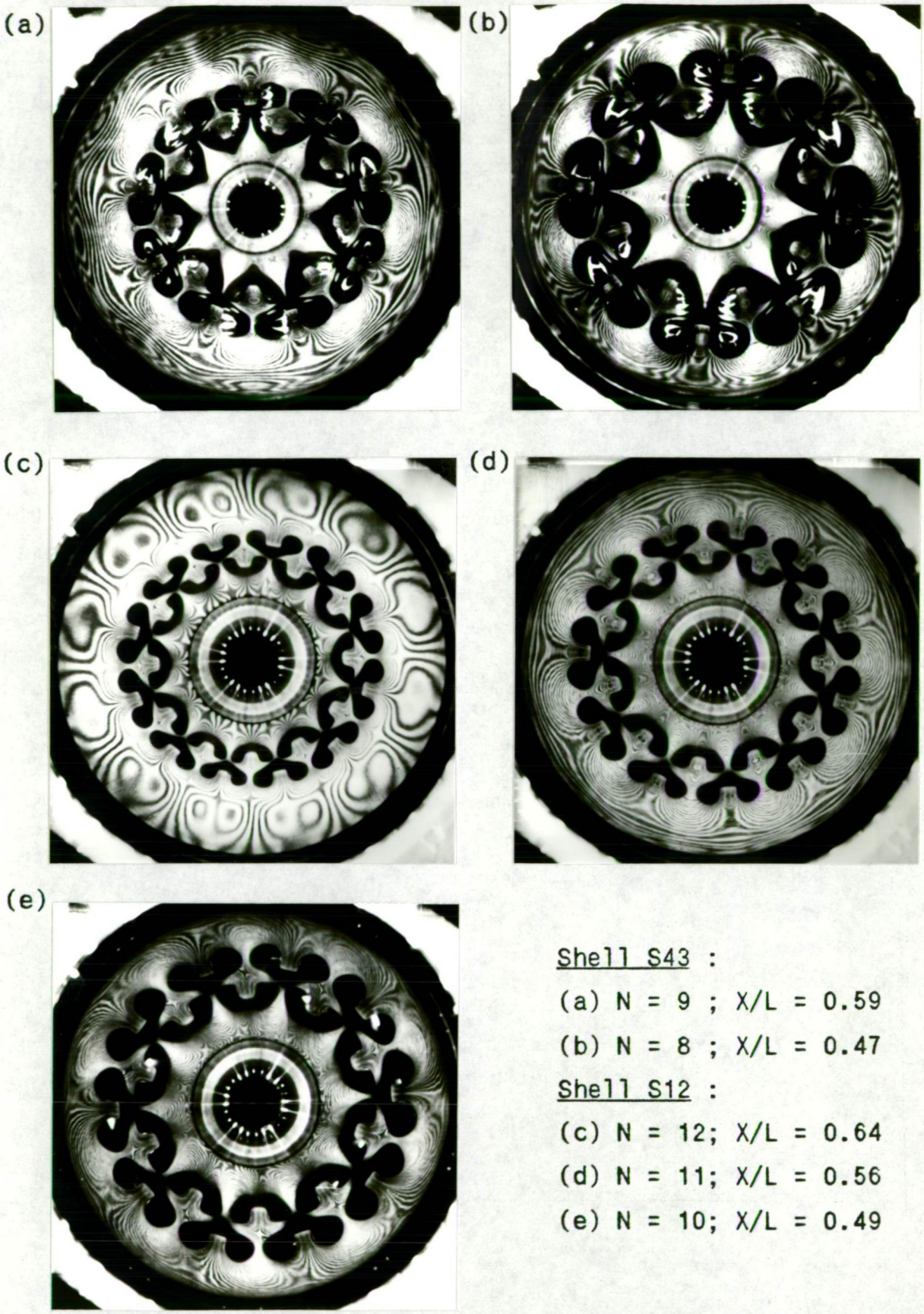

Shell S43 :

(a) N = 9 ; X/L = 0.59

(b) N = 8 ; X/L = 0.47

Shell S12 :

(c) N = 12; X/L = 0.64

(d) N = 11; X/L = 0.56

(e) N = 10; X/L = 0.49

Figure 8.11. Primary Collapse Modes with Different Numbers of Facets

the formation of buckle patterns closer to the middle of the shell in subsequent collapses occurs only in those shells which exhibit multiple primary modes; if the subsequent patterns are formed by secondary collapse, the secondary modes appear at the same location as the primary pattern, as illustrated by the photographs of the primary and secondary collapse modes of shell S33 in Figure 8.8.

8.5 Initial Post-buckling Load

In section 6.8, on comparing the linear approximation given by Kollár and Dulácska[72] for Pflügger's curves (relating the expected number of facets to the post-buckling load) with eqn.6.12 obtained from geometrical considerations, the end load after primary collapse was found to be inversely proportional to the fourth root of the Batdorf parameter Z (eqn.6.23). The values of the axial load measured in the initial stable post-buckling state after primary collapse in the current tests are plotted against Z in Figure 8.12. The suggested variation of the post-buckling load with the fourth root of the Batdorf parameter appears to hold good as may be seen from the fitted curve (the actual value of the index of Z for this curve was obtained as -0.2503). The coefficient obtained from the experimental data, however, is slightly less than half the value of 3.3 in the relation (eqn.6.23) obtained in Chapter 6. From the comparison it appears that in the linear relation (eqn.6.22) suggested in Ref.72 the coefficient is in error by a factor of 2. This seems quite likely since in Ref.72, the coefficient quoted for the empirical relation obtained by Hoff[56] (eqn.6.18) is also in error by a factor of 2 (this value is quoted as

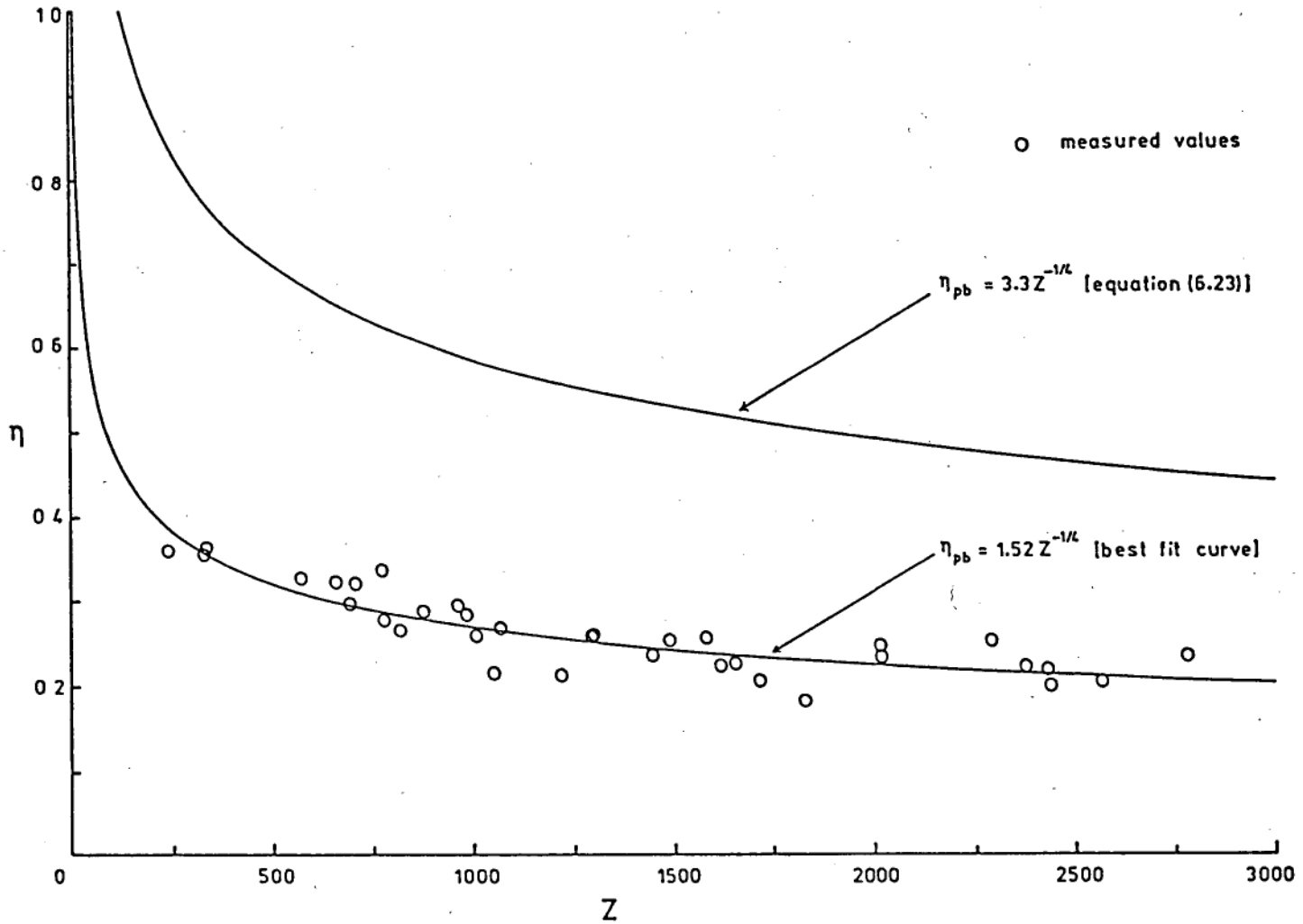

Figure 8.12. Initial Post-Buckling Loads

0.286 on page 39 of Ref.72, instead of 0.57). Unfortunately, the original work by Pflügger was not available for verification. In any case the approximation provided in Ref.72 has been useful in leading towards a possible relationship for the initial value of the post-buckling load which from the experimental data is found to be

$$\eta_{pb} = 1.52\ Z^{-1/4} \qquad (8.1)$$

8.6 Number of Facets Observed on Primary Collapse

In Figures 8.13a to 8.13d the circumferential number of facets observed after primary collapse in the tests are compared with the various relations presented in Chapter 6. It may be mentioned that only the minimum number of facets observed on complete collapse (when the facets have formed all round the circumference) have been used for comparison. In the first figure 8.13a, the observed circumferential number of facets are plotted against $(R/L)^{0.36}(R/t)^{1/2}$ and compared with the empirical formula (eqn.6.18) suggested by Hoff[56]. In Figure 8.13b, the values of N are plotted against $(R/L)^{1/2}(R/t)^{1/4}$. Eqn.6.19 which is the relation obtained by De Neuffville and Connor[55] and the best straight line fit to the experimental data are shown in solid lines. The relation obtained from geometrical considerations in Chapter 6 for the minimum number of facets for the two tier pattern (eqn.6.15) is shown in broken lines. Since the shell is expected to buckle into a pattern with the number of facets equal to the nearest higher integer, these values are shown by the stepped lines over the N_{min} line. (No stepped lines have been drawn for the predictions from

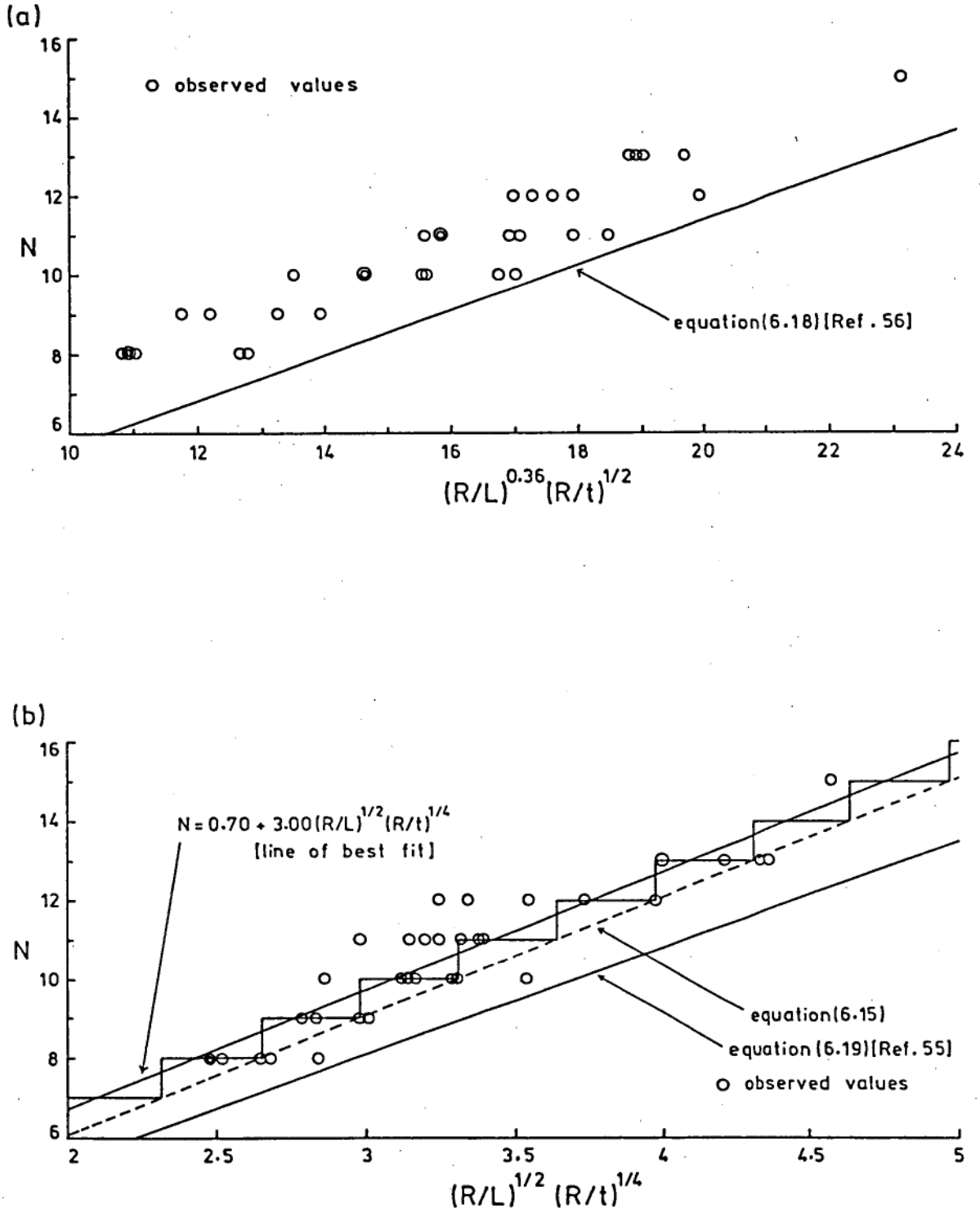

Figure 8.13.(a,b)
Number of Facets Observed in Primary Mode
- Comparison with Predictions

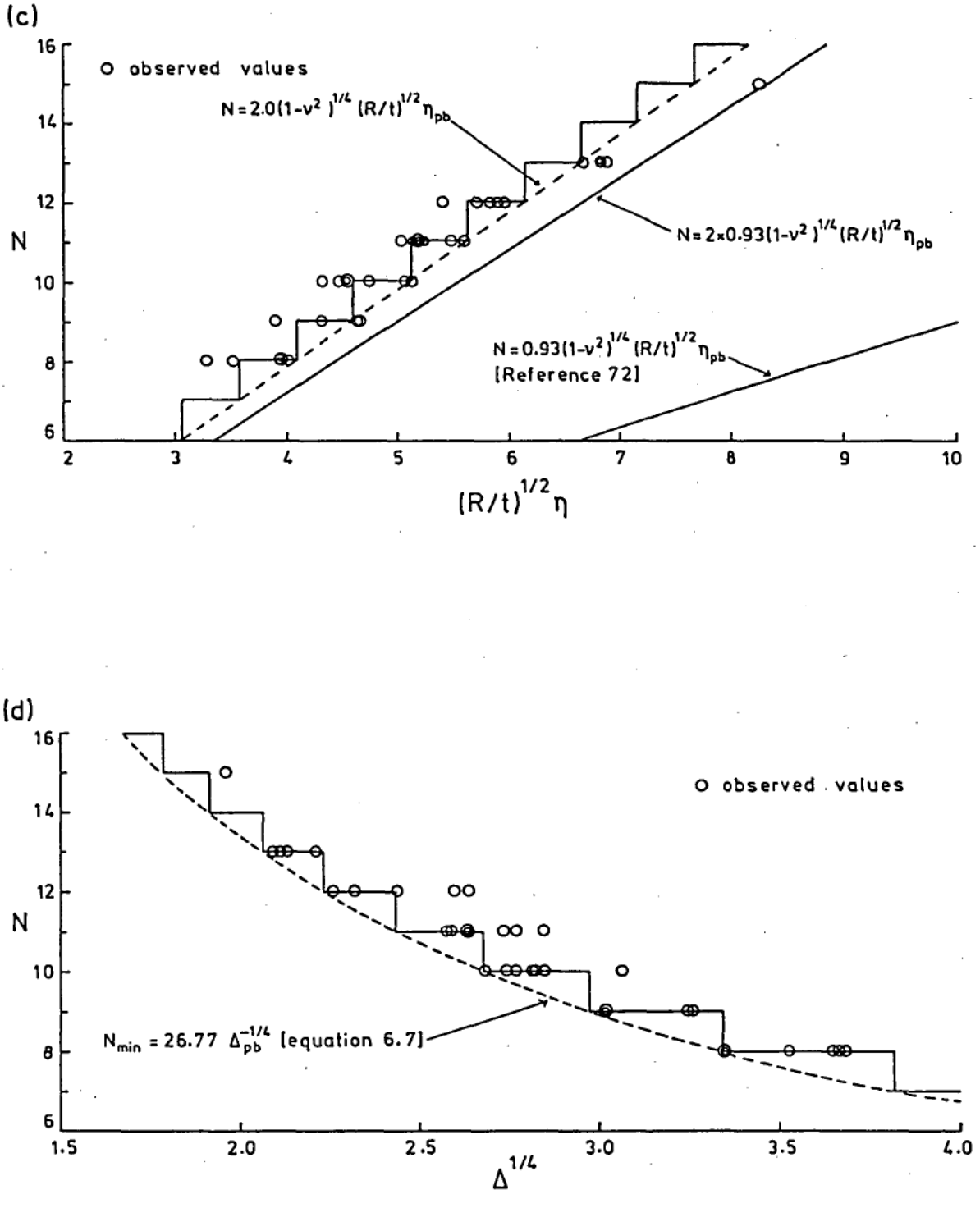

Figure 8.13.(c,d)
Number of Facets Observed in Primary Mode
- Comparison with Predictions

other references, since in these cases the expected number of facets is - presumably - to be taken as the nearest integer above or below the lines). The observed number of facets is plotted against $(R/t)^{1/2}\eta$ in Figure 8.13c. The linear approximation (eqn.6.22) of Ref.72 for Pflügger's curves, which has a slope of $0.93(1-\nu^2)^{1/4}$, can be seen to be too far below the experimental values. The agreement is much better when the slope is doubled (on the assumption, as mentioned in section 8.5, that the value of the coefficient has been erroneously quoted). The equation for the broken line in Figure 8.13c, with a slope of $2.0(1-\nu^2)^{1/4}$, was obtained by combining the best fit line for the experimental values of the initial post-buckling loads (eqn.8.1) with the relation obtained from geometric considerations for the expected minimum number of facets in the two tier pattern (eqn.6.12). As before the nearest higher integer values are indicated by stepped lines.

It can be seen from Figures 8.13a, b and c that the observed values are in closer agreement with the number of facets predicted by the relations based on the geometric criteria developed in Chapter 6 than with the empirical and semi-empirical formulae from previous works. It is however to be noted that the latter predictions are also not very far off (if the constant in eqn.6.22 is doubled). The lower estimates consistently obtained for the expected number of facets from these earlier formulae are possibly because these relations do not make a distinction between the one and two tier patterns (since for the same end-shortening the shell can geometrically accommodate a lower number of facets in the one tier pattern than in the two tier).

Although the majority of the experimental values for the observed number of facets lie on the stepped lines in Figures 8.11b and c, quite a number of points lie above and below the values expected from geometric considerations. Most of the values which lie above the theoretical lines were observed in shells which collapsed early and in those which developed buckle patterns away from the mid-section, while the experimental values below the stepped lines are mostly from tests on relatively thick shells, in which significant differences were observed between the value at collapse and the post-buckling value of the end-shortening. Either case involves considerable deviation from the assumption that the end-shortening in the buckled state is equal to that corresponding to the classical load, on the basis of which eqn.6.12 for predicting the number of facets on primary collapse has been derived.

In Figure 8.13d the values of the observed number of facets are plotted against the measured values of the end-shortening in the initial stable post-buckled state. Most of the experimental values in this case lie on the stepped lines denoting the nearest integer greater than or equal to the minimum given by eqn.6.7 which is plotted in broken lines. Although a few observed values are higher, in no case is the measured value of end-shortening lower than the required minimum that was established from the geometrical considerations in Chapter 6. It may be mentioned that even the secondary collapse modes satisfy this requirement, as may easily be verified from the values of the end-shortening tabulated in Table C1.

8.7 Predictions of Space Frame Theory for Primary Collapse Loads

The proposed application of the space frame theory for predicting the primary collapse loads of imperfect shells is based on the hypothesis that imperfections in the shell behave like the facets of a space frame and hence the load carrying capacity of the cylinder is limited to that of the space frame whose facets are of the same circumferential size as the largest initial imperfection in the shell. This suggestion by Foster was based on the observed agreement between buckling loads obtained in experiment and those predicted by the space frame theory, the latter being estimated in the majority of the cases (except for the four shells with imposed defects reported in Ref.24) from the circumferential sizes of observed initial imperfections similar to those described in section 8.2. Hence from the photographs of the unloaded shells tested in the current work, the circumferential sizes of the largest observable imperfections were measured, and the buckling loads estimated from the space frame theory which are compared to the observed collapse loads in Table 8.4. It is to be noted that while in some shells no defects were detected, the imperfections observed in some other shells (such as those described as out of round) were not measurable. Hence the comparison has only been made for shells with local imperfections whose circumferential size could be measured. The angular extend (θ) of the defect and the corresponding circumferential number of facets are presented in the fifth and sixth columns of the table. The theoretical buckling loads for the space frame model having the same number of facets and the appropriate value of R/t have been estimated using Foster's original

Table 8.4 Comparison of Observed Primary Collapse Loads with Predictions of Space Frame Theory

Sr. No.	Shell	Group	Observed η_{cr}	Circumf. Size of defect		Original Sp.Fr.		Modified Sp.Fr.	
				θ	N	$\eta_{pred.}$	% Error	$\eta_{pred.}$	% Error
1	S3	A	0.883	12.5^0	29	0.81	- 8%	0.91	+ 4%
2	S8	A	0.879	17^0	21	0.51	-42%	0.63	-28%
3	S12	A	0.916	10^0	36	>1.0	+ 9%	>1.0	+ 9%
4	S18	A	0.958	11.5^0	31	>1.0	+ 4%	>1.0	+ 4%
5	S22	A	0.975	11^0	33	>1.0	+ 3%	>1.0	+ 3%
6	S23	A	0.890	17^0	21	0.84	- 6%	0.75	-16%
7	S27	A	0.902	14^0	26	0.93	+ 3%	0.89	- 1%
8	S39	A	0.938	10^0	36	>1.0	+ 7%	>1.0	+ 7%
9	S40	A	0.907	14^0	26	>1.0	+10%	0.99	+ 9%
10	S42	A	0.960	16^0	23	>1.0	+ 4%	0.86	-10%
11	S44	A	0.895	14^0	26	0.93	+ 4%	0.89	- 1%
12	S20	B	0.867	18.5^0	19	0.77	-11%	0.69	-20%
13	S30	B	0.849	13.5^0	27	0.61	-28%	0.78	- 8%
14	S37	B	0.840	19^0	19	0.63	-25%	0.63	-25%
15	S2	B	0.837	22.5^0	16	0.40	-52%	0.49	-41%
16	S16	B	0.822	20^0	18	0.65	-21%	0.62	-25%
17	S29	B	0.763	18^0	20	0.54	-29%	0.62	-19%
18	S38	B	0.785	17^0	22	0.85	+ 8%	0.78	- 1%
19	S6	C	0.793	19^0	19	0.50	-37%	0.59	-26%
20	S17	C	0.774	20^0	18	0.47	-40%	0.56	-28%
21	S31	C	0.737	21^0	17	0.36	-51%	0.50	-32%
22	S32	C	0.719	13^0	28	0.81	+13%	0.89	+24%
23	S1	D	0.614	26^0	14	0.35	-42%	0.43	-30%
24	S9	D	0.661	16.5^0	22	0.66	+ 1%	0.70	+ 7%
25	S21	D	0.552	17.5^0	21	0.44	-20%	0.60	+ 9%

theory (with an effective flange width of 22.7*t and aspect ratio from eqn.3.17) as well as from the modified theory (the space frame model without springs, using K = 1.6 and λ = 0.5). For shells with estimated buckling loads greater than the classical load, the theoretical knock down factor is to be taken as equal to 1. It may be observed that about half the number of predictions based on either model are within 10% of the observed knockdown factors. Considering the differences between the irregular nature of the actual imperfections and the regular features of the diamond-shaped facets with which they are approximated, it appears encouraging that fifty percent of the results show an agreement within 10%; on the other hand, this could be fortuitous, particularly since most of the agreement obtained is in tests conducted on shells of group A, which had small imperfections and high values of buckling loads.

8.8 Measurements of the Aspect Ratio

Measurements of the axial heights (H/L) of the facets of the buckle patterns were taken from the photographs recorded immediately after primary and secondary collapse of the shells tested, which are presented in Table C1 (Appendix C) along with the corresponding values of the aspect ratio (ratio of the facet height to its circumferential length). It may be mentioned that in some cases the values are not tabulated since the size of all the facets were not uniform (this was mostly caused by the presence of additional buckles above or below the two tier patterns which usually occurred in the advanced post-buckling stages). The observed values of the aspect ratio showed considerable

scatter as may be seen from Figure 8.14a in which all the observed values are plotted against R/t. Also plotted in the figure is the empirical relation (eqn.3.17) obtained by Foster[58]. Since the equation was developed by Foster from values measured after primary collapse, the aspect ratios of only the primary buckling modes are plotted separately in Figure 8.14b along with the empirical curve. It may be observed that except for two cases all the plotted values are well below the curve; nor do they show any reduction with increasing values of R/t as suggested. The discrepancy observed could be due to the difference in the shell materials as was mentioned in section 5.6. It is felt that the scatter observed in the tests is due to the influence of other factors such as the length of the shell, the number of facets and the post-buckling load. The assumption that the aspect ratio of the facets in the initial post-buckling state depends only on the radius to thickness ratio does not appear to be valid, although it is to be admitted that no definite relations with other parameters could be established from the test data.

In spite of the large amount of scatter, some consistencies were noticeable in the values of the aspect ratio measured in the initial post-buckling state. It was mentioned earlier that in shells which exhibited multiple primary buckling modes, the axial height of the facets of the lower mode were much higher. In spite of the larger value of the circumferential length of the facets in the lower mode, the increase in the axial height usually resulted in an increase in the the aspect ratio as may be seen from the values tabulated in Table C1. Secondly it was found that when the reduction in the number of

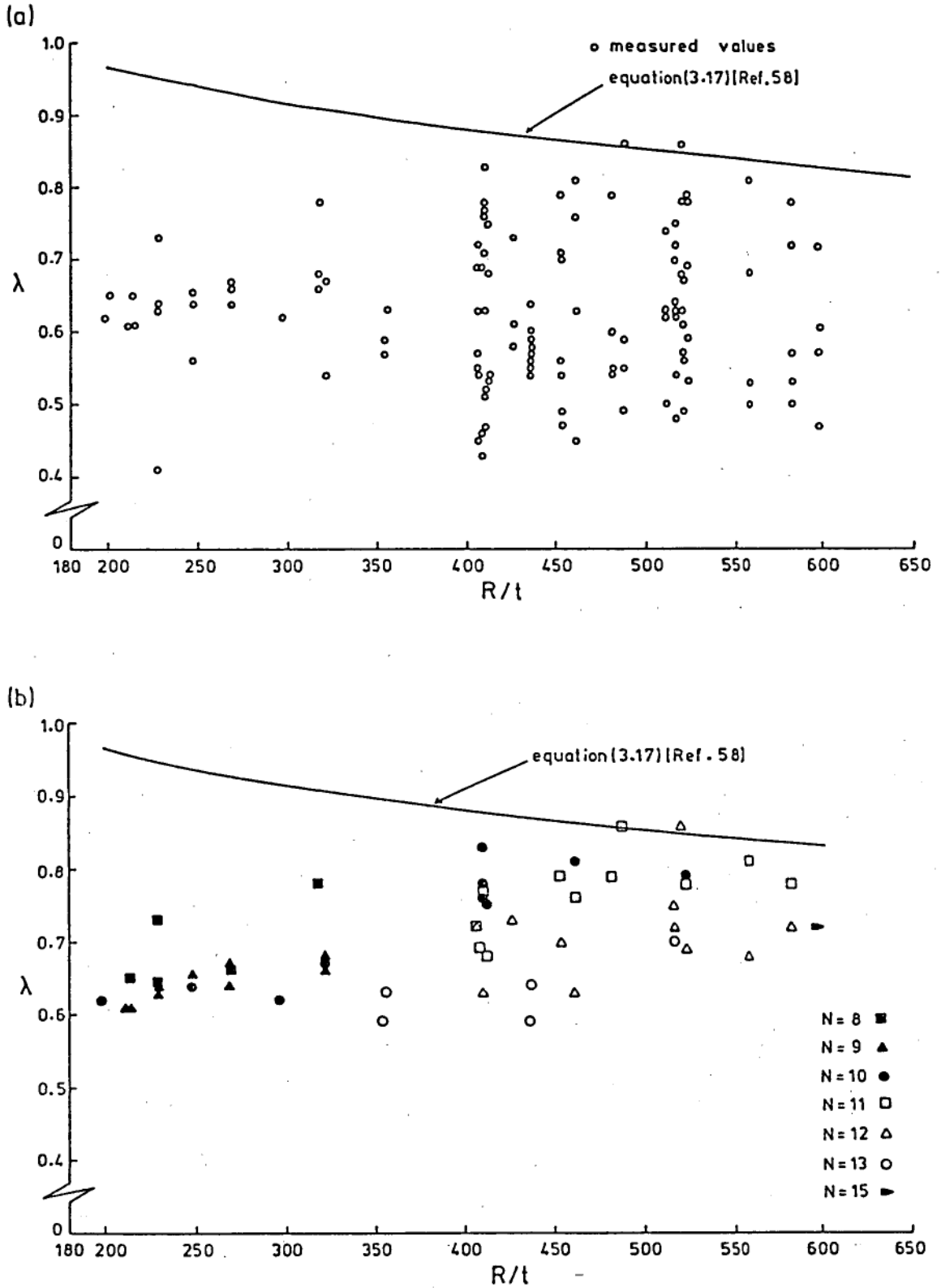

Figure 8.14. Measured Values of Aspect Ratio
(a) Primary and Secondary Buckling Modes
(b) Primary Modes Only

facets occurred due to a secondary collapse the aspect ratio generally decreased. Thus the facets in the secondary collapse patterns had lower aspect ratios than the facets of the primary buckling patterns; as may be seen from a comparison of the two plots in Figure 8.14.

The geometric considerations in Chapter 6 had revealed the possibility of a variation in the aspect ratio of the facets in shells which have buckled elastically in order to accommodate changes in the magnitude of the end-shortening in a near inextensional manner. To investigate this several photographs were taken of shells in advanced post-buckling states (that is after increasing the end-shortening considerably, but before the next collapse occurred) and compared with the photographs taken in the initial post-buckled state. In some cases the buckling patterns after partial unloading were also recorded. To illustrate the observed variation in the axial height and hence the aspect ratio of the facets, the photographs of shells S8 and S4, taken in the initial post-buckled state and after further loading are shown in Figure 8.15. The reduction in the axial height of the facets is quite discernible in the photographs of the loaded shells. It may be mentioned that the actual measurements were taken from enlarged photographs. In the photographs of the buckled shell taken with the circumferential grid, the grid-lines usually develop approximately into small ellipses at the mid-point of the the tangential folds, hence the boundaries of the facets are quite clearly defined, facilitating accurate measurement. Measurements of the axial heights taken in this manner are tabulated along with the calculated values of the aspect ratio in Table 8.5. In a few cases during the tests the

(a) 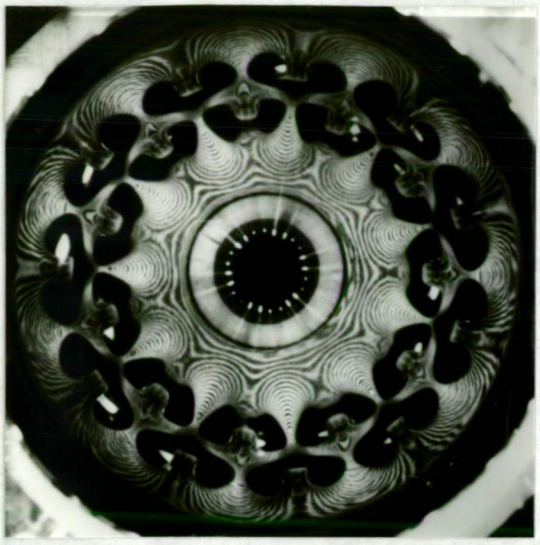

(b) 

(a) Shell S8 : Immediately after collapse
(Δ = 48.2, η = 0.22, H/L = 0.215, λ = 0.81)

(b) Shell S8 : On further loading
(Δ = 125, η = 0.315, H/L = 0.133, λ = 0.50)

(c) 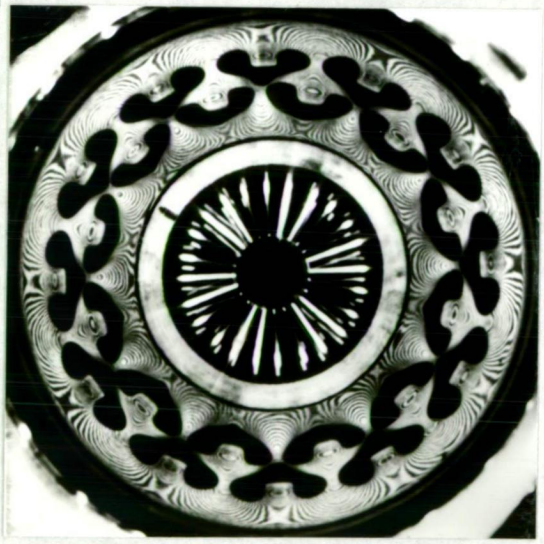

(d) 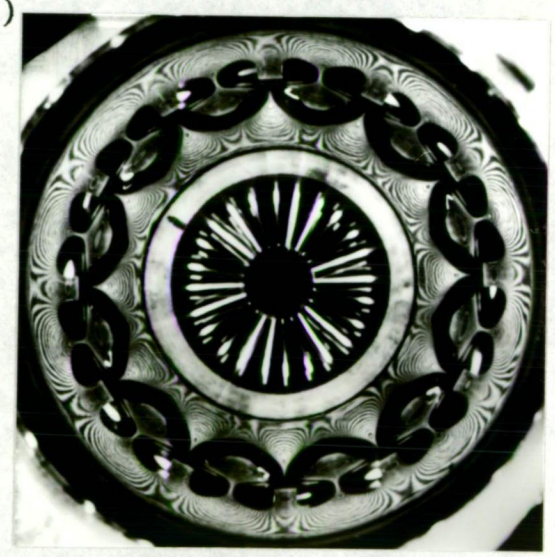

(c) Shell S4 : Immediately after collapse
(Δ = 25.9, η = 0.260, H/L = 0.260, λ = 0.72)

(d) Shell S4 : On further loading
(Δ = 59.5, η = 0.362, H/L = 0.210, λ = 0.58)

Figure 8.15. Changes in Axial Height of Facets due to Increase in End-Shortening

Table 8.5 Observed Changes in Aspect Ratio

Shell	N	η	Δ	H/L†	λ	$(H/L)^{*}_{dm}$	Remarks
S3	10	0.207	56.4	——	0.79	0.216	post-collapse value
		0.258	124	0.164	0.60	0.162	on loading
		0.281	167	0.112	0.41	0.126	on further loading
		0.180	41.3	0.250	0.91		on unloading
S4	12	0.260	25.9	0.260	0.72		post-collapse value
		0.362	59.5	0.210	0.58		on loading
		0.241	25.9	0.260	0.72		on unloading
		0.245	17.3	0.290	0.80		on further unloading
S8	11	0.220	48.2	0.215	0.81		post-collapse value
		0.292	102	0.152	0.57		on loading
		0.315	125	0.133	0.50		on further loading
S10	11	0.245	41.5	0.237	0.71		post-collapse value
		0.378	106	0.185	0.55		on loading
S11	10	0.213	50.4	0.255	0.81		post-collapse value
		0.301	137	0.171	0.54		on loading
		0.367	209	0.145	0.46		on further loading
S11	9	0.260	209	0.159	0.45		post-collapse value
		0.181	110	0.233	0.67		on unloading

†Ratio of axial height of the facets to the length of the shell measured from the photographs.

*Direct measurements taken during the tests.

Table 8.5 Observed Changes in Aspect Ratio (continued)

Shell	N	η	Δ	H/L	λ	$(H/L)_{dm}$	Remarks
S12	10	0.235 0.341	63.3 161	0.237 0.164	0.78 0.54		post-collapse value on loading
S12	8	0.206 0.158	237 102	0.197 0.237	0.52 0.63		post-collapse value on unloading
S13	10	0.241 0.292 0.185	96.0 141 53.0	0.175 0.143 0.234	0.59 0.48 0.78		post-collapse value on loading on unloading
S18	8	0.184 0.304 0.186	125 512 80.3	0.246 0.149 0.274	0.78 0.47 0.87	0.249 0.141 0.283	post-collapse value on loading on unloading
S22	9	0.213 0.323	79.5 311	0.236 0.153	0.68 0.44	0.261 0.168	post-collapse value on loading
S34	9	0.264 0.375	82.4 183	0.261 0.190	0.67 0.49	0.266 0.194	post-collapse value on loading
S41	8	0.259 0.369	182 408	0.233 0.151	0.73 0.47		post-collapse value on loading

folds of the buckle patterns were marked on the outside of the shell and measurements made after releasing the load. Direct measurements taken in this fashion are also listed. It can be seen that these are in reasonable agreement with the measurements from the photographs. From the values presented in the table, it is obvious that the aspect ratio changes considerably with changes in the end-shortening imposed on the shell. Although reductions in aspect ratio up to 0.41 have been measured, most of the values in the loaded condition are about 0.5, the value that has been assumed in the modified space frame theory.

8.9 Secondary Collapse Behaviour

Typical secondary collapse behaviour of good shells is illustrated by the load deflection diagram in Figure 2.5 (shell S2) and those in Figures 8.1 and 8.2 (shells S44 and S4, respectively). As in the case of primary collapse the instability occurs suddenly, the shell quickly snapping from one mode into another with a loud report caused by the release of energy. Successive collapses normally reduce the number of facets by one, and in the early stages the new patterns developed are as regular as the previous ones. However after three or four such collapses the shell usually starts developing additional isolated buckles which mar the regularity of the two tier pattern, and hinder the development of proper two tier patterns of lower modes in further collapses. Once the additional buckles are formed the shell often suffers partial collapses developing similar buckles instead of undergoing a normal secondary collapse with a reduction in the number of facets in the two tier pattern. In shells of lower quality this

begins to occur early so that often only one or two regular two tier patterns are obtained. It may be mentioned that partial collapses leading to the formation of isolated buckles, or completing partial patterns developed earlier are not being considered as secondary collapses in the following discussion.

Although a secondary collapse is normally expected to reduce the number of facets by one, on a few occasions the shells were observed to skip some value of N, snapping from one mode to another with the number of facets reduced by two. In some cases this happened due to the intermediate mode being unstable for some reason, and hence collapsing as soon as it formed into the next mode. However in most cases the secondary collapse with a reduction in the number of facets by two occurred at a higher load than the load at which the shell buckled into the intermediate mode (the same shell would, in other tests collapse into the expected mode). Since such behaviour was perceived only in a few shells, it can only be attributed to the presence of some imperfections in the shell (perhaps local variations in the wall thickness) which prevented the shell from developing the intermediate mode. It thus appears that the presence of imperfections can, at least in some cases, increase the load carrying capacity of the buckled shell, and cause secondary collapse to occur at a load higher than the secondary buckling load expected in a perfect shell with the same number of facets.

Three of the shells tested (S22, S41, S46) developed three tier patterns after secondary collapse. In the case of shells S22 and

S46, it appears to have been caused by the formation of the previous two tier mode towards one end of the shell. In all three cases, the three tier pattern was observed in only one of the tests conducted. The phenomenon thus appears to be rare and somewhat transitory (the pattern in shell S22 immediately collapsed into an irregular two tier mode). The buckles formed however were quite regular and symmetric as may be observed from the photograph shown in Figure 8.16b. The two tier mode which collapsed into the three tier pattern is shown in Figure 8.16a. The third photograph 8.16c, shows the return to the previous mode on partial unloading, and the last photograph shows the residual deformations on the shell wall immediately after complete unloading, in which the nodes of the three tier pattern are clearly visible. It may be mentioned that such residual deformations could be observed after most tests (the nodes were most clearly brought out by the reflections of the axial grid); these however soon disappeared and the shell regained its original strength within two or three hours.

The return of the shell to the previous mode on unloading was observed only when the three tier patterns were formed, although theoretically even the two tier patterns are supposed to exhibit such behaviour. In the present tests in hardly any of the cases in which two tier patterns were formed by successive secondary collapses, did the shells snap back into the previous modes on unloading. Instead the last (lowest) mode was retained with the facets gradually becoming longer in the axial direction as the end-shortening was reduced, until all of a sudden the buckles would vanish (sometimes one after another) and the shell snap back into its original straight configuration.

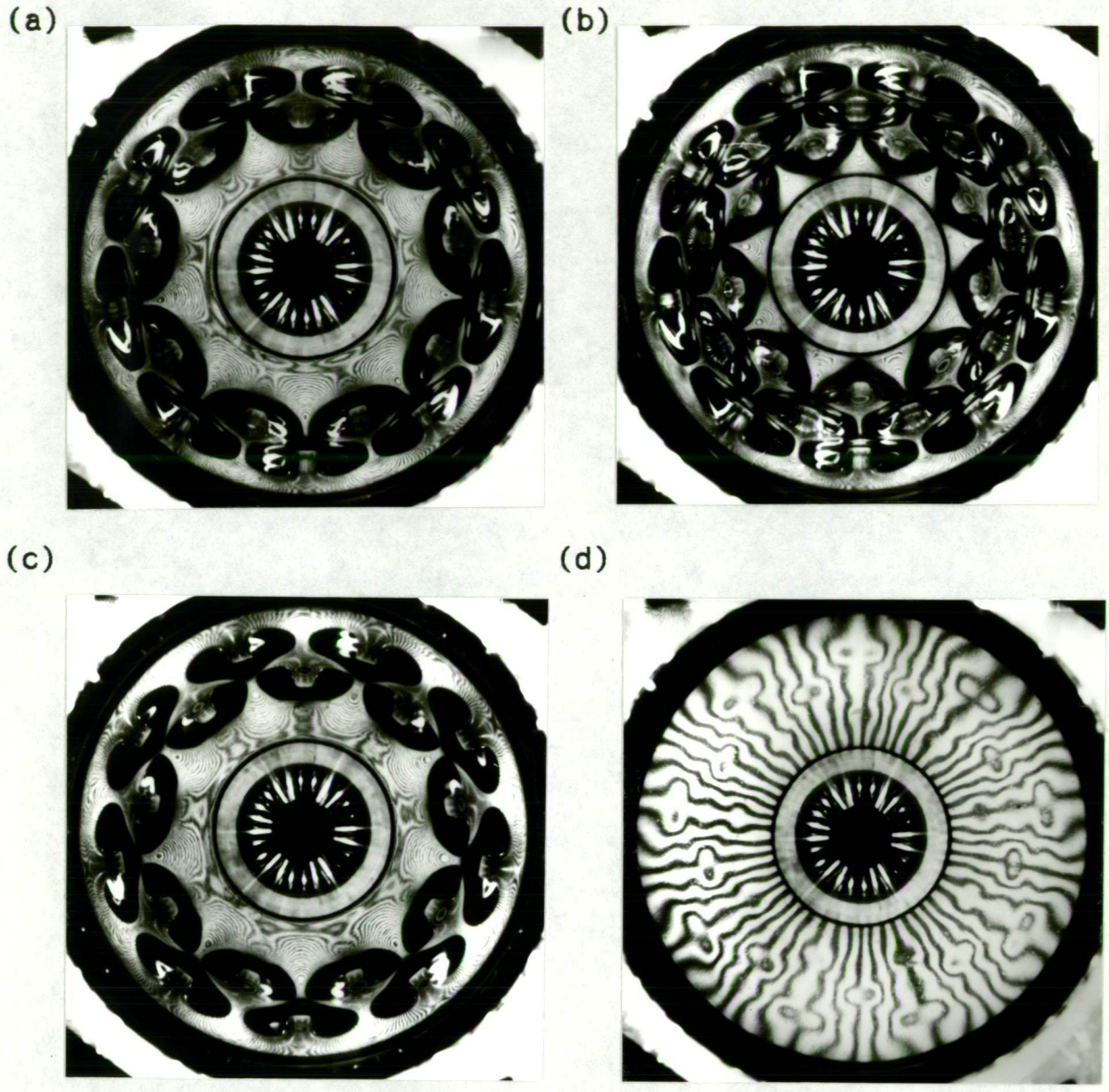

(a) Primary mode (N = 9 II)

(b) Secondary mode (N = 9 III)

(c) Return to primary mode (N = 9 II)

(d) On complete unloading

Figure 8.16. (Shell S46)
Formation of Three Tier Pattern

8.10 Comparison of Secondary Buckling Loads

Other than the deviations mentioned in the foregoing section, the secondary collapses observed in most tests conformed to the expected behaviour. All the secondary buckling data, the values of the end-shortening, the axial load as well as the number of facets before and after collapse is presented in Table C1 (Appendix C). The observed secondary buckling loads corresponding to each value of N are plotted against R/t in Figures 8.17a to 8.17e. The predictions from the space frame theory are also plotted for comparison. The curves from the original space frame theory, using an effective width ratio of W/t = 22.7 and the aspect ratio from eqn.3.17 as suggested by Foster, are shown in broken lines. The estimates from the space frame model without spring (using K = 1.6 and λ = 0.5) are shown in solid lines. For the range of R/t and the values of N observed the estimates from the modified model with spring (using K = 0.78 and λ = 0.5) are practically the same (within 1%) as those from the model without spring and hence lie along the same solid lines. It can be seen from the figures that the observed secondary collapse loads agree well with the predictions from the modified models. Taking into account the amount of scatter that is to be expected in any axial compression test on cylindrical shells, the modified space frame models appear to be reasonably accurate for estimating the secondary buckling loads of the axially loaded cylinder, at least in the range of the radius to thickness ratio of the shells tested.

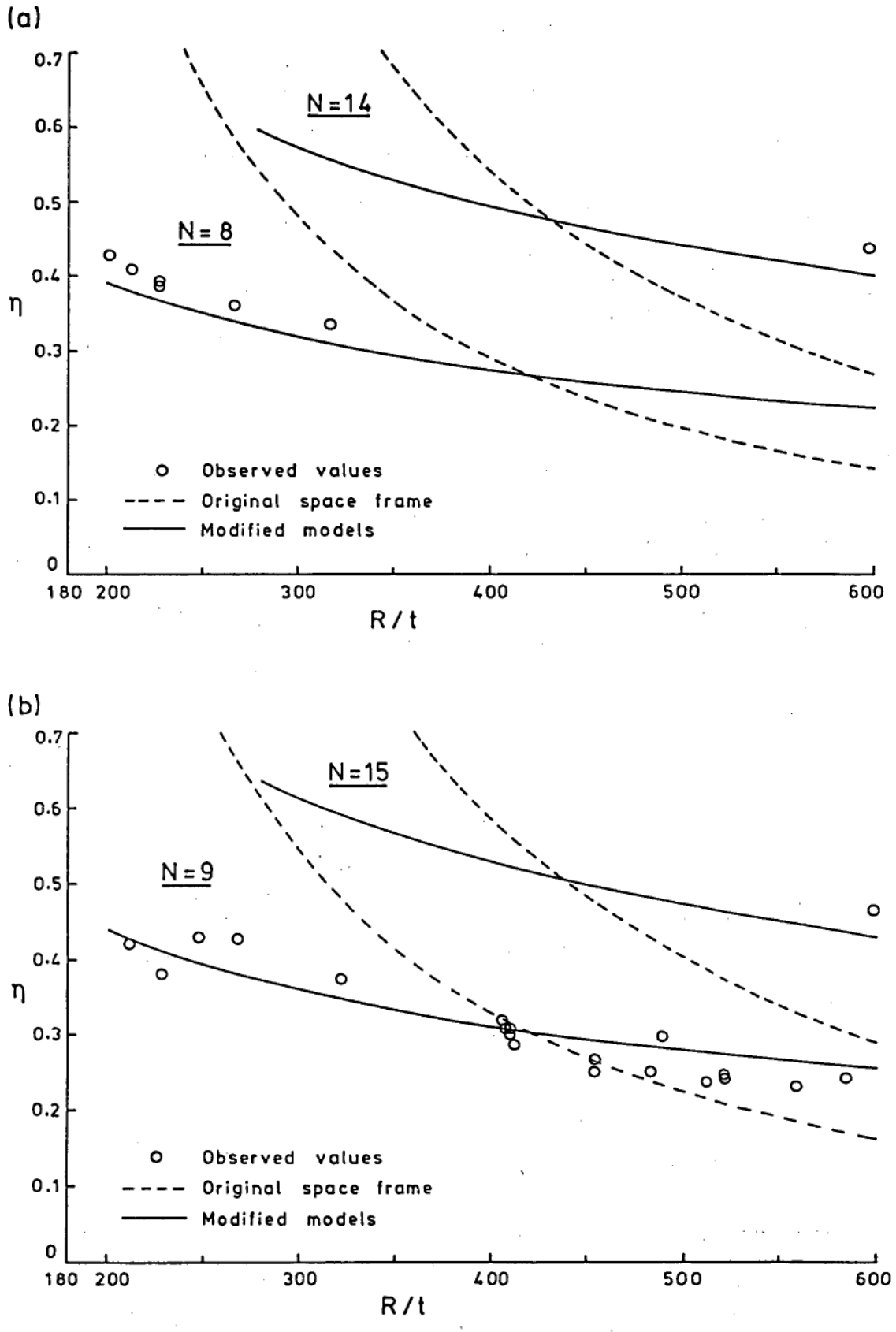

Figure 8.17. Secondary Buckling Loads
- Comparison with Space Frame Theory
(a) N = 8,14 (b) N = 9,15

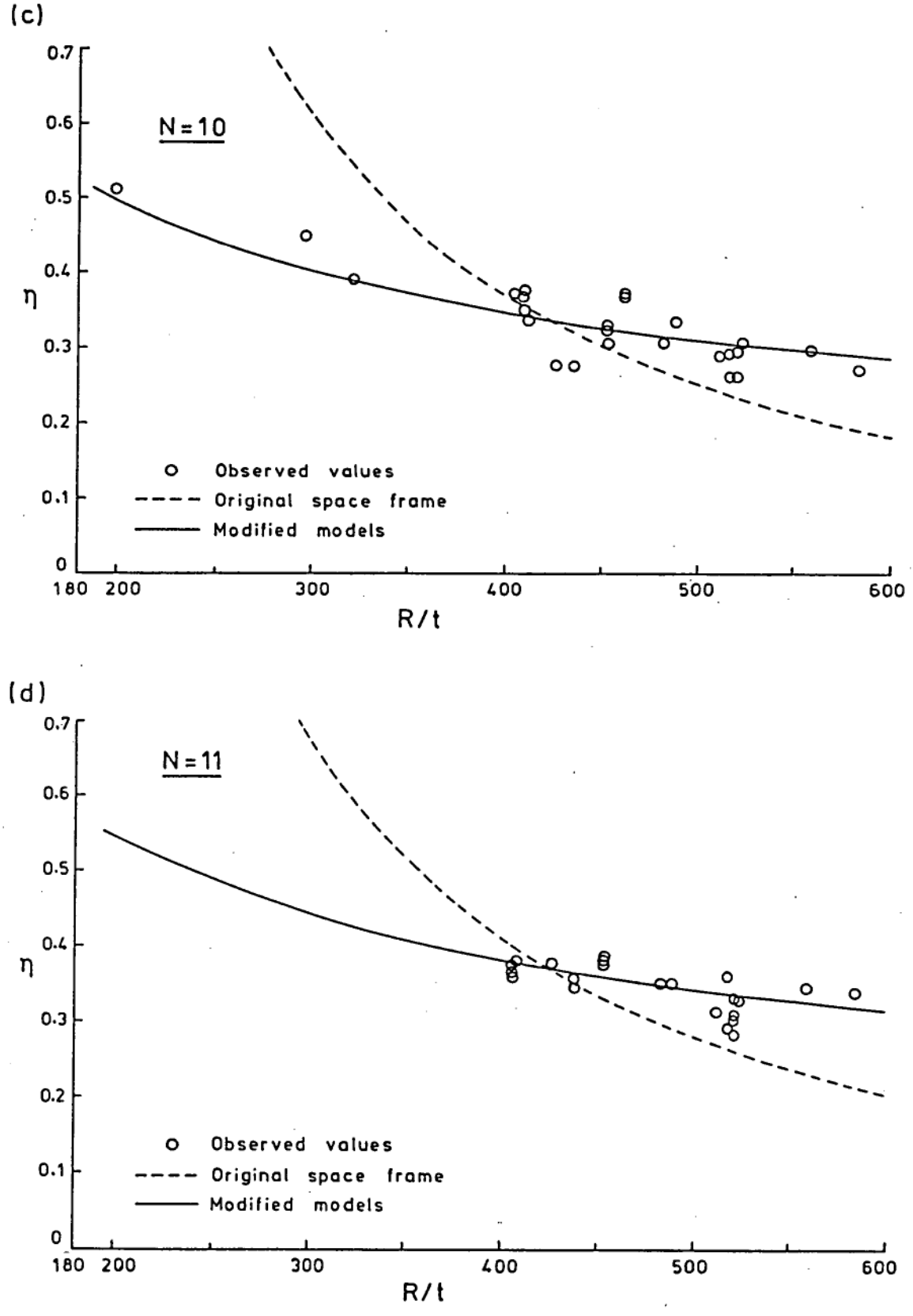

Figure 8.17. Secondary Buckling Loads
- Comparison with Space Frame Theory
(c) N = 10 (d) N = 11

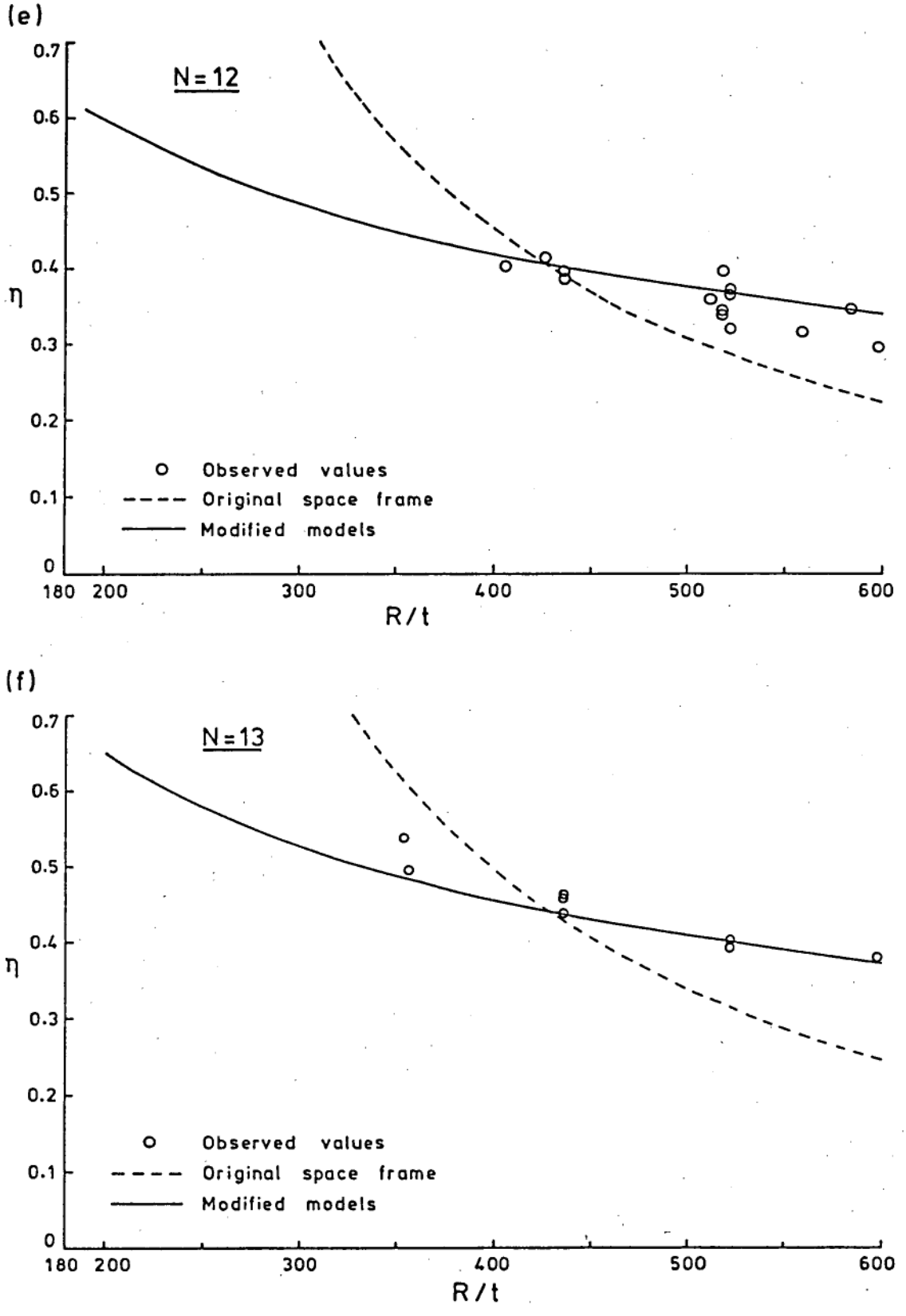

Figure 8.17. Secondary Buckling Loads
- Comparison with Space Frame Theory
(e) N = 12 (f) N = 13

CHAPTER 9

TESTS WITH IMPOSED DEFECTS

The present series of experiments were conducted with the objective of studying the effects of local geometric imperfections of large amplitude on the shell wall, in particular geometric deviations in the form of diamond shaped dimples, which appear to occur commonly in practical situations (see Figure 1 - Chapter 1). These localized imperfections, or defects, were imposed with the aid of a cylindrical wooden mandril, having a diameter slightly smaller than that of the test shells, which had cut into its surface two flat faces - similar to the facets of the Yoshimura pattern - forming a 'V' shaped notch of the required dimensions (Figure 9.1). (It was found convenient to use only a section of the wooden mandril, with the 'V' shaped notch on its cylindrical surface, instead of the whole wooden cylinder). After the preliminary tests on the shell (those described in Chapter 8) were completed, the shell was removed from the loading frame, and slipped over the mandril with the end-rings still attached to it. The location of the defect was marked on the shell surface and a cardboard mask, with a cut-out of the same shape and size, was placed over the shell and aligned with the notch on the wooden mandril. Hot air from a domestic hair dryer was directed on the exposed portion of the epoxy shell until it softened. Applying pressure with the finger tips, the softened shell wall was then impressed on to the notch in the wooden mandril and pressure maintained until it cooled. In this manner a permanent deformation, of the same shape as that on the mandril, was

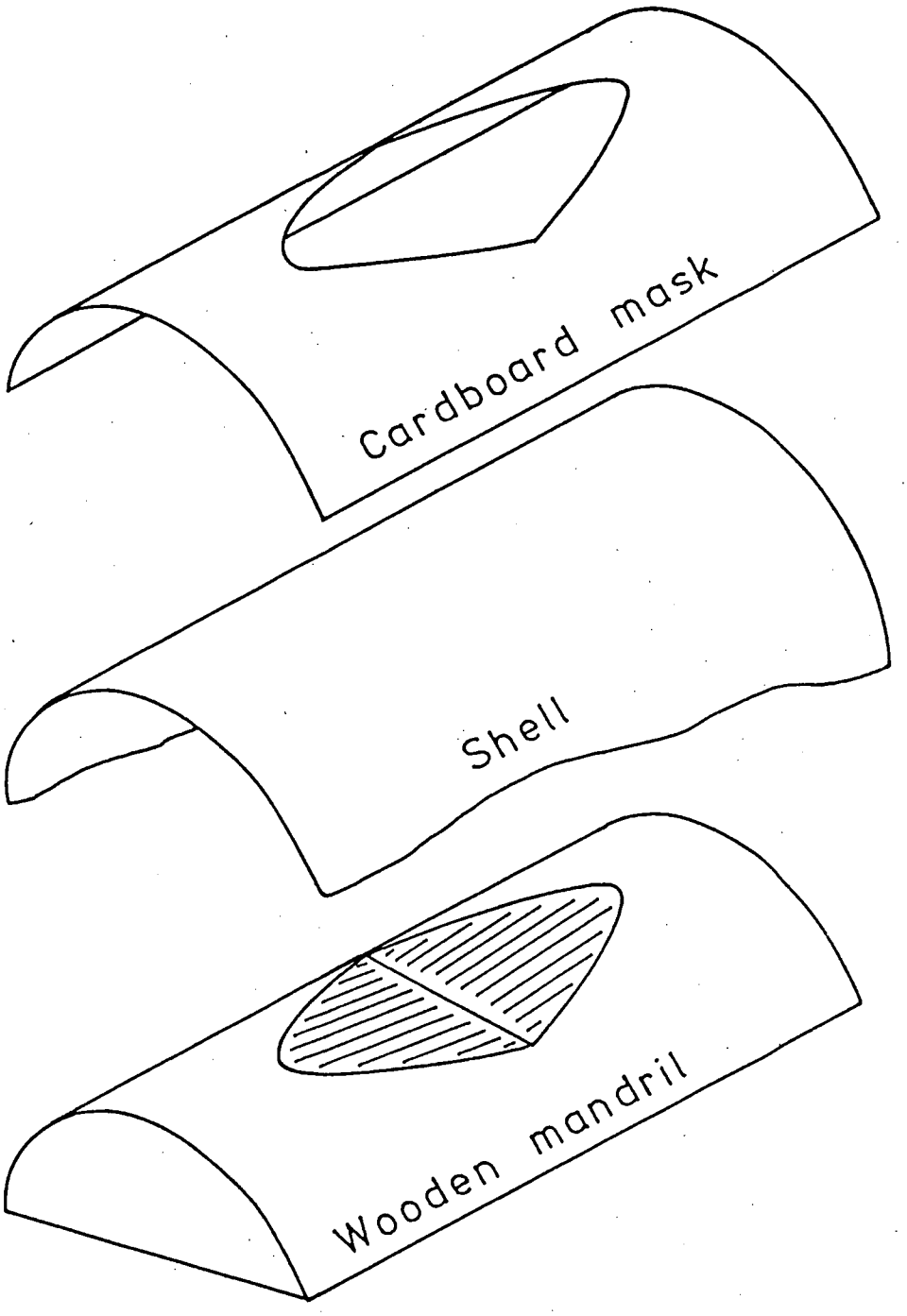

Figure 9.1
Method of Introducing Defects

introduced on the shell wall. It is to be mentioned that this technique of imposing defects was introduced by Foster and is described in Ref.24.

It is believed that the imposed defect which is formed by the local expansion of the epoxy material due to heating does not produce any local variations in the length of the generators of the shell owing to the presence of the end-rings. The fact that in shells which collapsed partially after introducing the defects the buckles were always formed next to the imposed defect attests to this; since if the length of the generators over the defect was smaller, the end load would have been mainly supported by the remaining portion of shell, causing the collapse to occur first in the area diametrically opposite to the imposed defect. A typical defect imposed on a shell (S43) is shown in Figure 9.2a; the photograph was taken at a load close to the collapse load of the shell. It can be seen that the defect is quite similar in shape and not easily distinguishable from the buckles formed after collapse, shown in the adjacent photograph (Figure 9.2b).

After the defect was introduced a period of at least three to four hours was allowed before the shell was mounted on the loading frame and tested again. As in the preliminary experiments, the tests were repeated three to four times and photographs were taken of the unloaded, loaded and buckled configurations of the shell. On shells which developed partial patterns on initial collapse the loading was continued and successive collapses recorded to check whether these

(a)

(b)

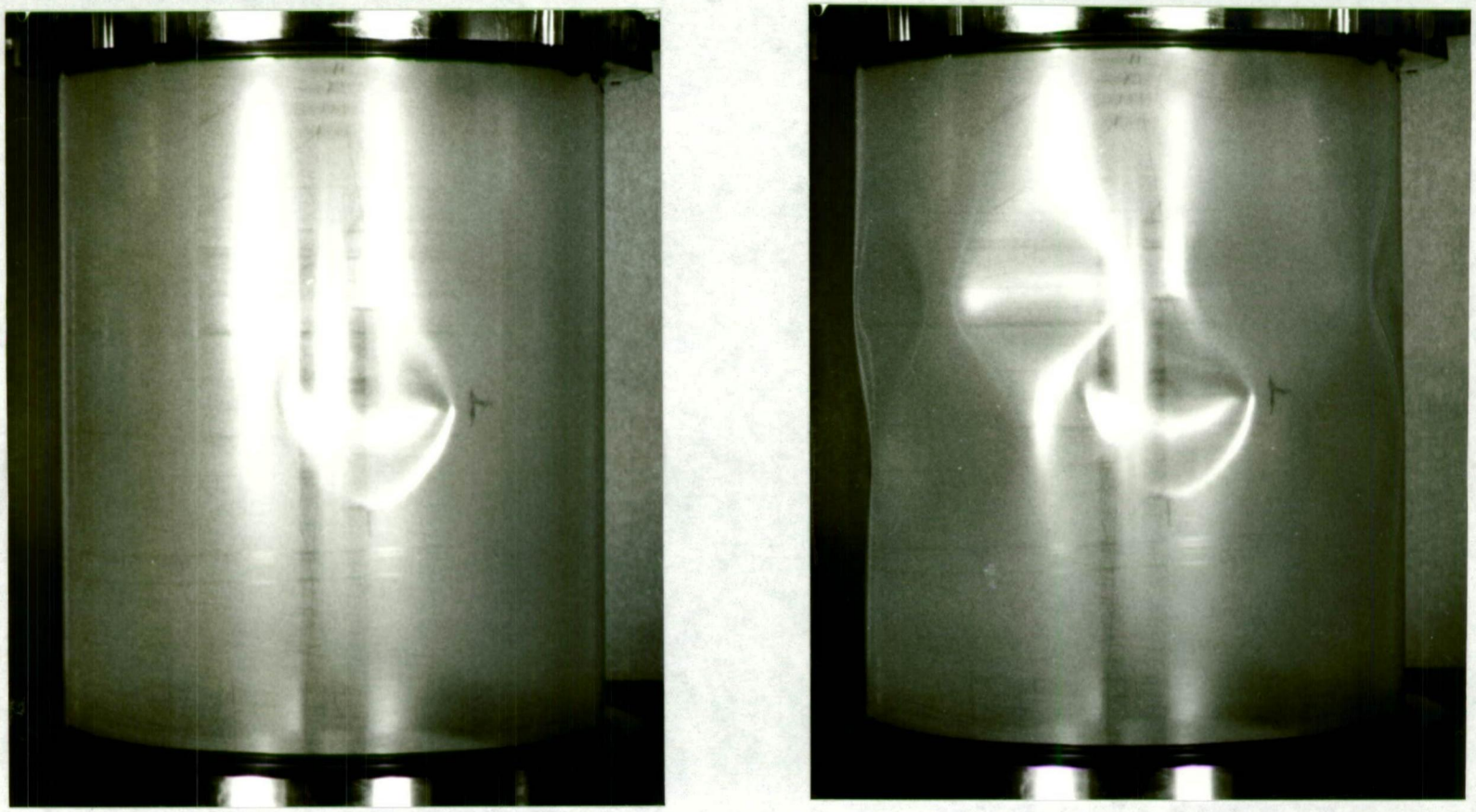

Figure 9.2. External View of Imposed Defect
Before and After Collapse (Size D3, Shell S43)

resulted in the formation of a complete pattern. In order to ascertain whether the removal of the shell and its replacement in the loading frame caused any reduction in its load carrying capacity by producing variations in alignment, some shells were removed, left overnight and replaced in the testing machine without introducing any defects. The buckling loads obtained in subsequent tests were always within 2% of the loads realized before the shell was removed, proving that errors from this source in estimating the detrimental effect of the imposed defects were negligible.

9.1 Size of the Defects Imposed

Defects of basically three different sizes were employed in the current series of tests. The geometric data of the notches in the mandrils used for producing these defects are shown in Figure 9.3. The most important parameter, the circumferential size of the defect, is given in terms of the angular measure θ (in degrees). The defects have been named D1 to D3 in increasing order of the circumferential size. The size of the defects (notches) in the mandril is referred to as the nominal size, to distinguish it from the actual size of the defect formed on the shell, which was usually smaller than the nominal size. The circumferential number of facets N corresponding to the nominal defect size, the aspect ratio and the maximum radial displacement (at the centre of the defect) are also given in the figure. The last value has been calculated from geometry for a shell diameter of 154 mm, on the basis that the two triangular facets meet along a chord of the circular section of the cylinder. For a wall thickness of 0.2 mm,

Defect D1

$\theta = 20.8°$

$N = 17.3$

$\lambda = 0.43$

$w_o = 1.3\,mm$

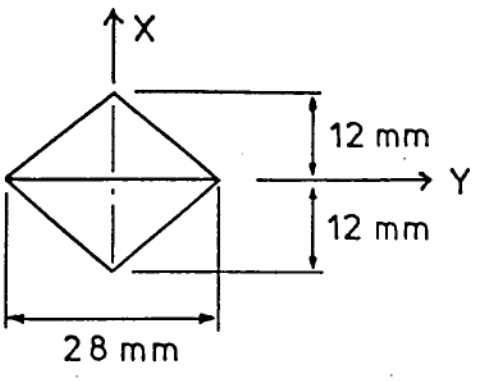

Defect D2

$\theta = 26.8°$

$N = 13.4$

$\lambda = 0.42$

$w_o = 2.1\,mm$

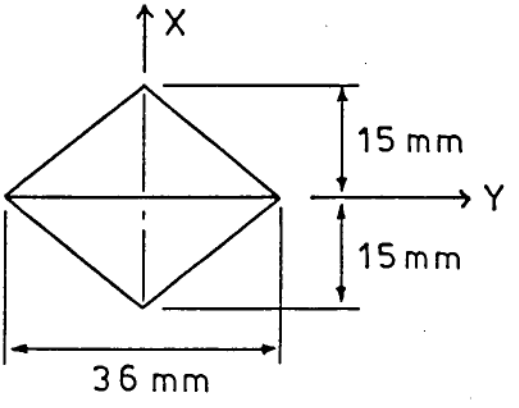

Defect D3

$\theta = 41.7°$

$N = 8.6$

$\lambda = 0.45$

$w_o = 5.0\,mm$

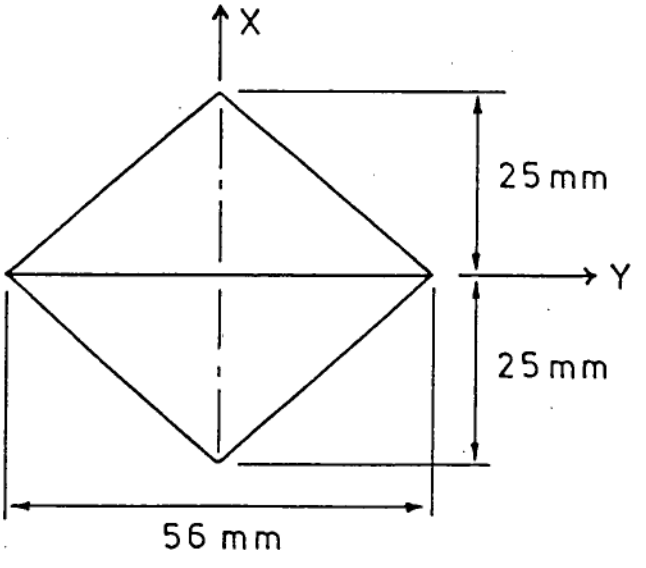

X : Axial direction. Y : Circumferential direction

w_o : Maximum radial deflection (at the defect centre)

Figure 9.3
Nominal Size of Imposed Defects

these represent central deflections of 6.5, 10.5 and 25 times the thickness of the shell, respectively, for the three defects.

The defects formed on the shells were smaller than their nominal sizes. Total replication of the 'V' shaped notches on the shells was rather difficult to achieve; in fact it was not attempted, the shells being very fragile and easily damaged if excess pressure or heat was applied on its surface. The actual sizes of the defects formed were measured from the photographs of the unloaded shells recorded through the optical system. The D1 defects formed on the shells had a circumferential size varying between 16° and 19°, their nominal size being about 21°. The D2 defects formed had sizes between 22° and 24°, their nominal size being about 27°; while the D3 defects, of nominal size about 42°, had actual sizes between 34° and 38°. For considering the effect of the defect size on the buckling load, the actual size measured from the photographs was used; however for the general description it is convenient to use the names D1 to D3, the three broad groups into which they have been classified. It may also be noted that although the actual defects impressed on the shell are somewhat smaller, the maximum deviations of the shell wall at the mid-point of the actual defects are of the same order of magnitude as those mentioned previously for each of the nominal sizes.

9.2 Description of the Tests

The experiments with local diamond shaped defects were conducted on thirty six of the forty six shells mentioned in the

previous chapter. The tests may be broadly classified into three categories: those with single, double and multiple defects. The shells were first tested with only a single defect imposed on them; defects of each size, D1 to D3, were introduced on twelve shells. A second defect was subsequently impressed on these shells and further tests conducted. On four of the shells, more defects were introduced until there were defects all round the circumference, with compression tests being carried out after imposing each additional defect.

Illustrations of the image recorded through the optical system of the single defects of nominal size D1 to D3 imposed on the shells are shown in Figures 9.4a, 9.5a and 9.6a respectively. The growth of the deformations in the vicinity of the defect with increase in load in the pre-buckling stage is illustrated by the photographs of shell S19 (with the defect D3) in Figures 9.6b to 9.6d. Shells S41 and S20 are shown in the loaded condition in Figures 9.4b and 9.5b. The defects in them (D1 and D2 respectively) can be seen to have grown considerably from their unloaded states (Figures 9.4a and 9.5a). Many shells developed complete patterns on first collapse like the two tier pattern of shell S41 (Figure 9.4c) and the one tier pattern of shell S34 (Figure 9.5e, the defect is the second buckle clockwise from the top). In some shells the initial collapse pattern extended over most of the circumference, and became complete with the next collapse, as seen in Figures 9.5c and 9.5d (shell S20). However in many cases the initial collapse produced only a few buckles adjacent to the imposed defect as in the case of S16 (unloaded and collapsed states in Figures 9.4d and 9.4e, respectively) and that of shell S11 in Figure 9.6e.

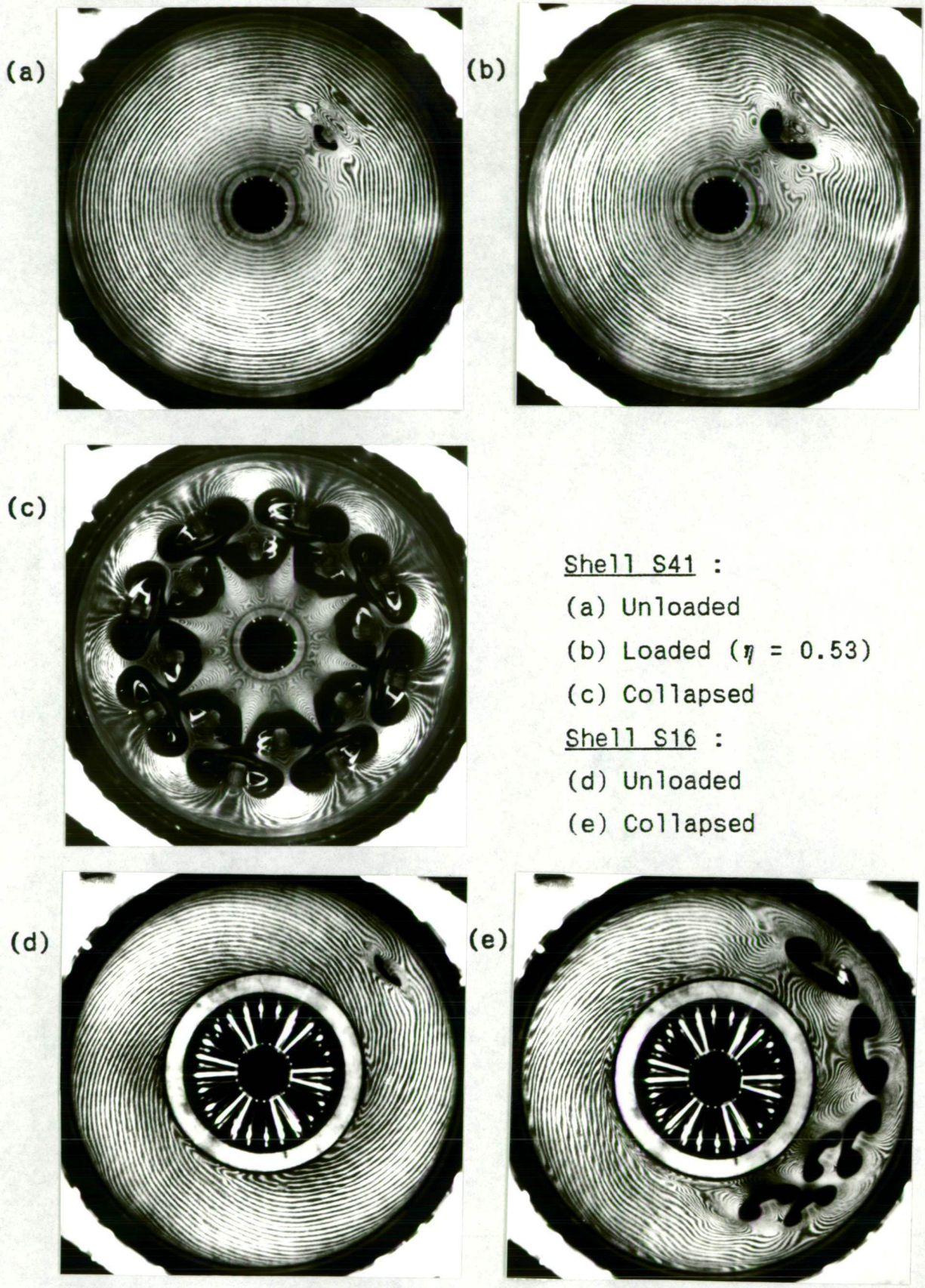

Shell S41 :

(a) Unloaded

(b) Loaded (η = 0.53)

(c) Collapsed

Shell S16 :

(d) Unloaded

(e) Collapsed

Figure 9.4. Illustrations
of Single Defect with Nominal Size D1

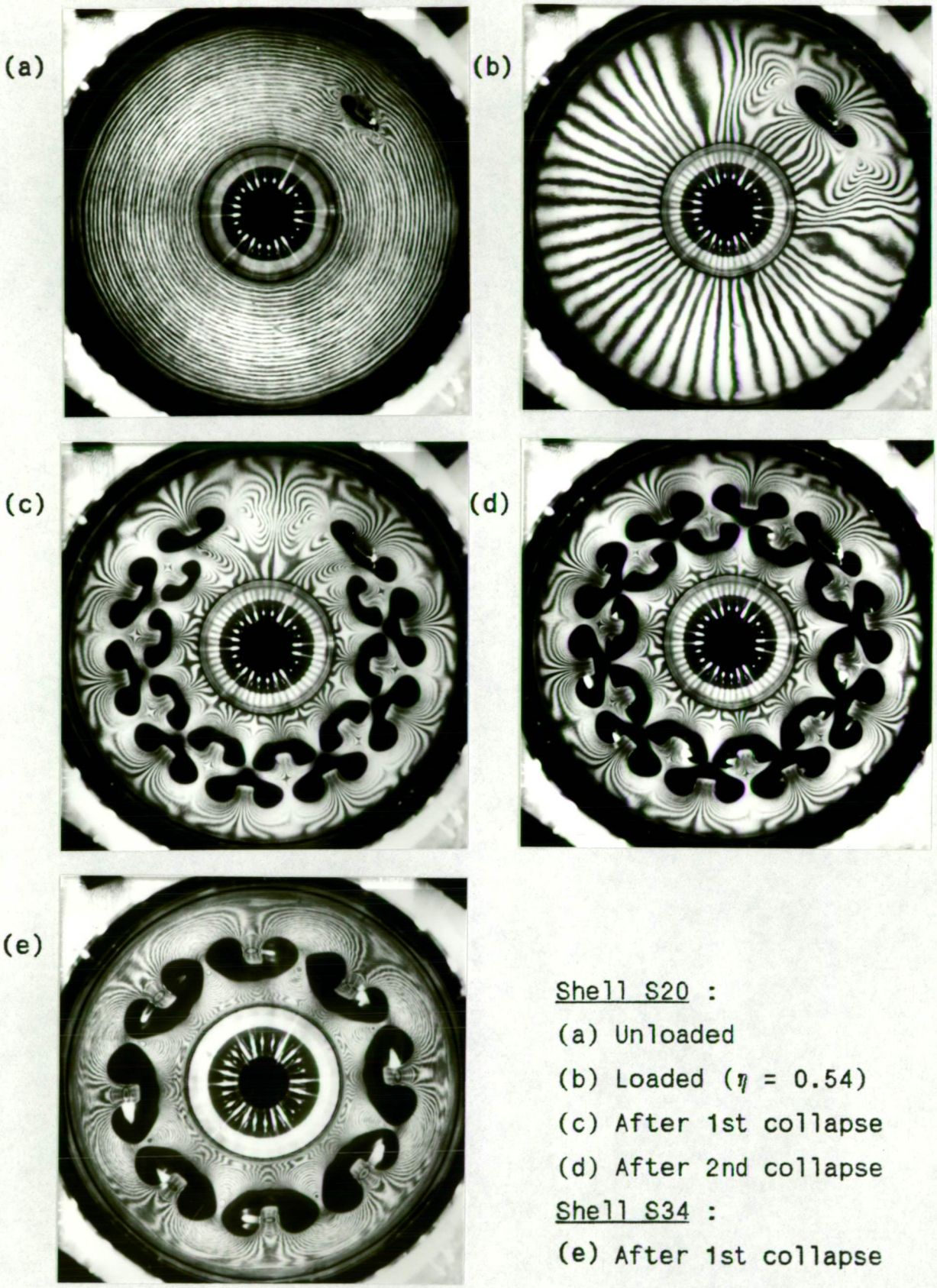

Shell S20 :

(a) Unloaded

(b) Loaded (η = 0.54)

(c) After 1st collapse

(d) After 2nd collapse

Shell S34 :

(e) After 1st collapse

Figure 9.5. Illustrations
of Single Defect with Nominal Size D2

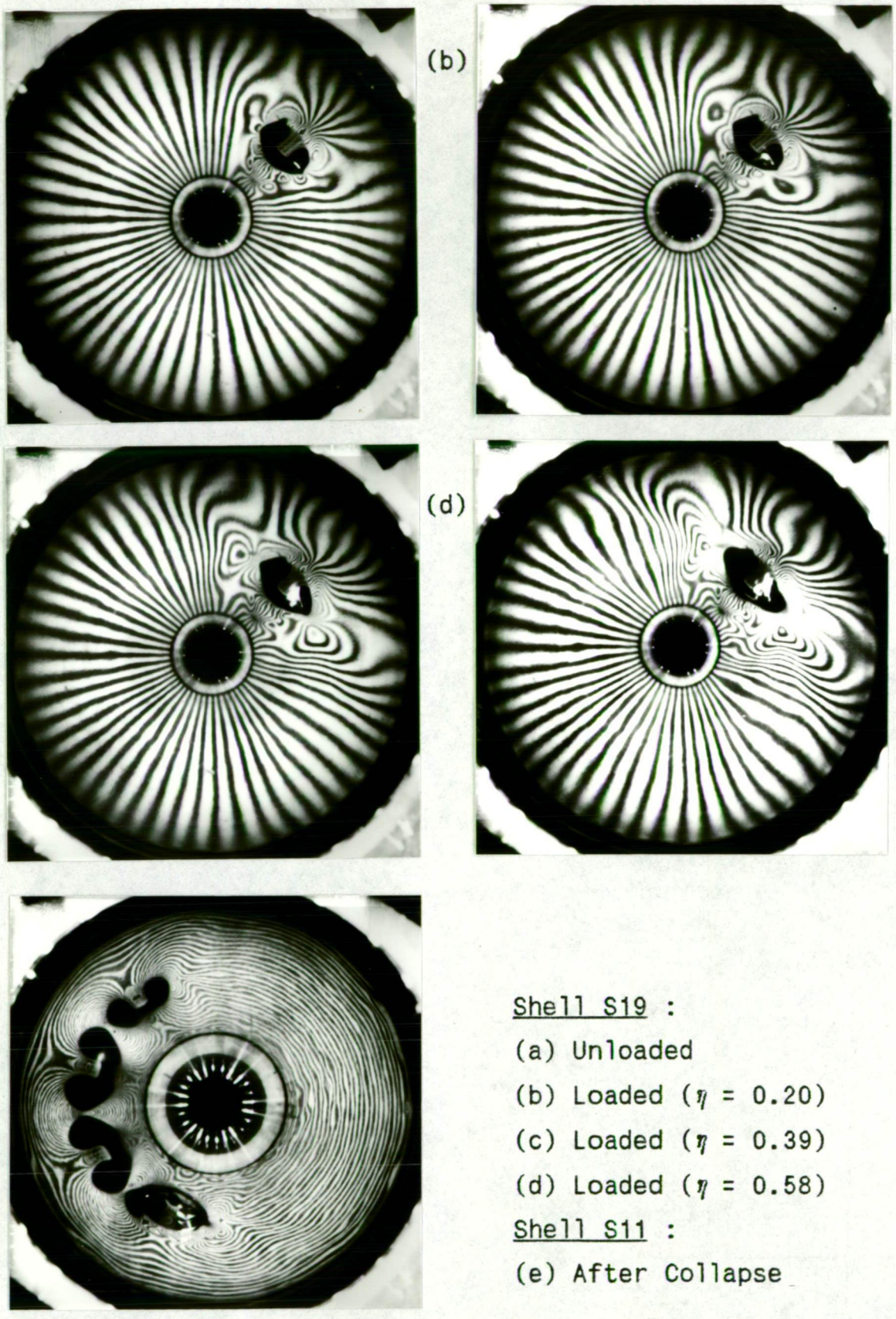

Shell S19 :

(a) Unloaded

(b) Loaded (η = 0.20)

(c) Loaded (η = 0.39)

(d) Loaded (η = 0.58)

Shell S11 :

(e) After Collapse

Figure 9.6. Illustrations
of Single Defect with Nominal Size D3

The growth of the defects with the increase in load in the pre-buckling stage is a rather interesting phenomenon. While even the largest defect D3 exhibited some growth (as seen in the Figures 9.6a to 9.6d), the maximum growth was observed in the smaller defects D1 and D2 (Figures 9.4b and 9.5b). Apparently the growth of the defects in the pre-buckling stage does not depend on the initial size of the imposed defect, but rather on its final size, which is the size of the remaining facets in the buckle pattern of the collapsed cylinder. The experiments were conducted with the expectation that the size of the imposed defects would dictate the buckle pattern of the collapsed cylinder, i.e., that the shell would collapse into a pattern with facets of the same size as the initial size of the imposed defect. Experience, however, was to the contrary; the defects always grew to the same size as the remaining facets in the buckled shell, whose size (or circumferential number) appears to be governed by the geometry of the shell and the end-shortening to which it is subjected, just as in the case of the perfect shells. (The fact that the largest defect grew the least is only because its initial size was closest to that of the buckles in the collapse patterns finally developed). While defects that were smaller than the final buckles could grow in size during the pre-buckling stage and in the process of collapse; if the initial size of the defects was larger than that of the facets in the complete pattern "expected" on collapse, the shells apparently preferred to develop incomplete patterns, rather than complete patterns with facets of a smaller size. It is to be noted that for the same value of the end-shortening, the one tier pattern requires a smaller number of facets around the circumference, and hence can accommodate buckles of

larger size than those of the corresponding two tier pattern. Thus if the defect was too large to develop a complete two tier pattern, some of the shells could still form a complete pattern of one tier; whereas in many cases even this was not possible. It is however to be noted that while all shells with defects which developed complete patterns appear to satisfy the geometrical requirements (see Table 9.3), not all shells which satisfied the requirements for complete patterns developed them; some still suffered partial collapse (a typical example is that of S20 in Figure 9.5c), due perhaps to the influence of other imperfections or lack of sufficient energy to go through the entire buckling process.

For the second defect imposed on the shells three positions (relative to the first defect) were chosen. Some of the second defects were introduced at the same level as the first one, and adjacent to it (Figure 9.7a, shell S20 with defects D2). Some others were introduced at the same level, but diametrically opposite to the first defect as shown in Figure 9.7c (shell S23, with defects D2). The third position chosen for the second defect was at a different height from that of the first defect but adjacent to it, so that the two defects appeared like adjacent facets in a two tier pattern, as in the photograph of shell S37 (with defects D1) in Figure 9.7e. The position of the second defect did not alter the type of patterns developed; as with a single defect some shells developed complete one or two tier patterns (though these were in number fewer than those with single defect), while the others buckled into partial patterns. The partial collapse patterns of shells S20 and S23 are shown in Figures 9.7b and 9.7d respectively.

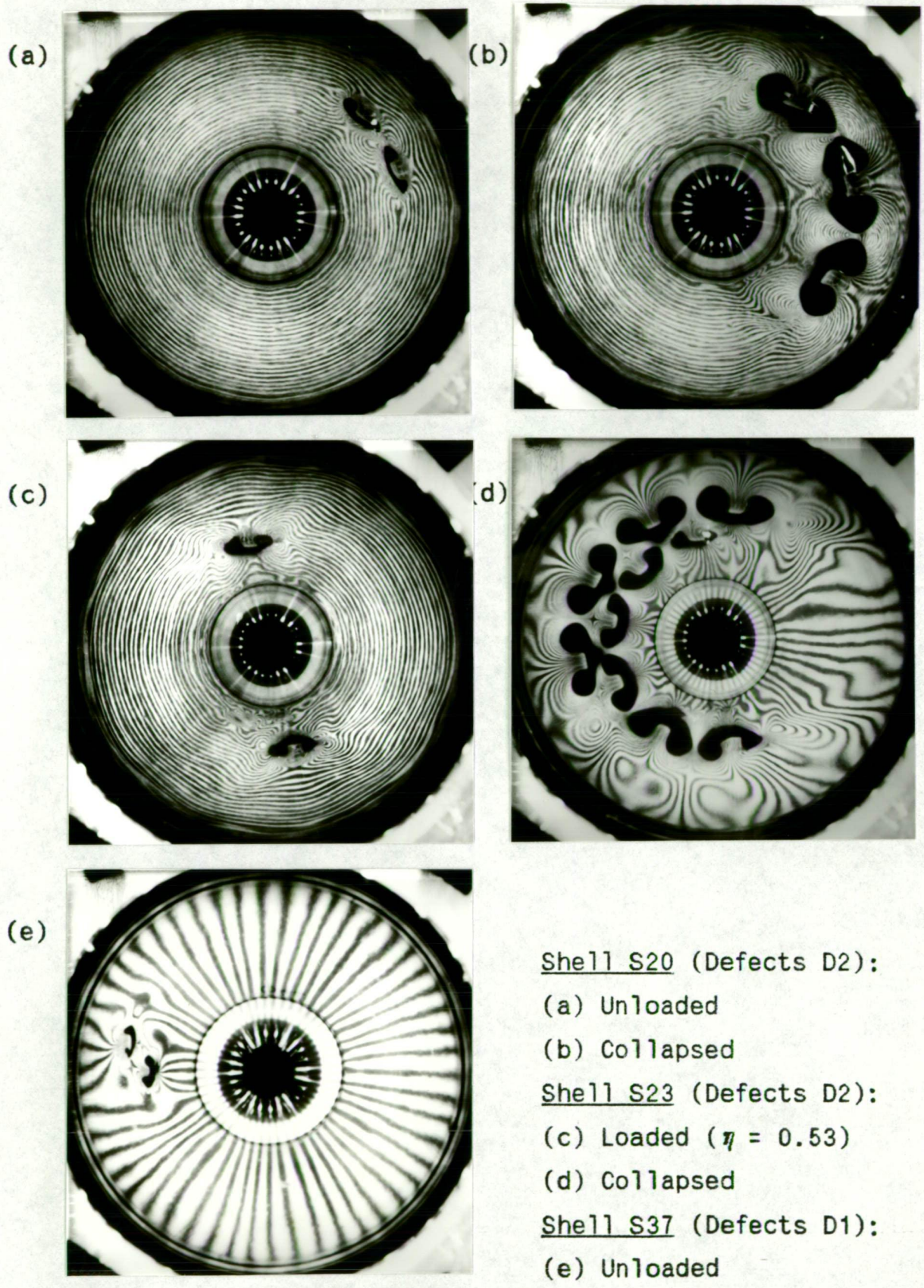

Shell S20 (Defects D2):
(a) Unloaded
(b) Collapsed
Shell S23 (Defects D2):
(c) Loaded (η = 0.53)
(d) Collapsed
Shell S37 (Defects D1):
(e) Unloaded

Figure 9.7
Illustrations of Shells with Two Defects

The second defect was introduced in the next tier in the hope that this would induce the shells to develop two tier patterns. Although some of these shells did buckle into two tier patterns (a typical example is that of shell S36, shown in Figure 9.8a - the defects in the shell are the second buckles in the clockwise direction from the top in both the tiers), most of the shells developed only one tier patterns. The percentage of two tier collapses observed in shells having two tier defects was no more than that in the case of shells with both defects in the same tier. Two further attempts to produce two tier buckle patterns are illustrated in the figures 9.8b to 9.8e. Figure 9.8b shows the unloaded photograph of shell S16 in which a third defect was introduced in the upper tier (towards the inner ring) after the tests with two adjacent defects in the lower tier were completed. The shell collapsed into a partial one tier pattern which was completed after one more collapse as shown in Figure 9.8c. Using a mandril in which three diamond shaped facets were carved, two at one level and the third located above and in between the first two, an attempt was made to impose a two tier defect in shell S13. The folds of the defect were very poorly formed on the shell, due to the difficulty of imprinting all three facets simultaneously, as can be seen from the unloaded photograph in Figure 9.8d. On loading, however, the defects developed into full-fledged facets; but the collapse was only partial and produced only two one tier buckles next to the imposed defects as depicted in Figure 9.8e. These early attempts served only to confirm the observation that the collapse pattern is largely governed by the end-shortening and the geometry of the shell, rather than the geometry of the defect imposed.

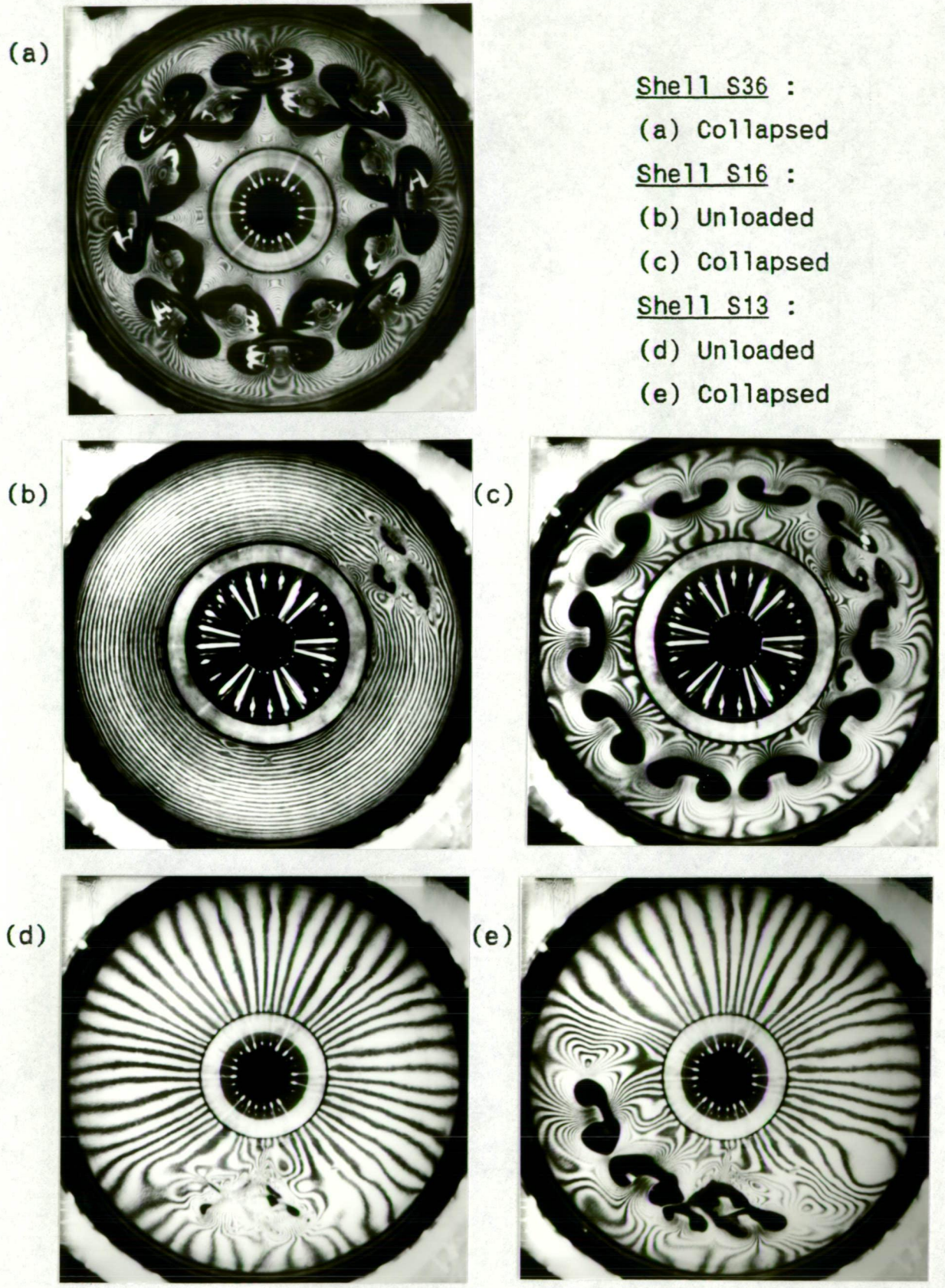

Figure 9.8. Effect of
Two Tier Defects on Collapse

The load deflection diagrams of two of the shells tested, S45 and S30 are shown in Figures 9.9a and 9.9b. In both the shells the defects introduced were of nominal size D1 and the second defect was imposed adjacent to the first one (at the same height). Both shells belong to group B and had developed complete two tier patterns (with N = 11 and 15 respectively) before introducing the defects. Shell S45 buckled again into a complete two tier pattern with N = 11 with one defect and developed a partial two tier pattern (N = 10) with two defects, which was completed after two more collapses. The initial collapses of shell S30 produced only a few buckles, of one tier (N = 12) with one defect, and of two tier (N = 13) with two defects. It may be noted that the initial post-buckling loads of shell S30 are very high in both tests, this being characteristic of shells which suffer partial collapse. It was also observed that if the number of facets formed initially was very low (as in this case), when the shell was subjected to further end-shortening the load exceeded the initial collapse value; the maximum load of the shell was attained only at the time of second or third collapse as seen in the plot in Figure 9.9b.

Even with the defects, the pre-buckling paths followed by the shells are fairly linear, as can be seen in the plots. In the advanced stages before buckling the path begins to curve (the linear path is indicated by the dash-dotted lines in Figure 9.9a), which is typical of the behaviour of most of the shells tested. It appears that this non-linearity arises from an increase in the rate of growth of the defect imposed. It is also to be mentioned that in a few cases when the folds of the defects imposed were not so well formed, some

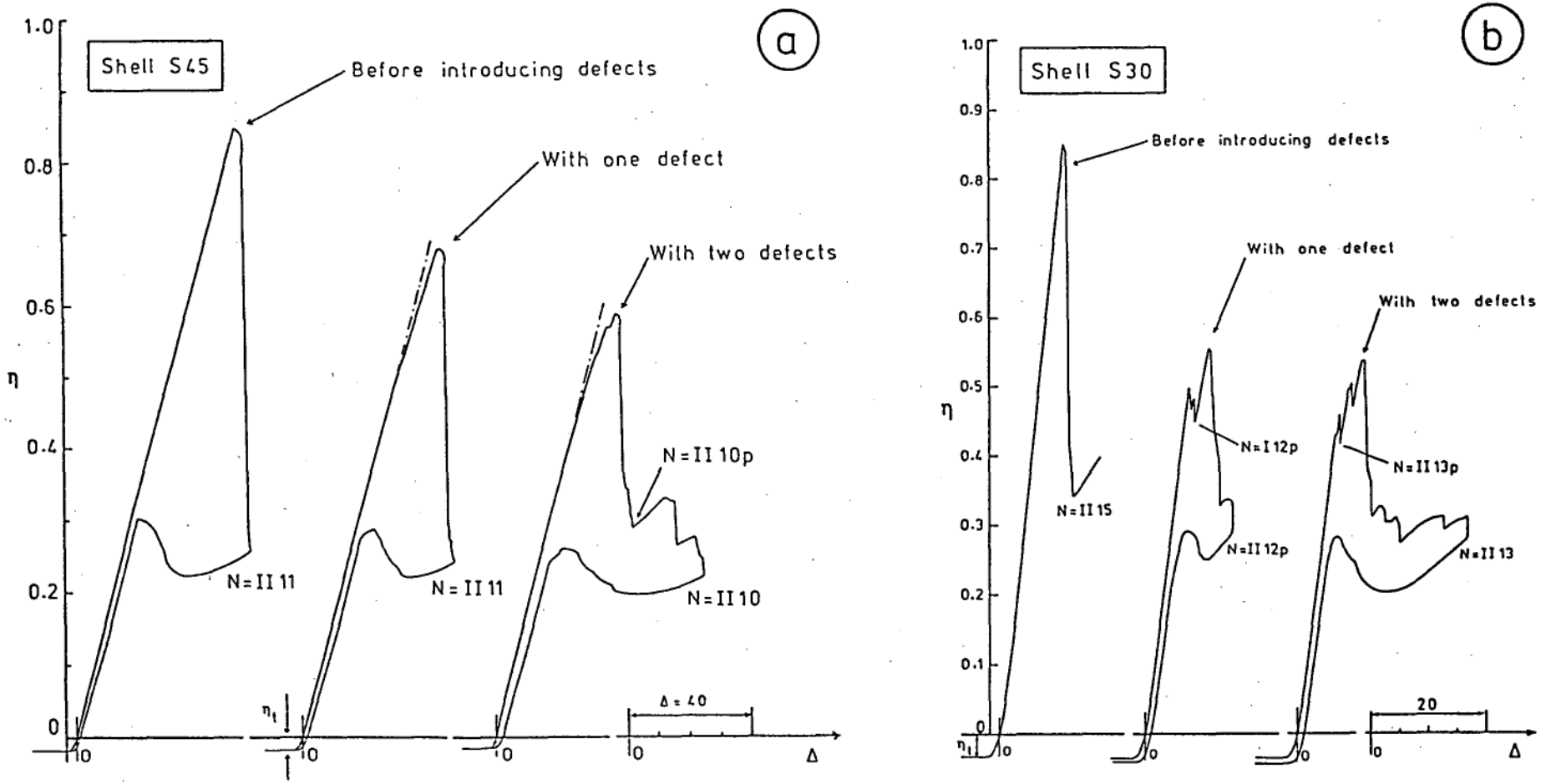

Figure 9.9. Load Deflection Diagrams of Shells with Imposed Defects (a) Shell S45 (b) Shell S30

non-linearity could be observed at the bottom of the pre-buckling path, i.e., in the initial stages of loading; this usually resulted in the defect developing into proper shape, the ensuing pre-buckling path becoming more or less linear. Comparison between the slopes of the linear sections of the pre-buckling paths of the shells with defects and the slopes recorded before imposing the defects shows that there is a reduction in the magnitude of the slope or the effective stiffness of the shell when the defect is introduced and that this reduction increases with increasing number of defects imposed. It was found that the reduction in stiffness is of the order of 5% with one defect and about 10% with two defects imposed on the shells.

Four shells belonging to group A, in which adjacent defects of the largest size D3 were imposed, were selected for the tests with multiple defects. Introducing additional defects adjacent to the first two (at the same height) in a serial fashion, these shells were tested after adding each new defect. The photographs of one shell tested with multiple defects (S43) are shown in Figure 9.10. The unloaded and collapsed states of the shell with four imposed defects are shown in Figures 9.10a and 9.10b. Figure 9.10c shows the unloaded photograph with eight defects around the circumference; the pattern observed after initial collapse is shown in Figure 9.10d. The two tier pattern is complete except for one buckle at the 10 o'clock position which is formed below the imposed defects instead of above, as if by mistake. The mistake was corrected in the next collapse, with the buckle moving to its proper position, as can be seen in the next photograph (9.10e). Interestingly, this apparently innocuous behaviour was observed in

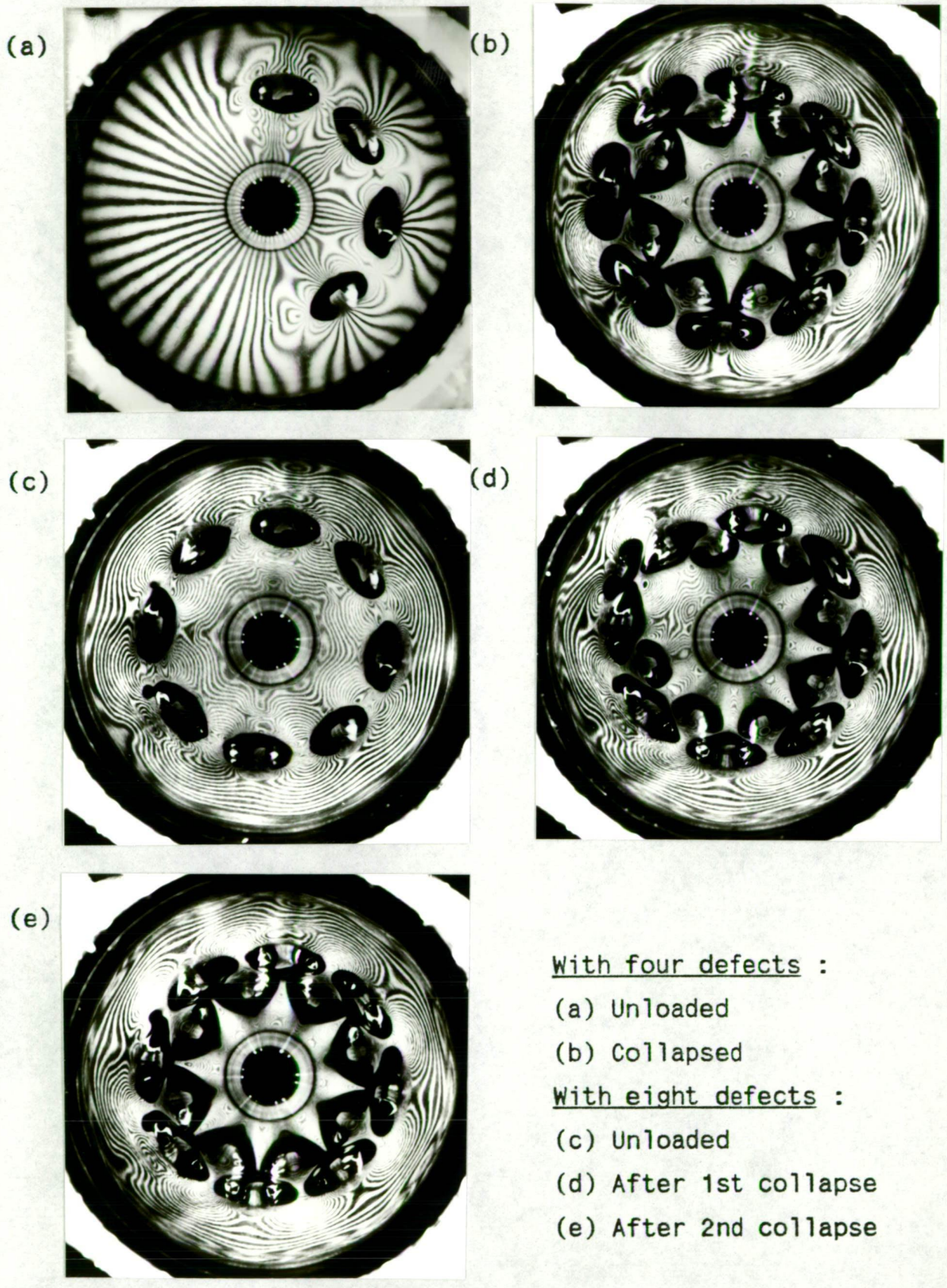

With four defects :

(a) Unloaded

(b) Collapsed

With eight defects :

(c) Unloaded

(d) After 1st collapse

(e) After 2nd collapse

Figure 9.10
Multiple Defects in Shell S43 (Size D3)

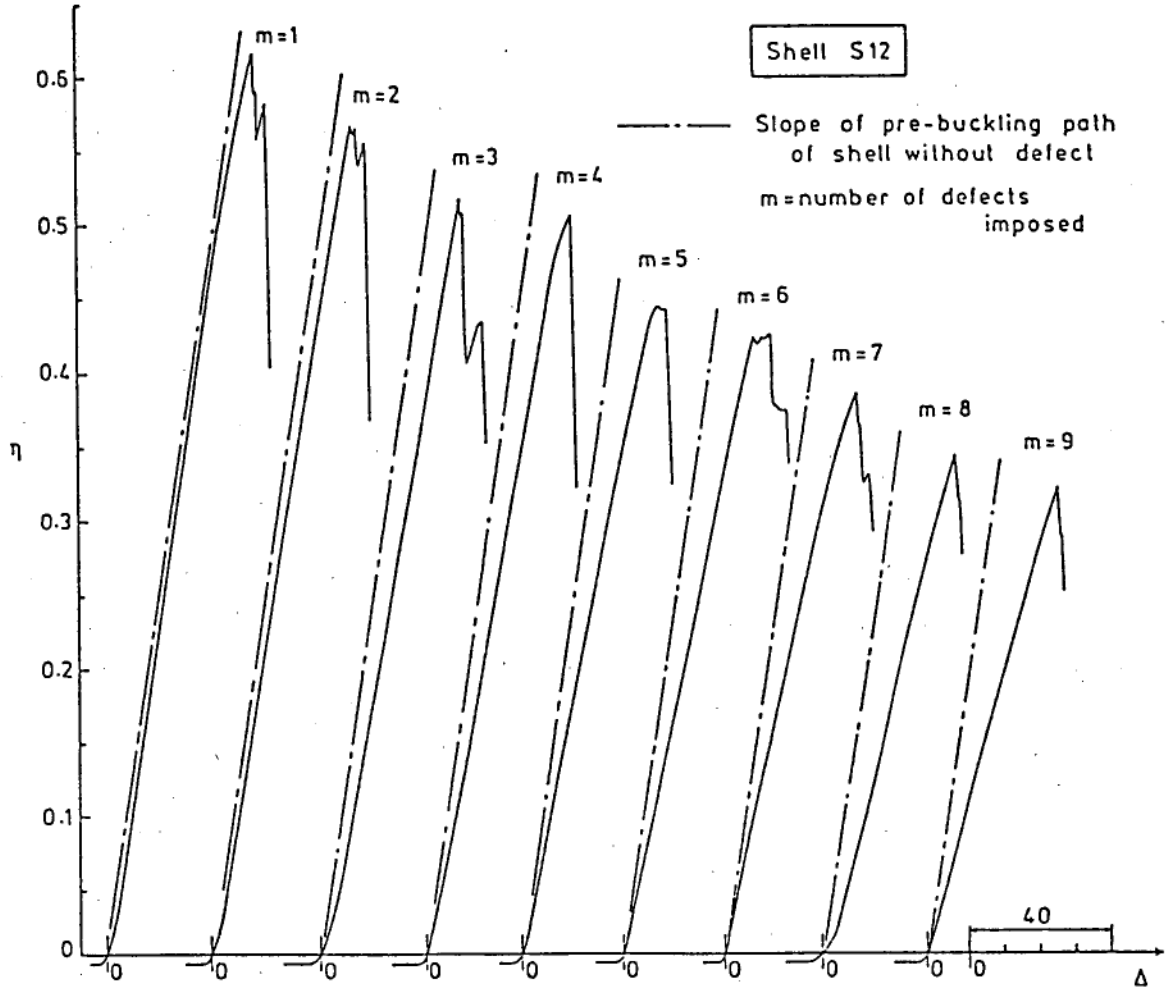

Figure 9.11. (Shell S12)
Reduction in Shell Stiffness
with Increasing Number of Defects

three of the four shells tested (S11, S12 and S43) with defects all round the circumference, and is being mentioned in passing only as a matter of curiosity.

The load deflection diagrams of shell S12 obtained after the addition of each successive defect (m = 1 to 9) are shown in Figure 9.11. The slope of the pre-buckling path observed before introducing any of the defects is shown in dash-dotted lines with each plot for comparison. The loading path in each case has been terminated after the occurrence of collapse, the main purpose being to indicate the decrease in the effective stiffness of the shell with the addition of each successive defect and the gradual reduction in the load carrying capacity of the shell.

9.3 Results of Tests with Single Defect

The buckling loads and modes observed in the tests with single defects are presented in Table 9.1. The maximum collapse load obtained with the single defect was about 76% of the classical load and the minimum value 52%. In general, the values of the knockdown factor η (ratio of the collapse load to the classical load) are higher for the shells which developed complete patterns on collapse than for those which suffered partial collapse. The modes indicated are those observed on initial collapse, the suffix "p" denoting partially formed patterns. In some shells, although the patterns formed were complete, they were somewhat irregular (that is the facets were not exactly aligned or were not all of the same size); these modes are indicated

Table 9.1 Buckling Data of Shells with Single Defect

Shells with Defect D1									
S.No.	Shell	Group	η_{cr}	Mode	S.No.	Shell	Group	η_{cr}	Mode
1	S35	A	0.740	II 9	7	S44	A	0.691	II 11i
2	S41	A	0.689	II 8	8	S40	A	0.757	I 12i
3	S45	B	0.681	II 11	9	S16	B	0.671	I 10p
4	S36	A	0.709	I 7	10	S27	A	0.647	I 12p
5	S39	A	0.692	I 9	11	S38	B	0.613	I 10p
6	S37	B	0.595	I 9	12	S30	B	0.554	I 12p

Shells with Defect D2									
S.No.	Shell	Group	η_{cr}	Mode	S.No.	Shell	Group	η_{cr}	Mode
1	S8	A	0.748	II 11	7	S33	B	0.691	II 10i
2	S32	C	0.696	II 11	8	S20	B	0.661	II 10p
3	S42	A	0.752	I 11	9	S23	A	0.649	II 10p
4	S46	A	0.711	I 7	10	S31	C	0.676	I 13p
5	S34	A	0.684	I 8	11	S17	C	0.628	I 11p
6	S22	A	0.621	I 9	12	S29	B	0.519	I 10p

Shells with Defect D3									
S.No.	Shell	Group	η_{cr}	Mode	S.No.	Shell	Group	η_{cr}	Mode
1	S43	A	0.730	II 8	7	S25	A	0.621	I 8p
2	S18	A	0.706	II 9	8	S11	A	0.619	I 9p
3	S26	A	0.721	I 8	9	S12	A	0.616	I 9p
4	S24	A	0.652	I 8	10	S9	D	0.578	I 9p
5	S19	A	0.693	II 7p	11	S14	C	0.577	I 10p
6	S28	B	0.574	II 11p	12	S15	C	0.565	I 10p

Note : I - one tier ; II - two tier ; p - partial ; i - irregular.

with the suffix "i". It may be mentioned that in the few cases wherein the shells sustained higher loads than the load at which the first collapse occurred (such as that of shell S30 in Figure 9.9b), the maximum loads attained by the shells have been presented.

The actual circumferential size of the imposed defect, measured from the photographs of the unloaded shells, are presented in Tables C2a to C2c in Appendix C. These tables also provide the remaining data observed in the tests with single defects, viz, the sizes of the defects in the loaded and collapsed states, the ratio of the effective stiffness of the shell with the defect (measured from the slope of the linear part of the pre-buckling path) to the stiffness recorded before introducing the defect, and the location of the defect (the distance of the central fold from the bottom end of the shell). Most of the defects were located slightly above or below the mid-section of the shells. (This was initially done with a view to inducing the shells to develop two tier patterns; and later continued so that when a second defect was imposed in the next tier, the two defects would be more or less symmetrically situated about the mid-section). It is however to be noted that in all cases the defects are located sufficiently away from the ends to be unaffected by the boundary conditions on the shells. The aspect ratios of the imposed defects ranged between 0.4 and 0.45. Although it was initially intended to perform tests with higher values of the aspect ratio for comparison, this was not carried out, mainly because of the scatter observed in the results, from which it would have been too difficult to isolate the effect of the aspect ratio.

The observed buckling loads are plotted against the measured circumferential sizes of the defects (unloaded) in Figure 9.12. The mean (the linear least square fit) and the 99% probability levels (given by $\pm 3\sigma$, where σ is the standard deviation of the sample) are indicated. The values obtained by Foster[24] in tests conducted on four shells with imposed defects are also plotted. As seen, the scatter in the observed knockdown factors is much greater than the small reduction (indicated by the mean) in the load carrying capacity of the shells with increasing defect size. While some of the scatter could be attributed to the variations in the location and the aspect ratio of the defects and perhaps to the presence of initial imperfections in the shells, it is felt that a significant portion of it arises from variations in the degree of sharpness with which the defects and their folds were imprinted on the shells. Unfortunately due to the delicate nature of the process by which the defects are introduced, greater uniformity could not be ensured. From a positive point of view, these irregularities in the formation of the defects may be regarded as typical of what may be expected in naturally occurring defects and the scatter as a more realistic representation of the practical situation.

Perhaps the most important observation to be made is that in no case is the buckling load less than 50% of the classical load, even with the largest defect D3 whose maximum radial deflection is of the order of 20 times the thickness of the shell. This is particularly significant in view of the fact that axisymmetric imperfections with an amplitude of about half the wall thickness reduces the buckling load to less than 25% of the classical load (see Figure 2.2).

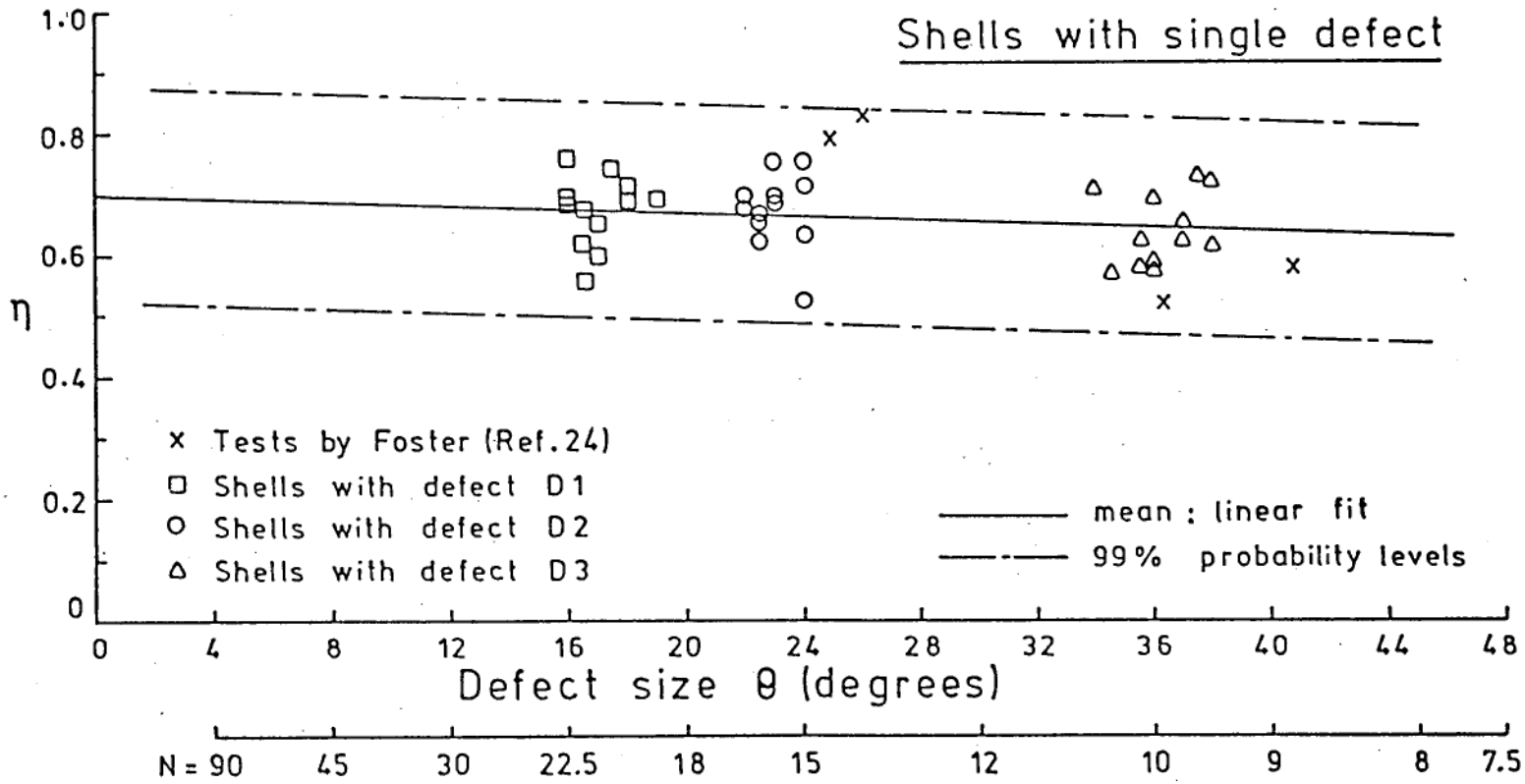

Figure 9.12. Effect of Variation in Defect Size on the Collapse Load of Shells with Single Defect

The test results are compared with the knockdown factors predicted by the space frame models in Figures 9.13a to 9.13c. The predictions of the original space frame theory (using an effective width ratio of 22.7 and aspect ratio from eqn.3.17) are indicated by the broken lines, and the values from the space frame model without spring (using K = 1.6 and λ = 0.5) are shown by the solid lines. For the smallest defect D1, the curves have been plotted for N = 22 and 19, since the measured sizes of the defects ranged between $\theta = 16^{\circ}$ and $\theta = 19^{\circ}$. The curves for the second defect D2 have been plotted for N = 16 and N = 15, corresponding to $\theta = 22.5^{\circ}$ and 24°. In Figure 9.13c the curves are shown for N = 10, corresponding to the average measured size of 36° for the largest defect D3. The agreement obtained by Foster[24], in tests conducted on four shells having defects of sizes N = 14.4, 13.8, 9.9 and 8.8, with the predictions of the original space frame theory is also indicated in the figures. For the larger range of results obtained in the present case however, the correlation between the experimental values and the predictions from the two models is quite poor. In general the predictions are too high for the smallest defect and too low for the largest defect. Further, while the original model predicts a steep reduction in the buckling load with increasing R/t for a given size of the defect, the observed values do not even show as much variation as that suggested by the modified model.

The ratio of the collapse load obtained with a single defect to the buckling load observed before introducing the defect (η_1/η_0) is plotted against the radius to thickness ratio of the shells in Figure 9.14a and against the length to radius ratio in Figure 9.14b. The mean

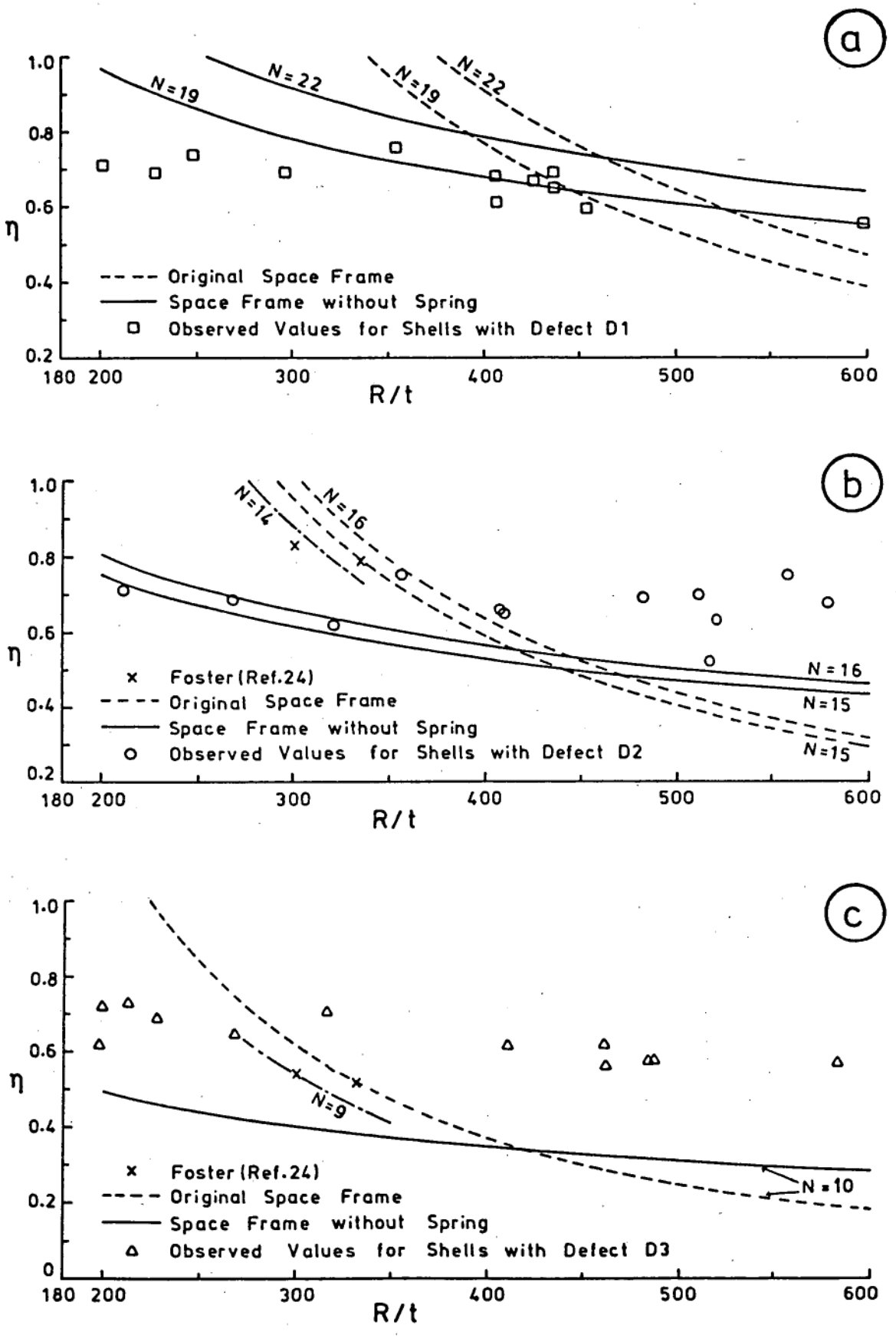

Figure 9.13. Comparison with Space Frame Theory
(a)Defect D1 (b) Defect D2 (c) Defect D3

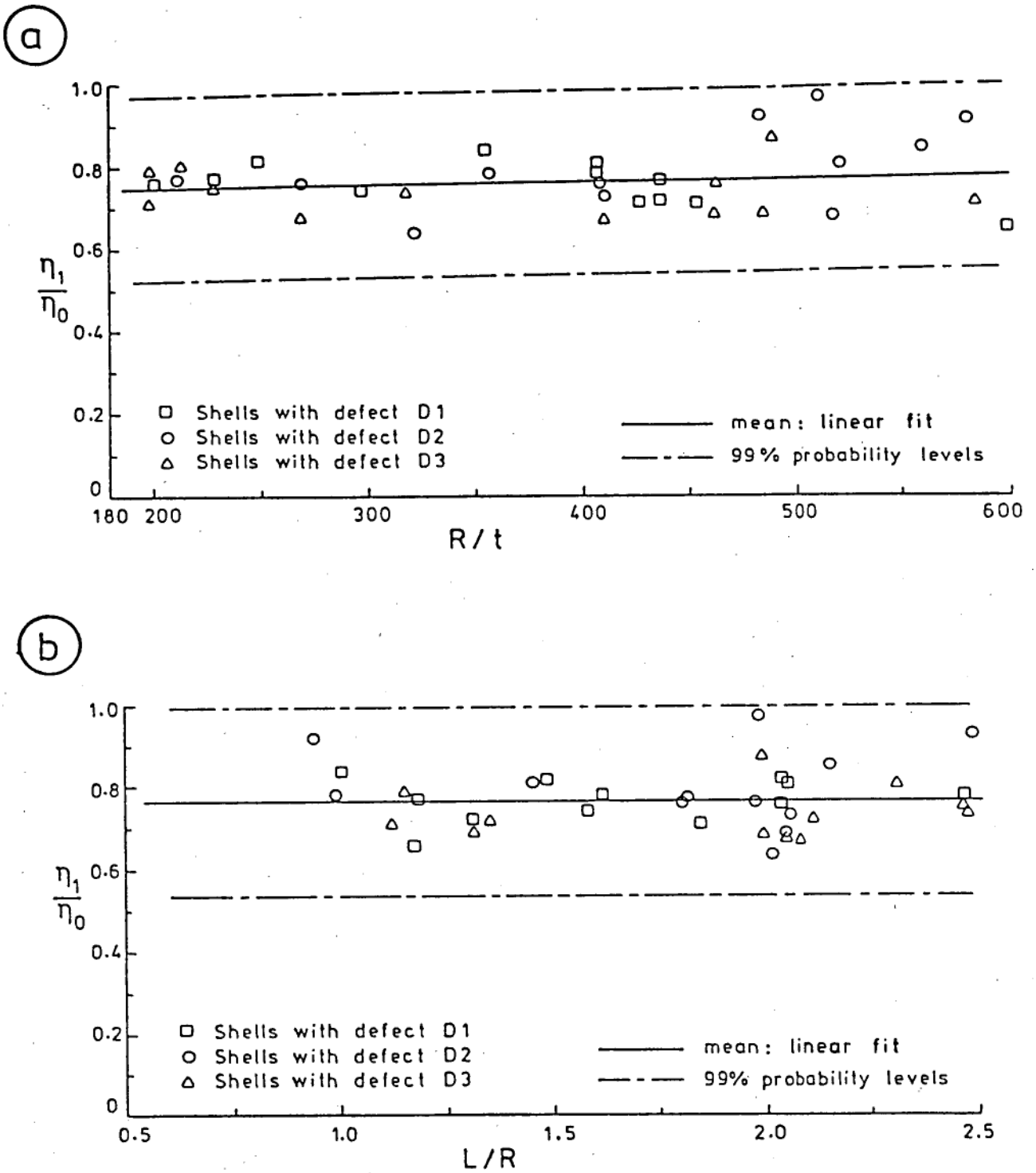

Figure 9.14. Effects on the Collapse Load
(a) of Radius to Thickness Ratio
(b) of Length to Radius Ratio

plotted in Figure 9.14a shows a slight *increase* with the radius to thickness ratio; this may however be attributed to the greater number of shells with high values of R/t which collapsed at lower values of η_0 in the tests conducted before introducing the defects. It therefore appears reasonable to conclude that the effect of diamond shaped local defects on the buckling of axially loaded cylindrical shells is more or less independent of the radius to thickness ratio as well as the length to radius ratio of the shells.

9.4 Results of Tests with Two Defects

The buckling loads and modes observed in tests conducted with two defects on the shells are presented in Table 9.2. Except for two shells S27 and S29 in which the second defects were interchanged, all shells were imposed with second defects of the same nominal size as the first one. In 26 shells the two defects were located at the same height: in six of them the defects were diametrically opposite to each other and in the remaining side by side. In ten shells the two defects were located at different heights simulating adjacent facets in a two tier configuration. The exact location of the second defect relative to the first one, as well as its circumferential size before loading and after collapse, and the ratio of the reduced stiffness of the shell to the stiffness measured before introducing the defects are presented in Appendix C in Tables C3a to C3c.

The knockdown factors obtained in the tests are plotted against the measured circumferential sizes of the second defects in

Table 9.2 Buckling Data of Shells with Two Defects

Adjacent Defects in the Same Tier											
S.No.	Shell	Defects		η_{cr}	Mode	S.No.	Shell	Defects		η_{cr}	Mode
		1st	2nd					1st	2nd		
1	S45	D1	D1	0.586	II 10p	11	S31	D2	D2	0.600	I 13p
2	S44	D1	D1	0.719	II 11i	12	S17	D2	D2	0.583	I 11p
3	S40	D1	D1	0.721	I 12i	13	S43	D3	D3	0.635	II 8
4	S16	D1	D1	0.558	I 10p	14	S18	D3	D3	0.499	I 8p
5	S38	D1	D1	0.588	I 10p	15	S26	D3	D3	0.689	II 9p
6	S30	D1	D1	0.537	II 13p	16	S19	D3	D3	0.591	I 7
7	S27	D1	D2	0.567	I 11p	17	S28	D3	D3	0.536	II 11p
8	S32	D2	D2	0.677	II 11	18	S25	D3	D3	0.607	I 8p
9	S42	D2	D2	0.762	I 12	19	S11	D3	D3	0.520	II 9p
10	S20	D2	D2	0.558	I 10p	20	S12	D3	D3	0.571	I 9p

Diametrically Opposite Defects in the Same Tier											
S.No.	Shell	Defects		η_{cr}	Mode	S.No.	Shell	Defects		η_{cr}	Mode
		1st	2nd					1st	2nd		
1	S41	D1	D1	0.580	I 7	4	S22	D2	D2	0.597	I 8
2	S29	D2	D1	0.543	I 10p	5	S23	D2	D2	0.604	II 10p
3	S8	D2	D2	0.706	II 10p	6	S24	D3	D3	0.593	I 8p

Adjacent Defects in Different Tiers											
S.No.	Shell	Defects		η_{cr}	Mode	S.No.	Shell	Defects		η_{cr}	Mode
		1st	2nd					1st	2nd		
1	S35	D1	D1	0.677	II 9	6	S34	D2	D2	0.697	I 8
2	S36	D1	D1	0.709	II 8	7	S33	D2	D2	0.647	II 10i
3	S39	D1	D1	0.655	I 9	8	S9	D3	D3	0.539	I 10p
4	S37	D1	D1	0.592	II 10p	9	S14	D3	D3	0.614	I 10p
5	S46	D2	D2	0.718	I 8	10	S15	D3	D3	0.568	I 10p

Note : I - one tier ; II - two tier ; p - partial ; i - irregular.

Figure 9.15a. Nearly the same amount of scatter is observed as with the single defects, although the mean values are slightly lower in this case. The minimum load recorded was about 50% of the classical value, while the maximum was 76.2% - slightly higher than the maximum recorded with single defects. In fact many shells registered higher collapse loads when tested with two defects than with one defect, as may be seen from the ratios of the knockdown factors with one and two defects plotted in Figure 9.15b. Most of these shells had the second defect in the next tier; six of the ten shells in this group reached higher collapse loads after the second defect was introduced, whereas only three of the remaining shells did the same. The average value of the ratio of the knockdown factors for the shells with the two tier defects is 0.98, while it is only 0.92 for the twenty six shells which had both defects in the same tier. The effect of having two defects at the same height appears to be nearly the same, whether the defects are located adjacent or diametrically opposite to each other. While the second defect introduced at the same level mostly reduced the strength of the shell, the results indicate that employing the second defect in the next tier can often increase the load carrying capacity of the shell, by mitigating the effect of the first defect in it.

As mentioned earlier, the geometrical relations developed in Chapter 6 for the post-buckling modes appear to hold good even for the shells with imposed local defects. In Table 9.3 the circumferential number of facets observed in shells with one and two defects which developed complete patterns on collapse is compared with the minimum number predicted from the value of the end-shortening measured in the

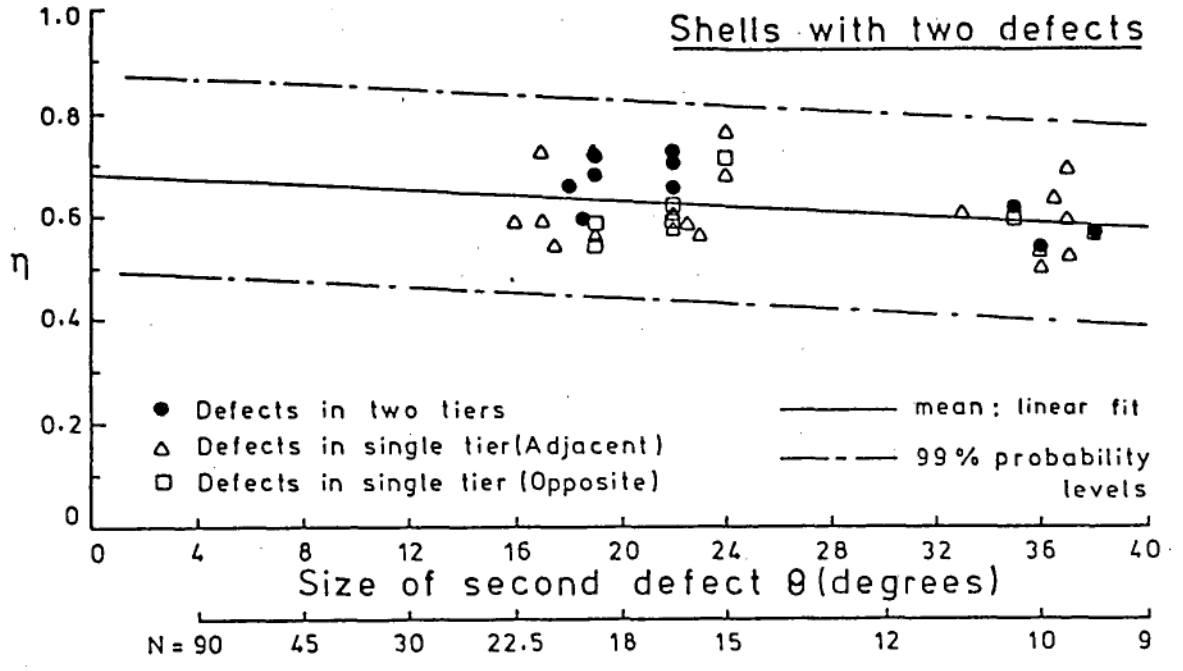

Figure 9.15a. Knockdown Factors of Shells with Two Defects

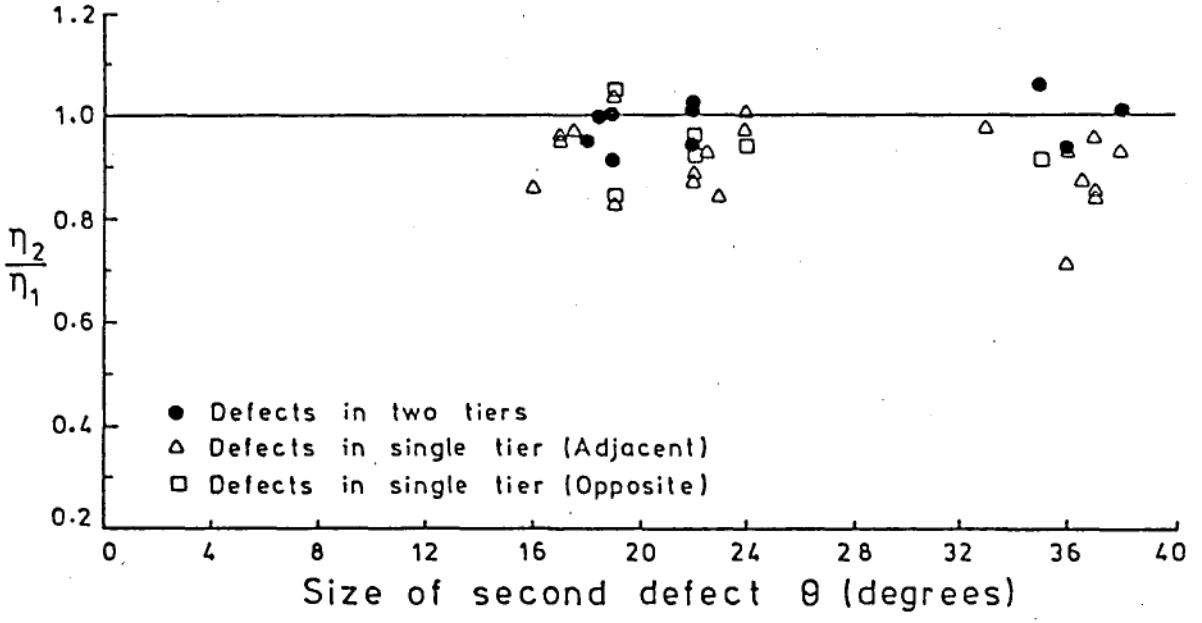

Figure 9.15b
Ratio of Collapse Load with Two Defects to the Collapse Load with the First Defect

Table 9.3 Comparison of Observed Buckling Modes with Predictions Based on Geometry†

Shell	with first defect			with second defect		
	$^*\Delta_{pb}$	N_{exp}	N_{min}	$^*\Delta_{pb}$	N_{exp}	N_{min}
S35	101	II 9	II 8.4	96.9	II 9	II 8.5
S41	157	II 8	II 7.6			
S41	145	I 7	I 6.2	136	I 7	I 6.3
S45	49.6	II 11	II 10.1			
S36	122	I 7	I 6.5	129	II 8	II 7.9
S39	42.8	I 9	I 8.4	39.0	I 9	I 8.6
S37	35.5	I 9	I 8.8			
S8	43.1	II 11	II 10.4			
S32	41.5	II 11	II 10.5	40.6	II 11	II 10.6
S42	16.4	I 11	I 10.7	18.8	I 12	I 10.4
S46	100	I 7	I 6.8	106	I 8	I 6.7
S34	58.3	I 8	I 7.8	59.2	I 8	I 7.8
S22	58.4	I 9	I 7.8	58.4	I 8	I 7.8
S33	64.4	II 10i	II 9.5	59.1	II 10i	II 9.7
S43	167	II 8	II 7.4	150	II 8	II 7.7
S18	102	II 9	II 8.4			
S26	52.1	I 8	I 8.0			
S24	77.8	I 8	I 7.3			
S19				143	I 7	I 6.2

† From eqns.6.7 (for two tier) and 6.9 (for one tier).

* Post-buckling deflection ($\dot{\Delta} = 10^4 \delta L/R^2$)

post-buckled state, using eqns.6.9 and 6.7 for the one and two tier patterns respectively. In most cases the observed value of N is equal to the nearest integer greater than N_{min}; although in a few cases it is higher, in no case is it less than the theoretical minimum. The agreement observed for the number of facets in the one tier patterns is particularly significant, as the relationship developed for this case could not be verified earlier.

9.5 Results of Tests with Multiple Defects

To study the effect of multiple defects in the same tier, four shells - S11, S12, S25 and S43 - were tested with increasing number of defects imposed on them, until each had defects all round the circumference. All the defects were of nominal size D3, and had an average circumferential size of 36° in the unloaded condition. In the first two shells, which were less than 0.2 mm thick, nine defects were introduced; whereas in the last two shells, which had thicknesses in excess of 0.36 mm, only eight defects were introduced with slightly larger gaps in between the defects, to allow for the greater radii of curvatures required at the nodes. The observed knockdown factors of these four shells are plotted against increasing number of defects in Figure 9.16a. (The numerical values and the observed modes are listed in Table 9.4). It may be observed that while there is a relatively large drop in the load carrying capacity of the shells due to the introduction of the first defect, further reductions in the values of η are less severe, more or less uniform, and appear to be linearly related to the number of defects added.

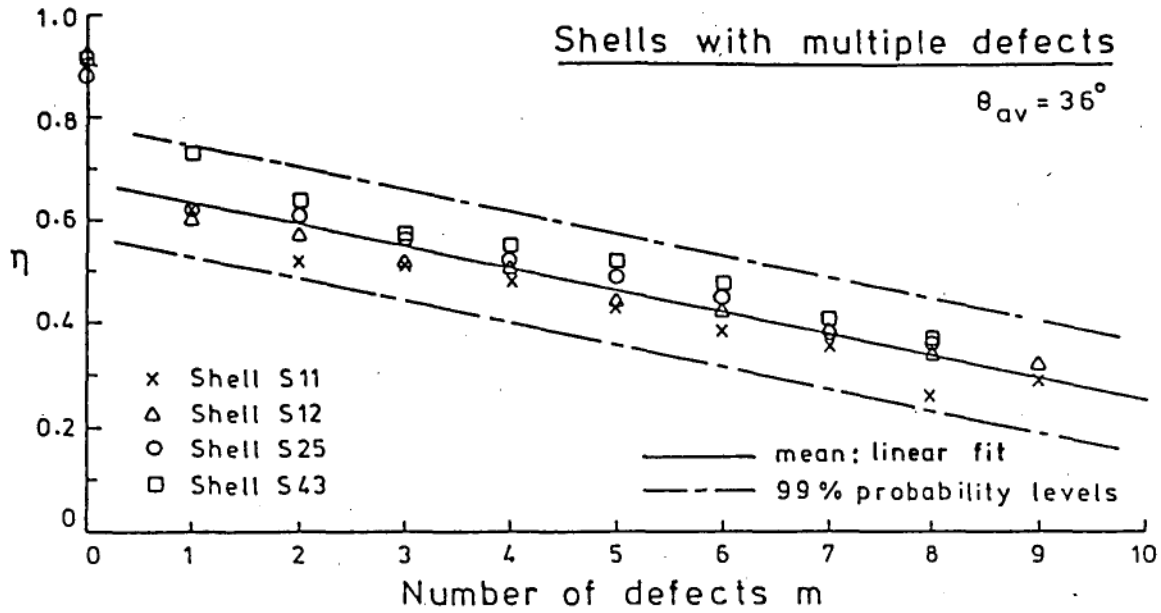

Figure 9.16a. Effect of Additional Defects On the Collapse Load

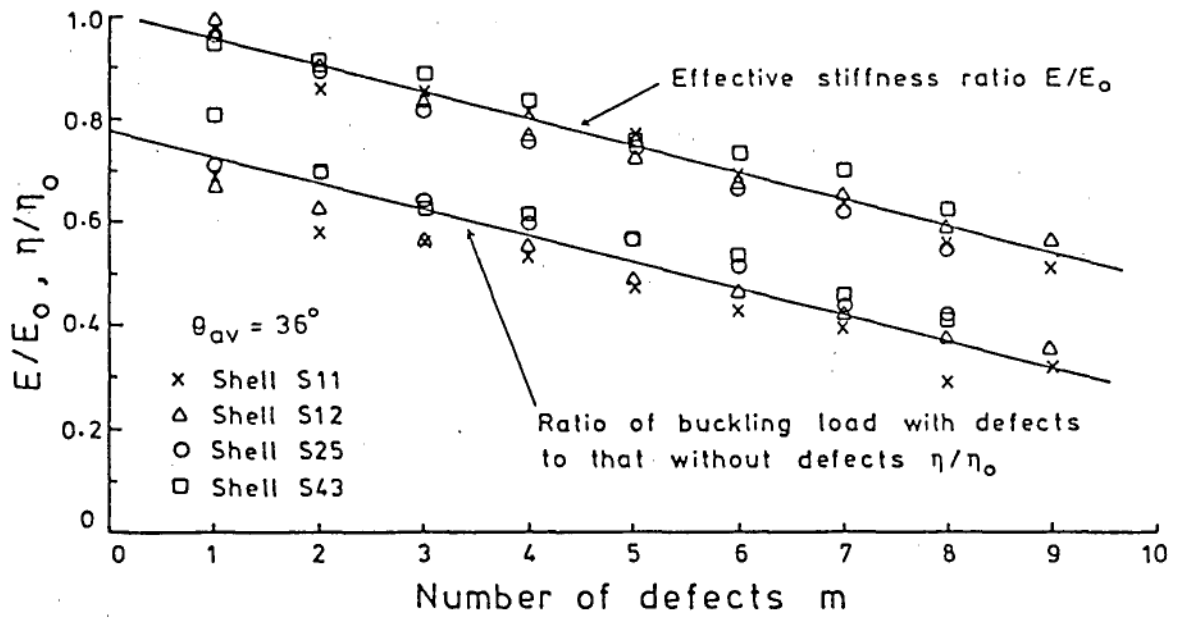

Figure 9.16b. Comparison between Changes in Effective Stiffness and Load Bearing Capacity of Shells with Multiple Defects

As may be seen from the load deflection diagrams of shell S12 in Figure 9.11, even with nine defects the pre-buckling paths are quite linear and provide a good measure of the value of the effective stiffness of the shell. The ratios of the effective stiffnesses thus measured to the stiffnesses recorded before introducing the defects (E/E_0) are compared with the ratios of the buckling loads with the defects to the maximum loads attained without the defects (η/η_0) in Figure 9.16b. (The numerical values of E/E_0 are given in Table C4 in Appendix C). The slopes of the least square fits to the two plots are very nearly identical, suggesting a close relationship between the two effects of the increase in the number of defects imposed. In fact, it appears that other than the initial jump caused by the first defect, the decrease in the load carrying capacity can be entirely accounted for by the reduction in the effective stiffness of the shells caused by the additional number of defects imposed.

One of the obvious reasons for the poor agreement observed between the predictions of the space frame theory and the buckling loads obtained in tests conducted on shells with single defects, is that the space frame model has facets all around the circumference, while the shells had only a single defect. According to the proposed hypothesis, the shell should collapse at the same load whether it has a single defect or a number of defects of the same size around the circumference. Since the experiments with multiple defects indicated to the contrary, it was decided to check whether the predictions of the space frame theory compare favourably with the experimental values obtained with defects all round the circumference. The comparison is

Table 9.4 Buckling Data of Shells with Multiple Defects

Shell	S11		S12		S25		S43	
Number of Defects	η_{cr}	Mode	η_{cr}	Mode	η_{cr}	Mode	η_{cr}	Mode
0	0.902	II 10	0.916	II 10	0.874	II 10	0.908	II 8
1	0.619	I 9p	0.616	I 9p	0.621	I 8p	0.730	II 8
2	0.520	II 9p	0.571	I 9p	0.607	I 8p	0.635	II 8
3	0.509	I 10p	0.517	I 9p	0.562	I 8	0.566	II 7p
4	0.479	I 10	0.506	I 9p	0.521	I 8p	0.550	II 8
5	0.427	I 9	0.444	I 9p	0.495	I 8	0.508	II 8p
6	0.382	I 9p	0.423	I 9p	0.451	I 8	0.478	II 8
7	0.353	I 9	0.384	I 9p	0.380	I 8	0.407	II 8
8	0.260	II 9p	0.339	II 9p	0.364	II 8p	0.368	II 8i
9	0.287	II 9p	0.323	II 9p	—	—	—	—

Table 9.5 Comparison with Space Frame Theory

Shell	R/t	N	η_{exp}	$^{*}\eta_{osf}$	$^{\dagger}\eta_{msf}$
S11	461	9	0.287	0.257	0.290
S12	410	9	0.323	0.315	0.308
S43	213	8	0.368	0.868	0.378
S25	198	8	0.364	0.985	0.392

* Original Space Frame Theory (W/t = 22.7, λ from eqn.3.17).
† Space Frame Model without Spring (K = 1.6, λ = 0.5).
Note : All defects in these shells were of nominal size D3.

provided in Table 9.5; it can be seen that the values predicted by the modified theory (space frame model without springs) agree reasonably well with the experimental collapse loads of all four shells. It must however be cautioned that the agreement observed in these four cases (which may be fortuitous) could be misleading. For instance, if the defects in the last two shells had been placed closer and a ninth defect introduced in them, the load carrying capacity of these shells would possibly have decreased further, while the predicted load remained the same, resulting in a less favourable agreement. Also, since the data of the tests with one and two defects indicate only a small variation in the collapse load with the defect size, it appears that if defects of a smaller size, say $\theta = 24^{\circ}$ (N = 15), had been introduced, the maximum load carried by the shell would have been nearly the same (if not lower, due to the larger number of defects), whereas the collapse load predicted by the space frame model would be much higher. It is therefore felt that the agreement observed in Table 9.5 cannot be taken as sufficient evidence for the applicability of the space frame theory to the collapse of shells with single tier defects all round the circumference.

9.6 Tests with Other Defects

In section 9.1 it was mentioned that an attempt was made to impose a two tier defect (three facets simultaneously) in shell S13, which was not very successful. This shell, with the defect, reached only a maximum load of 0.41 times the classical load. In three of the early shells, S2, S3 and S4, with lengths of 167, 176 and 111 mm

respectively, circular cut-outs of 30 mm diameter were introduced towards the mid-section. The knockdown factors obtained for these shells with the cut-outs were 0.47, 0.46 and 0.38 respectively. (The smaller value obtained in the last case appears to be due to the larger relative size - with respect to the length of the shell - of the cut-out in this shorter shell). In the tests conducted on these shells, it was observed that with increasing load in the pre-buckling stage, the shell wall around the cut-out begins to deform, leading to the development of tangential folds on either side of the cut-out, and resulting in the formation of diamond shaped facets on collapse, with the facets on either side having a common node over the centre of the cut-out.

The load deflection diagrams of shell S13 (with the poorly formed two tier defect) and one of the shells, S4, with the circular cut-out, are shown in Figures 9.17a and 9.17b. The non-linearities in these plots are to be compared with the non-linearities that are barely detectable in the pre-buckling paths in Figures 9.9 and 9.11, of the shells with one, two and multiple defects of properly formed diamond shape. It also appears that in shells having defects of other forms, the development of folds of regular shape in and around the region of the defect leads to an increase in the stiffness of the shell in the pre-buckling stage, as evidenced by the rising slopes of the pre-buckling paths in the load deflection diagrams in Figure 9.17.

The above comparison indicates that local defects in the shape of the facets of the buckle pattern have an advantage, in that

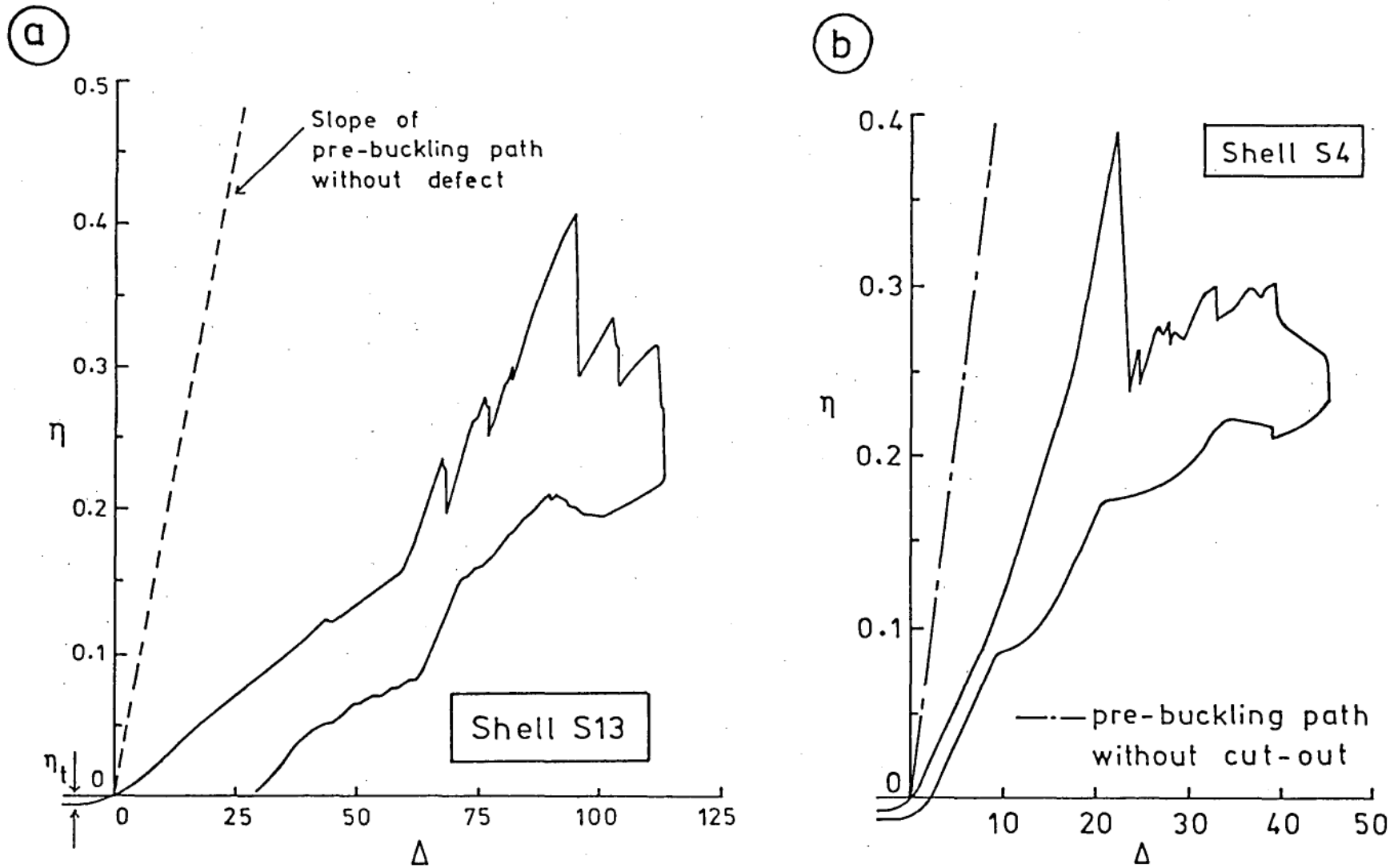

Figure 9.17. Load Deflection Diagrams of Shells with
(a) Irregular Two Tier Defect (b) Circular Cut-out

they cause much lower reductions in the effective stiffness of the shell than defects of other shape. On the basis of the discussions presented in Chapter 3 on the space frame analogy, the relatively higher stiffness of the shells with the facet-shaped defects can be attributed to the presence of the more or less sharp folds along the edges and in the middle of the deformed region which lend strength and rigidity to the structure of the defect. The stiffer structure of the defect probably also accounts for the relatively high buckling loads obtained in the case of shells with diamond-shaped defects.

9.7 Physical Aspects of Collapse Due to Diamond-Shaped Defects

Although the collapse of shells with facet-shaped defects is undoubtedly precipitated by the defects imposed on them, the physical nature of the collapse appears to be significantly different from that proposed in the model in Chapter 3 as the basis of the space frame theory. The space frame analogy is founded on the premise that the buckling of the diagonal folds of the facets results in the collapse of the whole shell. Indeed, photographic recordings of the process, the reduction in the circumferential number of facets observed after collapse, and the favourable agreement obtained between the test results and the theoretical predictions, all indicate that the space frame model satisfactorily describes the secondary collapse behaviour of axially compressed cylindrical shells *which have buckled into the two tier pattern*. In the collapse of shells with defects in the form of single tier diamond-shaped facets, however, there is no evidence of the buckling of the diagonal folds. In fact other than an increase in

their circumferential size, very little change is observable in the facets imposed. In particular, in the case of shells with multiple defects all round the circumference, the collapse was seen to produce additional buckles above or below the imposed defects, giving rise to a second tier (see Figure 9.10). At least in this case, the nature of the collapse appears to be similar to that proposed for the secondary collapse of one tier patterns in chapter 6; the collapse seems to occur mainly due to a concentration of stresses in the cylindrical sections of the shell in between the facets.

The growth of the deformations in the regions adjacent to the imposed defects in the prebuckling stage (Figure 9.6) and the formation of facets next to the defect seen in shells which buckled partially (Figures 9.4e, 9.6e, 9.7b, 9.7d) indicate that the collapse is initiated in these regions. It appears that owing to the particular structure of the defect, the defective area remains strong while the portions of the shell next to it become weak, and hence succumb under the load. The weakness in the adjacent regions may be regarded as that arising from a concentration of stresses in these areas, caused by the diversion of the axial stresses along the generators over the defect by the diagonal folds or edges of the defect to either side. As the load on the shell increases, these stress concentrations give rise to increasing local deformations, ultimately resulting in the loss of stability and the formation of facets adjacent to the imposed defect. The newly formed facets, being similar in structure to the imposed defect, would in turn produce stress concentrations in the cylindrical sections of the shell wall in their neighborhood. It can thus be

envisaged that the collapse begins with the formation of one facet adjacent to the imposed defect, which is replicated in a cyclic manner around the circumference of the cylinder until the pattern becomes complete. Of course, if the imposed defect is perfectly symmetrical, the buckle pattern could begin on both sides of the defect and meet half way round the circumference. But more often than not the collapse appears to begin only on one side, due perhaps to minor asymmetries in the geometry of the defect which are unavoidable. Assuming that a total collapse occurs in this fashion, it is likely that the presence of other imperfections, or the lack of sufficient energy in the shell (since each partial collapse, i.e., the formation of each facet, would involve the release of energy) could prevent the pattern from being completed. The partial collapse patterns observed in the tests and their subsequent completion by the development of neighbouring facets in successive collapses suggest strongly that the collapse begins with a single facet as envisaged and proceeds in a cyclic order to complete the pattern. It is to be noted that the facets formed initially could be of the one tier or the two tier type (which, it appears, depends on the geometry of the shell and the end-shortening applied, as mentioned earlier); in either case stress concentrations are likely to occur in the adjacent cylindrical sections, and the facets replicated around the circumference.

As proposed in the development of the space frame model, the central regions in the diamond-shaped defects would be somewhat ineffective in supporting the axial stresses in the cylinder (hence the flow of the stresses sideways, resulting in the concentration of

stresses in the regions adjacent to the defect). The reduction in the stiffness of the shell can be considered to be a direct consequence of the reduction in the effective area of cross-section of the shell, in which case the introduction of additional defects of the same size in the shell would result in a decrease in the effective stiffness of the shell in direct proportion to the number of defects introduced. More importantly, the introduction of further defects adjacent to those already existing, will not significantly alter the magnitude of the stress concentration (although its occurrence would be shifted to the neighborhood of the newly imposed defect). Hence further reductions in the load carrying capacity of the shell (due to the addition of more defects) would only result from the decrease in the stiffness of the shell, which is proportional to the number of defects introduced.

Admittedly, the model envisaged for the collapse of the cylindrical shells effected by the diamond-shaped single tier defects imposed on them is somewhat simplistic; it does not take into account the effects of bending or the non-linearities that are likely to be present due to the deviation of the shell wall from its cylindrical shape. It does however include the essential features observed in the tests and explain the two predominant aspects of the results obtained, namely, the relatively large initial reduction in the load carrying capacity of the shell caused by the introduction of the first defect, and the more gradual, almost linear, successive reductions caused by the addition of further defects. It also appears reasonable that as the size of the imposed defect is increased (from zero), the variation in the magnitude of the stress concentrations in the vicinity of the

defect will be very steep in the initial stages, and then become more gradual; so that once a certain size is exceeded, further increases in the defect size can be expected to produce only a small reduction in the load carrying capacity of the shell, as observed in the tests.

These considerations may perhaps serve as the starting point for an analytical approach to investigate the effect of diamond-shaped dimple defects on the collapse of axially loaded cylindrical shells. While no theoretical approach is attempted in the present work, an effort has been made to develop empirical relations to estimate the effect of diamond-shaped local defects on the load carrying capacity of axially compressed cylindrical shells, which is presented in the following sections.

9.8 Assumptions Involved in Developing Empirical Relations

The results of the tests conducted on shells with single defects plotted in Figures 9.14a and 9.14b indicate that the effect of the imposed diamond-shaped defects on the load carrying capacity of the shells can be considered to be independent of the two geometric parameters, the radius to thickness ratio and the length to radius ratio of the shells.

It appears reasonable to assume that variations in the location of the defect have very little effect on the magnitude of the collapse load, provided that the defect is placed sufficiently away from the ends so that it does not interact with the end conditions on

the shell. Hence the small deviations in the location of the imposed defects from the mid-section of the shell are not taken into account, it being considered that the means fitted to the experimental data will represent the effect of defects imposed in the middle section of the shell with sufficient accuracy.

From the physical considerations in the foregoing section, it appears that large variations in the aspect ratio of the defect can affect the magnitude of the collapse load, since the concentration of stresses in the regions outside the nodes is likely to be dependent on the aspect ratio of the defect imposed. (It is conceivable that a very long and narrow defect will produce less stress concentration in its neighborhood than a short and wide defect). However, the variation in the aspect ratios of the defects imposed in the tests is very small (between 0.4 and 0.45), and the scatter in the test data too large to provide any definite correlation. This small variation in the aspect ratio values is therefore neglected in analysing the results. It may however be noted that the data collected and the relations developed therefrom are to be taken as typical only of defects with aspect ratios in the range of 0.4 to 0.45, until the effect of changes in aspect ratio of the defect is investigated further.

The above assumptions reduce the number of parameters to be considered in determining the effect of the imposed defects to just two, viz, the circumferential size of the defect and the number of defects. The load carrying capacity of the shells obviously depends on the number of defects imposed, as shown by the tests with multiple

defects. Although the least square fits to the data of the tests with one and two defects (in Figures 9.12 and 9.15a) indicate only a small reduction in the load carrying capacity of the shells with increasing defect size, it will be erroneous to neglect this variation and infer that the knockdown factor is independent of the defect size; since, clearly, with defects of zero size (that is, without any imposed defects) the buckling loads were much higher than the values obtained in these tests. Nor can it be assumed that the relationship is a discontinuous one; it is more likely that the load carrying capacity reduces in an exponential fashion with increasing defect size.

Before attempting to formulate such a relationship, there is, however, one more aspect to be looked at, which is the role played by the initial (unintentional) imperfections in the collapse of the shells observed after introducing the diamond-shaped defects; this is considered in the next section.

9.9 Effect of Initial Imperfections

Regarding the effect of initial imperfections in the shell there are two assumptions that can be made: either that the initial imperfections have negligible effect on the magnitude of the collapse load obtained with the imposed defects, or that they have negligible effect on the *reduction* in the magnitude of the collapse load caused by the imposed defects. Using the notations η_0 and η for the knockdown factors observed before and after imposing a defect in the shell, the second statement amounts to taking the difference $\Delta\eta = \eta_0 - \eta$ to be

independent of the initial imperfections, which at first sight appears to be logical, since this observed difference in the loads sustained has been brought about entirely by the introduction of the defect.

Following this line of approach, the empirical relations were first developed by fitting curves to the plots of η/η_0, the ratio of the knockdown factor obtained with the defects to that observed before imposing the defects. It may be observed that taking the ratio η/η_0 to be dependent only on θ and m (the size and number of defects) implies that the reduction $\Delta\eta = \eta_0 - \eta$ is directly proportional to η_0, the knockdown factor with only the initial imperfections, rather than being independent of it. Subsequently a closer inspection of the test data in the light of the physical considerations presented earlier revealed that even this would be inadequate, that the first assumption - that initial imperfections have very little effect on the collapse load obtained with imposed defects - is a closer approximation to the observed behaviour. This may be seen from the plot of η_1/η_0, the ratio of the knockdown factors with the first defect to those obtained prior to introducing the defects, against η_0, presented in Figure 9.18.

The mean plotted in the figure shows a significant downward trend (it may be mentioned that the correlation coefficient for the data plotted is 0.52). The downward trend is mainly due to the four isolated points at the top (three with defects D2 and one with defect D3). At first glance one is tempted to disregard them, since even the other points show a considerable amount of scatter; but it is the deviation of these points from the scatter of the remaining data that

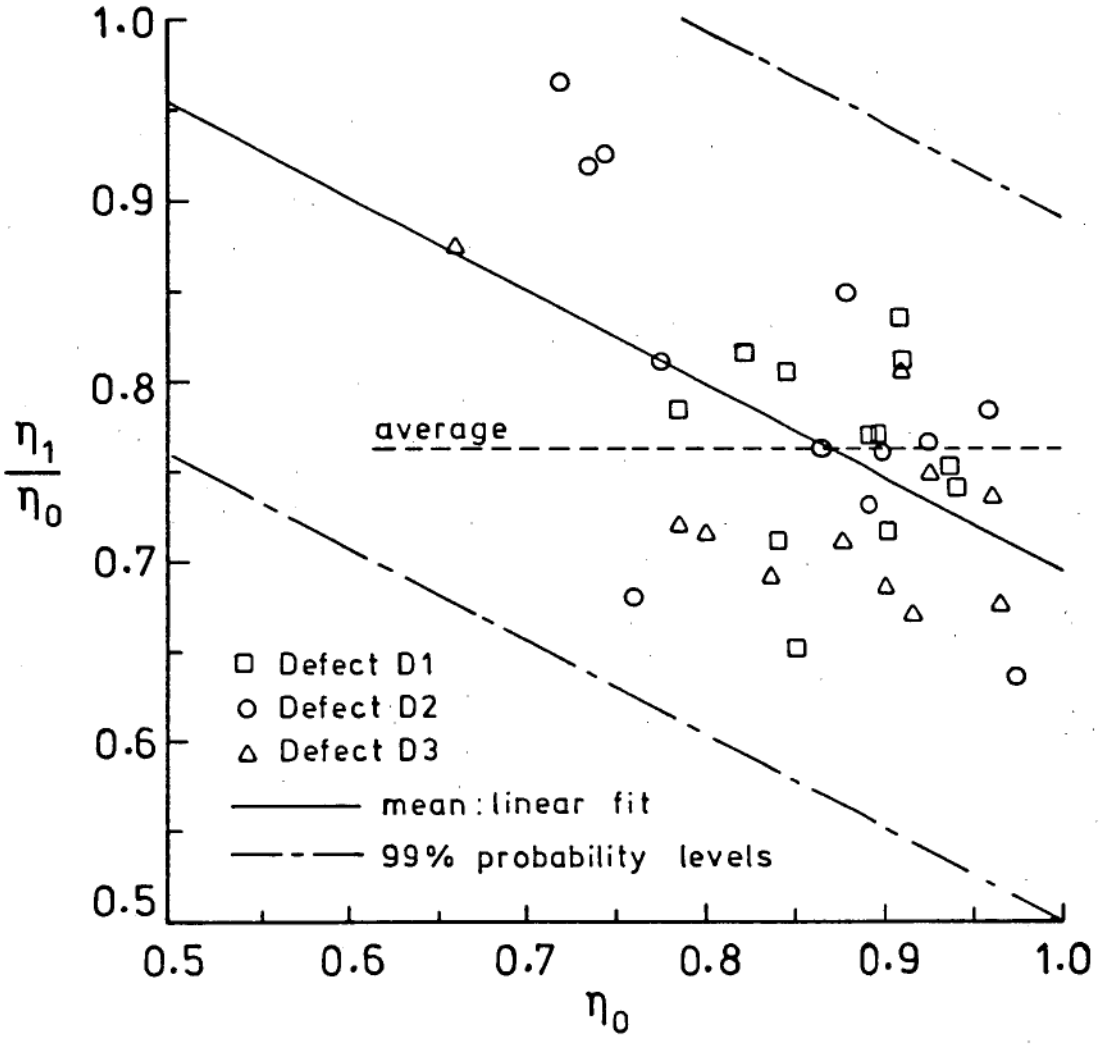

Figure 9.18
Variation in the Load Reduction
Caused by a Single Defect with the Initial
Load Bearing Capacity of the Shells

is significant. These four points belong to the four shells, S9, S31, S32 and S33, whose initial knockdown factors were less than 0.75. With the defects imposed, their knockdown factors were about the same as those obtained for the remaining shells with single defects; hence their ratios are much higher. Obviously, the initial imperfections in these shells had very little effect on the magnitude of their collapse loads with the imposed defect. Alternatively, it could be considered that the presence of the initial imperfections significantly reduced the detrimental effect of the defects imposed in these shells.

Actually it would be more appropriate to say that of the two imperfections (the initial and the imposed), the one which has greater effect will predominate, and the smaller one will become more or less ineffective. For instance, consider a shell with initial imperfections large enough to reduce its load carrying capacity by 40%, and that a defect, which in a perfect shell would have caused 30% load reduction, is imposed on it. It cannot be expected that with the defect, the load carrying capacity of this shell will be only 30% less than that of a perfect shell, i.e., that the defect will raise its capacity by 10%. However, it is also unlikely that the defect will lower its load carrying capacity by a further 30%. The chances are that the collapse load of the imperfect shell with the defect will be relatively close to the value obtained before imposing the defect, due to the effect of the defect being considerably reduced by the predominance of the initial imperfections. Since in the current tests, the imposed defects were so large that their effect was predominant (even for the four shells mentioned above), it was the effect of initial imperfections

which appeared insignificant.

The reduced effectiveness of the smaller imperfection can be better appreciated if one regards it as acting either as an extension to the larger imperfection or as an additional defect. In either case the load carrying capacity of the shell drops only a little, since the effect of an additional defect is small (the average knockdown factors for $\theta = 36^{\circ}$ with one and two defects in the same tier are respectively 0.64 and 0.59), and so is the effect of an increase in the size of the defect. (It is to be noted that if the second defect is at a different height, the reduction will be even smaller). Hence the knockdown factor obtained with an imposed defect in an imperfect shell will be nearly the same as that obtained with the same defect in a perfect shell (or that of the imperfect shell without the defect - whichever is lower). It may be mentioned that not only the results obtained in the current work, but even those observed by Ricardo[26,27] in his experiments on the effect of local radial deformations on cylindrical shells appear to confirm this hypothesis.

In his experiments, Ricardo applied concentrated lateral forces of constant magnitude on the shell wall, producing local dimple shaped deformations at the mid-section of the shell. By changing the magnitude of the applied force, dimples of different depths could be imposed and their effect on the collapse of the shell investigated. The dimples studied by Ricardo appear to be quite different in shape - due to the sharp indentation produced by the radial force applied - from the defects described herein. However, Ricardo reports that the

observed knockdown factors were in the range of 0.7 to 0.5 (nearly the same range as that observed in the tests with single diamond-shaped defects in the current study). Further, he observes that dimples with depths of less than 1.5 to 2 times the wall thickness did not alter the magnitude of the knockdown factor (from the value of 0.7 obtained without the lateral forces); whereas beyond this range, the buckling load dropped drastically to about half the classical value, remaining at this level for further increases in the depths of the dimples, up to 7 times the shell thickness. (This latter near invariance is also similar to the behaviour observed in the current tests). The reported ineffectiveness of the dimples with smaller size indicates to the probable predominance of the initial imperfections (which on their own reduced the load carrying capacity to 70%) over them. It also appears likely that a near perfect shell with dimples less deep than 1.5 times the thickness will collapse at loads over 70% of the classical value.

The above observations indicate that the interaction between the imposed defects and the initial imperfections in the shell is very little, and that their combined effect will be closer to the greater of the effects of the two imperfections considered separately. Hence for developing the empirical formulae, the first assumption mentioned, that the collapse load of the shells with the defects is relatively unaffected by its initial imperfections, is employed. The value of η_0 is therefore taken to be 0.92, the theoretical knockdown factor for the perfect shell with clamped ends. It is to be noted that since most of the shells tested were of high quality, in practice it makes very little difference to the curves fitted whether the theoretical value

or the actual experimental values are used. However when the formula developed is employed to predict the collapse load of a poor quality shell with imposed defects, the use of the actual η_0 observed before introducing the defects will result in a much poorer estimate of its load carrying capacity than the use of the theoretical value Of 0.92 (since the data has been mostly obtained from shells with high values of η_0). For instance, if in a shell with an observed value of η_0 = 0.6, a defect of size such that the predicted value of η/η_0 = 0.6 is imposed, it is more likely that the collapse load with the defect will be nearer to 0.55 (0.92*0.6) than to 0.36 (0.6*0.6). It may be also mentioned that using the theoretical value slightly over-estimates its strength; however a more conservative estimate may be obtained by considering the initial imperfection as a second defect in the shell.

9.10 Empirical Relations for Diamond-Shaped Local Defects

The results of the tests with multiple defects indicated a uniform reduction in the magnitude of the knockdown factor with the number of defects added to the shell. This suggests a relationship of the form

$$\eta = \eta_1 - (m-1).f(\theta_{av}) \qquad (9.1)$$

where η is the knockdown factor with one or more defects, η_1 is the knockdown factor for a single defect, and m is the number of defects imposed on the shell. The function $f(\theta_{av})$ becomes a constant for a given average circumferential size, θ_{av}, of the defects, producing a linear variation, as observed in the tests with the multiple defects

of size D3, which had an average value of $\theta = 36^{\circ}$. It is to be noted that the linear relationship (9.1) is valid only for $m \geq 1$, since the value of η for m = 0 does not lie on the same straight line.

The knockdown factor for the first defect η_1 was determined by fitting a curve of the form $\eta_1 = 0.92.\exp(-C_1.\theta^{X1})$ to the data of the shells with single defects. The best fit to the data was obtained for the values of $C_1 = 0.184$ and $x_1 = 0.19$. The empirical relation for the effect of the first defect on the shell is thus given by

$$\eta_1 = 0.92.\exp(-0.184.\theta^{0.19}) \qquad (9.2)$$

This curve is shown in Figure 9.19a, along with the least square fit (straight line mean) to the experimental data. Since the experiments with multiple defects were performed only for an average defect size of 36°, we have only one value available for the function $f(\theta_{av})$. It was therefore decided to fit an exponential curve of the same form as eqn.9.2 to the data obtained with two defects, and use this curve to establish $f(\theta_{av})$. The best fit to these data was obtained as

$$\eta_2 = 0.92.\exp(-0.260.\theta_{av}^{0.145}) \qquad (9.3)$$

which is plotted in Figure 9.19b, along with the experimental data and the straight line mean for comparison. It is to be noted that in the figure the knockdown factors are plotted against the average value of the circumferential sizes of the two defects on the shell. Further, only the data of the shells with the defects in the same tier (either

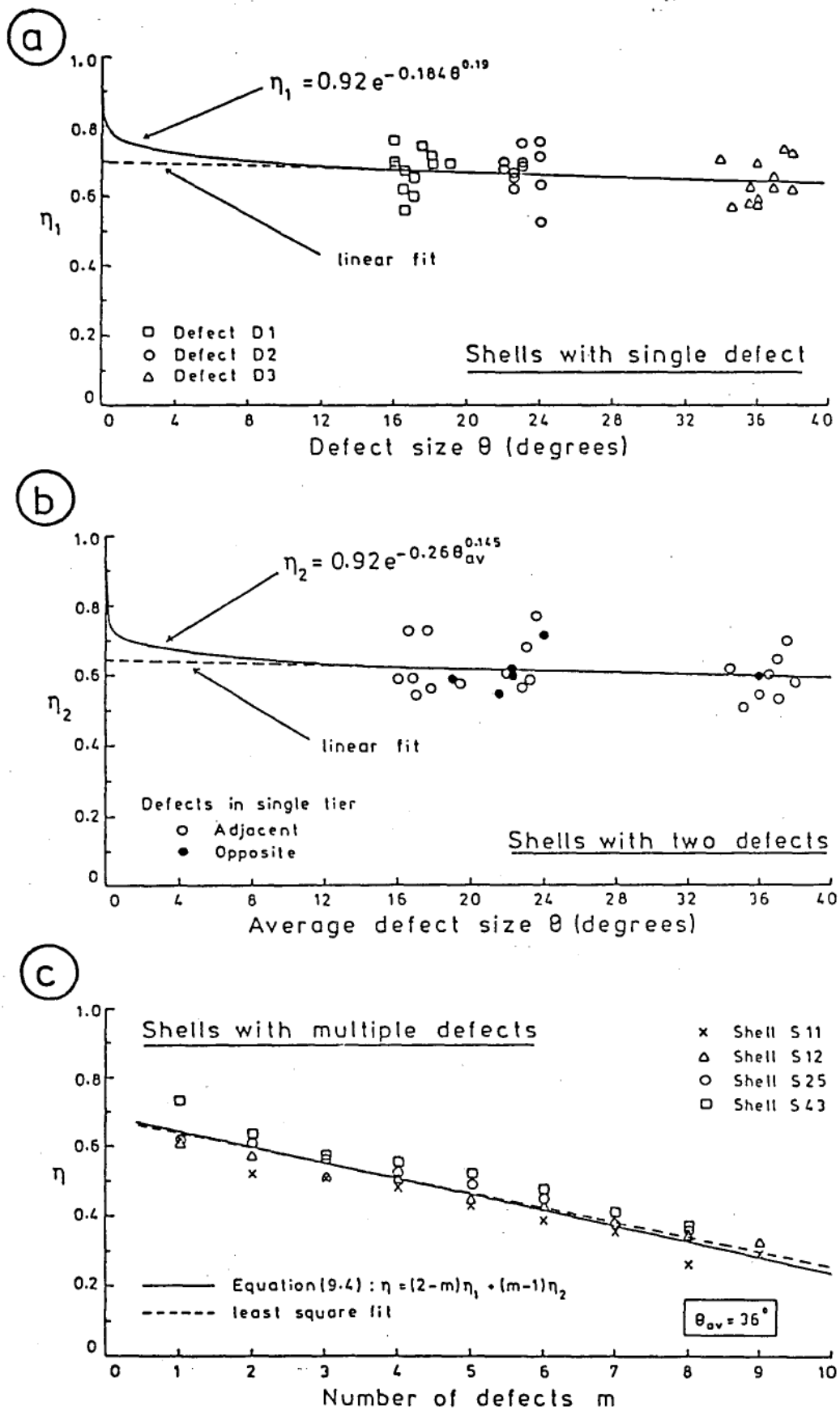

Figure 9.19. Empirical Formula (9.4) Fitted to Experimental Data (a) for Single Defects (b) for Two Defects (c) for Multiple Defects

adjacent or diametrically opposite) have been used to fit the curve. As pointed out in section 9.4, when the second defect is located in the next tier, it hardly reduces the buckling load, in comparison with the reduction caused by a second defect in the same tier; hence this data has not been considered. Thus the relations established are for multiple defects at the same height on the shell, these being found to have a greater detrimental effect.

Noting that $f(\theta_{av})$ is given by $\eta_1 - \eta_2$, equations 9.2 and 9.3 may be substituted in eqn.9.1 to obtain

$$\eta = 0.92\left[(2-m)\exp\left[-0.184.\theta_{av}^{0.19}\right] + (m-1)\exp\left[-0.26.\theta_{av}^{0.145}\right]\right] \qquad (9.4)$$

In this equation, the average size is used even for the effect of the first defect, since the predicted load would otherwise depend on the order in which defects of different sizes are imposed. It is however to be noted that the relationship is mainly developed for shells with multiple defects which do not vary greatly in size, since the experimental data has been obtained with defects of nearly the same size on each of the shells. The knockdown factor for the perfect shell with clamped ends, $\eta = 0.92$ is obtained from the above equation by putting $\theta_{av} = 0$. For finite values of θ_{av}, however, $m = 0$ is not admissible in the equation. Eqn.9.4 is plotted against m in Figure 9.19c for a value of $\theta_{av} = 36^{\circ}$, along with the data from the tests with multiple defects. It can be seen that the relationship obtained agrees well with the straight line mean fitted to the data.

In Figure 9.20, the knockdown factors from eqn.9.4 are plotted against the average size of the defects for different values of m, the number of defects imposed. Although the empirical relation fitted well with the experimental data, the curves in Figure 9.20 do not appear to be entirely acceptable. There are two aspects in the figure which are unsatisfactory: firstly, that the curve for m = 9 shows a slight increase in the knockdown factor with increasing defect size (for higher values of m this increase will be even greater); and secondly that the curves for the larger values of m appear to be too steep in the initial stages. Of course, both aspects are consequences of the assumption used, that for any given value of θ_{av}, the load carrying capacity decreases uniformly with the number of defects added. According to the trend of the curves, if a number of very small defects (say 12 or 15 defects with an average circumferential size of half a degree) are imposed on the shell, its knockdown factor will fall below zero, which is highly unlikely. It thus appears that the reduction in load carrying capacity with increasing number of defects cannot be uniform for small values of θ_{av}. The observed linearity may be applicable only to defects of fairly large size, just as even the variation in η with the defect size appears to be more or less linear for defects in the higher size range. It is therefore to be noted that the physical model suggested earlier may be valid only for defects that are fairly large in size, and that for very small defects, the model would need further modification.

Since the nature of the curves obtained from eqn.9.4 does not appear to be very satisfactory, at least in the lower range of the

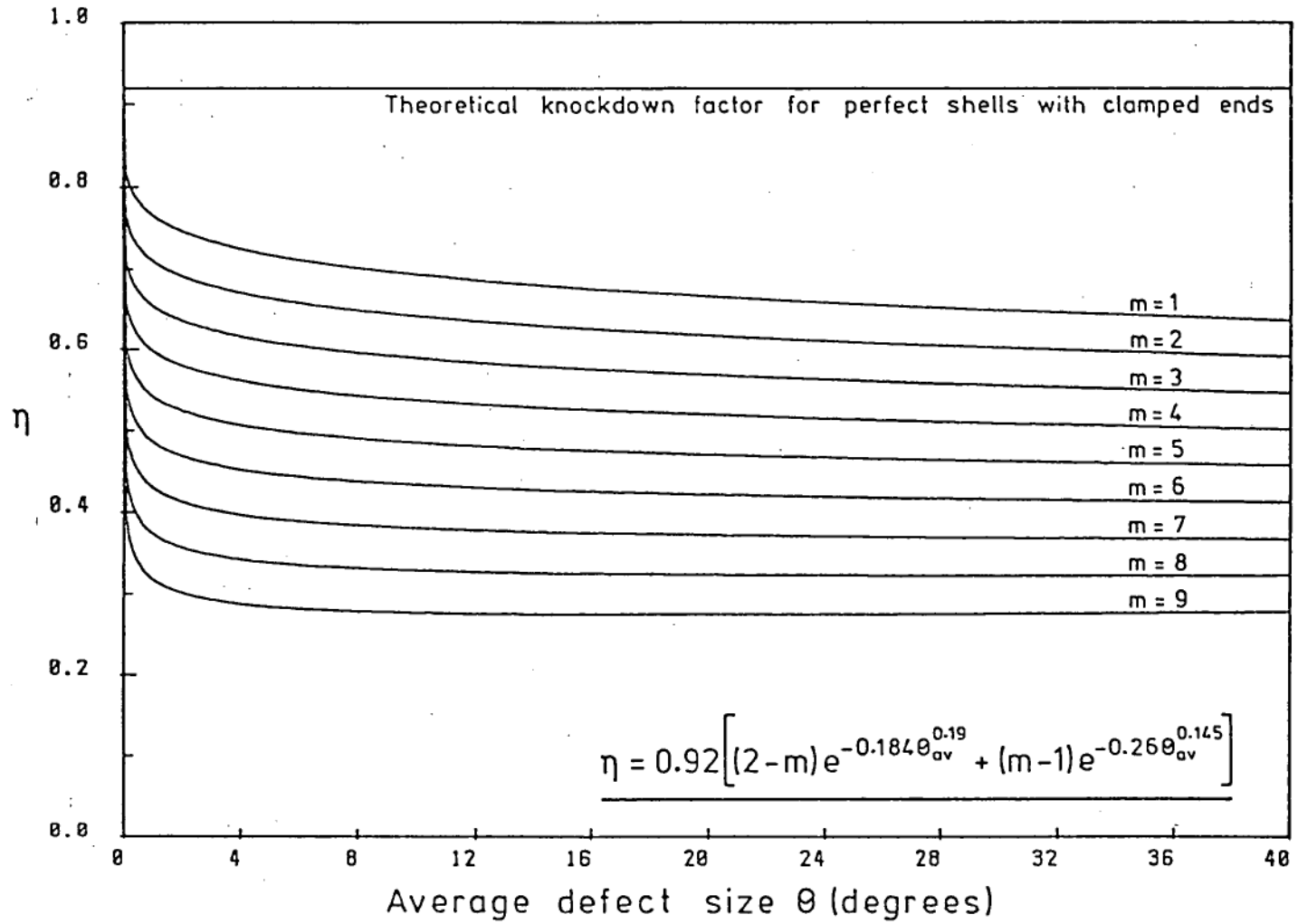

Figure 9.20. Estimations of Empirical Formula (9.4) for the Effect of Diamond-Shaped Local Defects

defect size, an attempt was made to obtain a simpler formula from the experimental data, without resorting to the assumptions involved in developing eqn.9.4. For this purpose, assuming a relationship in the form of $\eta = 0.92\exp(-C.m^{x}.\theta^{y})$, the values of the constants C, x and y were determined by obtaining the best fit curves to all the three sets of data, namely, those with single, double and multiple defects. (In the previous attempt, the data from the tests with multiple defects was used only for comparison, the unknowns in eqn.9.1 being determined from the first two sets only). Minimizing the variances of the data in all the three sets simultaneously, the values of the constants were obtained as C = 0.185, x = 0.45 and y = 0.175. Thus the new empirical relation is

$$\eta = 0.92.\exp(-0.185.m^{0.45}.\theta_{av}^{0.175}) \qquad (9.5)$$

It may be noted that in eqn.9.5, either m or θ_{av} can be set to zero to obtain the theoretical value of $\eta = 0.92$ for perfect shells with clamped ends. In Figures 9.21a to 9.21c, the knockdown factors given by eqn.9.5 are plotted along with the experimental data of shells with single, double and multiple defects. Although this equation does not fit the test data as well as the previous set of equations (since the constants in this case were determined so as to fit all three sets of data simultaneously to the best possible extend), it can be seen that they are fairly close to the straight line means fitted to the data. The values of the knockdown factor estimated from eqn.9.5 are plotted against the average defect size in Figure 9.22 for different values of m. Since the equation is not linear in m, the reduction in η with the number of defects is not uniform in this plot, even for the larger

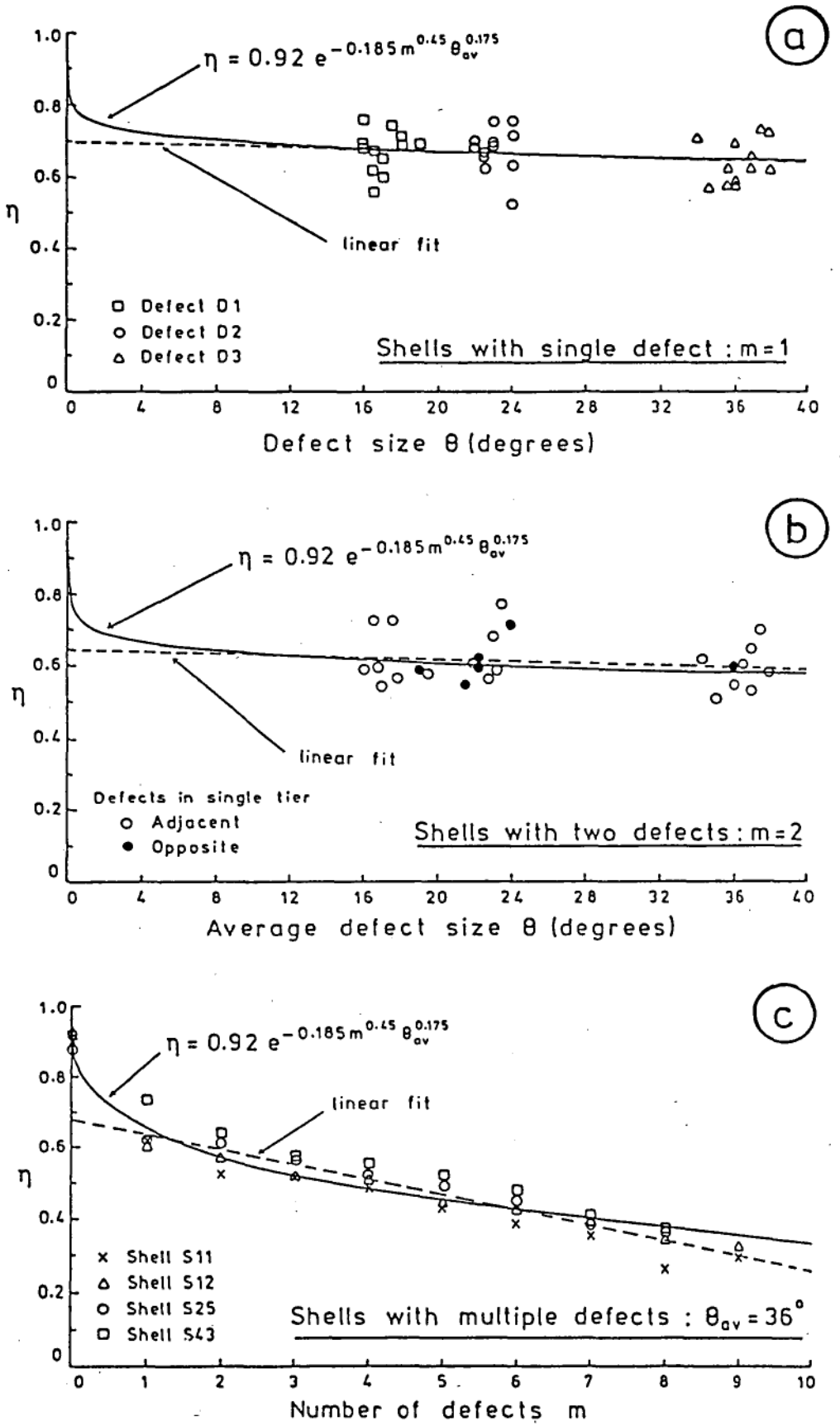

Figure 9.21. Empirical Formula (9.5) Fitted to Experimental Data (a) for Single Defects (b) for Two Defects (c) for Multiple Defects

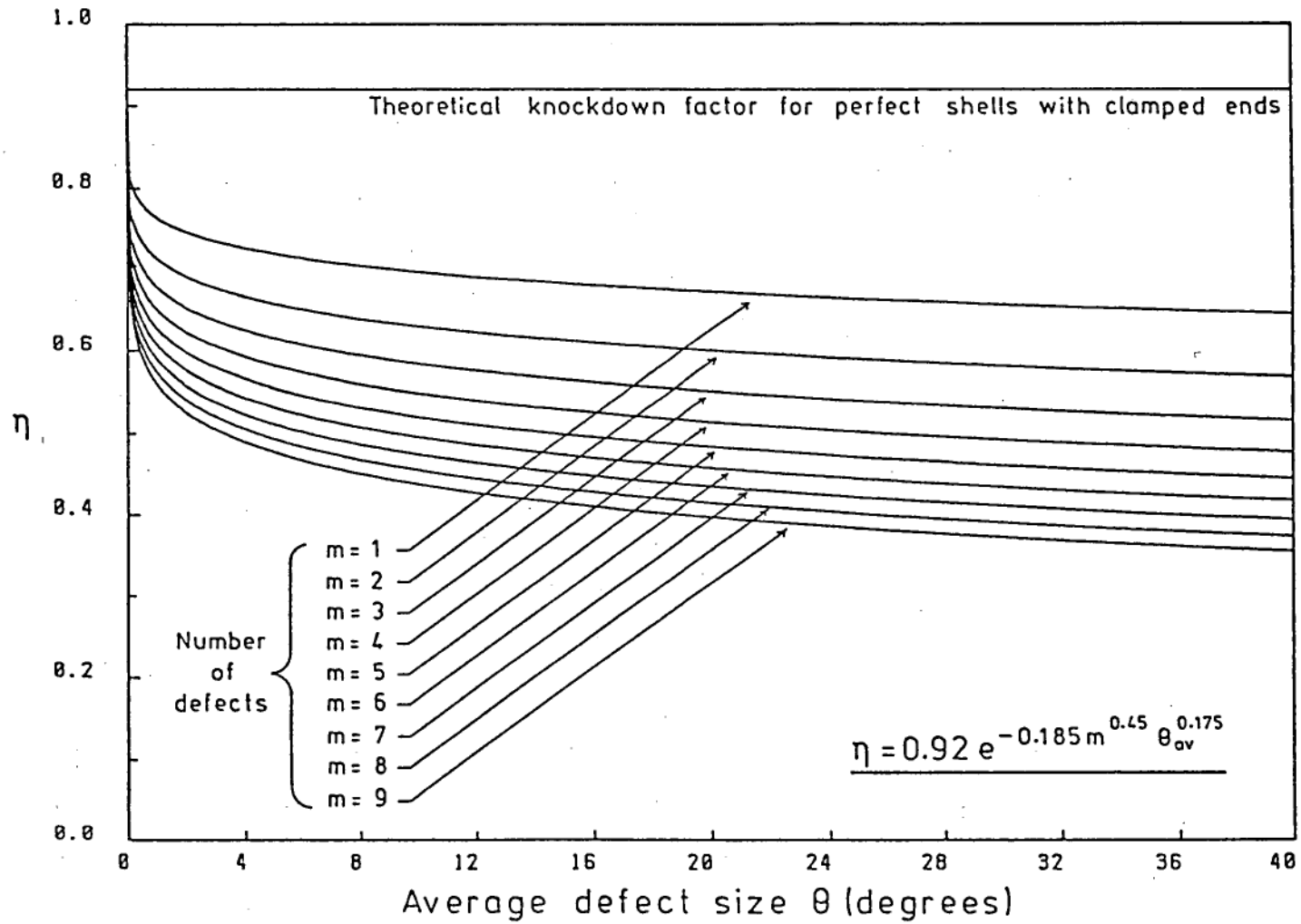

Figure 9.22. Estimations of Empirical Formula (9.5) for the Effect of Diamond-Shaped Local Defects

values of θ. However, the general appearance of the curves is much more satisfactory, than that of the equi-spaced curves in Figure 9.20. It is therefore felt that while eqn.9.4 may be applicable to defects of fairly large size, the current formula (eqn.9.5) offers a reasonably approximate estimate to defects of all sizes. The accuracy of the constants in either formula as well as the nature of the dependencies assumed has be verified by further tests conducted with defects having a wider range of sizes and by future analytical investigations on the effect of diamond-shaped defects on the collapse of axially loaded circular cylindrical shells.

It is to be emphasized that although the theoretical value of 0.92 has been used in the formulae, they are applicable to shells possessing initial imperfections in addition to facet-shaped defects, primarily because the combined effect of initial imperfections and the imposed defects is nearly the same as that of the imposed defect alone when the imperfections are small. Secondly, since the data has been obtained from shells with small initial imperfections, the relations are directly applicable to shells with imperfections of the same degree. For shells with more serious initial imperfections, a more conservative estimate may be obtained by considering the imperfection as an additional local defect. In this case, the equivalent size of the initial imperfection may be obtained from the plots for the single defect using the knockdown factor observed before imposing the defect. The combined effect of the imperfection and the imposed defect may then be estimated from the plots for m = 2, using the average defect size.

CHAPTER 10

CONCLUSION

The work presented herein was begun with the objective of investigating experimentally the effect of local facet-shaped defects on the collapse of axially loaded circular cylindrical shells and the applicability of the space frame theory in predicting the same. The investigations necessarily involved other issues: those related to the development of the space frame theory on the one hand; and on the other, those regarding the collapse behaviour of near perfect cylindrical shells, a better understanding of this being essential to proceed with the investigations on the effect of imposed defects.

Thus the major portion of the thesis is devoted to these allied investigations, some of which produced negative results - which were nevertheless useful. The analytical study conducted on triangular plates for instance, though perhaps of some import as an investigation into the post-buckling behaviour and the ultimate strength of simply supported isosceles triangular plates, only led to the discovery that the approach cannot yield the effective widths of the flanges of the diagonal members of the space frame. The study did however indicate that a significant portion of the interior of the triangular facets may be effective in supporting the load along the folds at the edges, which provided encouragement to carry on with the investigations into the modified theory using the simpler model (without springs) of the space frame. The approach that finally led to the determination of the

effective width of the flanges was considerably simpler: it is based on the premise that the maximum stress in the flanges is limited by the buckling stress of the column. By equating the flange buckling stress to this maximum stress, the effective width of the flange is obtained.

While the existing space frame theory was modified to accommodate the effective width determined in this manner, a closer inspection of the model revealed that the influence of the springs incorporated in the model produced deflection patterns in the diagonal member which did not appear to be entirely in accordance with the observed behaviour or with the basic premises upon which the theory was built. Elimination of the springs resulted in a model that was more consistent and at the same time much simpler, both physically as well as mathematically. The value of the flange buckling coefficient, the key factor in the mathematical model, was chosen on the basis of the agreement between the predicted values and the observed secondary buckling loads, such that the effective widths estimated for the flanges were not physically incompatible with the size of the facets.

The investigations regarding the aspect ratio of the facets in the buckled shell were not totally successful. The studies on the geometry of the buckled configurations of the cylinder presented in chapter 6 were begun with the aim of determining the aspect ratio of the facets analytically. However, they showed that the axial height of the facets formed on collapse depends on the resistance to bending at the folds of the buckle pattern and that without considering the

bending in the shell the exact value of the aspect ratio cannot be determined. But the study also revealed the possibility of the aspect ratio of the buckles changing with the amount of end-shortening applied on the shell, an aspect that seems to have been largely unnoticed in previous studies. The experimental observations confirmed the reduction in aspect ratio with increasing end-shortening. While the initial values of the aspect ratio recorded for the shells tested in the current work were widely scattered and lower than those predicted by the empirical formula of Foster, it was found that in the final stages towards the occurrence of secondary collapse the values were in the range of 0.4 to 0.5. On the basis that small variations in this range in the value of the aspect ratio do not affect the magnitude of the collapse load predicted significantly, the classical value of 0.5 has been taken for the aspect ratio of the facets in the modified space frame models for predicting the secondary buckling loads. Although this suffices in practice for the application of the space frame theory, it would be desirable to establish the exact value of the aspect ratio (in the initial buckled state as well as at the onset of the next collapse) and to identify its relation to the other geometric and loading parameters through more detailed experimental and/or analytical investigations in the future.

The discrepancy between the buckling mode and the observed post-buckling mode in the initial stable configuration of the axially compressed cylindrical shell has puzzled researchers for may years. Although it was obvious that the lower energy levels associated with the lower buckling modes were responsible for the jump from the higher

modes, it appears that the reason for the choice of one particular lower mode in preference to the many others below it was not clear. That the final stable configuration is determined purely by the geometry of the shortened cylinder was an unexpected discovery. The investigations in chapter 6 have shown that for a given value of end-shortening there is a minimum value for the circumferential number of facets that can be formed in a fully developed pattern in the shell. On the premise that the shell tries to develop this lowest possible stable mode in order to attain the minimum possible energy level, formulae have been developed from the geometric criteria to predict the number of facets observed on collapse of near perfect shells. It was also found that the same criteria can be used to establish the minimum value of the Batdorf parameter Z required for a shell to buckle into the two tier pattern.

The preliminary experiments conducted on the shells before introducing the defects served to verify the predictions of the modified space frame theory for the secondary buckling loads as well as those obtained from geometric considerations for the number of facets observed on primary collapse. Thus the applicability of the space frame model in describing the secondary collapse behaviour of axially loaded cylindrical shells (in the two tier mode) and the suggested dependency of the observed post-buckling mode on the geometry of the compressed shell were both confirmed. The experiments were also useful in providing information regarding the changes in aspect ratio and in establishing the relation for the initial post-buckling load as a function of the Batdorf parameter Z.

It is noteworthy that 23 of the 46 shells tested attained loads within 5% of the theoretical buckling load (for cylinders with clamped ends) and of the remaining, only four failed to reach 70% of the classical load. While the tests on the good shells contribute towards the existing data on near perfect shells, it is perhaps the tests conducted on the imperfect shells that have been more useful, in that they provided valuable information on the nature of some of the initial imperfections that occur in circular cylindrical shells. Other than the non-uniform loading resulting from the tilt caused by a thin film of epoxy under one of the shells and the local thinning of the shell wall in another, most of the imperfections observed were in the form of geometric deviations of the shell wall, these being mainly caused by imperfect fixing of the ends of the shell. It is obvious that similar imperfections are likely to have been present in many of the tests reported hitherto. In the present case, the observation and study of these imperfections were enabled by the whole field optical system employed. This system facilitated not only the detection and identification of the extent of coverage of the imperfections, but also the monitoring of their growth with increasing end-load in the prebuckling stage. The grid reflection technique incorporated in the optical set up was sensitive enough to record axisymmetric prebuckling deformations having an amplitude of only about 2% of the thickness of the shell. The remarkable aspect about these axisymmetric waves, which were observed to occur along the full length of the cylinder at about 70% of the classical load, is that their measured wavelengths were found to be nearly the same as those predicted by the classical theory for axisymmetric buckling.

The experimental investigation of the effects of local diamond-shaped dimple defects imposed on the shells was motivated by the observation that permanent deformations naturally occurring in shells often tend to take this shape. The study has shown that these defects are not as degrading as most of the imperfections investigated so far. Even with a defect extending over a tenth of the circumference and having a radial deviation at the centre of over 20 times the wall thickness, the buckling load of the shell does not fall below 50% of the classical load. It appears that this is mainly due to the rigidity of the folds along the edges of the defect, which makes it stronger than geometric deviations of other forms. The near developability of the diamond-shaped facet and its rigid structure probably account for the inclination of the shell to develop deformations of this shape when accidentally bumped or forced to deflect. Although it is too premature to make suggestions, there exists a strong possibility that by imposing a regular diamond-shaped facet over existing deformations of some other shapes on the shell wall, the load bearing capacity of an imperfect shell could be improved.

It is to be mentioned that the high buckling loads obtained with the defects in the present study are partly due to the technique adopted for introducing the defects, which avoided producing local variations in the length of the generators and hence eccentricities in the loading of the shell. In practice it is to be expected that the occurrence of such local defects will be accompanied by a tilting of the shell, producing eccentric and non-uniform loading conditions, and therefore greater reductions in the load bearing capacity of the

shell. The present attempt however has been to study the effect of the local facet-shaped defects in isolation, in order to obtain a proper understanding of their behaviour.

The test results indicate that the effect of facet-shaped local defects is independent of the thickness and the length of the shell. (The observations made herein are with regard to thin shells of medium length, in which the defects are introduced away from the ends so as not to interfere with the boundary conditions). It appears that the magnitude of the collapse load obtained with the defect is affected only by the ratio of the circumferential length of the defect to the radius of the cylinder (given by the angular measure θ), which, in this case, is also a measure of the ratio of the depth of the defect to the radius of the shell. In fact, provided that the defects are large, even the effect of changes in the circumferential size of the defect appears to be very small.

The current study indicates that the secondary collapse mechanism of the one tier buckle pattern is quite different from that of the two tier pattern. The secondary collapse of shells which have buckled into the two tier mode is precipitated by the buckling of a diagonal fold between the facets, leading to a reduction in the number of facets around the circumference by one. Whereas, it appears that the collapse of the one tier pattern occurs due to the concentration of stresses in the adjoining cylindrical sections and results in the formation of additional buckles above or below the existing row, with no reduction in the circumferential number of facets. The behaviour of

the diamond-shaped local defects seems to be similar to that of the facets in the one tier pattern in that they also produce stress concentrations in their neighborhood causing premature failure of the shell. Thus the collapse mechanism of shells with facet-shaped defects is closer to that of shells with (partial) one tier patterns rather than to the secondary collapse of shells which have developed complete two tier patterns. Even with two defects imposed side by side at different heights simulating neighbouring facets in the two tier pattern, the collapse occurs in a similar fashion, due to the weakening of the neighbouring regions, rather than due to the buckling of the diagonal fold in between the imposed facets. It therefore appears that the space frame model which describes the secondary collapse behaviour of shells with the two tier pattern is not suitable for predicting the effect of local facet-shaped defects in axially loaded cylindrical shells. The unfavourable comparison obtained between the predictions of the model and the test results with imposed defects also suggests the same.

The experiments show that the load bearing capacity of the shells decreases in direct proportion to the number of facets imposed on them. This reduction is caused by a decrease in the effective stiffness of the shell due to the introduction of the defect. While the stiffness of the shell reduces by about 50% when defects are imposed all around the circumference, the addition of a single defect reduces the stiffness by only about 5% which is small in comparison to the detrimental effect of the stress concentrations produced by the imposed defect in its vicinity. Since the latter effect is independent

of the number of defects, the knockdown factor of a shell with two defects is only marginally lower than that obtained with one defect. For the same reason, it is found that if a defect is imposed on a shell with initial imperfections, their combined effect can be approximated by that of the larger of the two imperfections. That is, either the effect of the initial imperfections predominates or that of the imposed local defect (depending on which is greater), while the effect of the other is significantly reduced. In any case the net reduction in load bearing capacity produced by a local defect occurring in an imperfect shell will be much smaller than that caused by the same defect in a near perfect shell. The practical implications of this finding, in the case of damage occurring to imperfect shell structures while in service, are significant.

The results of the experiments have been used to develop empirical relations for the collapse loads of shells with single or multiple defects (at the same level). In view of the scatter observed in the experimental data and the lack of comparable references on the effect of local defects in existing literature, it can only be said that the accuracy of the nature of relations assumed and that of the constants obtained remains to be verified. Meanwhile the formulae are presented only as tentative attempts at describing quantitatively the effect of diamond-shaped local defects on the collapse load. It is hoped that these empirical relations and the observations presented regarding the physical aspects of collapse will be useful in making advances in future investigations on the effect of facet-shaped local defects on the stability of axially compressed cylindrical shells.

REFERENCES

1. Timoshenko,S.P., and Gere,J.M., "Theory of Elastic Stability", McGraw-Hill International Book Company, Second Edition, 1963.
2. Donnell,L.H., "A New Theory for the Buckling of Thin Cylinders Under Axial Compression and Bending", Trans. A.S.M.E., Vol.56, No.11, pages 795-806, November 1934.
3. Flügge,W., "Stresses in Shells", Third Printing, Springer - Verlag, 1966.
4. Stein,M., "The effect on the Buckling of Perfect Cylinders of Prebuckling Deformations and Stresses Induced by Edge Support", NASA TN D-1510, pages 217-227, December 1962.
5. Fischer,G., "Influence of Boundary Conditions on Stability of Thin-Walled Cylindrical Shells under Axial Load and Internal Pressure", AIAA Journal, Vol.3, No.4, pages 736-738, April 1965.
6. Hoff,N.J., "Low Buckling Stresses of Axially Compressed Circular Cylindrical Shells of Finite Length", ASME Journal of Applied Mechanics, Vol.32, No.3, pages 533-541, September 1965.
7. Hoff,N.J., and Rehfield,L.W., "Buckling of Axially Compressed Circular Cylindrical Shells at Stresses Smaller Than the Classical Critical Value", ASME Journal of Applied Mechanics, Vol.32, No.3, pages 542-546, September 1965.
8. Hoff,N.J., and Soong,T.C., "Buckling of Circular Cylindrical Shells in Axial Compression", International Journal of Mechanical Sciences, Vol.7, No.7, pages 489-520, July 1965.
9. Simmonds,J.G., and Danielson,D.A., "New Results for the Buckling Loads of Axially Compressed Cylindrical Shells Subject to Relaxed Boundary Conditions", ASME Journal of Applied Mechanics, Vol.37,

No.1, pages 93-100, March 1970.

10. Almroth,B.O., "Influence of Edge Conditions on the Stability of Axially Compressed Cylindrical Shells", AIAA Journal, Vol.4, No.1, pages 134-140, January 1966; also NASA CR-161, February 1965.

11. Yamaki,N., "Elastic Stability of Circular Cylindrical Shells", North-Holland Series in Appl. Math. and Mechanics, Vol.27, 1984.

12. Almroth,B.O.,"Influence of Imperfections and Edge Restraint on the Buckling of Axially Compressed Cylinders", NASA CR-432, April 1966.

13. Von Kármán,Th., and Tsien,H.S., "The Buckling of Thin Cylindrical Shells under Axial Compression", Journal of the Aeronautical Sciences, Vol.8, No.8, pages 303-312, June 1941.

14. Tsien,H.S., "A Theory for the Buckling of Thin Shells", Journal of the Aeronautical Sciences, Vol.9, No.10, pages 373-384, August 1942.

15. Michielsen,H.F., "The Behavior of Thin Cylindrical Shells After Buckling Under Axial Compression", Journal of the Aeronautical Sciences, Vol.15, No.12, pages 738-744, December 1948.

16. Kempner,J., "Postbuckling Behavior of Axially Compressed Circular Cylindrical Shells", Journal of the Aeronautical Sciences, Vol.21, No.5, pages 329-335, 342, May 1954.

17. Almroth,B.O., "Postbuckling Behavior of Axially Compressed Circular Cylinders", AIAA Journal, Vol.1, No.3, pages 630-633, March 1963.

18. Hoff,N.J., Madsen,W.A., and Mayers,J., "Postbuckling Equilibrium of Axially Compressed Circular Cylindrical Shells", AIAA Journal, Vol.4, No.1, pages 126-133, January 1966.

19. Yoshimura,Y., "On the Mechanism of Buckling of a Circular Cylindrical Shell under Axial Compression", NACA T.M. 1390, 1955.

20. Babcock,C.D. and Sechler,E.E., "The Effect of Initial Imperfections on the Buckling Stress of Cylindrical Shells", NASA TN D-1510, pages 135-142, December 1962.

21. Sendelbeck,R.S., and Hoff,N.J., "Loading Rig in Which Axially Compressed Thin Cylindrical Shells Buckle Near Theoretical Values", Experimental Mechanics, Vol.12, No.8, pages 372-376, August 1972.

22. Tennyson,R.C., "A Note on the Classical Buckling Load of Circular Cylindrical Shells under Axial Compression", AIAA Journal, Vol.1, No.2, pages 475-476, February 1963.

23. Tennyson,R.C., "Buckling of Circular Cylindrical Shells in Axial Compression", AIAA Journal, Vol.2, No.7, pages 351-353, July 1964.

24. Foster,C.G., "Axial Compression Buckling of Conical and Cylindrical Shells", Experimental Mechanics, Vol.27, No.3, pages 255-261, September 1987.

25. Esslinger,M., and Geier,B., "Postbuckling Behavior of Structures", CISM Courses and Lectures No.236, Chapter 3, pages 101-132, Springer - Verlag, 1975.

26. Ricardo,O.G.S., "A Report on Three Series of Experiments and the Description of a Simplified Model of the Thin Wall Cylinder and Cone Buckling Mechanism", NASA TN D-1510, pages 163-172, December 1962.

27. Ricardo,O.G.S., "An Experimental Investigation of the Radial Displacements of a Thin-Walled Cylinder", NASA CR - 934, 1967.

28. Donnell,L.H., and Wan,C.C., "Effect of Imperfections on Buckling

of Thin Cylinders and Columns Under Axial Compression", Journal of Applied Mechanics ASME, Vol.17, No.1, pages 73-83, March 1950.

29. Lee,L.H.N.,"Effects of Modes of Initial Imperfections on the Stability of Cylindrical Shells under Axial Compression", NASA TN D-1510, pages 143-161, December 1962.

30. Lu,S.Y., and Nash,W.A., "Buckling of Initially Imperfect Axially Compressed Cylindrical Shells", NASA TN D-1510, pages 187-202, December 1962.

31. Dym,C.L. and Hoff,N.J., "Perturbation Solutions for the Buckling Problems of Axially Compressed Thin Cylindrical Shells of Infinite or Finite Length", ASME Journal of Applied Mechanics, Vol.35, No.4, pages 754-762, December 1968.

32. Bhatia,P., and Babcock,C.D., "Axial Buckling of Cylindrical Shells With Prismatic Imperfections", ASME Journal of Applied Mechanics, Vol.41, No.3, pages 731-736, September 1974.

33. Koiter,W.T.,"The Stability of Elastic Equilibrium", Ph.D. Thesis (in Dutch), Delft, Holland (1945), Translation by Edward Riks, Technical Report AFFDL TR-70-25, February 1970.

34. Hutchinson,J.W., and Koiter,W.T., "Postbuckling Theory", Applied Mechanics Reviews, Vol.23, No.12, pages 1353-1366, December 1970.

35. Tennyson,R.C., and Muggeridge,D.B., "Buckling of Axisymmetric Imperfect Circular Cylindrical Shells under Axial Compression", AIAA Journal, Vol.7, No.11, pages 2127-2131, November 1969.

36. Hutchinson,J.W., Tennyson,R.C., and Muggeridge,D.B., "Effect of a Local Axisymmetric Imperfection on the Buckling Behavior of a Circular Cylindrical Shell under Axial Compression", AIAA Journal, Vol.9, No.1, pages 48-52, January 1971.

37. Muggeridge,D.B., "The Effect of Initial Axisymmetric Shape

Imperfections on the Buckling Behaviour of Circular Cylindrical Shells under Axial Compression", University of Toronto Institute for Aerospace Studies Report No.148, December 1969.

38. Amazigo,J.C., and Budiansky,B., "Asymptotic Formulas for the Buckling Stresses of Axially Compressed Cylinders With Localized or Random Axisymmetric Imperfections", ASME Journal of Applied Mechanics, Vol.39, No.1, pages 179-184, March 1972.

39. Amazigo,J.C., "Buckling under Axial Compression of Long Cylindrical Shells with Random Axisymmetric Imperfections", Quarterly of Applied Mathematics, Vol.26, No.4, pages 537-566, January 1969.

40. Van Slooten,R.A., and Soong,T.T., "Buckling of a Long, Axially Compressed, Thin Cylindrical Shell With Random Initial Imperfections", ASME Journal of Applied Mechanics, Vol.39, No.4, pages 1066-1071, December 1972.

41. Hansen,J.S., "Influence of General Imperfections in Axially Loaded Cylindrical Shells", Intern. Journal of Solids Structures, Vol.11, No.11, pages 1223-1233, November 1975.

42. Hansen,J.S., "General Random Imperfections in the Buckling of Axially Loaded Cylindrical Shells", AIAA Journal, Vol.15, No.9, pages 1250-1256, September 1977.

43. Arbocz,J., and Babcock,C.D., "The Effect of General Imperfections on the Buckling of Cylindrical Shells", ASME Journal of Applied Mechanics, Vol.36, No.1, pages 28-38, March 1969.

44. Arbocz,J., and Sechler,E.E., "On the Buckling of Axially Compressed Imperfect Cylindrical Shells", ASME Journal of Applied Mechanics, Vol.41, No.3, pages 737-743, September 1974.

45. Elishakoff,I., Van Manen,S., Vermeulen,P.G., Arbocz,J.,

"First-Order Second-Moment Analysis of the Buckling of Shells with Random Imperfections", AIAA Journal, Vol.25, No.8, pages 1113-1117, August 1987.

46. Abramovich,H., Yaffe,R., Singer,J., "Evaluation of Stiffened Shell Characteristics from Imperfection Measurements", Journal of Strain Analysis, Vol.22, No.1, pages 17-23, January 1987.

47. Bushnell,D., "Computerized Buckling Analysis of Shells", Mechanics of Elastic Stability Vol.9, Martinus Nijhoff Publishers, 1985.

48. Ellinas,C.P., "Ultimate Strength of Damaged Tubular Bracing Members", ASCE Journal of Structural Engineering, Vol.110, No.2, pages 245-259, February 1984.

49. Ueda,Y., and Rashed,S.M.H., "Behavior of Damaged Tubular Structural Members", ASME Journal of Energy Resources Technology, Vol.107, No.3, Pages 342-349, September 1985.

50. Durkin,S., "An Analytical Method for Predicting the Ultimate Capacity of a Dented Tubular Member", International Journal of Mechanical Sciences, Vol.29, No.7, pages 449-467, July 1987.

51. Okubo,S., Wilson,P.E., and Whittier,J.S., "Influence of Concentrated Lateral Loads on the Elastic Stability of Cylinders in Bending", Experimental Mechanics, Vol.10, No.9, pages 384-389, September 1970.

52. Evensen,D.A., "High-speed Photographic Observation of the Buckling of Thin Cylinders", Experimental Mechanics, Vol.4, No.4, pages 110-117, April 1964.

53. Almroth,B.O., Holmes,A.M.C., and Brush,D.O., "An Experimental Study of the Buckling of Cylinders Under Axial Compression",

Experimental Mechanics, Vol.4, No.9, pages 263-270, September 1964.

54. Tennyson,R.C., "Buckling Modes of Circular Cylindrical Shells under Axial Compression", AIAA Journal, Vol.7, No.8, pages 1481-1487, August 1969.

55. De Neufville,R.L., and Connor,J.J., "Postbuckling Behavior of Thin Cylinders", Proc. ASCE Journal of the Engineering Mechanics Division, Vol.94, No.EM 2, pages 585-603, April 1968.

56. Hoff,N.J., "Some Recent Studies of the Buckling of Thin Shells", The Aeronautical Journal of the Royal Aeronautical Society, Vol.73, pages 1057-1070, December 1969.

57. Thielemann,W.F., "On the Postbuckling Behavior of Thin Cylindrical Shells", NASA TN D-1510, pages 203-216, December 1962.

58. Foster,C.G., "Deflections in Thin Cylindrical Shells", Ph.D. Thesis, University of Tasmania, September 1979.

59. Foster,C.G., "Some Observations on the Yoshimura Buckle Pattern for Thin-Walled Cylinders", ASME Journal of Applied Mechanics, Vol.46, No.2, pages 377-380, June 1979.

60. Foster,C.G., "Estimation of the Collapse Loads of Thin-Walled Cylinders in Axial Compression", ASME Journal of Applied Mechanics, Vol.46, No.2, pages 381-385, June 1979.

61. Foster,C.G., "On the Buckling of Thin Walled Cylinders Loaded in Axial Compression", Journal of Strain Analysis, Vol.16, No.3, pages 205-210, July 1981.

62. Foster,C.G., "Buckling of Very Thin, Nearly Perfect Axially Loaded Circular Cylindrical Shells", AIAA Journal, Vol.21, No.5, pages 794-796, May 1983.

63. Cox,H.L., "The Buckling of Plates and Shells", International Series of Monographs on Aeronautics and Astronautics, Div.1, Vol.4, Chapter 5, pages 71-120, Pergamon Press, 1963.

64. Klitchielf,J.M., "Buckling of a Triangular Plate by Shearing Forces", Quarterly Journal of Mechanics and Applied Mathematics, Vol.4, Pt.3, pages 257-259, September 1951.

65. Wakasugi,S., "Buckling of Right Angled Isosceles Triangular Plates Simply Supported at the Edges", Trans. Japan Soc. Mech. Engrs., Vol.19, No.83, pages 59-65, 1953.

66. Wakasugi,S., "Buckling of a Simply Supported Equilateral Triangular Plate", Japan Soc. Mech. Engrs. Bull., Vol.4, No.13, pages 20-25, February 1961.

67. Cox,H.L., and Klien,B., "The Buckling of Isosceles Triangular Plates", Journal of the Aeronautical Sciences, Vol.22, No.5, pages 321-325, May 1955.

68. Valisetty,R.R., and Reddy,A.D., "Design Data and Buckling of Laminated Composite Triangular Plates", Proceedings of the Gen. Aviation Aircraft Meeting & Exposition, Wichita, Kansas, published by the Society of Automotive Engineers, Inc., Warrandale, PA 15096, pages 25-29, April 1985.

69. Timoshenko,S.P., and Woinowsky-Krieger,S., "Theory of Plates and Shells", McGraw-Hill Kogakusha Ltd., Second Edition, 1959.

70. Trahair,N.S., "The Behaviour and Design of Steel Structures", published by Methuen of Australia, Sydney, pages 100-111, 1977.

71. Hoff,N.J., Soong,T.C., and Sendelbeck,R.L., "Remarks on the Buckled Shapes of Thin-Walled Circular Cylindrical and Conical Shells Subjected to Axial Compression", article in Problems of Hydromechanics and Continuum Mechanics, pages 390-401, published

by the Society for Industrial and Applied Mathematics, Philadelphia, Pennsylvania, 1969.

72. Kollár,L., and Dulácska,E., "Buckling of Shells for Engineers", John Wiley and Sons, page 40, 1984.

73. Foster,C.G., Private Communication.

74. Lindberg,H.E., Rubin,M.B., and Schwer,L.E., "Dynamic Buckling of Cylindrical Shells from Oscillating Waves Following Axial Impact", International Journal of Solids Structures, Vol.23, No.6, pages 669-692, June 1987.

75. Foster,C.G., "Measurement of Radial Deformations in Thin-walled Cylinders", Experimental Mechanics, Vol.18, No.11, pages 426-430, November 1978.

76. Ligtenberg,F.K., "The Moiré Method - A New Experimental Method for the Determination of Moments in Small Slab Models", Proc. SESA, Experimental Stress Analysis, Vol.12, No.2, pages 83-98, 1955.

77. Pham Lam and Gregory,M.S., "Measurement of Slope Changes on Cylindrical Shell Surfaces", Civil Engineering Transactions, I.E.Aust., Vol.CE 15, Nos.1&2, pages 94-98, 1973.

78. Rish,R.F., "Some Studies in Elastic Shell Structures", Ph.D. Thesis, Faculty of Engineering, University of Tasmania, pages 46-64, February 1971.

79. Harris,L.A., Suer,H.S., Skene,W.T. and Benjamin,R.J., "The Stability of Thin-Walled Unstiffened Circular Cylinders Under Axial Compression Including the Effects of Internal Pressure", Journal of the Aeronautical Sciences, Vol.24, No.8, pages 587-596, August 1957.

APPENDIX A

ULTIMATE STRENGTH OF ISOSCELES TRIANGULAR PANELS

In the design of light weight structures it is usual to allow the plate elements to buckle, making use of their post-buckled strength to obtain the maximum possible weight reduction. Of course in doing so, it is necessary to make certain that the ultimate strength of the plate is not exceeded. In the study conducted by Valisetty and Reddy[68], it was found that a triangular stiffening pattern is much more efficient than the rectangular stiffening traditionally used in stiffened panel construction. Although the concept is still new, it is likely that triangular stiffening will be employed more in the future in the construction of light weight structures. It is therefore of practical interest to determine the ultimate strength of isosceles triangular panels. Noting that analytical investigations regarding the ultimate strength of triangular panels is scarce in literature, the analysis conducted in Chapter 4 has been extended here to estimate the ultimate load of the simply supported isosceles triangular plate. Obviously the present analysis is also restricted to isotropic plates, subjected to the same two loading conditions that were investigated previously. The methods employed are similar to those used by Timoshenko and Gere for the rectangular plate[1], and it will be seen that the results are also qualitatively similar, except that the aspect ratio of the triangular plate appears as an additional parameter in this case.

A1 Ultimate Load for the Isosceles Triangular Plate Whose Edges are Constrained to Remain Straight

The results of the large deflection analysis conducted in Chapter 4 are used in this section to estimate the ultimate strength of an isosceles triangular plate, by applying the maximum shear stress criterion, that is, on the basis that the load carried by the plate reaches its maximum value when the maximum shear stress in the panel reaches the allowable shear stress; the latter being taken as half the yield stress σ_{yp} of the material.

The maximum shear stress in the panel τ_{mx} occurs at (X_0,Y_0) = (a,0) in case 1 and at (X_0,Y_0) = $(a,\pm 0.6b)$ in case 2. The shear stress τ_{xy} being zero along the edge x = a, $\tau_{mx} = \frac{1}{2}|\sigma_x - \sigma_y|$ at (X_0,Y_0). Substituting for σ_x , σ_y from eqns.4.19, and equating τ_{mx} to $\sigma_{yp}/2$, the value of n_0 corresponding to the maximum load may be obtained as,

$$n_0 = \left[\frac{\sigma_{yp}(1-\nu t_0)}{p_{cr}} + B_0^2\, Q_0\right]\left[T_0 + B_0^2\, Q_0\right]^{-1} \qquad \text{(A1)}$$

where $T_0 = (1 - \nu)(1 + t_0)$ and Q_0 is given by,

$$Q_0 = (1 - \nu)\left[\frac{a}{\pi}\right]^2\left[\frac{1}{2}\left[f_{,y}^{\,2} - f_{,x}^{\,2}\right] + \left[\frac{\pi}{a}\right]\sum_i\left[t_{2i}h_{,yi} - t_{1i}g_{,xi}\right]\right]_{(X_0,Y_0)}$$

Substituting the above value of n_0 in eqns.4.20 and 4.21, the ultimate load is obtained as,

$$P_u = 2bt\sigma_{yp}\left[K_1 + K_2\,\frac{p_{cr}}{\sigma_{yp}}\right] \qquad \text{(A2)}$$

where K_1 and K_2 are constants for a fixed value of a/b, given by,

$$K_1 = \left[\frac{R_0(1-\nu t_0)}{T_0 + Q_0 B_0^2}\right] \quad \text{and} \quad K_2 = \left[\frac{T_0(1-R_0) + Q_0 B_0^2}{T_0 + Q_0 B_0^2}\right] \tag{A3}$$

It may be noted that in case 1, $t_0 = -1$, so that $T_0 = 0$; hence $K_2 = 1$. Using the notation,

$$K_0 = \pi \alpha \sqrt{\frac{p_0}{3(1-\nu^2)}} \tag{A4}$$

where p_0 is the buckling coefficient given by $p_0 = (a^2 t/\pi^2 D)p_{cr}$, the ultimate load may be expressed in non-dimensionalized form as,

$$\frac{P_u}{t^2\sqrt{E\sigma_{yp}}} = \left[\frac{K_1}{\psi} + K_2 K_0^2 \psi\right] \tag{A5}$$

where ψ is a non-dimensional parameter, given by $\psi = \frac{t}{2b}\sqrt{\frac{E}{\sigma_{yp}}}$.

The values of K_0, K_1 and K_2 for the two loading cases are plotted against a/b in Figures A1 and A2. These values are also tabulated in Table A1. The non-dimensionalized values of ultimate load, obtained by using these values in eqn.A5, are plotted against ψ for constant values of a/b in Figures A3 and A4, for cases 1 and 2 respectively. It may be noted that the values of K_1 and K_2 are determined from the results of the large deflection analysis, which was conducted on the assumption that the edges of the plate remain straight even after buckling; hence the ultimate loads given by eqn.A5

are valid only for isosceles triangular panels whose edges are constrained to remain straight.

A2 Ultimate Load for the Unconstrained Isosceles Triangular Plate

An approximate estimate for the load carrying capacity of the isosceles triangular plate whose edges are not constrained to remain straight may be obtained in the same manner in which the ultimate load for the rectangular plate was estimated by Von Kármán (Ref.1, page 418). The total load carried by the buckled plate is given by eqn.4.20 as

$$P = (2bC_0)t(n_0 p_{cr}) \tag{A6}$$

which is equal to a uniform stress of intensity $(n_0 p_{cr})$ distributed over a length $(2bC_0)$ over the base. Hence the load carrying capacity of the buckled plate may be regarded as equivalent to that of a similar unbuckled plate of base length $(2bC_0)$. The maximum load that can be carried by the latter (unbuckled) plate is obtained when its buckling stress becomes equal to the yield stress of the material, i.e., when

$$\frac{\pi^2 \alpha^2 D}{C_0^2 b^2 t} \cdot p_0 = \sigma_{yp} \tag{A7}$$

Extracting the value of C_0 from eqn.A7 and substituting in eqn.A6, the ultimate load for the isosceles triangular plate is obtained as

$$P_u = \pi \alpha \sqrt{\frac{p_0}{3(1-\nu^2)}}\, t^2 \sqrt{E\sigma_{yp}} = K_0\, t^2 \sqrt{E\sigma_{yp}} \tag{A8}$$

In non-dimensional terms this ultimate load may be expressed as

$$\frac{P_u}{t^2\sqrt{E\sigma_{yp}}} = K_0 \qquad \text{(A9)}$$

The values of K_0 plotted for the two cases in Figure A1 thus also represent the non-dimensional values of the ultimate load for the isosceles triangular panel whose edges are not constrained to remain straight. It is to be noted that the assumptions involved in the derivation of equation A8 are the same as those of Von Kármán's hypothesis for the rectangular plate, except that, in addition to considering the base length of the equivalent plate to be that given by $(2C_0b)$, it is also assumed to be of the same aspect ratio as that of the original plate. The equations (A2 and A8) obtained by the two approaches here are similar to those given by Timoshenko and Gere for the rectangular plate (Ref.1, pages 416 and 419); the only difference being that the constants K_0 to K_2 involved in this case, are functions of the aspect ratio a/b of the isosceles triangular plate.

Finally it may be mentioned that the ultimate loads presented here are theoretical estimates for the perfect plate; and can serve only as upper bounds for the actual load carrying capacity of isosceles triangular plates. These values need to be corrected with some empirically obtained factors (as has been done in the case of rectangular plates) before they can be used for design purposes.

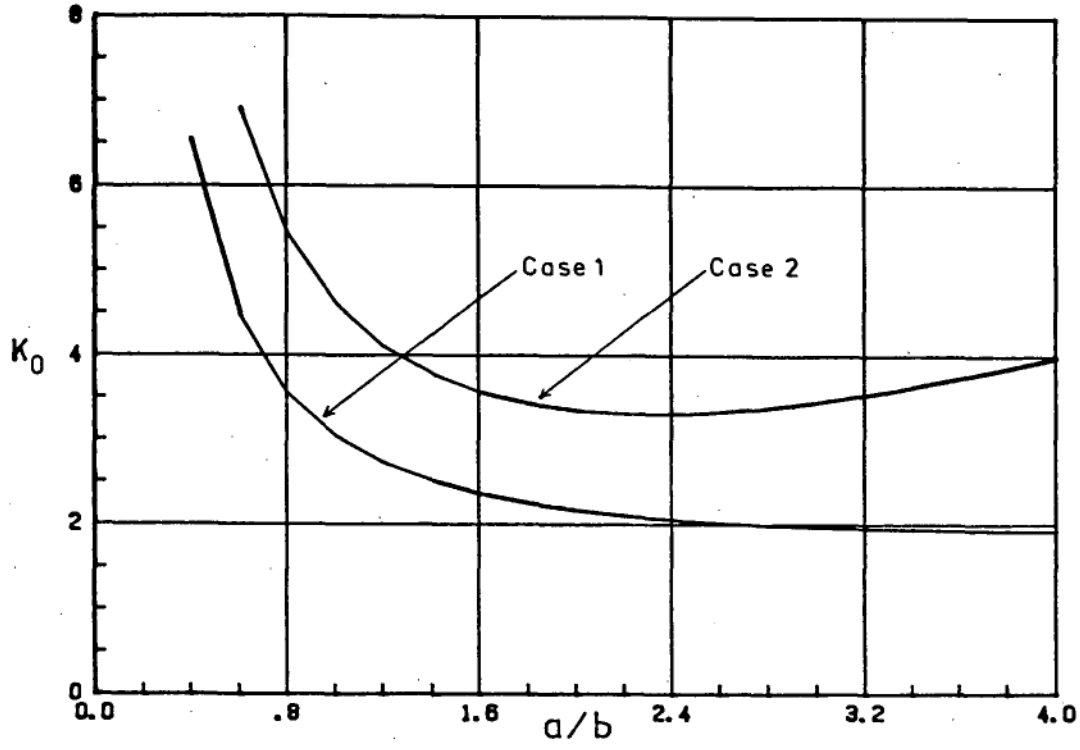

Figure A1
Constant K_0 for the Ultimate Load

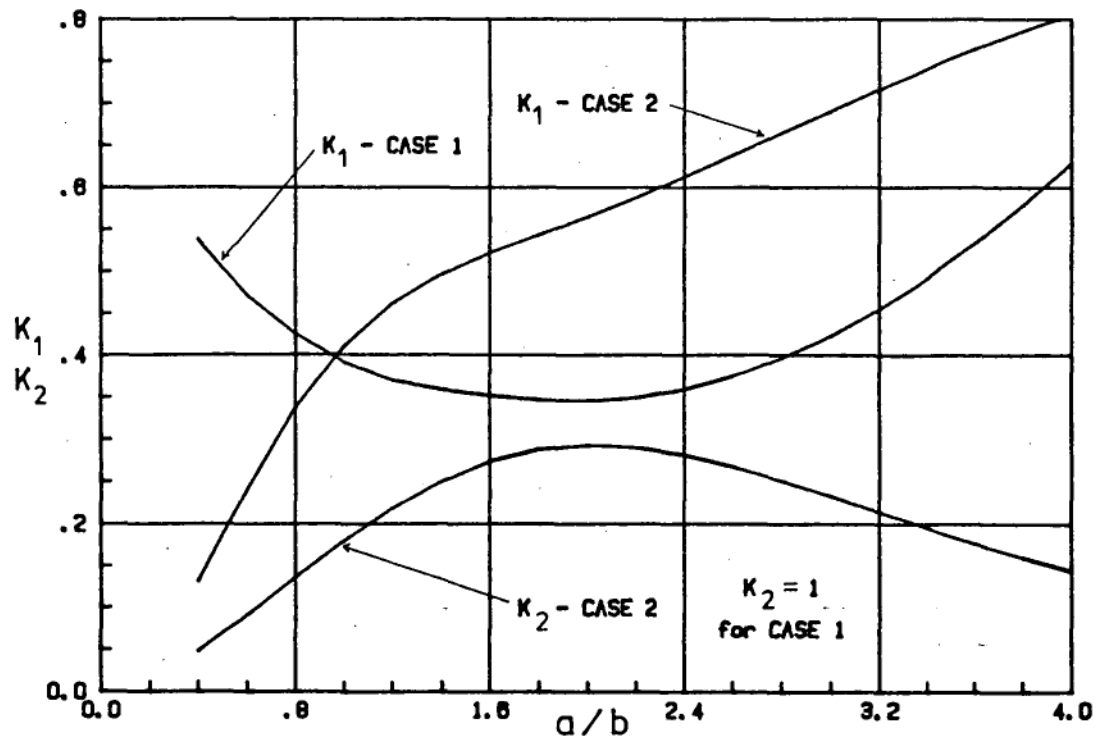

Figure A2
Constants K_1 and K_2 for Ultimate Load

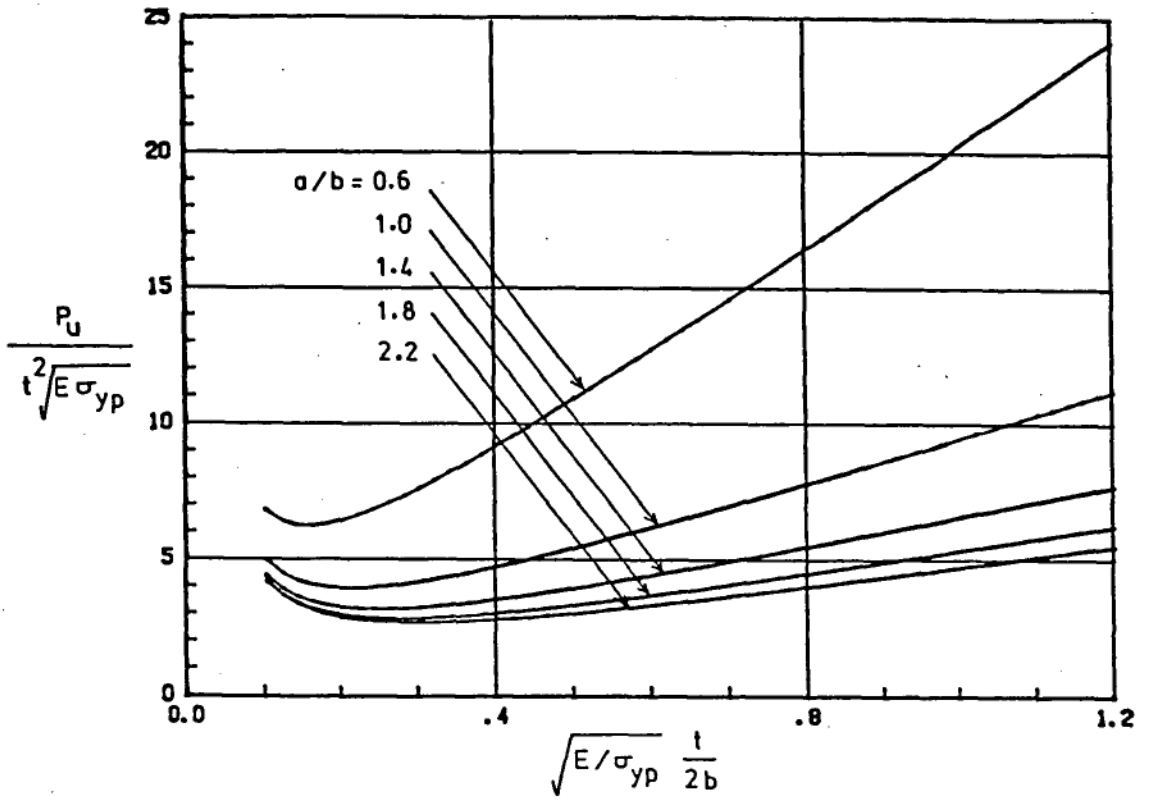

Figure A3. Ultimate Load Using Maximum Shear Stress Criterion - Case 1

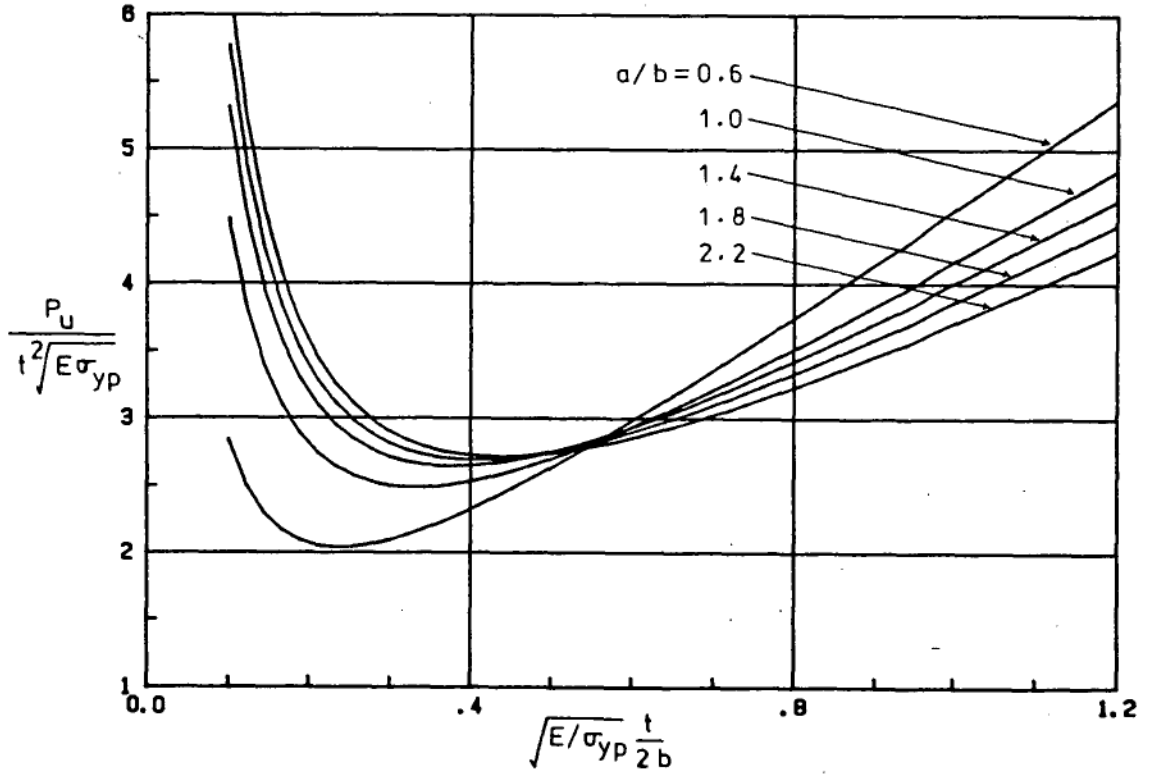

Figure A4. Ultimate Load Using Maximum Shear Stress Criterion - Case 2

Table A1 Constants for the Ultimate Load

	Case 1			Case 2		
a/b	K_0	K_1	K_2	K_0	K_1	K_2
0.4	6.52148	0.53743	1	10.0145	0.13133	0.04784
0.6	4.44863	0.47056	1	6.88239	0.24064	0.09091
0.8	3.51244	0.42380	1	5.39915	0.33705	0.13631
1.0	3.00638	0.38975	1	4.57217	0.41022	0.17957
1.2	2.69231	0.36925	1	4.06699	0.46135	0.21826
1.4	2.47841	0.35828	1	3.74177	0.49628	0.25051
1.6	2.32542	0.35121	1	3.52858	0.52186	0.27430
1.8	2.21324	0.34640	1	3.39239	0.54372	0.28847
2.0	2.12981	0.34515	1	3.31346	0.56531	0.29336
2.2	2.06735	0.34905	1	3.27918	0.58813	0.29035
2.4	2.02057	0.35883	1	3.28049	0.61251	0.28115
2.6	1.98569	0.37542	1	3.31038	0.63814	0.26747
2.8	1.95987	0.39585	1	3.36333	0.66443	0.25082
3.0	1.94096	0.42255	1	3.43491	0.69073	0.23252
3.2	1.92729	0.45434	1	3.52159	0.71645	0.21359
3.4	1.91758	0.49101	1	3.62055	0.74109	0.19481
3.6	1.91083	0.53236	1	3.72955	0.76428	0.17674
3.8	1.90628	0.57825	1	3.84681	0.78583	0.15975
4.0	1.90339	0.62854	1	3.97088	0.80561	0.14404

APPENDIX B

MOIRÉ METHOD FOR THE DETERMINATION OF RADIAL DEFORMATIONS IN CYLINDRICAL SHELLS

The adaptation of the optical system described in Chapter 7 for the whole field measurement of radial deformations in cylindrical shells is based on the principle of the photo-reflective moiré method introduced by Ligtenberg[76] for the determination of slope variations in rectangular plates. While the Ligtenberg method has been applied for the measurement of slope changes in cylindrical shell segments earlier[77], the adaptation of the method for whole cylindrical shells was only possible after Foster introduced his optical system employing the conical mirror to provide a total view of the entire inner surface of the shell. The method presented here is essentially the same as that described earlier by Foster[75], except that the theory has been developed for the modified optical system employing the new conical mirror. Further, while Foster developed the theory for the collimated field of view, the present theory takes into account the diverging conical view of the camera, and hence is applicable to optical systems without any collimating arrangement even with the camera placed at a finite distance from the shell.

In the reflective moiré method the fringes are produced by superposition of the images of the grid reflected by the deformed and undeformed surfaces of the specimen under investigation. Essentially each fringe is formed when a dark line from one of the images of the

grid falls over a bright line from the other image. Thus the first fringe forms when there is a relative displacement between the object grids equal to half the pitch of the grid, i.e., when the deformation of the reflecting surface causes the incident ray to shift on the grid surface by a distance equal to half the pitch in the direction normal to the grid-lines. Each subsequent fringe is produced by an additional relative shift of the incident ray equal to the pitch of the grid. This may be expressed mathematically as $S = n.p$, where S is the total shift of the incident ray on the grid surface in the direction normal to the grid-lines, p is the pitch of the grid and n is the fringe order which takes values of 1/2, 3/2, 5/2 and so on. In the present case, the axial shift of the incident ray on the grid surface S_a, the shift in the circumferential direction S_c, and that in the direction normal to the spiral grid-lines S_n, may respectively be expressed as

$$S_a = n_c P_c \quad ; \quad S_c = n_a p_a \quad ; \quad S_n = n_s p_s \tag{B1}$$

where n_c, n_a, n_s and p_c, p_a and p_s respectively denote the fringe orders and the pitches corresponding to the circumferential, axial and the spiral grids.

The relative shifts, caused by the deformation of the shell, of the incident ray in the axial and circumferential directions on the grid surface may be obtained from geometry as illustrated in Figure B1. The changes in slope of the shell surface in the circumferential and the axial directions, at the point where the incident ray gets reflected, are denoted by δ_c and δ_a respectively (assumed to be

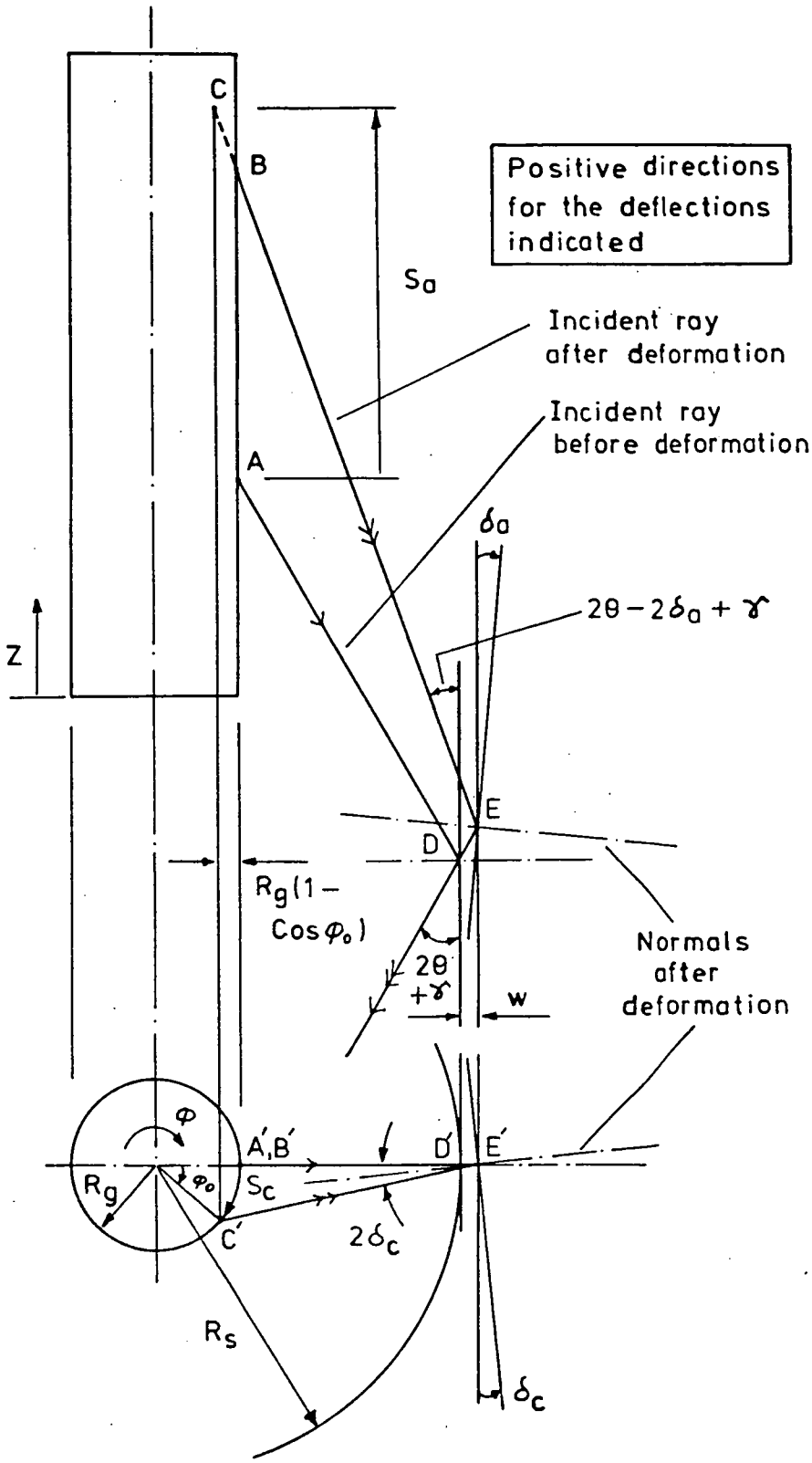

Figure B1. Effect of Deformations of the Shell on the Incident Ray

positive in the directions indicated in the figure). The outward radial displacement is denoted by w. From the bottom view we obtain

$$S_c = R_g\varphi_0 \quad ; \quad R_g\sin\varphi_0 = C'E'\sin(2\delta_c)$$

and

$$C'E' = \left[R_g^2 + (R_s+ w)^2 - 2R_g(R_s+ w)\cos\varphi_0\right]^{1/2}$$

Hence,

$$\cos(S_c/R_g) = \cos\varphi_0 = \left[\frac{R_s+ w}{R_g}\right]\sin^2(2\delta_c)$$

$$\pm\left[1 - \left[\frac{R_s+ w}{R_g}\right]^2\sin^2(2\delta_c)\right]^{1/2}\left[1 - \sin^2(2\delta_c)\right]^{1/2} \qquad (B2)$$

and

$$\tan(2\delta_c) = \frac{R_g\sin(S_c/R_g)}{R_s+ w - R_g\cos(S_c/R_g)} \qquad (B3)$$

In eqn.B2, the positive sign gives the required root. The maximum value of δ_c occurs when the incident ray after deformation becomes tangent to the grid and is given by

$$\delta_{cmax} = \frac{1}{2}\sin^{-1}\left[R_g/(R_s+ w)\right]$$

If δ_c is greater than δ_{cmax} the grid will no longer be reflected by that part of the shell and the image becomes dark. The relationship between the circumferential slope δ_c of the shell wall and the shift S_c of the incident ray on the grid surface in the circumferential direction is plotted in Figure B2 (page 338) for w = 0. It is apparent that this relation is approximately linear for values of δ_c less than about 2^o. From the geometry of Figure B1, we may also obtain

$$\tan(2\theta+\gamma-2\delta_a) = \frac{R_s + w - R_g\cos\varphi_0}{S_a + (R_s - R_g - w)\cot(2\theta+\gamma)}$$

Hence,

$$S_a = \frac{R_s + w - R_g\cos(S_c/R_g)}{\tan(2\theta+\gamma-2\delta_a)} - \frac{R_s - R_g - w}{\tan(2\theta+\gamma)} \qquad \text{(B4)}$$

and

$$\tan(2\delta_a) = \frac{S_a\tan(2\theta+\gamma) - R_g[1-\cos(S_c/R_g)] - 2w}{S_a + (R_s - R_g - w)\cot(2\theta+\gamma) + [R_s - R_g\cos(S_c/R_g) + w]\tan(2\theta+\gamma)} \qquad \text{(B5)}$$

The convergence angle γ in eqns.B4 and B5 is given by eqn.7.1. The variation of δ_a with S_a (for $w = 0$ and $\gamma = 0$) is plotted in Figure B3, for different values of the circumferential slope δ_c. The maximum value of δ_a is restricted only by the distances of the ends of the grid from the section of the shell under consideration.

The relative shift on the grid surface in the direction normal to the spiral grid-lines having a helix angle α is given by

$$S_n = S_a\cos\alpha - S_c\sin\alpha \qquad \text{(B6)}$$

The variation of δ_a with S_n for constant values of δ_c obtained from eqns.B2, B4 and B6, for $w = \gamma = 0$ and $\alpha = 79^\circ$, is plotted in Figure B4. It may be observed that the plots in Figures B3 and B4 are highly non-linear.

In general the radial deflection of the shell is small in comparison to the shell radius and w may be neglected in the above equations. Hence from eqns.B3, B5 the two unknown slope deformations can be determined from the shifts S_c and S_a at any particular position on the shell surface. The shifts normal to the grid lines are obtained

from the fringe orders in the superposed photographs using eqns.B1. If the spiral grid is employed in lieu of one of the other grids, then eqn.B6 can be used to determine S_a or S_c whichever is unknown. Since the circumferential shift of the incident ray on the grid surface is independent of the axial slope of the shell wall (see eqn.B2), the axial grid alone may be used to determine the variation in slope in the circumferential direction. However to determine the slope in the axial direction fringe orders from two grids are required.

B1 Verification - Cylinder with Tilted Axis

To validate the expressions obtained, a known tilt (rigid body rotation) was applied to a test cylinder and fringes obtained by double exposure using each of the three grids. The length of the test cylinder was 121 mm and the radius 77 mm. The tilt was obtained by inserting a small block on one side at the bottom of the cylinder, so that one side was raised by 2.8 mm with respect to the other side producing a rigid body rotation of 1.042°. The radial displacement w, the axial slope δ_a and the circumferential slope δ_c in this case are given by

$$\delta_a = -\frac{\delta_0}{2R_s}.\cos\varphi \quad , \quad w = x.\delta_a \quad , \quad \delta_c = -w.\tan\varphi/R_s$$

where δ_0 is the axial displacement (= 2.8 mm) at $\varphi = 0$, $x = 0$ (x being the axial co-ordinate). The fringes obtained by superposition of the photographs taken from a distance of D = 4267mm (14 ft.) (using the Pentax K1000 camera with 400 mm focal length telephoto lens attached) are shown in Figure B5 (a, b and c respectively for the three grids).

The fringes obtained from double exposures from a distance of 1225 mm, using an ARCA 5"x4" format camera, are shown in Figures B6 (a,b and c). It may be observed that reducing the distance slightly reduces the sensitivity of the system due to the increase in the convergence angle in the case of the spiral and circumferential grids. The fringes obtained optically are compared with those obtained from theory in Figures B7 (a and b, for D = 4267 mm) and B8 (a and b, for D = 1225 mm). It can be seen that the agreement between theory and experiment is very good. To obtain this agreement it was necessary to include the radial deflection "w" as well as the convergence angle "γ" in the theoretical analysis. The latter especially was important, even for the larger value of D in which case the maximum angle of convergence was only 1°. The omission of γ in the analysis predicted two fringes less than the number actually observed with the circumferential and the spiral grids.

B2 Cantilever Shell with Concentrated Lateral Load - Theory

The solution for the deformations of a cylindrical shell fixed at one end and subjected to a concentrated lateral load at the free end is obtained using a combination of the inextensional bending theory and the end-load theory as suggested by Rish[78]. First, the deformation of the shell due to inextensional bending under the action of the lateral load at the free end is determined, by assuming that axial displacement at the other end is not restricted. Subsequently, end loads are applied at the fixed end to cancel out this axial displacement. The total deformation of the shell is obtained by adding

the deformations due to the inextensional bending and those due to the end-loads, to the membrane deformations due to cantilever bending.

For a circular cylinder of length L, radius R , thickness t and modulus of rigidity D, the deformations due to inextensional bending are obtained as follows (Ref.69, pages 501-507):

The displacements u, v and w are assumed to be of the form

$$u = \sum \frac{R}{m} A_m \cos(m\varphi) \ , \ v = x \sum A_m \sin(m\varphi) \ , \text{ and } w = x \sum m A_m \cos(m\varphi) \ .$$

These functions satisfy the conditions of inextensibility, namely, that the membrane strains given by $\epsilon_x = \partial u/\partial x$, $\epsilon_\varphi = (\partial v/\partial \varphi - w)/R$ and $\gamma_{x\varphi} = \frac{1}{R}\partial u/\partial \varphi + \partial v/\partial x$ should vanish. The strain energy of the shell in bending is given by

$$U = \frac{D}{2} \iint \left[\aleph_x^2 + \aleph_\varphi^2 + 2\nu . \aleph_x \aleph_y + 2(1-\nu)\aleph_{x\varphi}^2 \right] (Rd\varphi)dx \ ,$$

where the curvatures in x and φ directions and the twist term are given by

$$\aleph_x = \partial^2 w/\partial x^2 = 0 \quad , \quad \aleph_\varphi = \left[\partial v/\partial \varphi + \partial^2 w/\partial \varphi^2 \right] / R^2$$

and

$$\aleph_{x\varphi} = \left[\partial v/\partial x + \partial^2 w/\partial x \partial \varphi \right] / R$$

The external work W done by the load P is equal to $P.w_0$, where w_0 is the deflection under the load. Hence by using the principle of virtual work, i.e., that $(\partial U/\partial A_m)\delta A_m = (\partial W/\partial A_m)\delta A_m$ the coefficient A_m is obtained as,

$$A_m = \left[\frac{P R^3}{\pi D} \right] \frac{m}{(m^2-1)^2 \ (m^2 L^2/3 + 2[1-\nu]R^2)} \ .$$

For any given value of m, the axial displacement of the shell due to inextensional bending is then given by $u = u_0 \cos(m\varphi)$ where $u_0 = \frac{R}{m} A_m$.

The deformations due to the end-loads required to bring the axial displacement at the fixed end back to zero is obtained by using a modified form of Schorer's end-load theory[78], wherein the governing partial differential equation in terms of the axial displacement u is obtained as

$$\partial^4 u/\partial x^4 + \frac{D}{EtR^6}\left[\partial^4 u/\partial\varphi^4 + 2\,\partial^6 u/\partial\varphi^6 + \partial^8 u / \partial\varphi^8\right] = 0$$

which is turned into an ordinary differential equation of the form

$$d^4\bar{u} / dx^4 + 4\beta^4 \bar{u} = 0 , \quad \text{where} \quad 4\beta^4 = \frac{D}{EtR^6}\left[m^4 - 2m^6 + m^8\right]$$

by using $u = \bar{u}\cos(m\varphi)$. The solution of the latter equation is

$$\bar{u} = e^{\beta x}\left[C_1\cos\beta x + C_2\sin\beta x\right] + e^{-\beta x}\left[C_3\cos\beta x + C_4\sin\beta x\right] .$$

The axial stress resultant and the transverse shear stress resultant are respectively given by $N_x = Et(\partial u/\partial x)$ and $S = -\frac{EtR}{m}\,\partial^2\bar{u}/\partial x^2 \sin(m\varphi)$, while the radial displacement w is given by $w = -(m^2/4\beta^4 R)(\partial^3 u/\partial x^3)$. The constants C_1 to C_4 corresponding to each value of m are obtained from the boundary conditions that the stress resultants N_x, S vanish at the free end $x = L$; $w = 0$ and $\bar{u} = -u_0$ at the fixed end $x = 0$.

It may be pointed out that in the above two analyses, m takes values greater than or equal to 2. The values of A_m decrease rapidly

with m so that only 10 to 12 terms are sufficient for convergence. The deflection for m = 1 is that corresponding to the lateral displacement of the shell as a cantilever beam subjected to a concentrated load at the tip. These deformations have also to be added to those given by the inextensional bending and those from the end-load theory to obtain the final values.

B3 Cantilever Shell with Concentrated Lateral Load - Experiment

As an illustration of the use of the proposed moiré method in shell investigations a spun-cast cylindrical epoxy shell, radius 77.5 mm, thickness 0.875 mm and length 125 mm, with the top end fixed rigidly, was investigated under the action of a lateral point load applied at its free (lower) end. The deflection under the load was measured at 1.05 mm. Photographs showing the moiré interference patterns obtained by superposing the images from the unloaded and the loaded shell for the three grids are shown in Figure B9 (a, b and c).

The fringes are quite clear allowing their locations and hence the slopes at these locations to be determined. Again in this case it was found that the radial deflection was too large to be neglected in the analysis. Because of the changing angle of convergence and the effect of the radial deflection the fringes do not represent contours of constant slope as in the conventional Ligtenberg technique. In Figure B10 the circumferential slope as determined from the fringes obtained with the axial grid (Figure B9a) is plotted as a function of the angle from the load point around the free end. Comparison with the

theoretically derived curve is excellent. Axial slopes along the generator under the load as well as corresponding shell deflections are shown in Figure 11. The agreement between the measured and calculated slopes is not as good in this case, but there is good agreement for the deflection values. To obtain these values from the fringe data it was necessary to resort to an iterative procedure between δ_a and w.

B4 Concluding Remarks

The theory for a moiré technique for the measurement of radial deformations in cylindrical shells, its verification, and application to shell bending problems have been described in the foregoing sections. The theory has been rigorously developed including the effect of the convergence angle "γ" and the radial displacement "w" of the shell wall. If the optical system is modified so that the camera receives only rays parallel to the optical axis, γ will be zero so that the expressions relating the deformations to the fringe orders are considerably simplified.

In the development of traditional moiré theories it is usual to neglect the effect of the lateral displacement "w". In the present case, if the radial deflection is ignored then the system becomes determinate, so that the two unknown slopes can be readily solved for, knowing the values of the two orthogonal shifts, S_a and S_c, of the incident ray on the grid surface from the fringe data. (It is to be noted, though, that unlike the moiré methods for plates, the relations

for that of the cylinder are not uncoupled; hence for determining the axial slope it is necessary to know the shifts in both directions). However, the application of the technique to the two illustrations considered has indicated that the radial displacement "w" cannot be ignored, without a considerable loss in accuracy. In the Ligtenberg method the neglect of the lateral deflection does not lead to serious errors because the "lever arm" - the distance between the grid and the reflecting plate is kept very large (at least a meter). Whereas, in the current set up the lever arm is of the order of the radius of the shell. Thus it appears that unless the technique is being used to measure deformations in cylinders with very large radii, it would be inappropriate to neglect the effect of the lateral displacement.

With w taken into account, the system becomes indeterminate, since there are three unknown quantities - the two slopes and the radial deflection - to be determined from the two known values of the axial and circumferential shifts of the incident ray. It then becomes necessary to use an iterative approach, making use of the fact that the two slopes are derivatives of the radial displacement, to obtain all three quantities.

It may finally be added that although the theory has been developed only for circular cylindrical shells, the technique may easily be adapted for the measurement of deformations in conical or other axisymmetric shells by extending the theory to take into account the varying radius of the shell.

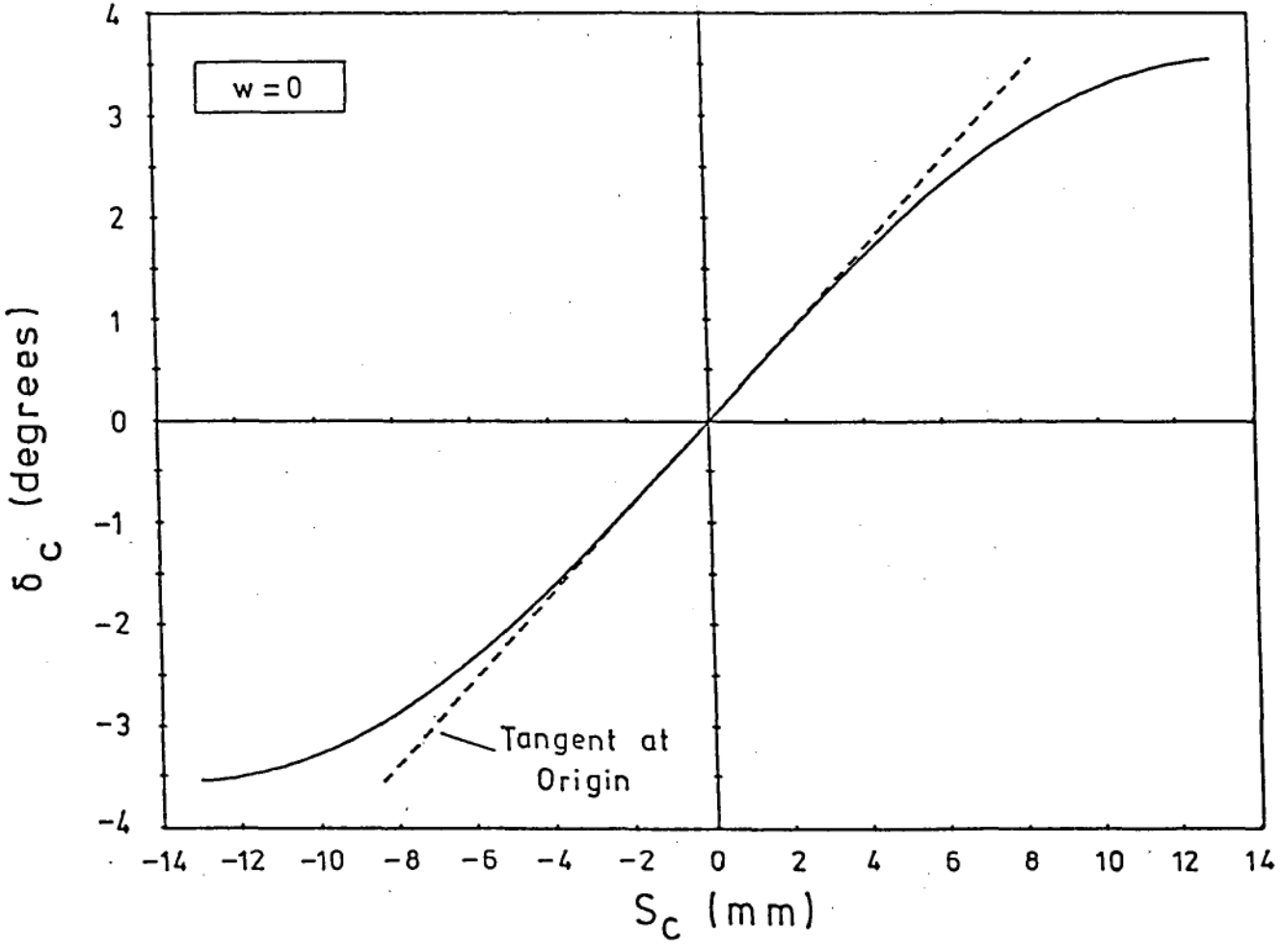

Figure B2
Effect of Circumferential Shift of Incident Ray
on the Circumferential Slope of the Shell

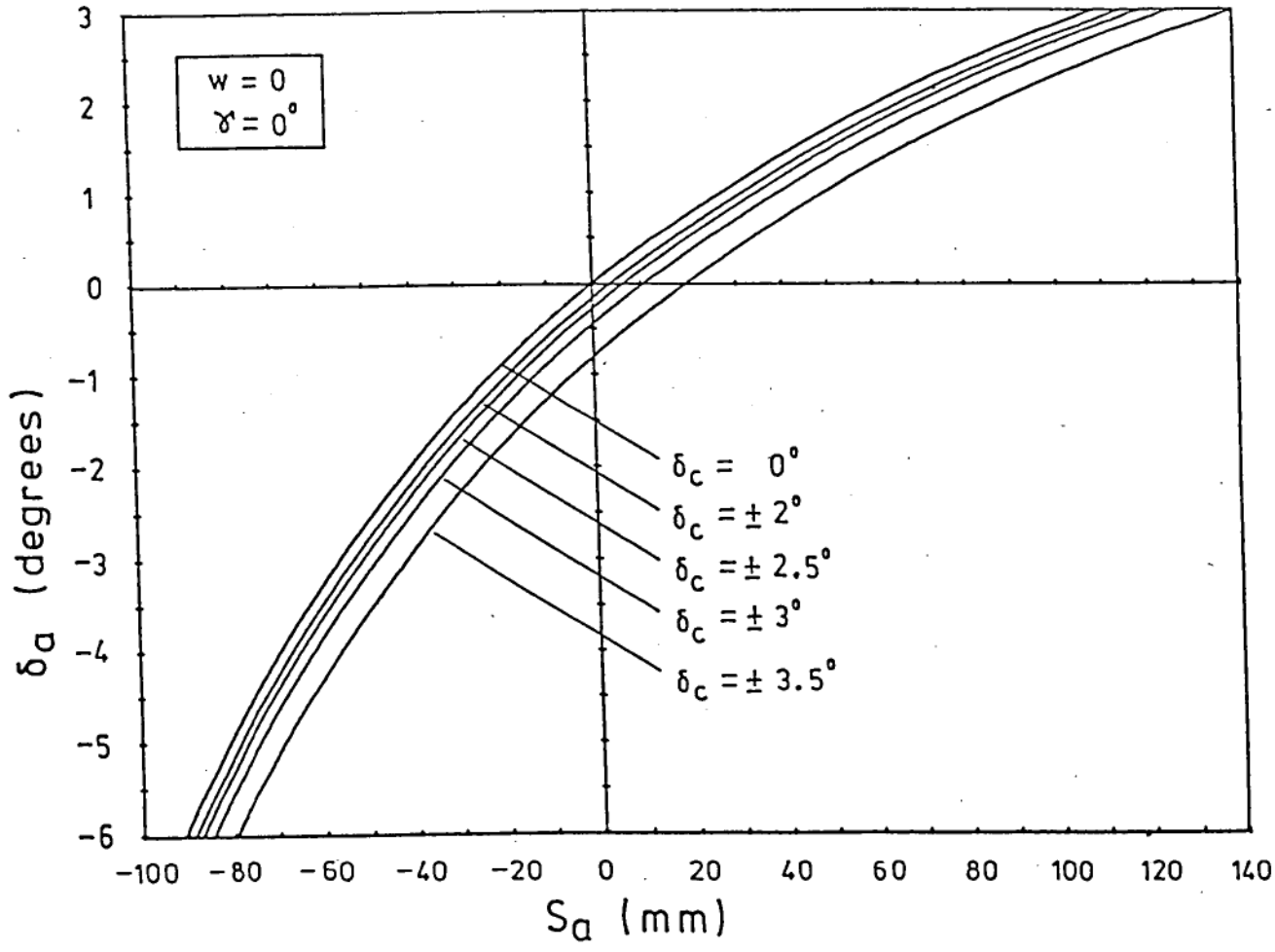

Figure B3
Effect of Axial Shift of Incident Ray
on the Axial Slope of the Shell

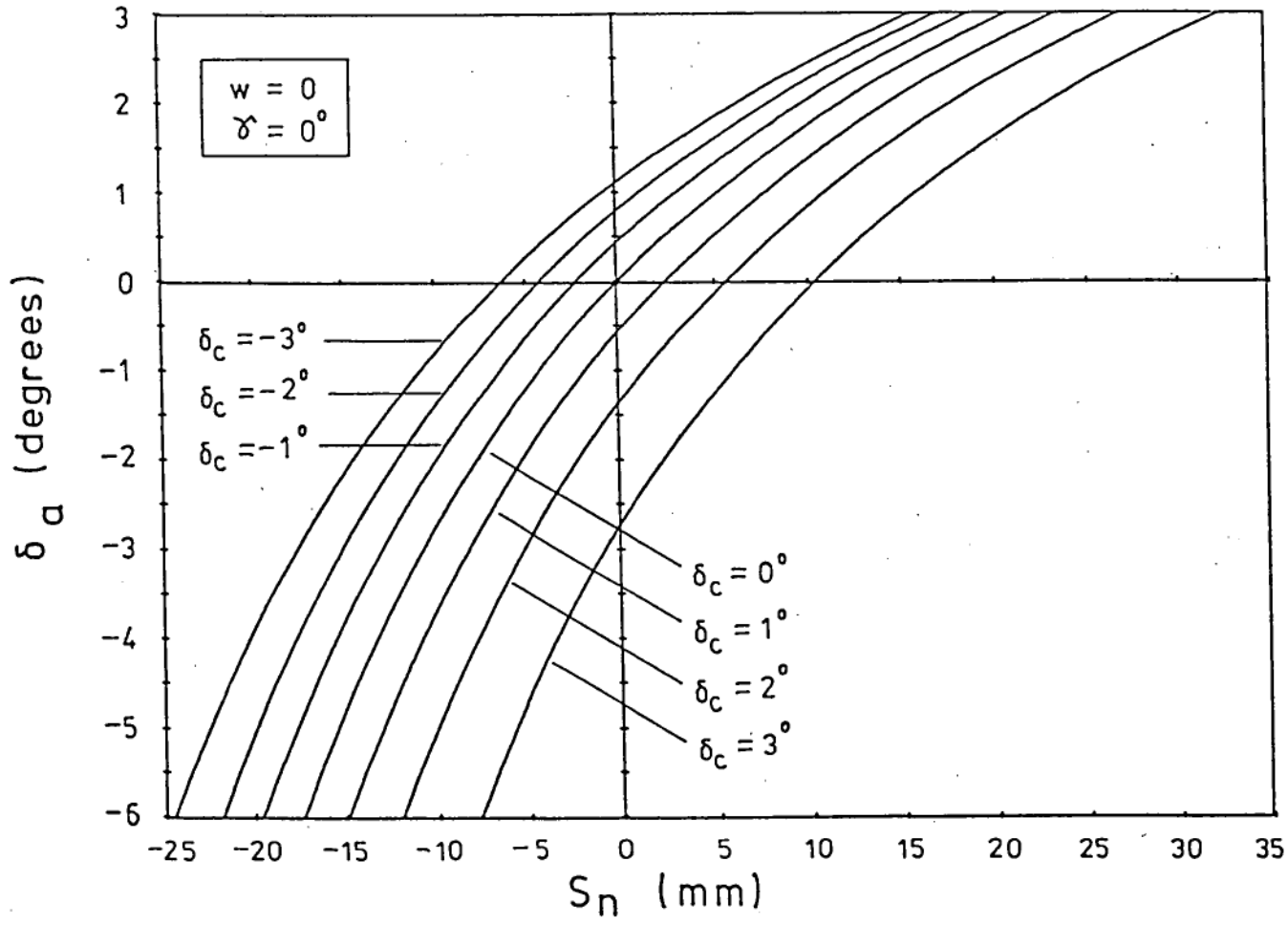

Figure B4
Variation of Axial Slope of the Shell with
Shift of Incident Ray Normal to the Spiral Lines

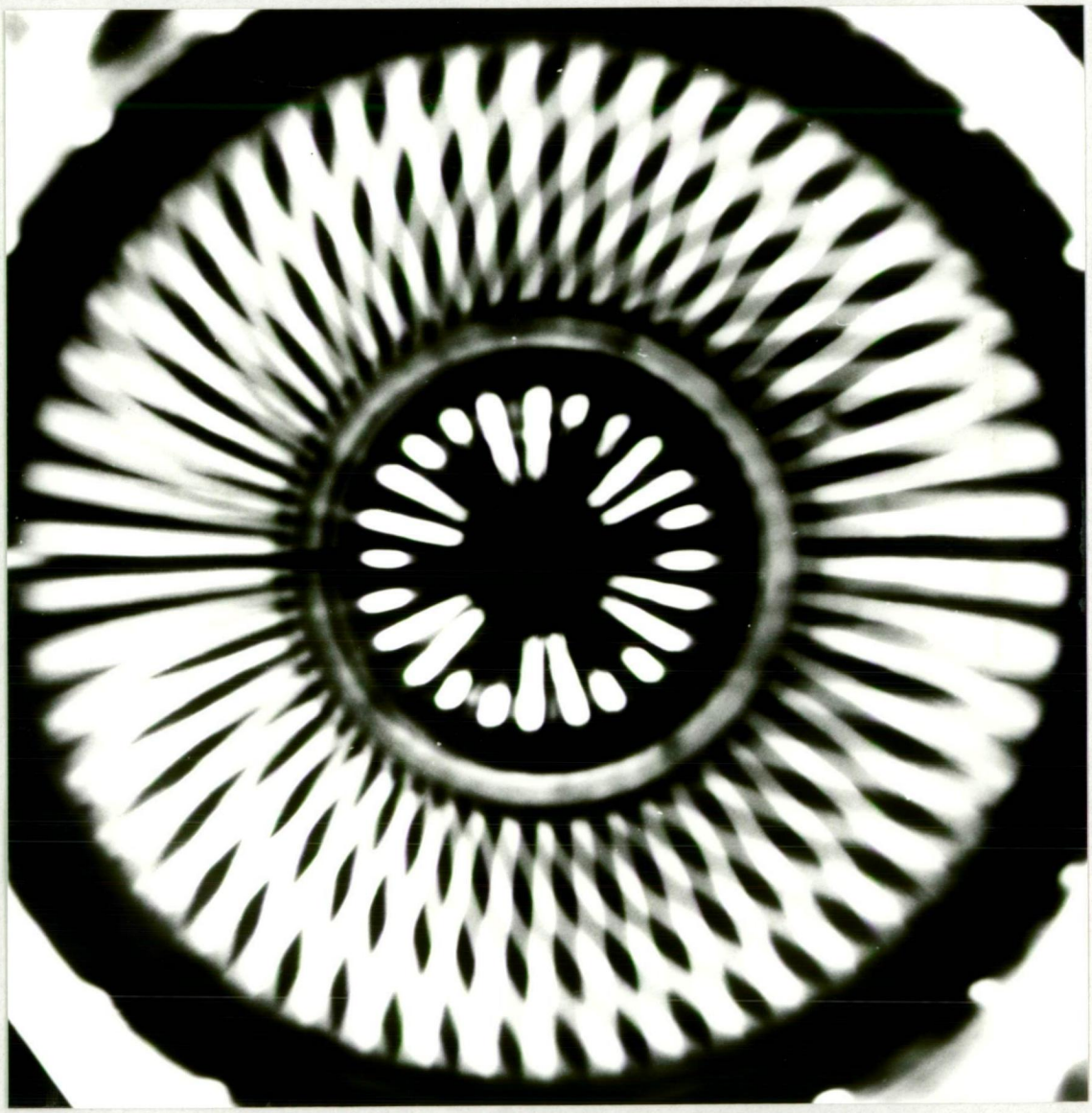

Figure B5a
Moiré Pattern of Shell with Tilted Axis
- Axial Grid (D = 4267 mm)

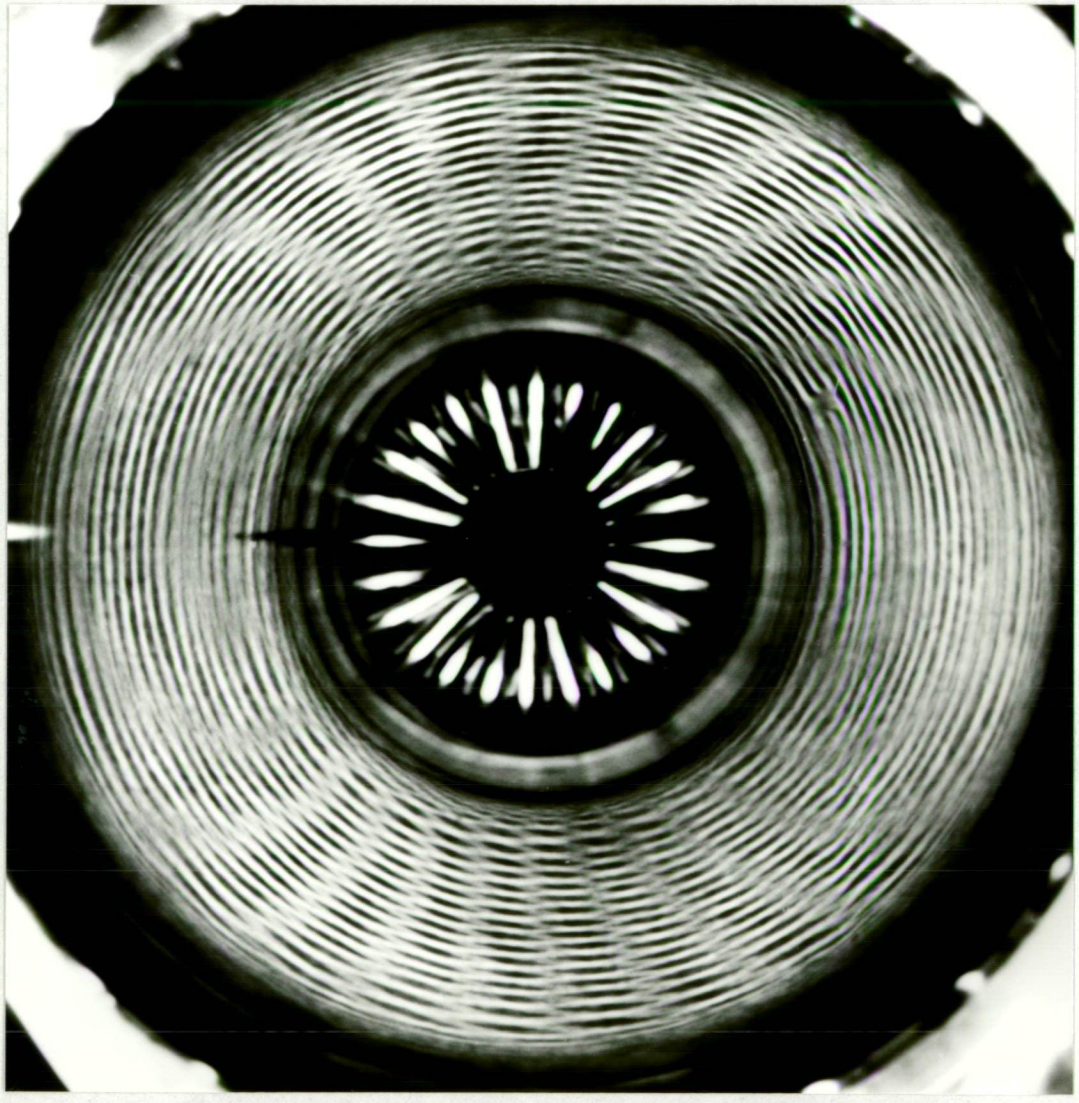

Figure B5b
Moiré Pattern of Shell with Tilted Axis
- Circumferential Grid (D = 4267 mm)

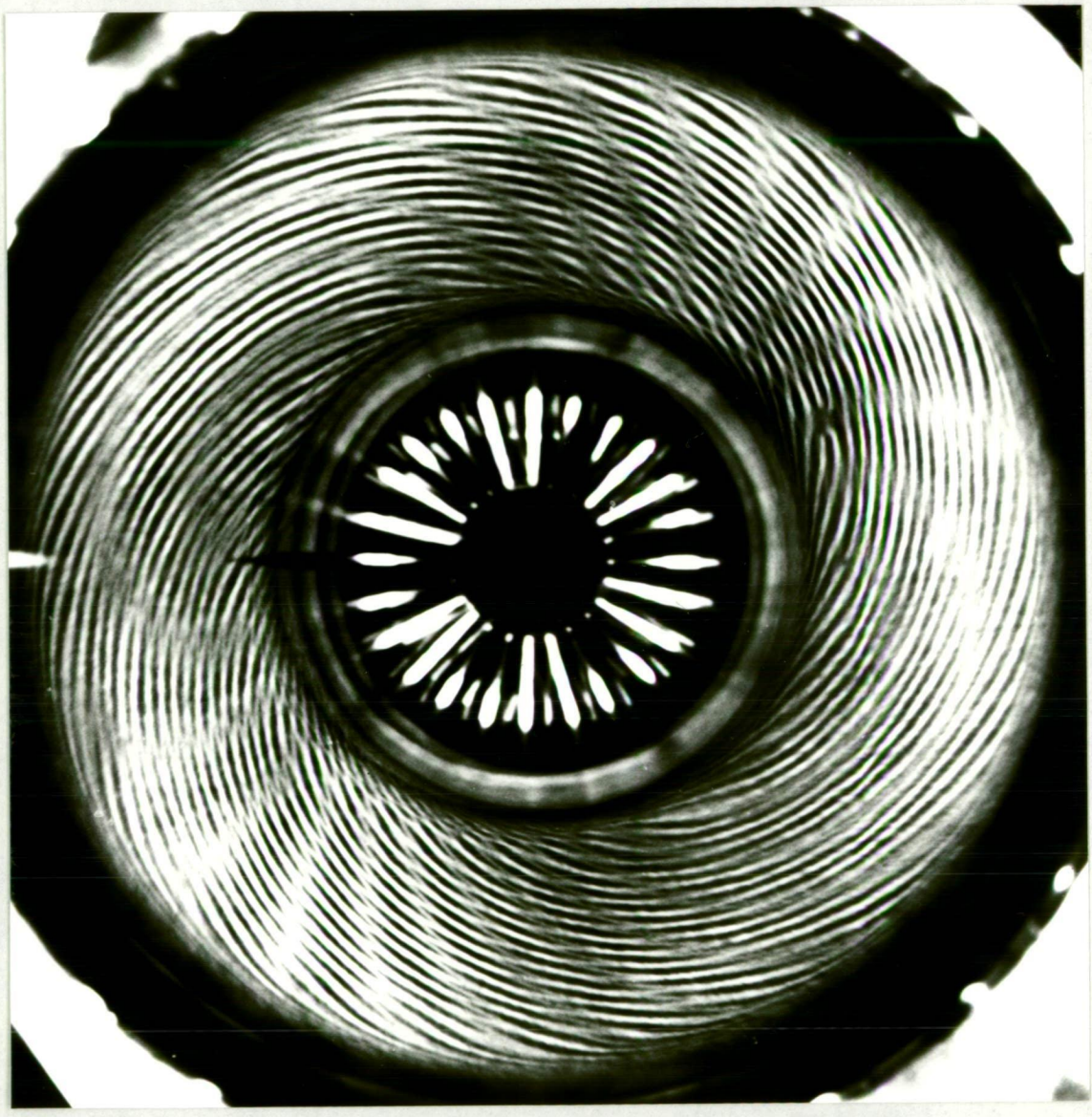

Figure B5c
Moiré Pattern of Shell with Tilted Axis
- Spiral Grid (D = 4267 mm)

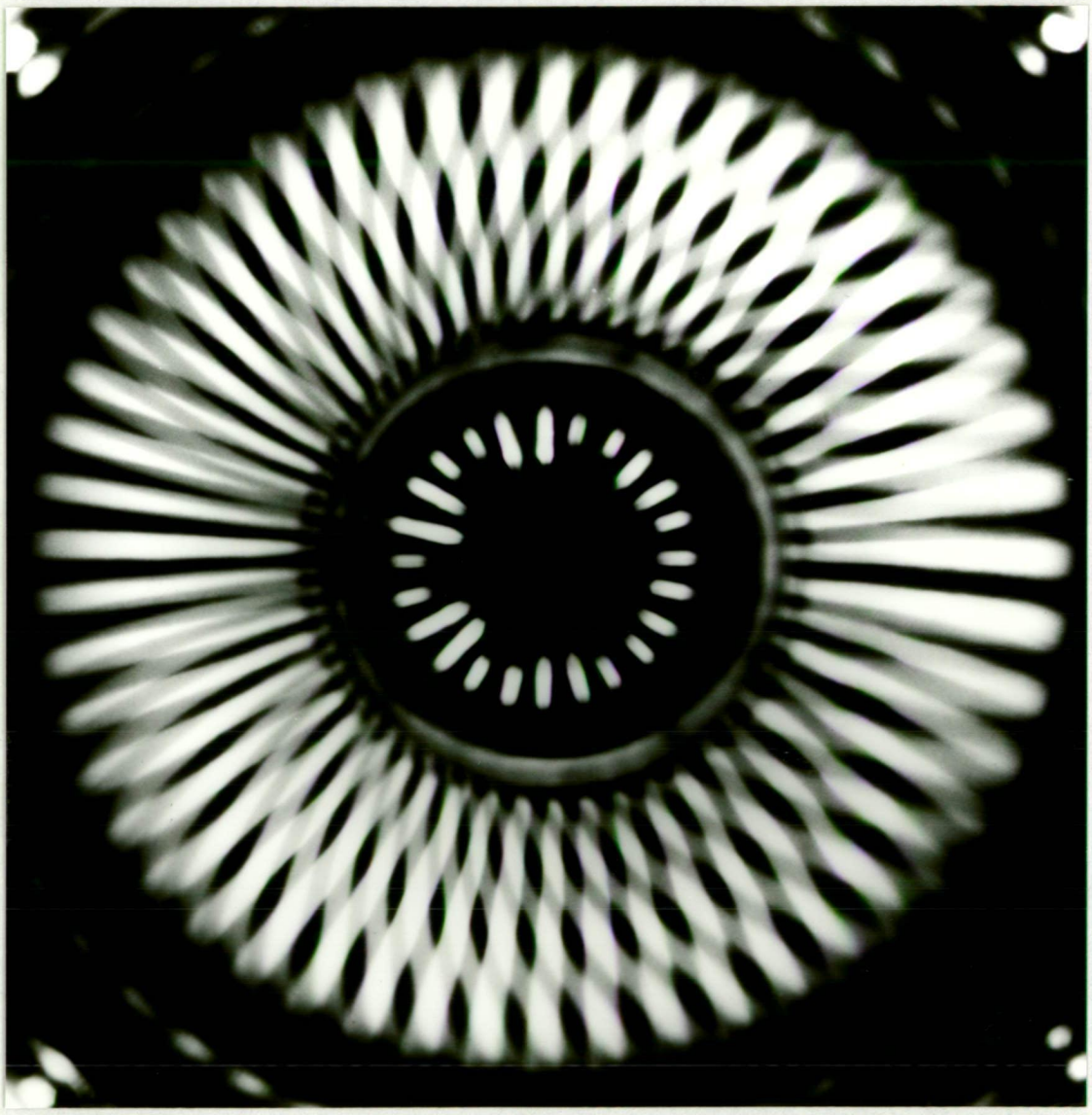

Figure B6a
Moiré Pattern of Shell with Tilted Axis
- Axial Grid (D = 1225 mm)

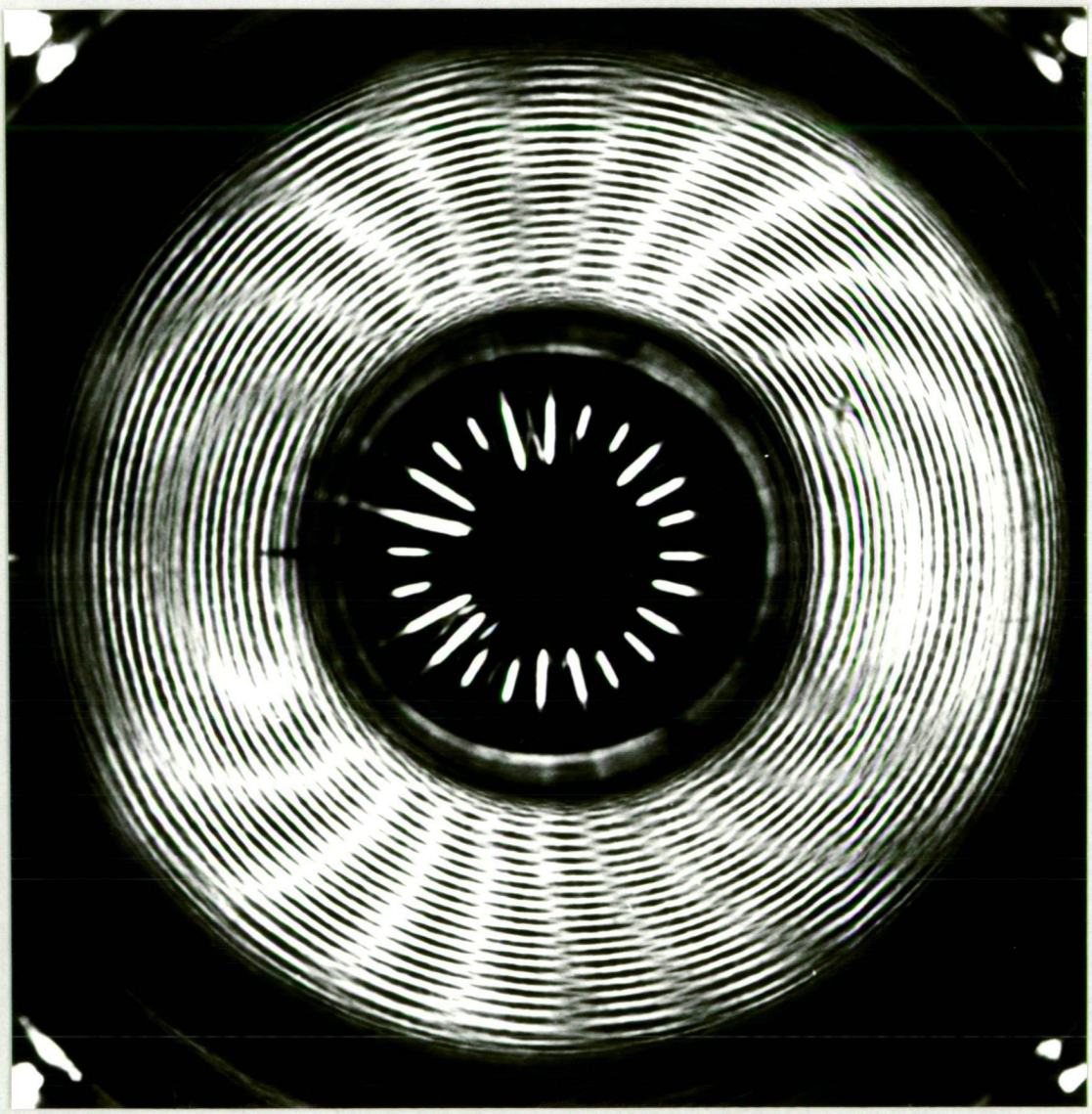

Figure B6b
Moiré Pattern of Shell with Tilted Axis
- Circumferential Grid (D = 1225 mm)

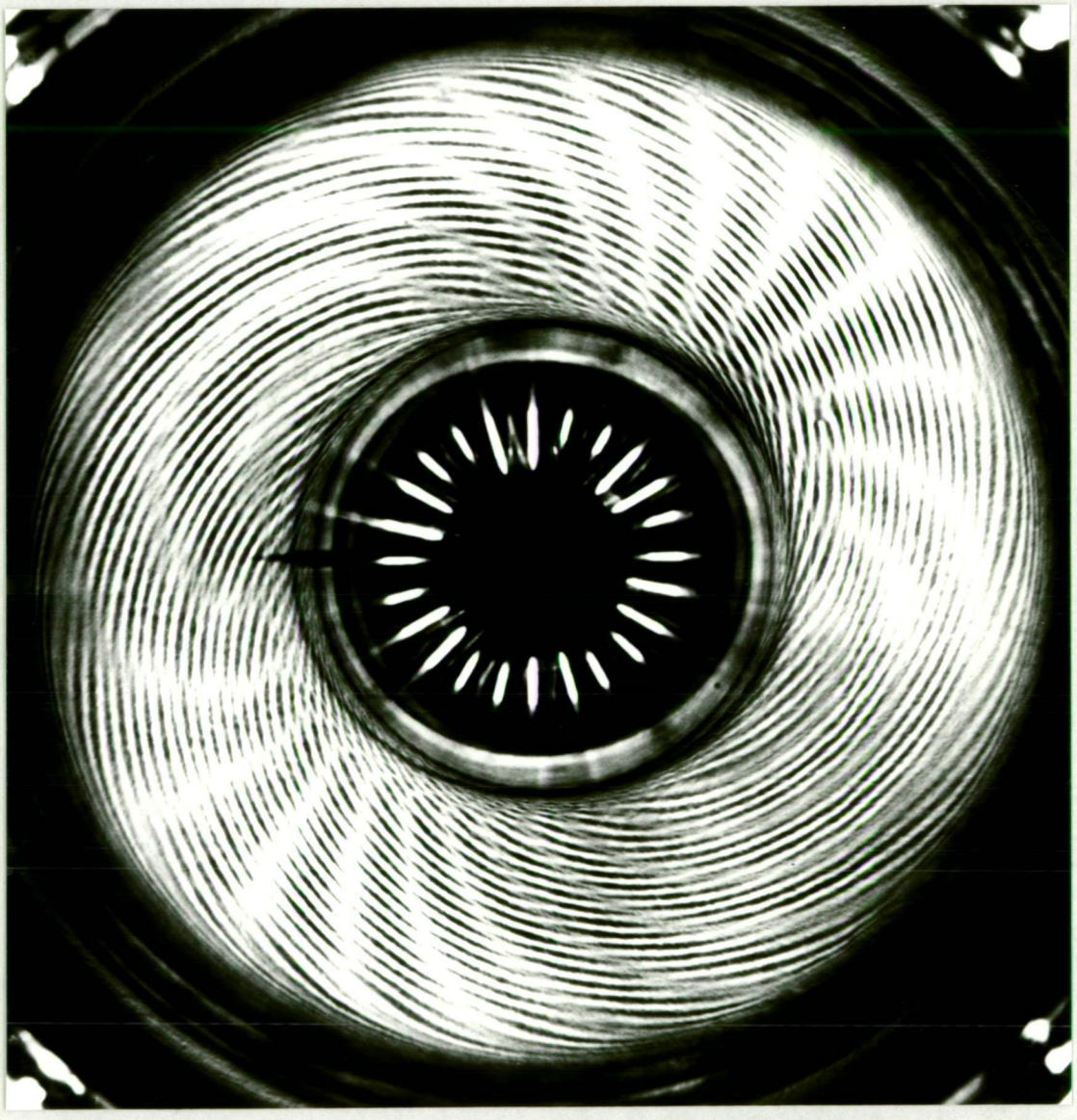

Figure B6c
Moiré Pattern of Shell with Tilted Axis
- Spiral Grid (D = 1225 mm)

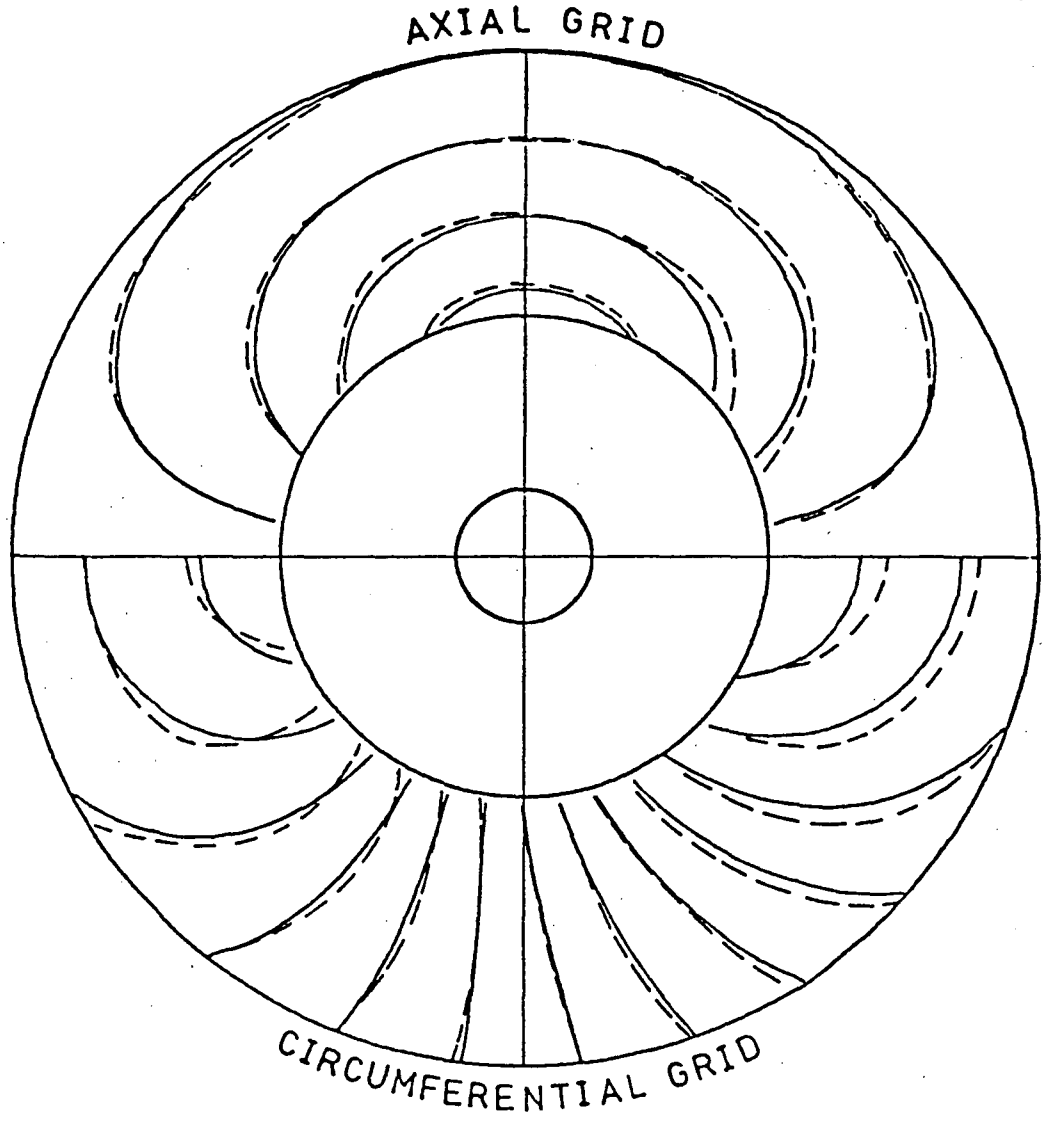

Full Lines — Theoretical Fringes
Dotted Lines — Observed Fringes

Figure B7a
Comparison of Fringes Obtained Optically
with Predicted Fringes (D = 4267 mm)
- Axial and Circumferential Grids

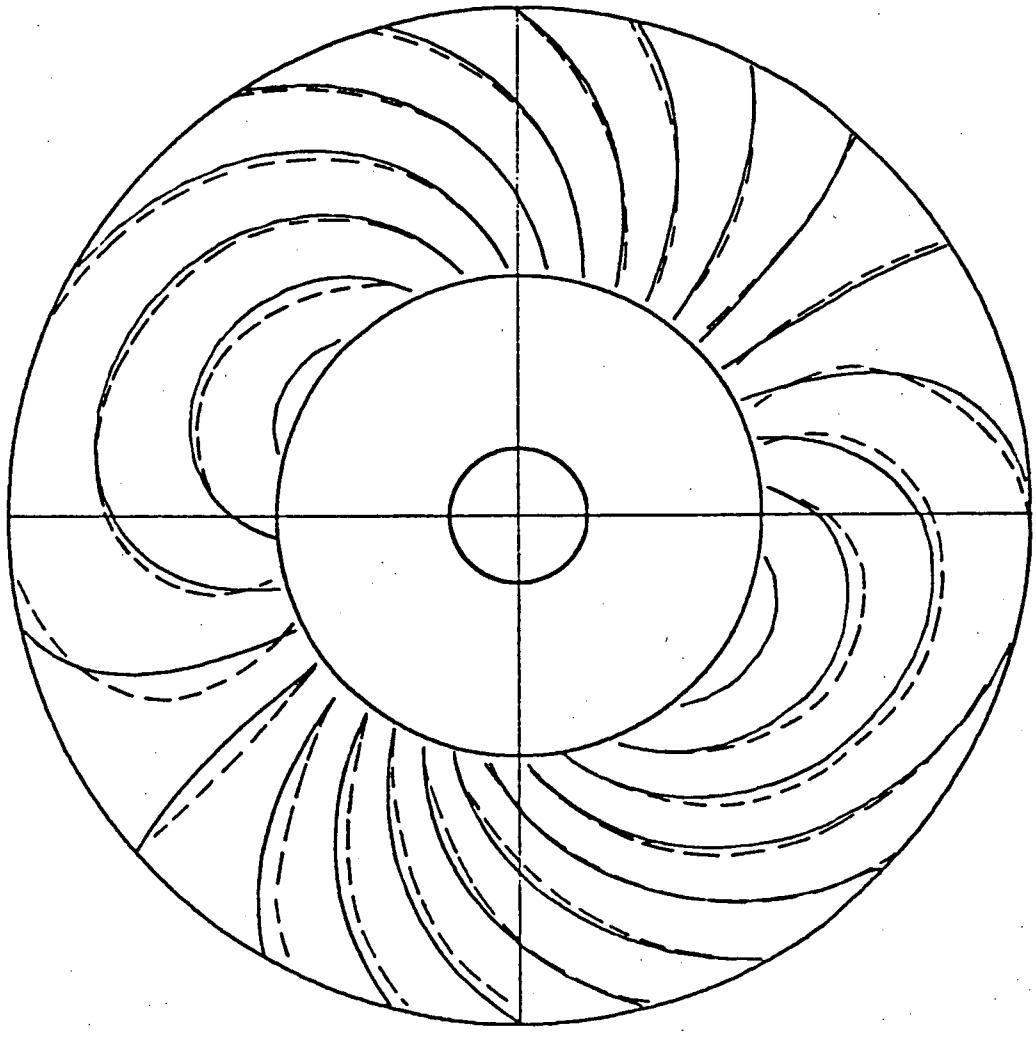

Full Lines — Theoretical Fringes
Dotted Lines — Observed Fringes

Figure B7b
Comparison of Fringes Obtained Optically
with Predicted Fringes (D = 4267 mm)
- Spiral Grid

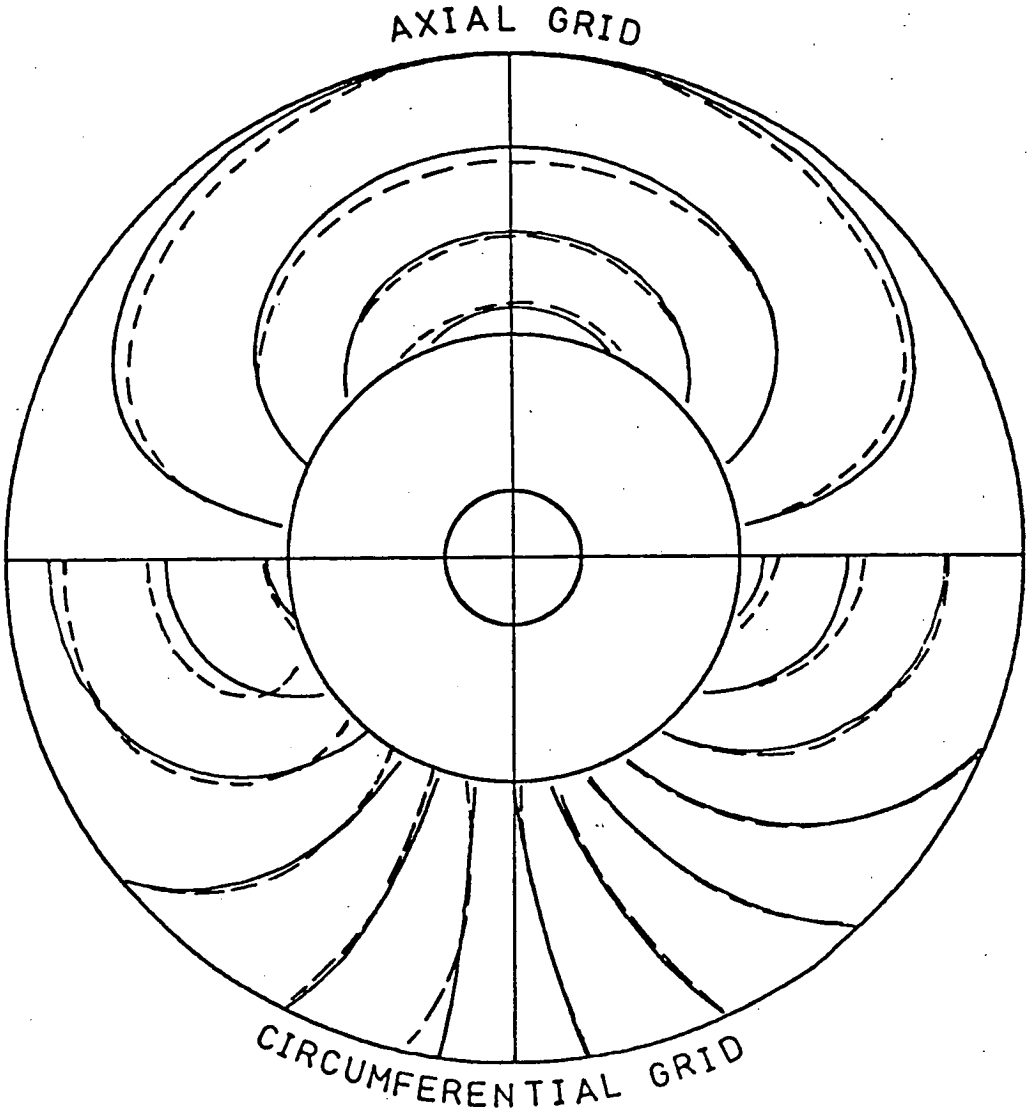

Full Lines — Theoretical Fringes
Dotted Lines — Observed Fringes

Figure B8a
Comparison of Fringes Obtained Optically
with Predicted Fringes (D = 1225 mm)
- Axial and Circumferential Grids

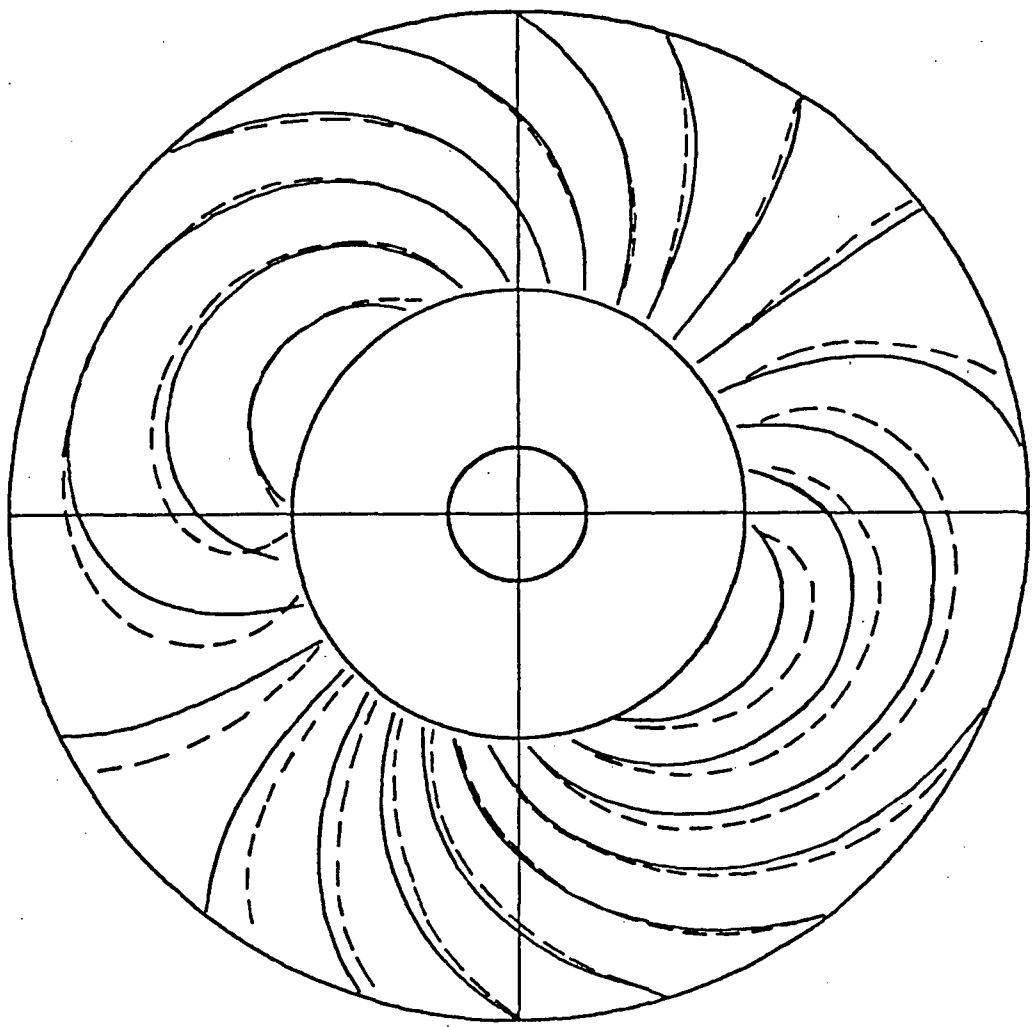

Full Lines — Theoretical Fringes
Dotted Lines — Observed Fringes

Figure B8b
Comparison of Fringes Obtained Optically
with Predicted Fringes (D = 1225 mm)
- Spiral Grid

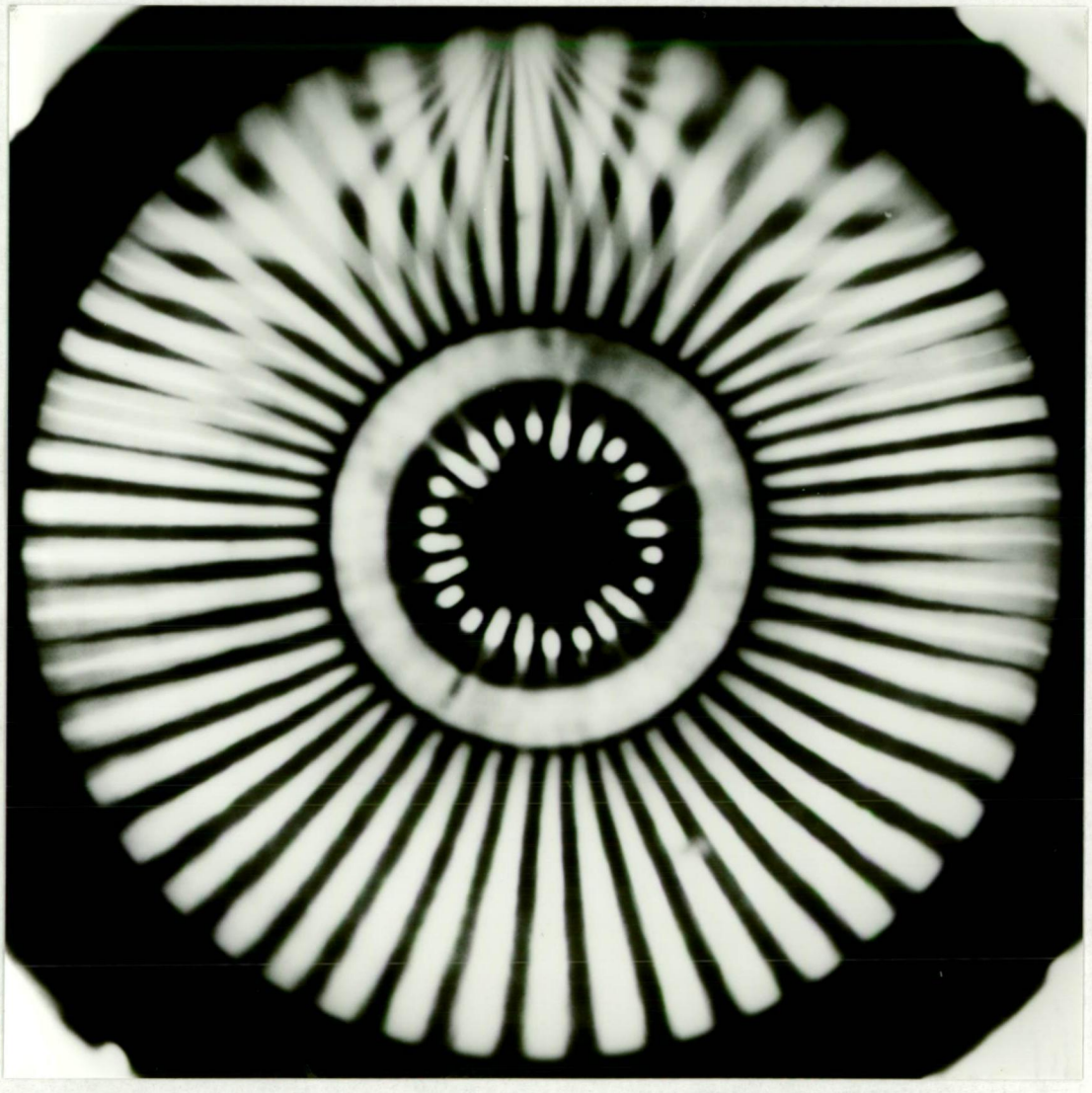

Figure B9a
Moiré Pattern of Shell With Lateral Load
- Axial Grid

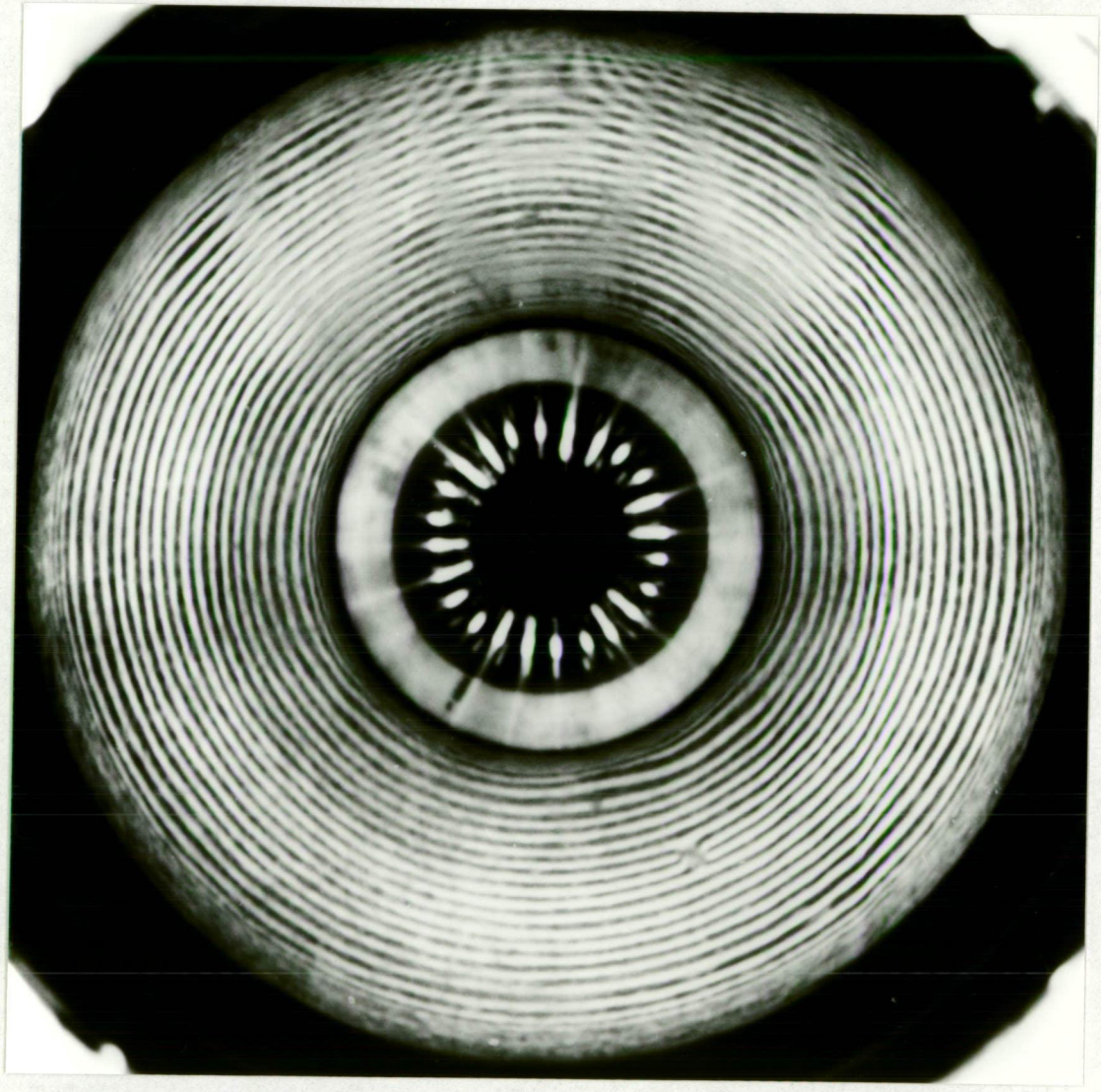

Figure B9b
Moiré Pattern of Shell With Lateral Load
- Circumferential Grid

Figure B9c
Moiré Pattern of Shell With Lateral Load
- Spiral Grid

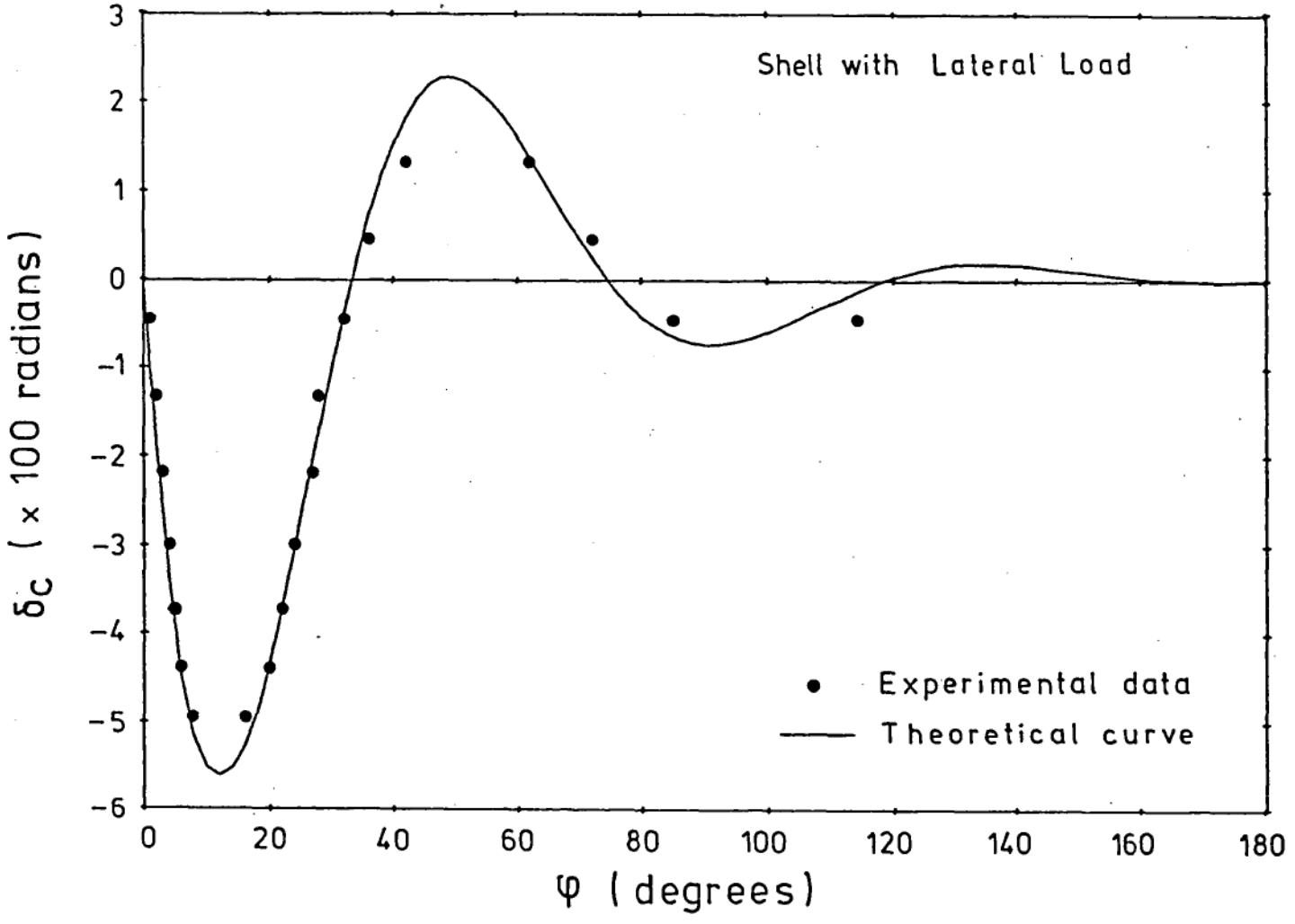

Figure B10. Variation of Circumferential Slope along the Free End of the Shell with Lateral Load

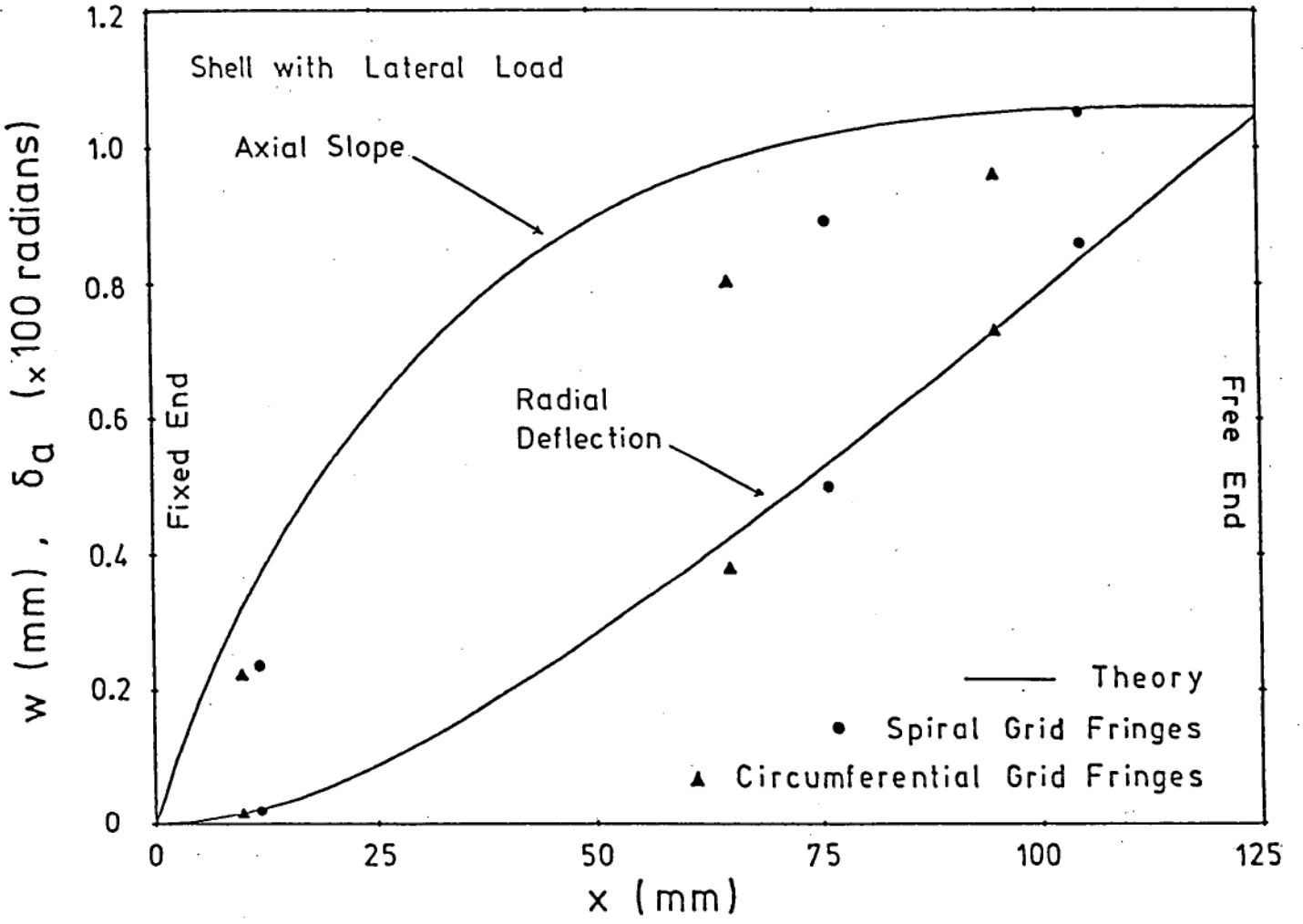

Figure B11. Radial Deflection and Axial Slope along the Generator under the Load

APPENDIX C

TEST DATA

Table C1 Buckling and Post-Buckling Data

Shell	Initial N	Final N	η_{cr}	Post-buckling values				
				η_{pb}	Δ_{pb}	H/L	λ	X/L
S1	0	I-12p	<u>0.614</u>	0.386	67.7	—	—	
S2	0	<u>12</u>	<u>0.837</u>	0.256	48.3	0.207	0.86	0.30
	12	11	0.319	0.254	80.5	0.207	0.78	0.30
	11	10	0.307	0.226	108	0.196	0.68	0.30
	11	9	0.331	0.188	124	0.202	0.63	0.30
	10	9	0.293	0.214	171	0.196	0.61	0.30
	9	8	0.246	0.153	186	0.202	0.56	0.30
S3	0	12	—	—	—	0.158	0.69	0.61
	0	11	0.864	0.229	55.4	0.195	0.78	0.54
	0	<u>10</u>	<u>0.883</u>	0.207	56.4	0.216	0.79	0.49
	11	10	0.327	0.244	123	0.161	0.59	
	10	8	0.312	0.151	212	0.182	0.53	
S4	0	13	0.880	0.297	25.2	0.235	0.70	
	0	<u>12</u>	<u>0.918</u>	0.260	25.9	0.260	0.72	
	12	11	0.394	0.303	67.4	0.250	0.63	
	11	10	0.360	0.236	91.1	0.270	0.62	
	10	9	0.260	0.214	128	0.260	0.54	

<u>Notes</u> : $\eta = P/P_{cl}$, $\Delta = 10^4.\delta L/R^2$. H = Axial height of facets.
X/L = Axial position of the buckles from the bottom (indicated only for those shells in which the buckles formed away from the mid-section).

I - one tier pattern (Values of N without prefix are two tier patterns).
"p" and "i" after the value of N respectively indicate partial (not extending over the whole circumference) and irregular buckle patterns.

Maximum load and minimum number of facets formed on primary collapse are underlined. (N = 0 denotes prebuckling state).

Table C1 (continued)

Shell	Initial N	Final N	η_{cr}	Post-buckling values				
				η_{pb}	Δ_{pb}	H/L	λ	X/L
S5	0	I-9p	0.710	0.311	38.6	—	—	
S6	0	13p	0.793	0.331	16.8	—	—	
	13p	13	0.337	0.278	19.9	0.237	0.64	
	13	12	0.391	0.305	37.2	0.194	0.48	
	12	11	0.364	0.262	54.6	*—	—	
	11	10i	0.301	0.236	79.1	—	—	
	10i	9	0.262	0.218	104.5	—	—	
	9	8	0.243	0.193	145	—	—	
S7	0	11	0.755	0.254	81.0	0.156	0.68	0.63
	0	10	0.837	0.224	87.5	0.189	0.75	0.56
	0	9p	0.887	0.212	92.2	0.200	0.71	0.49
	10	9	0.333	0.245	207	0.144	0.51	
	9	8	0.287	0.194	275	0.172	0.54	
S8	0	12	0.845	0.254	48.2	0.165	0.68	
	0	11	0.879	0.220	48.2	0.215	0.81	
	12	11	0.315	0.249	73.9	—	—	
	11	10	0.344	0.245	137	0.146	0.50	
	10	9	0.294	0.200	174	0.171	0.53	
	9	8i	0.231	0.164	218	—	—	
S9	0	10p	0.661	0.464	38.4	—	—	
S10	0	11p	0.827	0.271	38.3	—	—	
	11p	11	0.278	0.245	41.5	0.237	0.71	
	11	10	0.385	0.286	111	0.208	0.56	
	10	9	0.328	0.221	138	0.200	0.49	
	9	8i	0.266	0.195	211	—	—	

*Note : Occasionally, due to the formation of additional (third tier) buckles the axial height of the facets in the two tier pattern were not uniform. In such cases the axial height and hence the aspect ratio were not measured.

Table C1 (continued)

Shell	Initial N	Final N	η_{cr}	Post-buckling values				
				η_{pb}	Δ_{pb}	H/L	λ	X/L
S11	0	12	0.795	0.267	47.1	0.164	0.63	
	0	11	0.823	0.239	49.4	0.219	0.76	
	0	10	0.882	0.208	50.4	0.260	0.83	
	0	10	0.902	0.213	50.4	0.255	0.81	
	10	9	0.367	0.260	209	0.159	0.45	
	10	8	0.370	0.171	213	—	—	
S12	0	12	0.807	0.308	59.4	0.158	0.63	0.64
	0	11	0.759	0.257	55.4	0.211	0.77	0.56
	0	10	0.845	0.227	59.9	0.250	0.83	0.48
	0	10	0.916	0.235	63.3	0.237	0.78	0.49
	10	9	0.367	0.269	193	0.158	0.47	
	10	8	0.377	0.194	202	0.211	0.56	
	9	8	0.301	0.206	237	0.197	0.52	
S13	0	11	0.797	0.248	48.0	0.234	0.86	
	11	10	0.348	0.241	96.0	0.175	0.59	
	10	9	0.334	0.237	173	0.162	0.49	
	9	8	0.294	0.185	276	0.205	0.55	
S14	0	12p	0.837	0.352	20.0	—	—	
S15	0	12p	0.784	0.322	22.5	—	—	
S16	0	12	0.822	0.289	28.9	0.259	0.73	
	12	11	0.414	0.322	66.9	0.222	0.58	
	11	10	0.377	0.258	90.2	0.259	0.61	
	10	9	0.275	0.229	114	0.250	0.53	
S17	0	13p	0.774	0.297	23.2	—	—	
	13p	13	—	0.274	25.6	0.222	0.67	
	13	12	0.400	0.316	55.4	0.204	0.57	
	12	11	0.370	0.265	72.7	0.222	0.57	
	11	10i	0.278	0.233	85.2	—	—	

Table C1 (continued)

Shell	Initial N	Final N	η_{cr}	Post-buckling values				
				η_{pb}	Δ_{pb}	H/L	λ	X/L
S18	0	8	0.958	0.184	125	0.246	0.78	
	8	7	0.337	0.141	571	—	—	
S19	0	9	0.879	0.319	177	0.171	0.63	0.62
	0	8	0.926	0.260	177	0.205	0.64	0.49
	9	8	0.382	0.276	244	0.205	0.64	
	8	7	0.386	0.253	460	0.148	0.41	
S20	0	11	0.867	0.255	56.1	0.200	0.69	
	11	10i	0.378	0.222	119	—	—	
	10i	9	0.269	0.238	160	0.193	0.55	
	9	8	0.307	0.199	250	0.171	0.43	
S21	0	13p	0.552	0.294	11.9	—	—	
S22	0	10	0.915	0.265	80.5	0.208	0.67	0.40
	0	9	0.923	0.213	79.5	0.236	0.68	0.44
	0	9	0.975	0.217	82.4	0.229	0.66	0.44
	9	7	0.373	0.160	376	0.243	0.54	
	II-10	III-10	0.388	0.262	256	—	—	
S23	0	10	0.890	0.224	62.5	0.232	0.76	
	10	9	0.352	0.255	174	0.156	0.46	
	9	8i	0.307	0.146	271	—	—	
S24	0	9	0.946	0.275	121	0.218	0.64	
	0	8	0.964	0.214	126	0.254	0.66	
	8	7	0.361	0.185	397	—	—	
S25	0	10	0.874	0.362	58.1	0.346	0.62	
	10	9	0.508	0.320	135	—	—	

Note : III - Three tier pattern.

Table C1 (continued)

Shell	Initial N	Final N	η_{cr}	Post-buckling values				
				η_{pb}	Δ_{pb}	H/L	λ	X/L
S26	0	I-8p	0.687	0.395	51.6	—	—	
S27	0	13	0.902	0.319	24.0	0.219	0.59	
	13	12	0.433	0.339	45.6	0.240	0.60	
	13	11	0.454	0.276	54.4	0.240	0.55	
	12	11	0.384	0.287	58.1	0.240	0.55	
	11	10	0.346	0.246	93.1	0.271	0.57	
	10	9i	0.275	0.231	127	—	—	
S28	0	12	0.782	0.232	42.2	0.178	0.72	0.58
	0	11	0.801	0.203	44.2	0.211	0.78	0.47
	12	10	0.348	0.200	97.4	0.171	0.57	
	11	9	0.338	0.186	152	0.164	0.50	
	9	8i	0.241	0.167	236	—	—	
S29	0	12	0.763	0.238	45.2	0.192	0.75	
	12	11	0.338	0.253	86.9	0.178	0.64	
	12	10	0.345	0.198	91.3	0.192	0.62	
	11	10	0.288	0.229	109	0.192	0.62	
	10	9	0.292	0.220	186	0.164	0.48	
S30	0	15	0.849	0.337	14.6	0.256	0.72	
	0	14p	0.837	0.330	15.1	—	—	
	14p	14	0.340	0.305	17.4	0.233	0.61	
	15	13	0.465	0.313	27.4	0.233	0.57	
	14	13	0.433	0.340	38.6	0.233	0.57	
	13	12	0.377	0.266	49.8	0.209	0.47	
	12	11i	0.293	0.222	75.0	—	—	
S31	0	14p	0.737	0.381	8.7	—	—	

Table C1 (continued)

Shell	Initial N	Final N	η_{cr}	Post-buckling values				
				η_{pb}	Δ_{pb}	H/L	λ	X/L
S32	0	12p	0.719	0.271	39.6	—	—	
	12p	12	0.293	0.236	45.3	0.196	0.74	
	12	11	0.361	0.271	59.4	0.182	0.63	
	11	10	0.308	0.227	104	0.192	0.62	
	10	9	0.287	0.204	185	0.175	0.50	
	9	8i	0.238	0.204	208	—	—	
S33	0	11	0.747	0.236	65.2	0.182	0.79	0.60
	11	10	0.352	0.260	149	0.139	0.55	0.60
	10	9	0.304	0.214	194	0.182	0.65	0.60
	9	8	0.252	0.172	243	0.170	0.54	0.60
S34	0	9	0.902	0.264	82.4	0.261	0.67	
	9	7i	0.428	0.222	230	—	—	
S35	0	10	0.846	0.350	105	0.197	0.64	0.34
	0	9	0.910	0.295	111	0.225	0.66	0.42
	9	7	0.431	0.196	244	0.246	0.56	0.42
S36	0	8	0.936	0.278	154	0.253	0.65	
	8	7i	0.426	0.223	382	—	—	
S37	0	12	0.811	0.274	43.9	0.200	0.70	
	0	11	0.840	0.237	44.8	0.246	0.79	
	11	10	0.375	0.277	119	0.185	0.54	
	11	9	0.382	0.205	135	0.177	0.47	
	10	9	0.304	0.217	143	0.177	0.47	
	10	8	0.324	0.164	175	—	—	
S38	0	12	0.785	0.284	35.3	0.234	0.72	
	12	11	0.325?	0.261	49.8	0.246	0.69	
	12	10	0.403	0.245	72.9	0.211	0.54	
	11	10	0.373	0.273	101	0.211	0.54	
	10	9i	0.370	0.182	165	—	—	

Table C1 (continued)

Shell	Initial N	Final N	η_{cr}	Post-buckling values				
				η_{pb}	Δ_{pb}	H/L	λ	X/L
S39	0	10	0.938	0.298	65.3	0.246	0.62	
	10	9i	0.448	0.261	143	—	—	
S40	0	13	0.907	0.365	19.0	0.328	0.59	0.43
	13	12	0.545	0.338	60.4	0.344	0.57	0.43
S41	0	9	0.869	0.318	182	0.180	0.64	0.61
	0	8	0.892	0.259	182	0.233	0.73	0.51
	II-8	III-8	0.392	0.248	471	0.203	0.64	0.41
S42	0	13	0.960	0.361	19.7	0.309	0.63	
	13	12i	0.495	0.297	44.1	—	—	
S43	0	9	0.870	0.337	183	0.184	0.61	0.59
	0	8	0.882	0.268	181	0.221	0.65	0.47
	0	8	0.908	0.268	183	0.209	0.61	0.46
	8	7i	0.407	0.229	462	—	—	—
S44	0	13	0.895	0.327	20.5	0.262	0.64	
	13	12	0.459	0.363	42.8	0.250	0.56	
	12	11	0.397	0.302	51.8	0.262	0.54	
	11	10	0.356	0.265	86.4	—	—	
S45	0	11	0.845	0.257	58.3	0.201	0.72	
	11	10	0.366	0.264	122	0.194	0.63	
	11	9	0.366	0.213	122	0.194	0.57	
	9	8	0.318	0.205	285	0.174	0.45	
S46	0	9	0.927	0.322	112	0.236	0.61	0.36
	9	8i	0.421	0.236	228	—	—	—
	II-9	III-9	0.424	0.325	209	0.231	0.60	0.46

Table C2a Data of First Defects with Nominal Size D1

Sr. No.	Shell	Dist from base X/L	Unloaded Size		Pre-buckled Size			Post-buckled Size				E_1/E_0
			θ	N	η	θ	N	η	Δ	θ	N	
1	S35	0.57	17.5^0	20.6	0.619	34^0	10.6	0.279	101	39^0	9.2	0.96
2	S41	0.61	19^0	18.9	0.531	40^0	9.0	0.237	157	45^0	8.0	0.97
3	S45	0.57	16^0	22.5	0.555	32.5^0	11.1	0.245	49.6	32.5^0	11.1	1.01
4	S36	0.37	18^0	20.0	0.587	36^0	10.0	0.381	122	46^0	7.8	0.97
5	S39	0.61	18^0	20.0	0.498	30^0	12.0	0.382	42.8	41^0	8.8	1.00
6	S37	0.38	17^0	21.2	0.448	31^0	11.6	0.284	35.5	41.5^0	8.7	0.97
7	S44	0.52	16^0	22.5	0.522	18.5^0	19.5	0.336	19.4	21^0	17.1	0.96
8	S40	0.50	16^0	22.5	0.608	19^0	18.9	0.404	33.8	20^0	18.0	0.97
9	S16	0.35	16.5^0	21.8	0.362	20^0	18.0	0.505	25.0	36.5^0	9.9	0.96
10	S27	0.49	17^0	21.2	0.454	18^0	20.0	0.572	21.9	21^0	17.1	0.90
11	S38	0.40	16.5^0	21.8	0.470	29^0	12.4	0.530	31.1	42^0	8.6	0.95
12	S30	0.53	16.5^0	21.8	0.411	25^0	14.4	0.327	14.6	30^0	12.0	0.94

Table C2b Data of First Defects with Nominal Size D2

Sr. No.	Shell	Dist from base X/L	Unloaded Size		Pre-buckled Size			Post-buckled Size				E_1/E_0
			θ	N	η	θ	N	η	Δ	θ	N	
1	S8	0.62	24^0	15.0	0.548	34.5^0	10.4	0.222	43.1	35^0	10.3	0.96
2	S32	0.52	22^0	16.4	0.567	24^0	15.0	0.210	41.5	26^0	13.9	0.99
3	S42	0.50	23^0	15.7	0.581	25^0	14.4	0.399	16.4	35.5^0	10.1	0.95
4	S46	0.51	24^0	15.0	0.580	40^0	9.0	0.318	100	52^0	6.9	0.99
5	S34	0.60	23^0	15.7	0.512	32^0	11.3	0.343	58.3	46.5^0	7.7	0.98
6	S22	0.39	22.5^0	16.0	0.270	25^0	14.4	0.315	58.4	39^0	9.2	0.97
7	S33	0.50	23^0	15.7	0.544	35^0	10.3	0.214	64.4	38^0	9.5	0.98
8	S20	0.42	22.5^0	16.0	0.540	35.5^0	10.1	0.252	54.5	36^0	10.0	0.89
9	S23	0.65	22.5^0	16.0	0.479	27^0	13.3	0.249	48.8	37.5^0	9.6	0.97
10	S31	0.56	22^0	16.4	0.454	24^0	15.0	0.400	8.9	28^0	12.9	0.95
11	S17	0.67	24^0	15.0	0.451	32.5^0	11.1	0.543	20.8	39^0	9.2	0.96
12	S29	0.48	24^0	15.0	0.270	26^0	13.9	0.275	36.9	26^0	13.9	0.99

Table C2c Data of First Defects with Nominal Size D3

Sr. No.	Shell	Dist from base X/L	Unloaded Size		Pre-buckled Size			Post-buckled Size				** E_1/E_0
			θ	N	η	θ	N	η	Δ	θ	N	
1	S43	0.50	37.5^0	9.6	0.588	41.5^0	8.7	0.252	167	47^0	7.7	0.94
2	S18	0.62	34^0	10.6	0.418	39^0	9.2	0.220	102	43^0	8.4	0.94
3	S26	0.51	38^0	9.5	0.548	44^0	8.2	0.375	52.1	48^0	7.5	1.01
4	S24	0.37	37^0	9.7	0.500	42^0	8.6	0.298	77.8	48^0	7.5	0.92
5	S19	0.62	36^0	10.0	0.610	54.5^0	6.6	0.229	160	58^0	6.2	0.95
6	S28	0.51	36^0	10.0	—	—	—	0.237	35.7	37^0	9.7	0.96
7	S25	0.50	35.5^0	10.1	—	—	—	0.415	44.2	43^0	8.4	0.96
8	S11	0.65	37^0	9.7	0.445	42^0	8.6	0.497	38.0	45^0	8.0	0.97
9	S12	0.41	38^0	9.5	0.369	40.5^0	8.9	0.555	46.5	45^0	8.0	1.00
10	S9	0.64	36^0	10.0	0.514	37^0	9.7	0.319	33.7	40^0	9.0	0.96
11	S14	0.65	35.5^0	10.1	—	—	—	0.502	16.3	39^0	9.2	0.91
12	S15	0.35	34.5^0	10.4	0.448	35.5^0	10.1	0.380	21.6	37^0	9.7	0.91

Table C3a Data of Second Defects Imposed (Opposite)

Sr. No.	Shell	Nominal size of second defect	Location of defect		Unloaded Size		Post-buckled Size				** E_2/E_0
			†$\Delta\theta$	*$\Delta X/L$	θ	N	η	Δ	θ	N	
1	S41	D1	180^0	0.00	19^0	18.9	0.326	136	52.5^0	6.9	0.95
2	S29	‡D1	180^0	0.00	19^0	18.9	0.462	33.0	42^0	8.6	1.03
3	S8	D2	180^0	-0.01	24^0	15.0	0.207	41.6	35^0	10.3	0.94
4	S22	D2	180^0	-0.04	22^0	16.4	0.296	58.4	45^0	8.0	0.97
5	S23	D2	180^0	0.00	22^0	16.4	0.277	47.8	28^0	12.9	0.97
6	S24	D3	180^0	0.00	35^0	10.3	0.273	75.9	50^0	7.2	0.86

** Ratio of shell stiffnesses with and without defect.
E_0 = Stiffness (Young's Modulus) of shell without imposed defects.
E_1, E_2 = Effective stiffness (Average stress/Average strain) of shell with one and two defects respectively.
† Angular displacement measured from the first defect.
* Axial distance measured from the first defect (positive upward).

Table C3b Data of Second Defects Imposed (Adjacent)

Sr. No.	Shell	Nominal size of second defect	Location of defect		Unloaded Size		Post-buckled Size				E_2/E_0
			$\Delta\theta$	$\Delta X/L$	θ	N	η	Δ	θ	N	
1	S45	D1	21^0	0.00	16^0	22.5	0.301	45.7	39^0	9.2	1.02
2	S44	D1	19^0	0.00	19^0	18.9	0.310	19.4	21^0	17.1	0.97
3	S40	D1	16^0	0.00	17^0	21.2	0.363	33.8	29^0	12.4	0.92
4	S16	D1	19^0	0.00	19^0	18.9	0.485	25.0	36^0	10.0	0.94
5	S38	D1	18^0	0.00	17^0	21.2	0.511	30.3	38^0	9.5	0.94
6	S30	D1	17^0	0.00	17.5^0	20.6	0.310	13.4	28^0	12.9	0.96
7	S27	‡D2	26^0	0.01	22^0	16.4	0.492	21.9	26^0	13.9	0.91
8	S32	D2	25^0	0.00	24^0	15.0	0.208	40.6	28.5^0	12.6	0.96
9	S42	D2	25^0	0.00	24^0	15.0	0.372	18.8	36^0	10.0	0.90
10	S20	D2	27.5^0	0.00	23^0	15.7	0.507	44.2	43.5^0	8.3	1.00
11	S31	D2	29^0	0.00	22^0	16.4	0.388	8.7	26^0	13.9	0.97
12	S17	D2	28^0	0.00	22.5^0	16.0	0.310	18.7	34.5^0	10.4	0.96
13	S43	D3	44.5^0	0.00	36.5^0	9.9	0.239	150	45^0	8.0	0.91
14	S18	D3	45^0	0.00	36^0	10.0	0.236	99.2	49^0	7.4	0.81
15	S26	D3	42^0	0.00	37^0	9.7	0.358	54.8	43^0	8.4	0.96
16	S19	D3	42.5^0	0.00	37^0	9.7	0.282	143	44^0	8.2	0.87
17	S28	D3	45^0	0.00	36^0	10.0	0.203	35.2	42^0	8.6	0.88
18	S25	D3	44.5^0	0.00	33^0	10.9	0.421	44.8	45^0	8.0	0.90
19	S11	D3	40^0	0.00	37^0	9.7	0.400	38.0	45^0	8.0	0.85
20	S12	D3	40^0	0.00	38^0	9.5	0.541	46.5	45^0	8.0	0.90

‡ Note : The first and second defects imposed on all shells except S27 and S29 (Table C3a) were of the same nominal size.
The first defect on shell S27 was of nominal size D1.
The first defect on shell S29 was of nominal size D2.

Table C3c Data of Second Defects Imposed (Next Tier)

Sr. No.	Shell	Nominal Defect Size	Location of defect		Unloaded Size		Post-buckled Size				E_2/E_0
			$\Delta\theta$	$\Delta X/L$	θ	N	η	Δ	θ	N	
1	S35	D1	9.5^0	-0.14	19^0	18.9	0.265	96.9	41.5^0	8.7	0.97
2	S36	D1	10^0	0.26	19^0	18.9	0.265	129	45^0	8.0	0.98
3	S39	D1	9^0	-0.22	18^0	20.0	0.340	39.0	37^0	9.7	0.99
4	S37	D1	11.5^0	0.21	18.5^0	19.5	0.269	37.8	32^0	11.3	0.96
5	S46	D2	18^0	-0.17	22^0	16.4	0.277	106	42^0	8.6	0.98
6	S34	D2	11.5^0	-0.26	22^0	16.4	0.358	59.2	40^0	9.0	0.98
7	S33	D2	13^0	-0.08	22^0	16.4	0.202	59.1	37^0	9.7	0.96
8	S9	D3	26.5^0	-0.23	36^0	10.0	0.315	37.9	38^0	9.5	0.86
9	S14	D3	19^0	-0.29	35^0	10.3	0.501	17.5	37^0	9.7	0.87
10	S15	D3	23^0	0.30	38^0	9.5	0.361	22.5	43.5^0	8.3	0.87

Table C4 Effective Stiffness of Shells with Multiple Defects

Number of Defects	†Effective stiffness ratio (E/E_0)			
	Shell S11	Shell S12	Shell S25	Shell S43
1	0.97	1.00	0.96	0.94
2	0.86	0.90	0.90	0.91
3	0.85	0.83	0.81	0.88
4	0.81	0.77	0.76	0.83
5	0.75	0.72	0.75	0.75
6	0.69	0.68	0.66	0.73
7	0.64	0.65	0.61	0.70
8	0.55	0.58	0.54	0.62
9	0.51	0.56	——	——
E_0 (Gpa)	3.10	2.91	3.05	3.13

† Effective stiffness E = Average stress/Average strain.
E_0 = Stiffness measured before introducing any defect.

PUBLICATIONS

Part of the work presented in this thesis has been reported for publication in the following two papers:

1. "Large Deflections of Simply Supported Isosceles Triangular Plates Subjected to Edge Shear and Compressive Loading", S.Krishnakumar, International Journal of Engineering Sciences, Vol.26, No.7, pages 673-685, 1988.
2. "Wholefield Optical Examination of Cylindrical Shell Deformations", S.Krishnakumar and C.G.Foster (awaiting publication in Experimental Mechanics).